PREPARATION AND CHARACTERIZATION OF NAFION-BASED NANOCOMPOSITE MEMBRANES FOR FUEL CELL APPLICATIONS

Nonhlanhla Precious Cele

A thesis submitted to the Faculty of Science and Agriculture

University of Zululand

In fulfilment of the requirements for the Degree of

Doctor of Philosophy

2010

Copyright © 2010
Nonhlanhla Precious Cele, All rights reserved.

Declaration

I declare that this thesis is my own, unaided work. It is being submitted for the degree of Doctor of Philosophy at the University of Zululand, KwaDlangezwa. It has not been submitted before for any degree or examination at any other University.

_____ _____Day of _____2010

Nonhlanhla Precious Cele

As the candidate's supervisors we have approved this thesis for submission

_____ _____Day of _____2010

Suprakas Sinha Ray

_____ _____Day of _____2010

Muzi Osman Ndwandwe

Abstract

The Nafion-based nanocomposite membranes with improved properties were prepared by melt-extrusion process at 250°C. The compression molding was then used for the preparation of thin films of about 0.1–0.3 mm. Carbon nanotubes (CNTs) were used as nanofiller to improve Nafion properties. CNTs were chemically treated with nitric acid and hexadecaylamine before incorporation into Nafion. Transmission electron microscopy showed that chemical treatment did not cause any damage to the tubes. Differently treated tubes were incorporated into Nafion in different loadings. CNTs containing Nafion nanocomposite membranes showed significant improvement in thermal stability. Nitric acid treated CNTs (oCNTs) containing Nafion membranes showed excellent thermo-mechanical properties. A balance in water uptake and proton conductivity was observed with Nafion/oCNTs (1wt %) nanocomposite membrane.

Methyl tallow bis(2-hydroxylethyl) quaternary ammonium salt modified montmorillonite, commercially known as Cloisite®30B (C30B), was also used as nanofiller to reduce methanol permeability of Nafion membrane. The content of C30B was varied from 0.5–2 wt% and its effect on different properties of Nafion was studied. Thermo-mechanical properties of Nafion were found to improve dramatically after incorporation of C30B. Methanol permeability of Nafion was decreased after nanocomposite formation with C30B and the electrical conductivity is independent of C30B amount.

Titanium dioxide nanotubes (TNTs) were prepared by hydrothermal treatment of titanium dioxide in presence of potassium hydroxide as a base. TNTs were then used as nanofiller in different proportions to improve Nafion properties so that it can be used as a membrane for fuel cell fabrication. Improved thermal stability of Nafion was observed with incorporation of 0.5 and 2 wt% of TNTs. Methanol permeability was highly reduced with incorporation of 2 wt% TNTs, indicating possible improved fuel cell performance.

Dedication

This thesis is dedicated to my mom Ntombifuthi Cele, for her love, care, and support throughout my studies. Without her endless patience, encouragement, and motivation, this would not have been successful. The values she has instilled in me, her belief in me and her guidance throughout my life have allowed me to be here this day. A special dedication goes to Mrs Nozipho and her late husband Siyabonga Mbhele for always being there for me. Their amazing support over the years has pushed me to the end. An exceptional dedication goes to my lovely kids, Sibulelo and Alondwe, for their love, laughter, and passion. They renew my strength every day of my studies; this is all due to these young angels.

Acknowledgements

"Kepha abamethembayo uJehova, bayothola amandla amasha, bayokhuphuka ngamaphiko njengezinkozi, bagijime bangakhathali, bahambe bangapheli amandla" (Isaiah 40:31).

I thank Almighty God and my ancestors for giving me wisdom and strength throughout my life.

I would like to express my sincere gratitude to the following people for their assistance, guidance, dedication, and persistence during this research project:

- ★ My CSIR supervisor Prof. Suprakas Sinha Ray for his undivided attention, invaluable support, time, and stimulating discussions. He made this research project successful.
- ★ My university supervisor Prof. Muzi Ndwandwe for his invaluable support, guidance, and countless suggestions. His contribution and caring support is much appreciated and has made me a better person.
- ★ Dr. Lucky Sikhwivhilu for his invaluable support, stimulating discussions, meticulous proof reading, knowledge sharing, and his patience. It has made me a better researcher.
- ★ Mr. Manfred Scriba for his engineering skills and technical assistance
- ★ Ms. Retha Roussow and all the members of the National Metrology Institute for South Africa in Pretoria for assistance with Scanning Electron Microscopy and X-ray diffraction measurements.
- ★ Dr. Gerald Malgas and Dr. Christopher Arendse for assistance with the electron microscopy and electrical conductivity studies.
- ★ Mr. Mathew Moodley and Dr. Mani Elayaperumal for their assistance with Raman spectroscopy analysis.
- ★ Dr. Shakes Nonjola and Dr. Kenny Mathe for their knowledgeable discussions and support and all the members of the Energy and Processing unit for assisting with electrochemical impedance spectroscopy measurements.
- ★ All my colleagues at the DST/CSIR Nanotechnology Innovation Centre, the National Center for Nanostructured Materials for general assistance and discussions.

★ All my friends for their contribution, encouragement, and support throughout my studies.
★ Kenneth Fulufhelo Maphaha for his love, encouragement, and incredible support, he gave me courage everyday of my studies. I could not have finished this work without him.
★ My family for their prayers, contribution, and support they gave me throughout my studies. I could not have done this without them.
★ Department of Science and Technology, Council for Scientific and Industrial Research, and the University of Zululand for financial support.

Scientific Output Emanating From This Work

Publication in International Journals

1. "Recent progress on Nafion-Based Nanocomposite Membranes for fuel cell Application", **N. P. Cele** and S. Sinha Ray*, Macromol. Mater. Eng*. **2009**, 294, 719–738.
2. ''Effect of multi–walled carbon nanotubes dispersion on the properties of Nafion fuel cell membranes'', **N. P. Cele**, S. Sinha Ray, and M. Ndwandwe, *OAtube Nanotechnology* **2009**, 2, 510.
3. "Carbon Nanotubes Based Nafion Composite Membranes for Fuel Cell Applications", **N. P. Cele**, S. Sinha Ray, S. Pillai, M. Ndwandwe, L. Sikhwivhilu, and M. K. Mathe, *Fuel Cells* **2010**, 10, 64-71.
4. "Effect of Multi–walled Carbon Nanotubes loading on the properties of Nafion membranes", **N. P. Cele**, S. Sinha Ray, S. Pillai, and M. Ndwandwe, *Macromol. Mater. Eng*. **2010** (*submitted*).
5. "Nafion–Titania Nanotubes Composite Electrolytes for High Temperature Direct Methanol Fuel Cells", **N. P. Cele**, S. Sinha Ray, L. M. Sikhwivhilu, and M. Ndwandwe, *J. Nanosci. Nanotechnol*. **2010** (*accepted*)
6. "Low Methanol Permeable Montmorillonite-Containing Nafion Membranes". **N. P. Cele**, S. Sinha Ray, and M. Ndwandwe, *under preparation* (**2010)**.

Oral Presentations in Conferences

1. Nafion multi-walled carbon nanotubes nanocomposite membranes for fuel cells, **N. P. Cele**, S. Sinha Ray, S. Pillai, and M. Ndwandwe, Nanoscience Young Researcher Symposium, Council for Scientific and Industrial Research (CSIR), Pretoria, *September 2009.*
2. Carbon Nanotube Based Nanocomposites membranes for Fuel Cells, **N. P. Cele,** International Polymer Progressing Society, American regional meeting, South Carolina, Charleston, USA, *October 2008.*

3. Effect of Incorporation of Multi–Walled Carbon Nanotubes on the Properties of Nafion Fuel Cell Membranes, **N. P. Cele,** National Center for Nanostructured Materials Colloquium*,* CSIR, SA, *August 2008.*
4. Effect of Multi–Walled Carbon Nanotubes on the Properties of Nafion Fuel Cell Membranes, **N. P. Cele,** South African Institute of Physics conference*,* University of Limpopo, SA, *July 2008.*
5. Effect of Multi–Walled Carbon Nanotubes on the Properties of Nafion Fuel Cell Membranes, **N. P. Cele,** National Center for Nanostructured Materials, CSIR, SA *July 2008.*

Poster Presentations in Conferences

1. Modification of Multi–Walled Carbon Nanotube Surface for Binding into Polymers, **N. P. Cele**, South African Institute of Physics Conference*,* University of KwaZuluNatal, SA, *July 2009.*
2. Carbon Nanotubes Based Polymer Membranes for Fuel Cells, **N. P. Cele**, NanoAfrica Conference*,* Council for Scientific and Industrial Research, SA, *February 2009.*
3. Nafion Based Nanocomposites Membranes, **N. P. Cele**, Council for Scientific and Industrial Research (CSIR) 2nd Biennial Real and Relevance Conference, CSIR Convention Center, SA, *November 2008* [**Best poster**].
4. Synthesis of Aligned Multi–Walled Carbon Nanotubes by Thermal Chemical Vapor Deposition, **N. P. Cele,** South African Nanotechnology Initiative Conference*,* University of Cape Town, *November 2006*
5. Effect of Nitrogen Flow Rate on Carbon Nanotube Growth, **N. P. Cele,** South African Institute of Physics conference*,* University of the Western Cape, SA, *July 2006.*

Abbreviations and Acronyms

Abbreviations or acronyms	Description
AFM	: Atomic force microscopy
AC	: Alternating current
AFCs	: Alkaline fuel cells
BET	: Brunauer Emmett Teller
CNTs	: Carbon nanotubes
CV	: Cyclic voltammetry
DC	: Direct current
DMSO	: Dimethyl sulfoxide
DMFCs	: Direct methanol fuel cells
DMA	: Dynamic mechanical analysis
EIS	: Electrochemical Impedance Spectroscopy
FT-IR	: Fourier Transform Infra—Red
FCNTs	: Amine functionalized carbon nanotubes
GC	: Gas chromatography
H_2	: Hydrogen
H_2O	: Water
HNO_3	: Nitric acid
PEM	: Proton exchange membrane
PTFE	: Polytetraflouroethyleyne
PNC	: Polymer nanocomposites
MeOH	: Methanol
EtOH	: Ethanol
MMT	: Montmorillonite
PVDF	: Polyvinylidene fluoride
Pt	: Platinum
PAFCs	: Phosphoric acid fuel cells
PBI	: Polybenzimidazole
MWCNTs	: Multi–walled carbon nanotubes

PEMFCs	: Proton exchange membrane fuel cells
PNCs	: Polymer nanocomposites
SOFCs	: Solid oxide fuel cells
MCFCs	: Molten carbonate fuel cells
oCNTs	: nitric acid oxidised carbon nanotubes
TiO_2	: Titanium dioxide
ZrP	: Zirconium phosphate
SiO_2	: Silicon oxide
Pd	: Palladium
pCNTs	: Neat–carbon nanotubes
XRD	: X–ray diffraction
SEM	: Scanning electron microscopy
TGA	: Thermogravimetric analysis
TEM	: Transmission electron microscopy

Keywords

Carbon nanotubes
Conductivity
Electrical properties
Electron
Electrolyte
Fabrication
Filler
Fuel cells
Inorganic
Mechanical
Membranes
Montmorillonite
Nafion
Nanoparticles
Nanocomposite
Physical properties

Polymer

Properties

Proton

Research

Review

Thermal properties

Titania nanotubes

Water uptake

Table of Contents

Declaration ii
Abstract iii
Dedication iv
Acknowledgements v
Scientific Output Emanating from this Work vii
Oral Presentations in Conferences vii
Poster Presentations in Conferences viii
Abbreviations and Acronyms ix
Keywords x

1: General Introduction

1.1 Introduction ..... - 1 -
1.2 Objectives ..... - 3 -
1.3 Thesis Overview ..... - 4 -
1.4 References ..... - 6 -

2: Recent Progress on Nafion-based Nanocomposite Membranes for Fuel Cell Applications

2.1 Introduction ..... - 9 -
2.2 Fuel Cells ..... - 11 -
2.2.1 Alkaline Fuel Cells (AFCs) ..... - 11 -
2.2.2 Phosphoric Acid Fuel Cells (PAFCs) ..... - 11 -
2.2.3 Molten Carbonate Fuel Cells (MCFCs) ..... - 11 -
2.2.4 Solid Oxide Fuel Cells (SOFCs) ..... - 12 -
2.2.5 Proton Exchange/Electrolyte Membrane Fuel Cells (PEMFC) ..... - 12 -
2.3 Chemistry and Synthesis of Nafion ..... - 16 -
2.4 Preparation and Characterization of Nafion-based Nanocomposite ..... - 17 -
2.4.1 Clay-containing Nafion-based Composite Membranes ..... - 18 -
2.4.2 CNTs Containing Nafion Composite Membranes ..... - 25 -
2.4.3 Silica Containing Nafion Composite Membranes ..... - 29 -
2.4.4 Various Nanoparticles Containing Nafion Composite Membranes ..... - 32 -

2.5 Properties of Nafion-based Composite Membranes ..... - 33 -
2.5.1 Mechanical Properties ..... - 33 -
2.5.2 Thermal Stability ..... - 37 -
2.5.3 Methanol Permeability ..... - 40 -
2.5.4 Proton Conductivity ..... - 44 -
2.5.6. Water Uptake/Hydration ..... - 48 -
2.6 Fuel Cell Efficiency ..... - 49 -
2.7 Conclusion ..... - 51 -
2.8 References ..... - 52 -

3: Experimental Methods

3.1 Introduction ..... - 59 -
3.2 Materials ..... - 60 -
3.2.2.1 Carbon Nanotubes (CNTs) ..... - 61 -
3.2.2.2 Layered Silicates ..... - 62 -
3.2.2.3 Titanium Dioxide (TiO2) Nanotubes (TNTs) ..... - 63 -
3.3 Preparation of Polymer Nanocomposites Membranes ..... - 63 -
3.3.1 Solvent Casting Method ..... - 64 -
3.3.2 Melt–Blending Method ..... - 64 -
3.4 Characterization Techniques ..... - 65 -
3.4.1 Fourier Transforms Infrared (FTIR) spectroscopy ..... - 65 -
3.4.2 Raman Spectroscopy ..... - 66 -
3.4.2.1 Setup of Raman ..... - 68 -
3.4.3 Brunauer Emmett and Teller (BET) Surface Area Determination ..... - 69 -
3.4.4 Thermogravimetric Analysis (TGA) ..... - 69 -
3.4.5 Dynamic Mechanical Analysis (DMA) ..... - 69 -
3.4.6 Electron Microscopy ..... - 70 -
3.4.6.1 Scanning Electron Microscopy ..... - 71 -
3.4.6.2 Transmission Electron Microscopy (TEM) ..... - 72 -
3.4.7 Atomic Force Microscopy (AFM) ..... - 73 -
3.4.8 X–ray Diffraction ..... - 75 -
3.4.8.1 Wide Angle X-ray Diffraction (WAXRD) ..... - 76 -
3.4.8.2 Small Angle X-ray Scattering (SAXS) ..... - 77 -

3.4.9 Electrochemical Characterization Techniques ..... - 78 -
3.4.9.1 Cyclic Voltammetry (CV) ..... - 78 -
3.4.9.2 Electrochemical Impedance Spectroscopy (EIS) ..... - 78 -
3.4.9.2.1 EIS Fundamentals ..... - 78 -
3.4.9.2.2 Data Presentation ..... - 80 -
3.4.9.2.3 EIS and Electrical circuit modelling ..... - 83 -
3.4.9.2.4 EIS and Proton Conductivity ..... - 84 -
3.5 Water/Methanol Uptake ..... - 84 -
3.6 Methanol Permeability Measurement ..... - 85 -
3.7 Electrical Conductivity Measurements ..... - 85 -
3.8 References ..... - 86 -

4: Modification of Multi–Walled Carbon Nanotube Surface for Binding into Nafion

4.1. Introduction ..... - 90 -
4.2. Experimental Procedure ..... - 91 -
4.2.1 Materials ..... - 91 -
4.2.2.1 Oxidation of CNTs ..... - 91 -
4.2.2.2 Functionalization of CNTs with Hexadecylamine ..... - 91 -
4.2.2 Characterization Techniques ..... - 92 -
4.3 Results and Discussions ..... - 93 -
4.3.1 FT-IR ..... - 93 -
4.3.2 Raman ..... - 93 -
4.3.3 Morphology ..... - 95 -
4.3.4 X-ray Diffraction ..... - 97 -
4.3.5 Thermal Stability ..... - 98 -
4.4. Conclusion ..... - 100 -
4.5 References ..... - 100 -

5: Effect of Multi–Walled Carbon Nanotubes loading on the Properties of Nafion Membranes

5.1 Introduction ..... - 103 -

5.2 Experimental Part ..... - 104 -
5.2.1 Membrane Preparation ..... - 104 -
5.2.2 Characterization and Property Measurements ..... - 105 -
5.3. Results and Discussions ..... - 105 -
5.3.1 Morphology ..... - 105 -
5.3.2 Electrical Conductivity and Water Uptake of the Membranes ..... - 110 -
5.3.3 Thermal Properties ..... - 114 -
5.3.4 Dynamic Mechanical Measurements ..... - 116 -
5.3.5 Electrochemical Impedance Spectroscopy Measurements ..... - 118 -
5.4 Conclusion ..... - 121 -
5.5 References ..... - 121 -

6: Carbon Nanotube-based Nafion Composite Membranes for Fuel Cell Applications

6.1 Introduction ..... - 124 -
6.2 Experimental Procedure ..... - 124 -
6.2.1 Membrane Preparation ..... - 124 -
6.2.2 Characterization and Property Measurements ..... - 125 -
6.3 Results and Discussion ..... - 126 -
6.3.1 Studies on CNTs and Composites Morphology ..... - 126 -
6.3.2 Thermogravimetric Analysis ..... - 129 -
6.3.3 Mechanical Properties ..... - 130 -
6.3.4 Bulk DC Electrical Resistivity Measurements ..... - 132 -
6.3.5 Proton Conductivity ..... - 132 -
6.4 Conclusion ..... - 136 -
6.5 References ..... - 137 -

7: Low Methanol Permeable Nafion-Organically Modified Montmorrilonite Nanocomposite Membranes

7.1 Introduction ..... - 140 -
7.2 Experimental Details ..... - 141 -
7.2.1 Membrane Preparation ..... - 141 -
7.3 Results and Discussions ..... - 142 -

7.3.1 Morphology ..... - 142 -
7.3.2 FT-IR analyses ..... - 143 -
7.3.3 X-ray Diffraction ..... - 144 -
7.3.4 Thermal Stability ..... - 146 -
7.3.5 Mechanical Properties ..... - 147 -
7.3.6 Electrical Conductivity and Water Uptake of the Membranes ..... - 148 -
7.3.7 Proton Conductivity and Methanol Permeability ..... - 149 -
7.4 Conclusion ..... - 150 -
7.5 References ..... - 150 -

8: Nafion-Titania Nanotubes Nanocomposite Electrolytes for High Temperature Direct Methanol Fuel Cells

8.1 Introduction ..... - 153 -
8.2 Experimental ..... - 154 -
8.2.1 Membrane Preparation ..... - 154 -
8.3 Results and Discussions ..... - 154 -
8.3.1 Structure, Morphology and Thermal Stability of Titania Nanotubes ..... - 154 -
8.3.2 Structural Properties of Nanocomposite Membranes ..... - 157 -
8.3.3 Morphology ..... - 159 -
8.3.5 Water Uptake and Electrical Conductivity ..... - 160 -
8.3.6 Thermal Stability ..... - 161 -
8.3.7 Proton Conductivity and Methanol Permeability ..... - 162 -
8.4 Conclusion ..... - 165 -
8.5 References ..... - 165 -

9: General Conclusions

9.1 Conclusions ..... - 167 -
9.2 References ..... - 169 -

Appendixes

A1. Constants and Conversions ..... - 170 -
A2. Bode Plots Interpretations ..... - 170 -

A3. Small Angle XRD Patterns ..... - 171 -
A5. Methanol Permeability and BET Surface Area..... - 172 -

List of Figures

Figure 1.1 Distribution of South African power plants by fuel type based on 2004 annual production..... - 2 -
Figure 2.1 A schematic diagram of methanol PEM fuel cell. Reproduced from Ref. [9] with permission from John Wiley & Sons. ..... - 13 -
Figure 2.2 Chemical structure of Nafion perfluorinated ionomer. ..... - 15 -
Figure 2.3 TEM micrographs for Nafion membranes filled with 2 wt%: (a) CNa^+, (b) ClH^+, (c) C25A, and (d) C30B. Reprinted from Ref. [21] with permission from Elsevier Science Ltd..... - 21 -
Figure 2.4 XRD Patterns of recast Nafion membrane and Nafion/MMT nanocomposite membranes. Reprinted from Ref. [53] with permission from Elsevier Science Ltd..... - 23 -
Figure 2.5 Computer simulated picture: (a) SWCNT and (b) MWCNT. Reproduced with permission from NASA website. ..... - 26 -
Figure 2.6 TEM migrographs of Nafion membranes filled with 1 wt%:(a) MWCNT, (b) lab. MWCNT–COOH and (c) com. MWCNT–COOH. Reproduced from Ref. [74] with permission from Elsevier Science Ltd. ..... - 28 -
Figure 2.7 XRD patterns of commercial Nafion membrane: (a) Nafion/ silica/PWA composite membranes at different immersion times (b) 5 min and (c) 30 min. Reproduced from Ref. [84] with permission from Elsevier Science Ltd. ..... - 30 -
Figure 2.8 X–ray diffraction profiles: Nafion 117 (A) and composite membranes with different immersion times ((B) 5 min, (C) 30 min). Curve (a) is the convolution of curves (b and c). Measured data are shown by dots. Reproduced from Ref. [84] with permission from Elsevier Science Ltd.- 31 -
Figure 2.9 Storage modulus as a function of temperature of Nafion and Nafion–clay nanocomposites containing 10 and 20 wt% H^+–MMT. Reproduced from Ref. [57a] with permission from Elsevier Science Ltd. ..... - 34 -

Figure 2.10 Tensile properties of Nafion/MMT nanocomposites: (a) stress–strain curves and (b) tensile elongation. Reproduced from Ref. [53] with permission from Elsevier Science Ltd. ..... - 35 -

Figure 2.11 Young's modulus of Nafion membranes filled with MWCNT, com. MWCNT–COOH and lab. MWCNT–COOH as a function of the filler content. Reproduced from Ref. [74] with permission from Elsevier Science Ltd. ..... - 36 -

Figure 2.12 TGA thermo–diagrams: (a) MMT and (b) Nafion/m–MMT composite membrane with various content of MMT. Reproduced from Ref. [20] with permission from Elsevier Science Ltd. ..... - 38 -

Figure 2.13 TGA thermograms for commercial Nafion without treatment N117 and Nafion/silica/PWA composite membrane with silica content of 38.2 μg/g. Reproduced from Ref. [84] with permission from Elsevier Science Ltd. ..... - 39 -

Figure 2.14 Methanol concentration: (a) MMT and (b) Nafion/m–MMT composite membrane with various content of MMT or m–MMT as a function of time. Reproduced from Ref. [20] with permission from Elsevier Science Ltd. ..... - 41 -

Figure 2.15 The methanol permeability of the MWCNTs containing Nafion membranes. Reproduced from Ref. [74] with permission from Elsevier Science Ltd. ..... - 42 -

Figure 2.16 Relative methanol permeability for Nafion nanocomposite membranes as a function of volume fraction of clay: (–) Dispersion medium: low aliphatic alcohols and water. ..... - 44 -

Figure 2.17 Schematic view of proton conductivity cell for four–point–probe electrochemical impedance spectroscopy technique. ..... - 45 -

Figure 2.18 Proton conductivity as a function of temperature for: (a) normal membrane and Nafion resin/MMT composite membrane, and (b) m–MMT (with 3, 5, and 7 wt% clay loading) at completely humidified stage. Reproduced from Ref. [20] with permission from Elsevier Science Ltd. ..... - 46 -

Figure 2.19 Dependence of the C/P ratio on the content of native and modified MMT in Nafion membranes. Reproduced from Ref. [21] with permission from Elsevier Science Ltd. ..... - 47 -
Figure 3.1 Hydrolysis of the Nafion precursor ..... - 60 -
Figure 3.2 Chemical structure of methyl tallow bis(2-hydroxylethyl) quaternary ammonium salt used to modify MMT (Cloisite 30B), where T is Tallow (~65% C18; ~30% C16; ~5% C14) ..... - 63 -
Figure 3.3 Three different possible scattering scenarios are shown here. E1 is the lowest vibrational energy level while E3 is a excited higher energy level. E2 is a metastable state ..... - 67 -
Figure 3.4 Schematic diagram of a Raman spectrometer. ..... - 68 -
Figure 3.5 Illustration of possible signals generated when a high beam interacts with a thin specimen ..... - 71 -
Figure 3.6 The vertical deflection of the cantilever is detected by reflecting a laser beam onto a 2–segment photodiode. ..... - 74 -
Figure 3.7 Interference of radiation between atomic planes in a crystal. Reproduced from Ref. [31] with permission from John & Wiley ..... - 75 -
Figure 3.8 Nyquist plot with impedance vector and its equivalent circuit ..... - 81 -
Figure 3.9 Bode plots with one time constant: (a) frequency vs Z and (b) frequency *vs* phase angle ..... - 82 -
Scheme 4.1 Schematic grafting: (a) neat–MWCNT by carboxylic acid, and futher (b) functionalized by hexadecylamine group. ..... - 92 -
Figure 4.1 FTIR spectra of neat–MWCNTs (pCNTs), oxidized MWCNTs (oCNTs) and amine functionalized MWCNTs (fCNTs). ..... - 94 -
Figure 4.2 Raman spectra of neatpCNTs, oCNTs and fCNTs. ..... - 95 -
Figure 4.3 The SEM micrographs: (a) pCNTs, (b) oCNTs, (c) fCNTs, and TEM images:(d) pCNTs, (e) oCNTs, (f) fCNTs. ..... - 96 -
Figure 4.4 X–ray diffraction patterns of pCNTs, oCNTs, and fCNTs ..... - 97 -
Figure 4.5 Thermogravimetric analysis of pCNTs, oCNTs, and fCNTs ..... - 98 -
Figure 4.6 Dynamic mechanical analysis of pCNTs, oCNTs, and fCNTs ..... - 99 -
Figure 5.1 Scanning electron microscopic images of the cross sectional surface morphology for Nafion pCNTs nanocomposites with different pCNTs loadings: (a) 0.2 wt%, (b) 0.5 wt% and (c) 1.0 wt% ..... - 106 -

Figure 5.2 Scanning electron microscopy images of the cross sectional surface morphology for Nafion–oCNTs nanocomposites with different weight loadings of the oCNTs: (a) 0.2 wt%, (b) 0.5 wt%, and (c) 1.0 wt%... - 107 -
Figure 5.3 Scanning electron microscopy images of the cross sectional surface morphology for Nafion–fCNTs nanocomposites with different weight loadings of the fCNTs: (a) 0.2 wt%, (b) 0.5 wt%, and (c) 1.0 wt% ... - 108 -
Figure 5.4 Optical microscopy images of Nafion nanocomposite films with different weight loadings of pCNTs: (a) 0.2 wt% , (b) 0.5 wt%, and (c) 1.0 wt%..... - 109 -
Figure 5.5 Optical microscopy images of Nafion nanocomposite films with different weight loadings of oCNTs: (a) 0.2 wt%, (b) 0.5 wt%, and (c) 1.0 wt%..... - 110 -
Figure 5.6 Optical microscopy images of nanocomposites films with different weight loadings of fCNTs: (a) N–0.2 wt% fCNTs, (b) N–0.5 wt% fCNTs, and (c) N–1.0 wt% fCNTs. ..... - 111 -
Figure 5.7 Electrical conductivity and water–uptake measurements of Nafion and its nanocomposites with different filler loadings: (a) pCNTs, (b) oCNTs and (c) fCNTs ..... - 113 -
Figure 5.8 Thermogravimetric analysis scans of Nafion and CNTs based Nafion nanocomposites membranes with different filler loadings: (a) pCNTs and (b) oCNTs. ..... - 115 -
Figure 5.9 Temperature dependence of storage modulus for Nafion and its CNTs based nanocomposites with different CNTs loadings: (a) pCNTs, (b) oCNTs, and (c) fCNTs. ..... - 116 -
Figure 5.10 The equivalent circuits for all membranes, where R1 is the electrolytes resistance, R2 is the charge transfer resistance ..... - 119 -
Figure 5.11 Nyquistry plots of Nafion and CNTs nanocomposite membranes with different filler loadings: (a) pCNTs, (b) oCNTs and (c) fCNTs. ..... - 120 -
Figure 6.1 Four–point probe cell for the measurements of proton conductivity. . - 126 -
Figure 6.2 Scanning electron microscopy images of freeze–fractured surface of CNTs–containing Nafion composite membranes: (a) pCNTs, (b) oCNTs, and (d) fCNTs. ..... - 127 -
Figure 6.3 Atomic microscopy images: (a) Nafion and (b) fCNTs containing composite ..... - 128 -

Figure 6.4 Thermogravimetric analysis scans of various samples under air atmosphere at heating rate 10°C/min. ..... - 130 -

Figure 6.5 Temperature dependence of tan delta (tan δ) of neatneat Nafion and its CNTs–containing composite membranes. ..... - 131 -

Figure 6.6 Nyquist impedance plots and their equivalent circuits for: (a) neatneat Nafion membrane and N–pCNT and N–oCNTs composite membranes; (b) N–fCNTs composite membranes measured at room temperature. ..... - 134 -

Figure 6.7 Bode plots of impedance spectra of neatneat Nafion and three different composite membranes. The red plot represents the phase angle and the black one represents the impedance. ..... - 135 -

Figure 7.1 High resolution optical micrographs of Nafion nanocomposite films with different C30B loading (a) 0.5 wt% (b) 1.0 wt% and (c) 2.0 wt%. .... - 143 -

Figure 7.2 Fourier transform infra-red spectra of Nafion, C30B and Nafion nanocomposite films with different loading of C30B. ..... - 144 -

Figure 7.3 X–ray diffraction patterns of Nafion, N–0.5wt% C30B, N–1 wt% C30B and N–2 wt% C30. ..... - 145 -

Figure 7.4 Thermogravimetric analysis scans of Nafion and (a) N–0.5 wt% C30B, (b) N–1 wt% C30B and (c) N–2 wt% C30B measured in air at 5 °C/min. . - 146 -

Figure 7.5 The temperature dependence of tan delta (tan σ) of neat Nafion and its C30B–containing nanocomposite membranes with different C30B loadings. ..... - 147 -

Figure 7.6 Electrical conductivity and water–uptake measurements of Nafion and nanocomposite membranes with different C30B loadings. ..... - 148 -

Figure 8.1 Scanning electron microscopy images of titanium dioxide nanotubes synthesided using convectional autoclave method. ..... - 156 -

Figure 8.2 Fourier transform infra-red spectra of Nafion and its TiO_2 based nanocomposite membranes with different TiO_2 weight percentage. .. - 157 -

Figure 8.3 X-ray diffraction patterns of Nafion, TiO_2 tubes and its TiO_2 based nanocomposite membranes with different TiO_2 weight percentages. - 159 -

Figure 8.4 Electrical conductivity and water–uptake of plots of Nafion, N–0.5 wt% TiO_2NTs, N–1 wt% TiO_2NTs and N–2 wt% TiO_2NTs. ..... - 161 -

Figure 8.5 Thermogravimetric analysis scans of Nafion, N–0.5wt % C30B, N–1 wt% C30B and N–2 wt% C30B measured in air at 5 °C per min. ..... - 163 -
Figure 8.6 Nyquistry plots of Nafion and its TNTs based nanocomposite with different TNTs loadings (0.5 wt%, 1.0 wt% and 2.0 wt%) measurments done at 26 °C and 100% humidity. ..... - 164 -

List of Tables

Table 2.1 Properties of a standard Nafion membrane..... - 15 -
Table 3.1 Common electrical elements for electrochemical impedance ..... - 83 -
Table 5.1 Processing parameters for Nafion nanocomposites preparation..... - 104 -
Table 5.2 Average storage modulus (E') values of membranes at different temperatures..... - 118 -
Table 5.3 Proton conductivity of Nafion and its multi–walled nanocomposite membranes. ..... - 119 -
Table 6.1 Electrical conductivity measurements of nafion and its carbon nanotubes–based nanocomposites..... - 132 -
Table 6.2 Parameters for circuit elements evaluated by fitting data to the equivalent circuit and calculated conductivity for prepared composite membranes. The average calculated error is about 8%. ..... - 136 -
Table 7.1 Processing parameters for Nafion–C30B nanocomposites preparation - 141 -
Table 7.2 Interlayer distances of Nafion and Nafion–C30B nanocomposite membranes. ..... - 145 -
Table 7.3 Comparison of proton conductivity (C) and methanol permeability (P) of neat Nafion resin and Nafion–C30B nanocomposite membranes, with different C30B wt% loadings measured at 25 °C and 100% humidity.. - 149 -
Table 8.1 Proton conductivity (C) and methanol permeability (P) values of Nafion and its TNTs based composite with different TNTs loadings in wt%..... - 164 -

1

General Introduction

1.1 Introduction

Imagine driving home in a polymer electrolyte membrane (PEM) fuel cell car with nothing but water vapor dripping from the tailpipe. Imagine a laptop computer that runs for 30 hours on a single charge. Imagine a world where you plug your house into your car and power lines are a distant memory. These dreams motivate today's fuel cell research. While some dreams like powering your home with your fuel cell car may be distant, others like a 30-hour fuel cell laptop may be closer than you think.

The growing global population and world mobility demands are leading to higher carbon dioxide emissions and creating unprecedented demand on our resources. This has led to intensive research in renewable and alternative energy sources. Fossil fuels are one of the major contributions to global warming. **Figure 1.1** shows the distribution of South African power plants by fuel type based on 2004 annual production and the most electrical power is derived from conventional coal-fire power plants that burn coal in a boiler to generate steam that runs through a steam turbine. The second largest portion of electrical power comes from nuclear power plants that extract heat from nuclear fission reactions to generate steam in a boiler, which then runs a steam turbine. The third most prevalent form of electrical power is natural gas plants that burn gas in a turbine. [1–5]

The main crisis we are facing is that the world is at the point at which global energy demand begins outstripping supply. This has led to a growing demand of renewable and alternative

energy sources. New technologies, such as 'nanotechnology,' also play major roles in ongoing research concerning the electrical energy crisis and the planet's warming.

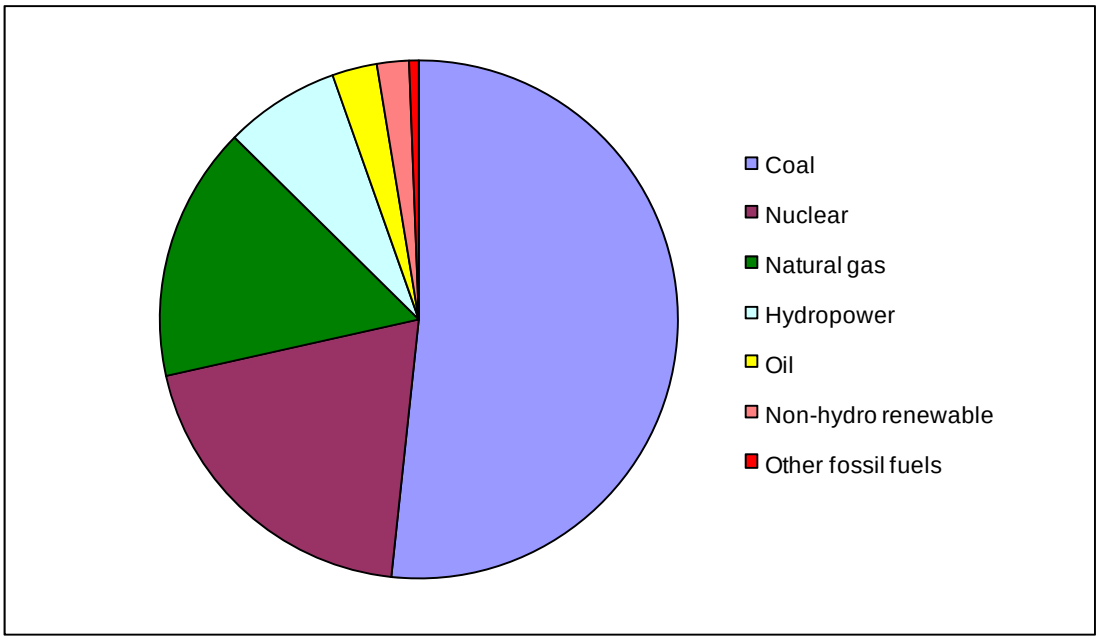

Figure 1.1 Distribution of South African power plants by fuel type based on 2004 annual production [2].

Fuel cells are one of the answers to such problems. A fuel cell is an elegant device that generates electricity quietly and efficiently without pollution. The fuel cell was initially developed by Sir Williams Grove in 1839.[6] Unlike power sources that use fossil fuels, the polymer electrolyte membrane (PEM) fuel cell uses hydrogen or methanol (MeOH) to produce electricity, with the by-products being heat and water vapor. A single PEM fuel cell is comprised of a solid polymer membrane (i.e., Nafion from DuPont) coated with a catalyst on both sides. The membrane is sandwiched between two electrode plates that allow hydrogen and oxygen to flow. By combining single fuel cells, one can make a fuel cell stack to produce enough electricity for vehicular applications. Within a fuel cell stack, chemicals constantly flow into the cell so, unlike a battery, it never goes flat. As long as there is availability of chemicals electricity flows out of a fuel cell.

PEM fuel cells are being developed for automotive applications since it is the most likely alternative energy candidate for transportation. PEM fuel cells offer a high power density, low operating temperature (to ensure quick start-up), high efficiency (twice that of a gasoline car), quiet operation, low operational costs, and most importantly zero tailpipe emissions and independence on crude oil.[5–10]

The major drawback with neat hydrogen (H_2) PEM fuel cells in transportation is the hydrogen storage. Due to many challenges associated with H_2 storage, methanol is used as fuel in transportation and portable electronic device applications. Other challenges associated with the MeOH PEM fuel cells include:

i. Polymer membrane excess methanol permeability
ii. Poor membrane thermal stability
iii. Poor membrane proton conductivity at temperatures above 80°C
iv. Reduced mechanical properties at temperatures above 80°C
v. Uncontrollable membrane water uptake

1.2 Objectives

The aim of this project is to overcome the aforementioned challenges. These challenges can be solved using polymer nanocomposite technology. This technology incorporates nanosize material (nanofiller) into a polymer matrix. This is done to improve the properties of a polymer without destroying its inherent properties. In this project, Nafion blends and Nafion-based nanocomposite membranes have been prepared using nanofillers, such as CNTs, MMT, and titanium dioxide derived nanotubes (TNTs). The main aim is to improve the properties of the Nafion membrane so that it can be used in transportation or automobile applications and in portable electronic devices. With the introduction of this evolutional technology in PEM fuel cells, these energy sources can be used efficiently. The reliance on fossil fuels can also be reduced while providing the comfort and dynamic energy demanded by consumers.

1.3 Thesis Overview

In this thesis, emphasis is placed on fuel cell properties and their applications, which can be beneficial to the environmental and energy sector. This project is about the synthesis and characterization of Nafion-based nanocomposite membranes for fuel cell applications. Its main focus is the preparation of nanocomposite membranes and their properties, such as thermal stability, methanol permeability, and ionic conductivity. The unique advantages of fuel cells make them suitable for automobiles and portable electronic devices.

i. General Introduction (Chapter 1):

   This is devoted to the basic introduction of the energy crisis and demands for alternative energy sources and possible improvements of current technologies. Diagrams and examples of the environmental impact and greenhouse effects of fossil energy are presented.

ii. Recent Progress on Nafion-based Nanocomposite Membranes for Fuel Cell Applications (Chapter 2):

   The aim is to give a brief introduction on fuel cells and the practical aspects of fuel cells focusing on the PEM fuel cell, its Nafion membranes and applications. It includes informative diagrams and tables and a literature review/survey of the Nafion nanocomposite membrane technologies. This chapter shows the preparation of different Nafion nanocomposite membranes and their properties.

iii. Experimental Methods (Chapter 3):

   Of course, no experiment is done without giving a brief discussion of experimental methods and characterization techniques.

iv. Modification of CNTs for Binding into Polymers (Chapter 4):

This contains insightful information about the chemical treatments done to make CNTs compatible with Nafion matrix. Scanning and transmission electron microscope images of neat CNTs, nitric acid treated CNTs and hexadecylamine modified CNTs tell the story about the morphology and sizes of the tubes.

v. Effect of CNT Loading on Nafion Membrane Properties (Chapter 5):

Differently treated CNTs were then incorporated into Nafion membranes, forming polymer nanocomposite-based membranes. The effect of varying CNTs content on thermal and mechanical properties of Nafion are studied and discussed in this chapter. The nanocomposite membrane of Nafion with 1 wt% of CNTs performed better and further studies were reported in next chapter.

vi. CNT-based Nafion Composite Membranes for Fuel Cell Applications (Chapter 6):

This gives details about nanocomposite membrane's properties such as water uptake, proton conductivity with 1 wt% of differently treated CNTs.

vii. Nafion/MMT Nanocomposite Membranes for Polymer Electrolyte Fuel Cell Applications (Chapter 7):

This focuses on the modified MMT as nanofiller to improve Nafion barrier properties. This can reduce methanol permeability of the Nafion membranes. The effect of different loadings of MMT on Nafion properties were studied in this chapter.

viii. Nafion/TNTs Composite for Polymer Electrolyte Membrane Application (Chapter 8):

Titanium dioxide derived nanotubes were also used as a nanofiller in different proportions and their effects on Nafion membranes properties such as water uptake, thermal stability, mechanical properties, and ionic conductivity were studied.

ix. General Conclusions (Chapter 9):

Finally, this chapter gives a general summary and conclusions of all the results. The potential nanocomposite membrane is known and future suggestions are discussed in this chapter.

1.4 References

[1] J.H. Hirschenhofer, D.B. Stauffer, R.R. Engleman, and M.G. Klett, Fuel Cell Handbook 6th ed. *US Department of Energy*, WV **2003**.

[2] A. Engelbrecht, A. Golding, S. Hietkamp, and B. Scholes, The potential sequestration of carbon dioxide in South Africa, CSIR report 86DD/HT339, *SA Department of Mineral and Energy*, **2004**.

[3] [3a] K. Scott, W. Taama, and J. Cruickshank, *J. Appl. Electrochem.* **1998**, *28*, 289–297. [3b] D.S. Scott and W. Hafele, *J. Hydrogen Energy* **1990**, *15*, 727–736. [3c] D.H. Jung, Y.B. Myoung, S.Y. Cho, D.R.Shin, and D.H. Peck, Intl. *J. Hydrogen Energy* **2001**, *26*, 1263–1269.

[4] L. Carrette, K.A. Friedrich, and U. Stimming, *Chem. Physchem* **2000**, *1*, 162–193

[5] A. Hamnett, *Catalysis Today* **1997,** *38*, 445–357.

[6] C.R.Wilke, *J. Chem. Phys.* **1950**, *18*, 517–519.

[7] P.P. Kundu, B.T. Kim, J.E Ahn, H.S. Han, and Y.G. Shul, *J. Power Sources* **2007**, *171*, 86–91.

[8] Y.A. Eladb, E. Napadensky, C.W. Walker, and K.I. Winey, *Macromolecule*s **2006**, *39*, 399–407.

[9] K. Okamato, Y. Yin, O. Yamada, M.N. Islam, T. Honda, T. Mishima, Y. Suto, K, Tanaka, and H. Kita, *J. Membr. Sci***. 2005**, *258*, 115–122.

[10] M. Sankir, Y.S. Kim, B.S. Pivovar, and J.E. McGrath, *J. Membr. Sci* **2007**, *298*, 48–55.

2

Recent Progress on Nafion-based Nanocomposite Membranes for Fuel Cell Applications

Abstract

The proton exchange membrane fuel cells have attracted tremendous attention in recent years because of their highest efficiency compared to other types of fuel cells. Nafion, a perfluorinated polymer substituted by sulfonic acid groups, is the most commonly used polymer for the fabrication in proton exchange fuel cell membranes. A large variety of nanoparticles of different natures and sizes can be blended with the Nafion matrix, therefore, generating a new class of nanostructured electrolyte membranes with interesting physical properties. The main aim of this chapter is to review the latest research in the field of Nafion-based nanocomposite membranes for fuel cell applications. These membranes have attracted both academic and industrial attention because they exhibit significant improvement in thermo-mechanical and thermal stability as well as proton conductivity at very low filler content. Herein, the preparation, characterization, and properties of various types of Nafion-based nanocomposite membranes are critically reviewed in general, and detailed examples are summarized from the available literature.

2.1 Introduction

Hydrocarbon fuels, such as coal, oil, and natural gas, are widely used as electricity sources. Depletion of hydrocarbon fuels will lead to electricity shortage in most countries, especially in developing countries, where storage is not sufficient. The disadvantage of these hydrocarbon fuels is their toxic emissions into the atmosphere. This has led to an ever growing need to find cleaner and pollution free alternative power sources, which will not only decrease environmental pollution but also decrease the shortage of electrical energy. Fuel cells are one of the most promising alternative power sources, with efficiency of up to 60%, higher energy densities relative to batteries, and the ability to operate on clean fuels while producing no pollutants.[1–4] They also operate very quietly, reducing noise pollution.[5] The only by-product of proton exchange membrane (PEM) fuel cells is water, thus completely eliminating all emissions. Because of these advantages, fuel cells are being developed for numerous applications, such as automobiles, portable electronic devices, and mobile and stationary power generation. It is widely known that there are still many technical and market-related issues to overcome before fuel cells can become commercially viable technology on a large scale. These challenges include decreasing the fuel cell cost, choosing the appropriate fuel source and infrastructure, and increasing its performance at higher temperatures of about 100°C.[11–12]

Research in the area of fuel cells has exponentially grown over the last 20 years, [3–12] especially in PEM fuel cells. These are inexpensive to operate and give the highest efficiency compared to other types of fuel cells. They operate at relatively low temperatures of about 80°C, which makes them ideal to be used in homes and automobile applications. PEM fuel cell uses a polymer membrane as an electrolyte, which conducts protons to the cathode side. The most commonly used membrane is Nafion, a perfluorosulfonyl fluoride copolymer from DuPont. Nafion is the standard by which all new materials are compared.

Although Nafion is the most suitable candidate for the fabrication of fuel cell membrane, Nafion-based membranes have major drawbacks such as high production cost, low conductivity at low humidity and/or high temperature (>100°C), loss of mechanical stability at high temperature (~100°C), elevated methanol permeability, and restricted operation temperature. The higher

methanol/water permeability at high temperature must be overcome because high methanol permeability not only decreases the fuel cell efficiency, but also the cathode performance. Furthermore, solid electrolyte membranes with high proton conductivity (> 0.01 S/cm) and little or no dependence on humidity above 100°C are very desirable, because of the beneficial effect of elevated temperatures on electrode kinetics, carbon monoxide (CO) tolerance of the electro-catalysts as well as the use of lower amounts of precious platinum (Pt) metals.[2, 9, 14–17] Thomassin et al. measured the methanol permeability of the MWCNTs containing Nafion membranes, and the corresponding results are reported in **Figure 2.17**.[74] Upon the addition of 2 wt% of MWCNTs, the permeability value of neat Nafion membrane decreased to 60%, and this value is much higher than that of clay-containing Nafion membranes.[21] This may be due to the fine dispersion of MWCNTs in Nafion matrix, although MWCNTs are expected to be less effective than the platelet-like fillers such as layered silicates. The permeability value further decreased when lab. MWCNT-COOH dispersed in Nafion matrix, which may reflect a better dispersion of the MWCNTs into Nafion matrix compared to the unfunctionalized MWCNTs. However, beyond 2 wt% MWCNTs incorporation, the permeability did not improve anymore, rather permeability efficiency decreased with the MWCNTs loading. This may be due to the aggregation of MWCNTs in Nafion matrix. On the other hand, the effect of incorporation of com. MWCNT-COOH was lower than in the other two cases, more likely because of the shorter length of these tubes. One of the most commonly used strategies to overcome these drawbacks is the modification of Nafion by using polymer nanocomposite technology.

This chapter provides a snapshot of the recent developments in fabrication, characterization, and properties of the high temperature Nafion-based nanocomposite membranes for PEM fuel cell applications. Over the past few years various types of nanoparticles, such as clay, carbon nanotubes, silica, etc., have been incorporated into the Nafion matrix for the preparation of high temperature proton exchange membranes.[6–11] Progress and ongoing developments on the fabrication and characterization of Nafion-based nanocomposite membranes are discussed. The improved thermal and thermo-mechanical properties, methanol permeability, and proton conductivity of various types of Nafion-based nanocomposite membranes are summarized. Finally, the suitable application possibilities and the future prospect of Nafion-based nanocomposite membranes for fuel cell applications are reviewed.

2.2 Fuel Cells

A fuel cell is an electrochemical device that converts chemical energy of a fuel into electrical energy.[2, 5, 6] Fuel cells can be classified based on the type of electrolyte used and are of five main types.[7, 8]

2.2.1 Alkaline Fuel Cells (AFCs)

AFCs operate on compressed hydrogen and oxygen. They generally use a solution of potassium hydroxide (KOH) in water as their electrolyte. Efficiency is about 70% and operating temperatures are 150–200°C. The cell output ranges from 300W to 5kW. AFCs require neat hydrogen fuel and platinum as electrode catalysts.

2.2.2 Phosphoric Acid Fuel Cells (PAFCs)

PAFCs use phosphoric acid as the electrolyte. Efficiency ranges from 40–80% and operating temperatures are in the range of 150–200°C. These types of cells have outputs of up to 200kW. PAFCs tolerate a carbon monoxide concentration of about 1.5%, which actually broadens the choice of fuels. For these cells, platinum electrode catalysts are needed and internal parts must be able to withstand the corrosive acid.

2.2.3 Molten Carbonate Fuel Cells (MCFCs)

MCFCs generally use the high temperature metal carbonate salts, such as sodium or magnesium carbonates, as the electrolyte. The operating temperature is about 650°C and the efficiency ranges from 60–80%. For these types of cells nickel electrode catalysts are used and are inexpensive compared to a platinum (Pt) based one. However, the high temperature operation limits the materials and safe uses of MCFCs. The reaction products from the electrolyte carbonate ions make it necessary to inject carbon dioxide to compensate.

2.2.4 Solid Oxide Fuel Cells (SOFCs)

SOFCs use metal oxides such as calcium oxide, zirconium oxide, etc., as the electrolyte. The performance efficiency is about 60% and the operating temperature is about 1000°C. Cells output is up to 100 kV. One of the biggest advantages of SOFCs is that the electrolyte is solid; however, the high temperature operation limits the applications of SOFCs.

2.2.5 Proton Exchange/Electrolyte Membrane Fuel Cells (PEMFC)

PEMFCs use a membrane that conducts only protons to the cathode side. They are inexpensive to operate and give the highest efficiency compared to other types of fuel cells discussed above. These cells operate at a low enough temperature (80°C) to make them suitable for homes and cars. However, their fuels must be purified and a platinum catalyst is used on both sides of the membrane, raising costs.

PEM fuel cells can be divided into fuel cells and direct methanol fuel cells (DMFC), depending on the nature of the fuel use. The hydrogen fuel cell uses H_2 gas as fuel and provides excellent fuel cell performance and efficiency. While the direct methanol fuel cell uses liquid methanol (MeOH) as a fuel that provides relatively low performance, due to the methanol permeability through the membrane, it prevents the use of a reformer to produce hydrogen.[1–3, 9] The main components of a representative PEM fuel cell are:

- Electrodes (anode and cathode)
- Membrane electrode assembly (MEA)
- Gas diffusion layer (GDL)
- Collector graphite plates (CGP)

At the interface between the anode catalyst, which is typically Pt-based, and the electrolyte, fuels are converted into protons (H^+) and electrons (e^-). The protons enter through a PEM that prohibits electrons to the cathode side. This is the unique property of a PEM, and it only allows protons to diffuse, hence avoiding shorting out the circuit. The electrons (e^-) are conducted

through the external circuit and delivers energy to do useful work such as turning a motor on the way to the cathode. At the cathode, the transferred protons and the energy-depleted electron combine with oxygen to form water. Theoretically, any substance capable of chemical oxidation and can be supplied continuously can be used as fuel. Also the oxidant can be any fluid that can be reduced at a sufficient rate. However cost, reactivity, and availability are the key issues in their selection. [9] A schematic diagram of a representative methanol PEM fuel cell is shown in **Figure 2.1**.

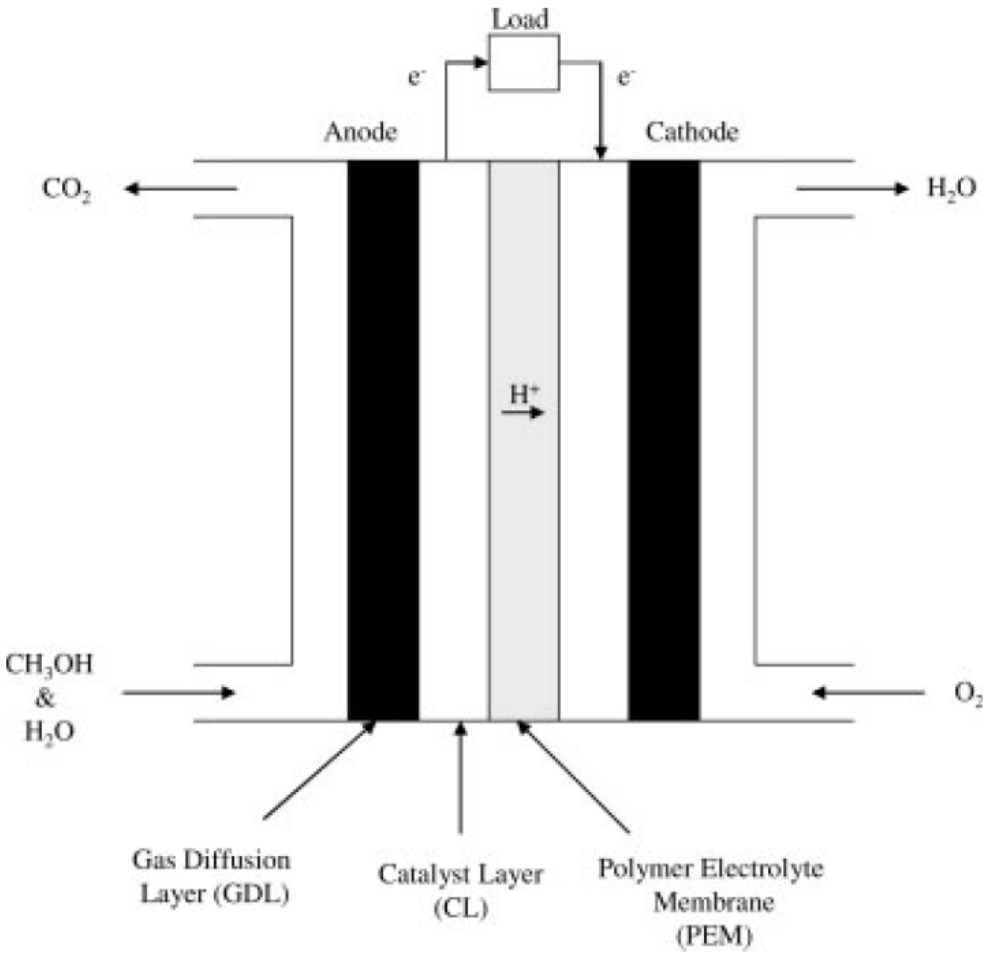

Figure 2.1 A schematic diagram of methanol PEM fuel cell. Reproduced from Ref. [9] with permission from John Wiley & Sons.

The chemical reaction takes place at the surface of the electrodes that are attached to a carbon paper or carbon cloth, called the GDL. The electrochemical reactions for a direct methanol PEM fuel cell are as follows:

Anode : $CH_3OH + H_2O \rightarrow 6H^+ + CO_2 + 6e^-$ (2.1)

Cathode : $\frac{3}{2}O_2 + 6H^+ + 6e^- \rightarrow 3H_2O$ (2.2)

Net reaction : $CH_3OH + \frac{3}{2}O_2 \rightarrow 2H_2O + CO_2$ (2.3)

For hydrogen PEM fuel cell as follows:

Anode : $H_2 \rightarrow 2H^+ + 2e^-$ $\Delta G° = 0.00$ (2.4)

Cathode : $2H^+ + \frac{1}{2}O_2 + 2e^- \rightarrow H_2O$ $\Delta G° = -237$ kJ/mol (2.5)

Net reaction : $H_2 + \frac{1}{2}O_2 \rightarrow H_2O$ $\Delta G° = -237$ kJ/mol (2.6)

The cell voltage is well related to the Gibbs energy change of a chemical reaction as:

$$\Delta G = -nFV \quad (2.7)$$

where n is the number of electrons involved in the reaction, F is the Faraday constant, and V is the cell voltage for thermodynamic equilibrium in the absence of current flow i.e., open circuit equilibrium.[10, 11]

The most widely used membrane in PEM fuel cells is typically a solid electrolyte called Nafion. Nafion is a perfluorinated polymer that contains small proportions of sulfonic or carboxylic ionic functional groups. Its general chemical structure can be seen in **Figure 2.2**, where X is either a

sulfonic or carboxylic functional group, and M is either a metal cation in the neutralized form or an H^+ in the acid form.

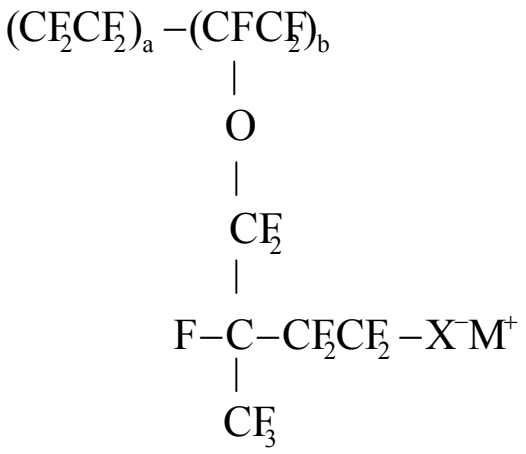

Figure 2.2 Chemical structure of Nafion perfluorinated ionomer.

This membrane allows protons to travel through but restrain the electrons from passing through it. The proton transfers through the membrane by virtue of the electric field created across the membrane. The performance of the fuel cell is depicted by current vs. voltage plots, known as the polarization curves. It is evident from the literature that Nafion is the leading candidate for PEM fuel cells, though other membranes such as poly(vinylidene-fluoride) (PVDF), poly(ether-ether-ether-ketone) (PEEK), and poly(tetrafluoroethylene) (PTFE) have also been investigated.[12] In addition to fuel cell applications, Nafion has been widely used in metal ion recovery as a super acid catalyst in organic reactions and different electrochemical devices. [13, 14] Various properties of Nafion membranes are illustrated in **Table 2.1**.

Table 2.1 Properties of a standard Nafion membrane

Molecular weight (g/mol)	100 000
Glass transition temperature Tg (K)	339
Density (g/cm^3) at 300K	2.074
Dielectric constant	3.04

2.3 Chemistry and Synthesis of Nafion

The development of Nafion began in the early 1960s when the DuPont Company's plastics exploration research group was expanding to fluorine technology that had previously resulted in the development of Teflon fluorocarbon resins and Viton fluoroelastomers.[22–24] The group was studying new monomers for copolymerization with tetrafluoroethylene (TFE). They also developed a general method to synthesize perfluorinated vinyl ethers from perfluorinated acid fluorides, which resulted in vinyl ether-monomers, the starting point for Nafion as well as other novel commercial polymers. One of the acid fluorides studied, based on the reaction product of TFE and sulphur trioxide, led to an unusual TFE copolymer containing branches with pendant sulfonic acid groups (see **Scheme 2.1**).

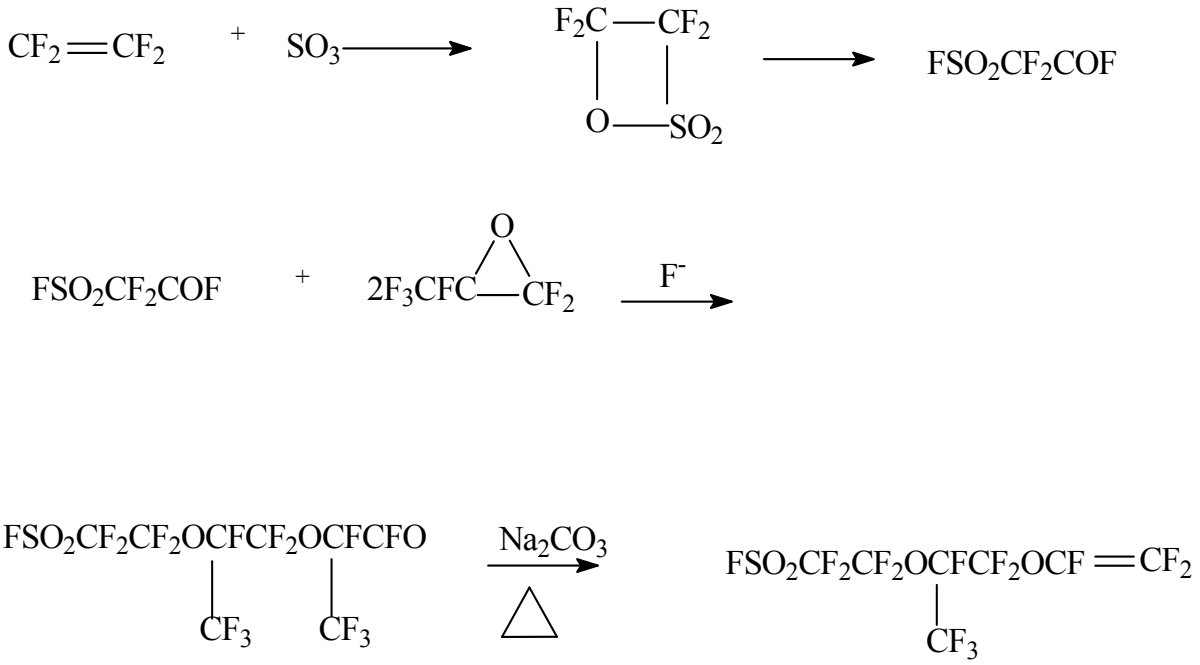

Scheme 2.1 Synthetic pathway process of Nafion membrane comonomer. Reproduced from Ref. [22] with permission from Elsevier Science Ltd.

Considering the properties that make Teflon so valuable for many applications in particular its unequalled dielectric properties, the exceptionally low coefficient of friction, and its artistic and chemical barrier properties, one would expect that all of these properties would be adversely affected by the introduction of sulfonic acid groups.

On the other hand, this proposed copolymer was believed to be fundamentally different from all other TFE copolymers made before, having the potential to interact with the environment instead of merely resisting severe chemical or thermal environments. Many of the various perfluorinated copolymers under consideration in the early 1960s appeared to be good candidates that would meet identified market needs such as improved high temperature stability and mechanical properties without sacrificing any of the other desirable properties of Teflon. The copolymer that became known as Nafion did not have the properties believed at that time to be desirable in a fluorocarbon polymer. However, DuPont proceeded with its development because it was truly different from any previously made fluorocarbon polymer. The Nafion polymer functionally interacted with its environment, whereas perfluorinated polymers were valued for their inertness. A number of excellent review articles exist covering the subject of perfluorinated ionomer membranes with emphasis on transport processes, [25, 26] applications, [27] and structural studies and physical properties.[22, 28–30]

2.4 Preparation and Characterization of Nafion-based Nanocomposite Membranes

The term polymer nanocomposite (PNC) is generally defined as the combination of a polymer matrix and a filler that has at least one dimension in the nanometer range (< 100 nm). The filler can be one-dimensional, such as nanotubes and fibres; two-dimensional, such as layered silicate minerals like clay; and three-dimensional, such as spherical nanoparticles. Over the past two decades, PNC technology has attracted great interest in both academia and industry because of its outstanding mechanical as well as improved thermal properties with a very small amount (2–5 wt%) of filler incorporation.[31–41] The main reason for these improved properties in PNCs is the

strong interfacial interactions between the matrix and the filler surface, as opposed to the conventional composites. Other interesting properties of PNCs include barrier resistance, [42] flame retardency, [43] scratch/wear resistance, [44] as well as optical, [45] magnetic, [46] and electrical properties.[47]

2.4.1 Clay-containing Nafion-based Composite Membranes

In recent years, one of the most extensively used nanoparticles for the preparation of polymer nanocomposites is the layered silicate or clay. The layered silicate particles generally used for the preparation of nanocomposites belong to the same general family of 2:1 layered or phyllosilicates.[31, 32] The layer thickness is around 1 nm, and the lateral dimensions of these layers may vary from 30 nm to several microns or larger depending on the particular layered silicate. Montmorillonite (MMT) is the most commonly used clay mineral for the preparation of nanocomposites.[31, 32]

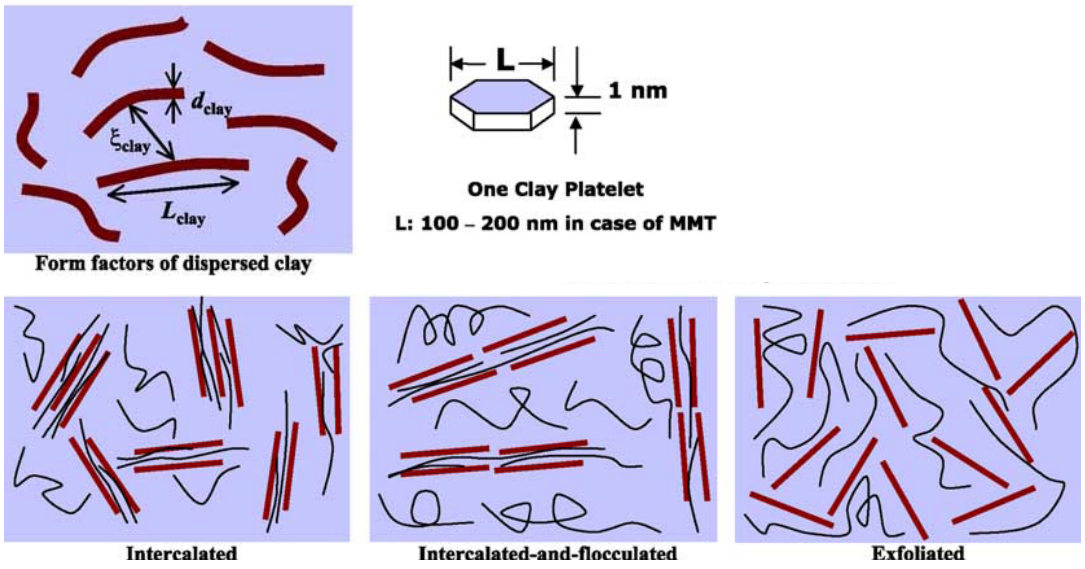

Scheme 2.2 Schematic illustration of three different types of thermodynamically achievable polymer/layered silicate nanocomposites [48b]. Reproduced from Sinha Ray and Okamoto with permission from American Chemical Society, USA.

The presence of high aspect ratio (length to width) filler is expected to decrease significantly the methanol cross-over of Nafion membrane as a result of a much longer path way. The success of this strategy relies, however, on the degree of dispersion of silicate layers in the polymer matrix, which may lie between three typical situations such as (i) microcomposites, where the silicate layers are not intercalated by the polymer chains, (ii) intercalated nanocomposites, where insertion of polymer chains into the silicate structure occurs in a crystallographically regular fashion, regardless of polymer to layered silicate ratio, and a repeat distance of a few nanometers, and (iii) exfoliated nanocomposites, in which the individual silicate layers are separated in polymer matrix by average distances that totally depend on the layered silicate loading (see **Scheme 2.2**). [32–47]

For the barrier properties of the polymer matrix to be improved, particularly towards methanol permeability, the fine dispersion of the silicate layers in the Nafion matrix is a prerequisite for maximizing the tortuosity factor (τ) that retards the progress of molecules through the matrix resin. According to the Nelsen model, when plates of length (L) and width (D) of the layered silicate are dispersed in the polymer matrix, then the tortuosity factor (τ) can be expressed as: [31]

$$\tau = 1 + (L/2D)\phi \qquad (2.8)$$

where ϕ is the volume fraction of dispersed layered silicate particles into the polymer matrix.
Two particular characteristics of layered silicates that are generally considered for the preparation of PLS-nanocomposites: the first is the ability of the silicate particles to disperse into the polymer matrix as individual layers. The second characteristic is the ability to modify their surface chemistry through ion exchange reactions with organic and inorganic cations. These two characteristics are, of course, interrelated since the degree of dispersion of layered silicate in a particular polymer matrix depends on the interlayer cation.

One successful method to prepare layered silicates containing polymer nanocomposites is to intercalate polymer chains into the silicate galleries. Generally, the intercalation of polymer chains into the silicate galleries is done by using one of the following two approaches: the insertion of suitable monomers in the silicate galleries and subsequent polymerization or direct

insertion of polymer chains into the silicate galleries from either solution or melt. [32] Recently, the melt intercalation technique has become the main stream for the preparation of polymer nanocomposites because it is quite compatible with the recent industrial polymer processing techniques. This method involves annealing, statically or under shear, a mixture of the polymer and layered silicate above the softening point of the polymer. During the annealing, the polymer chains diffuse from the bulk polymer melt into the galleries between the silicate layers. [48] On the other hand, during polymer intercalation from solution, a relatively large number of solvent molecules have to be desorbed from the host to accommodate the incoming polymer chains. The desorbed solvent molecules gain one translational degree of freedom, and the resulting entropic gain compensates for the decrease in conformational entropy of the confined polymer chains.[48] Therefore, there are many advantages to direct melt intercalation over the solution intercalation. For example, direct melt intercalation is highly specific for the polymer, leading to new hybrids that were previously inaccessible. In addition, the absence of a solvent makes direct melt intercalation an environmentally sound and an economically favorable method for industries from a waste perspective.[31–33] Up to this date various research groups used different methods for the fabrication of layered silicates containing Nafion membranes. H^+–MMT is a proton conductor with reported ionic conductivities of ~10^{-4} S/cm at room temperature. [49]

In 2003 Jung et al. first reported the preparation of Nafion/MMT composite membranes for fuel cell applications.[20] They used both pristine and organically modified MMT (oMMT) for the preparation of nanocomposite membranes. In a typical preparative method, a perfluorosulfonyfluoride copolymer and MMT were first mechanically mixed by internal mixer. The prepared composite was then pulverized by universal grinder and was taken in a stainless steel grinder and preformed as a sheet shape of 130–140 μm thick by hot pressing at temperatures of about 200–230°C at 6000 psi. The composite material based membranes were fabricated by annealing the membrane at a temperature greater than the glass transition temperature (T_g) of copolymer resin. The protonation of composite membranes were made by immersing the membrane in a solution of 20% sodium hydroxide (NaOH) and MeOH.

The XRD patterns revealed that the polymer chains were not intercalated into the two–dimensional gallery of silicate when pristine MMT was used for the preparation of

nanocomposite. However, XRD patterns of oMMT based nanocomposites showed the formation of intercalated nanocomposite.

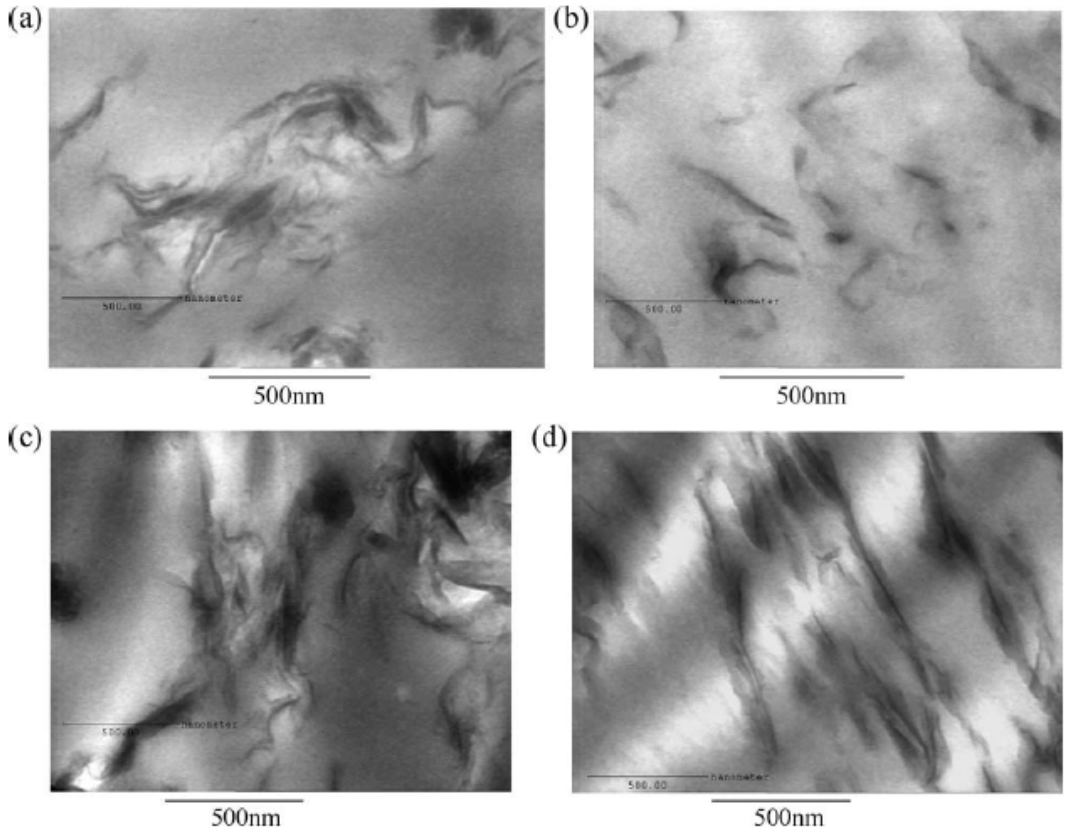

Figure 2.3 TEM micrographs for Nafion membranes filled with 2 wt% of: (a) CNa^+, (b) CH^+, (c) C25A, and (d) C30B. Reprinted from Ref. [21] with permission from Elsevier Science Ltd.

Thomassin et al. [21, 50, 51] prepared clay-containing Nafion nanocomposite membranes by melt-mixing a Nafion precursor (R1100 pellets) with clays. They have used four different types of oMMT such as (a) pristine MMT (CNa^+), (b) H-substituted MMT (CH^+), (c) MMT modified with nonfunctional alkyl-ammonium (C25A), and (d) MMT modified with a hydroxyl-containing alkylammonium (C30B) for the preparation of nanocomposites with Nafion. TEM micrographs for four different types of composite membranes are shown in **Figure 2.3**. C30B is homogeneously dispersed within the Nafion matrix, although the nanoclay particles are not completely exfoliated. Individual platelets can be observed within stacks, which results in a highly anisotropic filling of the polymer. This improvement in dispersion is due to the favorable

interactions between the –OH groups of C30B and the sulfonic acid functions of Nafion. Dispersion of C25A is not as good as that one of C30B, this might reflect the negative impact on the shorter spacing between the nonfunctional alkyl-ammonium in C25A on the interaction with the sulfonic acid function of Nafion matrix. The barrier properties were also improved as assessed by lower MeOH permeability. This improvement was, however, observed at the expense of the ionic conductivity, more likely as a result of the exchange of protons of Nafion with much less mobile ammonium cations of the nanoclay. The best performances were observed with C30B content as low as 0.5 wt%.

However, the addition of MMT particles, whether organically modified or not, results in decreased ionic conductivity in parallel to lower methanol permeability.[21, 50, 51] Rhee et al. have made claims on overcoming this drawback by grafting an organic sulfonic acid containing compound onto the surface of the alumina-silicates layers by silane condensation. [52] But this did not yield significant improvement on the ionic conductivity of composite membrane.

In another method, a Nafion solution in DMA was ultrasonically mixed with organically modified MMT clay (here Cloisite® C10A, C10A) at an elevated temperature.[53] Nafion/MMT composite membranes were casted on a glass substrate above 100°C in a vacuum oven. The casted composite membranes were boiled in 1 M hydrogen peroxide and rinsed with deionised water. Finally, the composite film was boiled in 1 M sulphuric acid, followed by rinsing with deionised water several times in order to remove the excess acid.

Figure 2.4 represents the XRD patterns of Nafion/MMT composite membranes at different clay loadings. Compared with unmodified MMT, the relatively large initial interlayer spacing of the modified MMT was observed, and it generally makes polymer chains intercalation much easier. Both neat Nafion and Nafion/MMT composite membranes showed featureless diffraction patterns in the region from $2\theta = 2$ to 10° until the loading of MMT reached 20 wt%. This strongly implies that a disordered and exfoliated nanocomposite was formed.

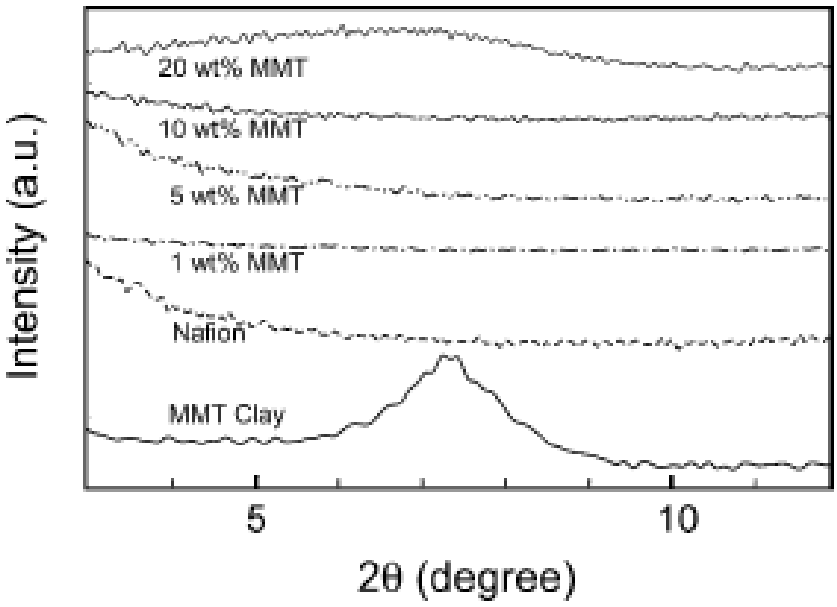

Figure 2.4 X-ray diffraction patterns of recast Nafion membrane and Nafion/MMT nanocomposite membranes. Reprinted from Ref. [53] with permission from Elsevier Science Ltd.

Like Jung et al.,[20] Silva et al.[54] also used the solvent casting method to prepare MMT containing Nafion membranes and results showed that the addition of a very small amount of MMT (~1 wt%) did not alter the ionic conductivity, however, the technique or their method produced a marked decrease in MeOH permeability.

Kim et al. attempted to overcome the problem of MeOH permeability while at the same time increasing the ion conductivity of the composites membrane by preparing Nafion/sulfonated clay (S–MMT) nanocomposite membranes via the film coating process.[55] Although, their attempt was not successful, their results, however, showed that many factors strongly affect MeOH permeability as well as the conductivity of the membranes. Results also showed that the humidity should be considered and controlled during synthesis and characterization membranes, especially for mechanical properties improvements.

Recently, Zhang et al. used sol-gel method for the fabrication of clay containing Nafion composite materials.[56] In a reported method, a desire amount of oMMT was added to a Nafion solution, then stirred mechanically for 8 h followed by ultrasonication degassing so as to make the contents of oMMT (based on the Nafion resin) in the mixture 3, 5, 8, and 10 wt%, respectively. The prepared mixture was then slowly poured into a Petri dish to form a composite membrane with a thickness of about 0.1 mm. The filled glass dish was placed in a vacuum oven and dried slowly by increasing the temperature from 80 to 130°C to prevent the formation of crevices in the composite membrane. The residual solvent in the composite membrane was fully removed by evacuation at 130°C for 12 h. The composite materials were finally obtained by annealing the membranes at temperatures higher than the T_g of Nafion resin.

XRD studies showed that the d_{001}-spacing of oMMT in nanocomposite increased moderately compared to that of neat oMMT and d_{001}-spacing of oMMT in nanocomposite systematically increases with oMMT loading. This observation indicates that the side chain groups of Nafion resin are probably not intercalated into the two-dimensional gallery of oMMT and most of the Nafion chains are probably located outside the galleries of oMMT.

In a recent report, Alonso et al.[57] report the preparation of Nafion/MMT nanocomposite membranes by the solvent casting method. They used H^+ exchanged MMT clay for the preparation of the nanocomposite membranes. To find out the effect of the solvent on the properties of composite membranes, two different types of casting techniques were used. The first involves heating the solution over a glass substrate in an oven at 75°C overnight, and in the second procedure, the dispersion was placed under high pressure at 180°C and 180 psi for 8h. To maintain a constant pressure of 180 psi and to keep the environment inert, dry nitrogen gas was continuously fed to the chamber.

The morphology of the nanocomposite membranes as a function of clay loading was investigated with small-angle X-ray scattering (SAXS), and results showed that the composite membranes are composed of polymer aggregates oriented parallel to the membrane surface. Results also showed that clay particles are also tending to orient parallel to the surface. With increase in clay loading in the composite membranes, the ionic cluster peak tends to shift monotonically to a higher

scattering vector value. Because of this preferred orientation of the clay particles, membranes are much stiffer and can withstand much higher temperatures compared to the neat polymer based membrane.

The same group also reported the preparation of Nafion/MMT hybrid membranes using the depletion aggregation of suspended particles method.[58] This phenomenon is very popular in the colloids area. In a typical preparative method, a known amount of Na^+–MMT was added to the Nafion solution, the mixture was stirred at 70°C for 24 h, and then left untouched for seven more days. Membranes were then fabricated by casting the Nafion/Na^+–MMT mixture on to a Teflon mold and placing it into a high-pressure chamber at 160°C and 160 psi (under dry nitrogen) for 6 h. Morphological analyses using XRD patterns and cryo-TEM images showed that the clay particles in the hybrid gels form a network structure with an average cell size of 500 nm.

2.4.2 CNTs Containing Nafion Composite Membranes

CNT is one of the most interesting materials discovered in the last fifty years and this is one of the most basic materials in the field of nanoscience and nanotechnology. In recent years, CNTs and CNT-based polymer nanostructured materials have inspired a range of potential applications.[57–60] More specifically, the use of CNTs in polymer/CNT composites has attracted wide attention.[61–67] CNTs have a unique atomic structure, a very high aspect ratio, extraordinary mechanical properties, strength, and flexibility, making them ideal for reinforcing fibers in nanocomposites.[62] Not only that they have capacity to improve the electrical properties as well.[68–70]

CNTs are giant fullerenes. A fullerene, by definition, is a closed, convex cage molecule containing only hexagonal and pentagonal faces. CNTs have many structures, differing in length, thickness, types of spiral, and number of layers, although they are formed from essentially the same graphite sheet. Graphite has three-coordinate sp^2 carbons forming planer sheets, whose motif is the flat six-member benzene ring. In fullerenes, the best known example is C_{60}, the three coordinate carbon atoms are tiling the spherical surfaces,[68–70] There are two main types of CNTs: single-walled CNTs (SWCNTs) and multi-walled CNTs (MWCNTs) (see **Fig. 2.5**).

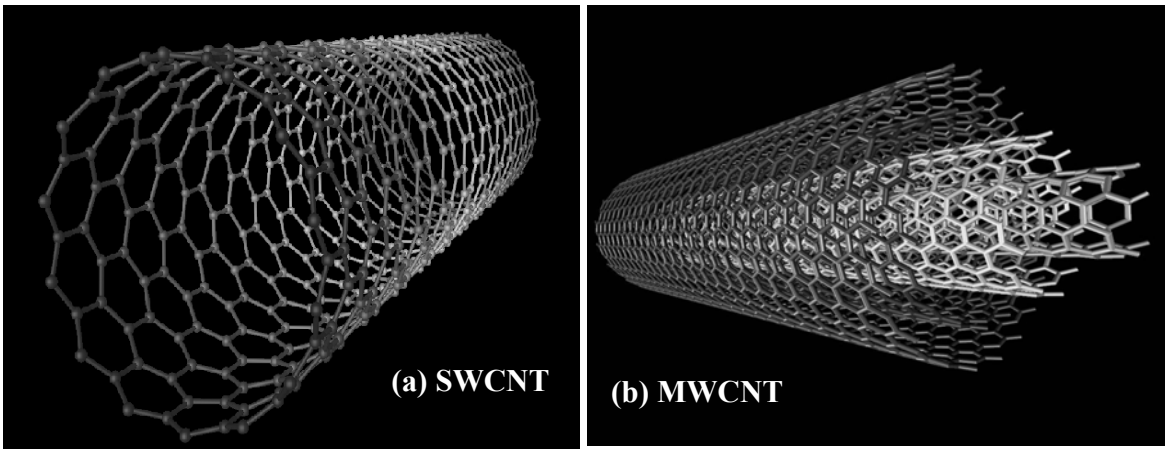

Figure 2.5 Computer simulated picture: (a) SWCNT and (b) MWCNT. Reproduced with permission from NASA website.

The structure of a SWCNT can be conceptualized by wrapping a one atom thick layer of graphite (called graphene) into a seamless cylinder. Most SWCNTs have a diameter of close to 1 nm, with a tube length that can be many thousands of times larger. SWCNTs with lengths up to orders of centimeters have been produced. MWCNTs consist of multiple layers of graphite rolled up to form a tube shape. There are two models that can be used to describe the structures of MWCNTs. In the Russian Doll model, sheets of graphite are arranged in concentric cylinders. In the Parchment model, a single sheet of graphite is rolled around itself, resembling a scroll of parchment or a rolled up newspaper.[68, 71, 72]

Although CNTs have a capacity to improve the mechanical and electrical properties of the polymer matrix at the same time, however, because of risk of short-circuit caused by a non-electrically isolated electrolyte, their dispersion within fuel cell polymer matrix was not considered. Another drawback of CNTs is the cylindrical shape. For DM fuel cell, the MeOH permeability of the matrix membrane is a problem because cylindrical shape is less suited than the platelet-like geometry of nanoclay. Therefore, the effective dispersion of CNTs within the membrane might significantly decrease the MeOH permeability, while improving the performance and durability of the fuel cell.

In 2006, Liu et al. [73] have tried to fabricate CNTs containing Nafion membranes by keeping the content of CNTs lower than the percolation threshold. According to them, the mechanical stability of membranes was improved by dispersing 1 wt% CNTs, without affecting the performances of H_2/O_2 fuel cell. However, the method used for the dispersion of CNTs was a ball milling followed by solvent casting. This method is not suitable for up-scaling.

Recently, Thomassin et al.[74] prepared a MWCNT-based Nafion membrane by melt-extrusion method in order to decrease the MeOH permeability without deleterious effect on the ionic conductivity. In a typical preparative method, a required amount of CNTs were (at 180°C, 200 rpm for 5 m, under nitrogen) microextruded with Nafion powder. The membranes were prepared with a laboratory two–roll mill at 200°C. The sulfonyl fluoride groups were then hydrolyzed by immersion in a solution of KOH/water/dimethylsulfoxide (1.5/3.5/5) at 80°C for 2 h, followed by repeated immersion in a fresh solution of HNO_3 (20%) for 1 h.

For the preparation of composites, two different types of MWCNTs were used: commercially available MWCNTs containing carboxylic group (comer. MWCNT–COOH) and MWCNTs grafted by radicals bearing COOH group. Again to avoid short-circuiting, the MWCNT content was very low, less than 2 wt%. The degree of dispersion of MWCNTs in the Nafion matrix was studied by TEM. **Figure 2.6** represents the TEM images of composite membranes prepared with three different types of MWCNTs. In each case, the MWCNTs were uniformly dispersed as individual tubes, no agglomeration was observed by TEM. MWCNT–COOH was much smaller than the neat MWCNT, which confirms that these are more fragile than that prepared by the grafting method. Nevertheless, the length of MWCNTs seems to be shortened by the melt-mixing process as testified by the TEM micrographs.

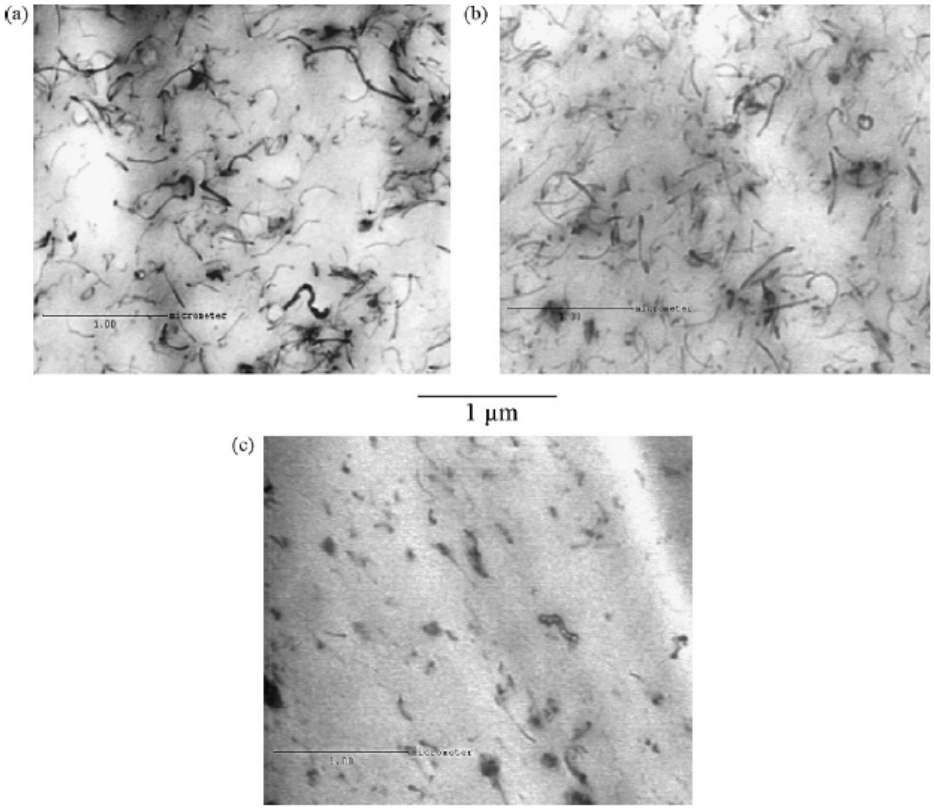

Figure 2.6 Transmission electron microscopy images of Nafion membranes filled with 1 wt%: (a) MWCNT, (b) lab. MWCNT–COOH, and (c) com. MWCNT–COOH. Reproduced from Ref. [74] with permission from Elsevier Science Ltd.

Recently, Cele et al.[75] reported the preparation of MWCNT-based Nafion composite membranes by the melt-blending technique. They used neat, oxidized, and amine functionalized MWCNTs to investigate the effect of MWCNTs' surface functionalization on the thermal stability, mechanical properties, and proton conductivity of Nafion composite membranes for fuel cell applications. Results showed the significant improvement in mechanical properties and thermal stability in the case of oxidized MWCNT-based Nafion composite membrane compared to other MWCNT-based composite membranes.

2.4.3 Silica Containing Nafion Composite Membranes

Silica is another commonly used particle to modify the Nafion membrane. In 1989, Mauritz et al. [76] first reported a simple method for production of unique composite membranes of Nafion by the in situ growth of silicon oxide phase in hydrated perfluorosulfonic acid-catalysed sol-gel reaction for tetraethoxysilane (TEOS). This method was allowed to diffuse silica particles into the films from the external alcohol solution.[77, 78] After immersion in these solutions for prescribed times, the membranes were carefully dried/annealed to optimize the network connectivity of the incorporated gel component by condensation involving unreacted 'OH' groups.

In recent years, many researchers have reported the preparation, characterization, and properties of Nafion/silica-based composite membranes. Dimitrova et al. [79] have recasted Nafion/silica composite membranes from Nafion solution in DMS. In short, a known amount of commercially available Nafion solution was mixed with DMS solvent with a known amount of silica powder. After 15 m of ultrasonic dispersion, the homogeneous substrate was casted on a smooth Petri dish and kept at room temperature for 24 h. Then the plate was heated step by step to a maximum temperature of 150°C. After cooling down, the membrane was peeled off the bottom by adding water. The next step was the protonation of the membrane by treating it in boiling sulphuric acid (1.5 mol/l) followed by rinsing with deionised water several times in order to remove the excess acids. Antonucci et al.[80] and Shao et al.[81] have used the same recast technique to fabricate Nafion/silica composite membranes. In another report, Staiti et al.[17] fabricated Nafion/silica/phosphotungstic acid composite by solvent recasting technique.

Adjemian et al.[82] and Jung et al.[83] modified the commercial Nafion 115 membranes with the sol-gel reaction of TEOS and applied them to the H_2/O_2 fuel cells and DM fuel cell, respectively. They found that the silica incorporated into the membrane decreases the proton conductivity of the membrane at low temperatures (< 100 °C).

Recently, Xu et al. reported the preparation of Nafion/silica/phosphotungstic acid (PWA) composite membranes for the application in low temperature DM fuel cell.[84] In a typical

method, the composite membranes were prepared by in situ sol-gel reaction in pre-treated initially hydrated Nafion 117 that contained alcohol was immersed in TEOS/methanol solutions of 3:2 (v/v) for different prescribed times and subsequent treatment in PWA solution. After different intervals of time, membranes were taken out, surface-blotted dry, and then, placed under high vacuum for 72 h at room temperature, and then dried at 110°C for 2 h. The membranes were subsequently immersed in saturated phosphotungstic acid/water solution for 24 h. The membranes were then washed with deionised water for three times to remove the surface absorbed PWA molecules and finally, dry–annealed under high vacuum at 80°C for 24 h.

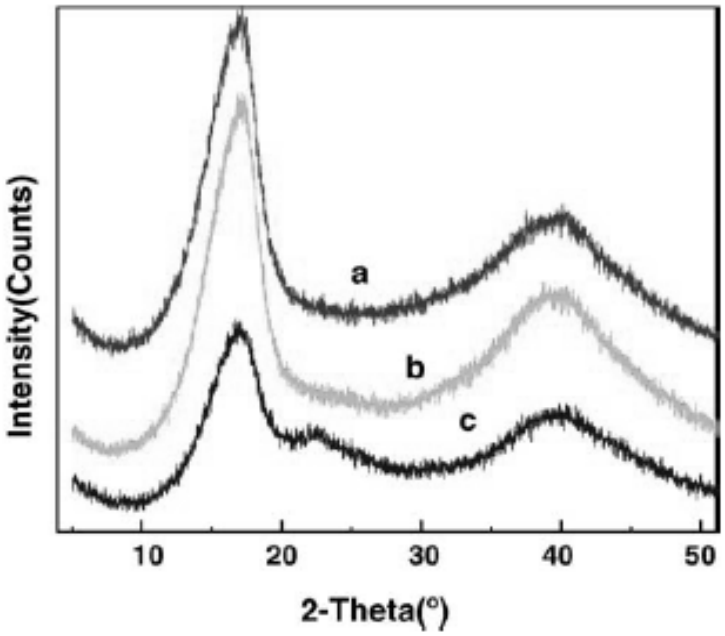

Figure 2.7 X-ray diffraction patterns of commercial Nafion membrane: (a) Nafion/ silica/PWA composite membranes at different immersion times (b) 5 m and (c) 30 m. Reproduced from Ref. [84] with permission from Elsevier Science Ltd.

XRD analysis was used to study the effect of the addition of silica particles on the degree of crystallinity of Nafion membranes. Typical XRD patterns of Nafion/silica/PWA composite membranes are shown in **Figure 2.7**, and the corresponding peak profile analyses are presented in **Figure 2.8**. By comparing these diffraction patterns, a decrease of the ratio between the area

of crystalline peak and the amorphous diffraction with the increasing silica content was clear in composite membranes. However, these results are completely different from the results reported by others, where membranes were prepared using the same recast technique.[81–83] The difference in crystalline behavior of prepared membranes may be due to the different conditions and solvents they used for membrane preparation.

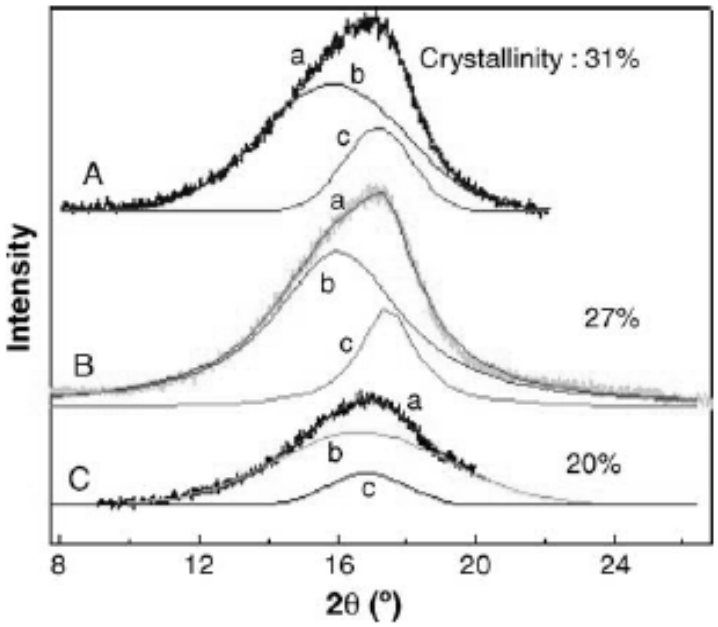

Figure 2.8 X-ray diffraction profiles of Nafion 117 (A) and composite membranes with different immersion times ((B) 5 m, (C) 30 m). Curve (a) is the convolution of curves (b) and (c). Measured data are shown by dots. Reproduced from Ref. [84] with permission from Elsevier Science Ltd.

Li et al.[85] reported the casting of Nafion-based sulfonated organosilica nanocomposite membranes for the use in DM fuel cell. They found that sulfonated silica composite membranes perform better than the unsulfonated silica/Nafion composite membranes when the same amount of silica was used for the membrane preparation. Results showed that the methanol permeability was reduced though the proton conductivity of the composite membrane decreases.

2.4.4 Various Nanoparticles Containing Nafion Composite Membranes

Recently, the research on oxide nanoparticle-based polymer nanocomposite materials became more and more important for industrial applications. The reduced size of oxide nanoparticles plays an important role in different fields of research. This nanosize structure brought improvement in mechanical properties of the metal oxide particles, e.g. consolidated TiO_2 nanoparticles have improved mechanical properties compared to the coarse grained TiO_2.[86] The reason for this behavior is that, in the case of the nanocrystals the enhanced self-diffusion among the grains helps the grain boundaries slide by one another and henceforth improve the ductility.[87]

Up to now, various groups have used different types of oxide nanoparticles to improve the properties of Nafion based membranes for fuel cell applications. For examples, Watanabe et al. reported the modification of Nafion PEM by incorporation of nanoparticles of TiO_2, Pt, Pt–SiO_2 and Pt–TiO_2 in order to decrease the humidification requirements.[88–90] These modified PEMs showed a much higher water uptake and lower resistance than the neat Nafion-based membrane when operated at 80°C. This improvement was attributed to the suppression of hydrogen cross over by in-situ Pt and to the subsequent sorption of the water produced on the incorporated oxides. Another attempt was the incorporation of zirconium phosphate (ZrP) into Nafion 115 membrane by Yang et al.[91] Their hypothesis was that the addition of ZrP to Nafion would increase the water uptake of the membrane at elevated temperature, thereby increasing the proton conductivity and thus improving the fuel cell performance.

Results indicated that Nafion 115/ZrP phosphate composite membranes enhanced fuel cell performance compared to neat Nafion 115 membrane at an elevated temperature and reduced water activity. Nafion 115/ZrP composite membrane had a greater ion-exchange capacity and took up more water than Nafion 115 membranes. Similar observations were made by Hinatsu et al.,[92] Futerko et al.,[93] and Alberti et al.[94] Though the composite membranes showed reduced proton conductivity and water transport, the data do not fully resolve these conflicting observations. On the other hand, the results are consistent with the suggestion that mechanical

properties of the composite membranes may be the key to the performance of composite membranes.

Kim et al. have produced self-humidifying membranes by dispersing palladium (Pd) nanoparticles into the Nafion matrix.[95] These nanoparticles triggered water formation as a result of oxygen reduction and also methanol consumption by oxidation. This type of self-humidified membrane with a lower methanol cross-over exhibits a proton conductivity (C) and methanol permeability (P), i.e., P/C of 1.5, which is higher than that of neat Nafion membrane. In recent years, preparation and characterization of various other types of nanoparticles containing Nafion membranes have also been reported.[97–101]

2.5 Properties of Nafion-based Composite Membranes

Intrinsic properties of unmodified Nafion, such as lower thermal stability, poor mechanical properties, and high liquid permeability, puts limit on its applications. Nafion based nanostructured membranes consisting of nanofillers, such as clay, CNTs, silica or metal oxides, etc., frequently exhibit significant improvement of various properties when compared to those of neat polymer. Improvements generally include increased thermo-mechanical properties and thermal stability, and increased ion conductivity and liquid permeability.

2.5.1 Mechanical Properties

Dynamic mechanical analysis (DMA) has been used to study the temperature dependence of the storage modulus (G') of Nafion matrix on nanocomposite formation under different experimental conditions.[96] In general, Nafion shows two typical glass transition temperatures: α–transition at about 120°C and β–transition at about 20°C, which are assigned to the nonpolar backbone and polar clusters, respectively.[77] The DMA results of neat Nafion and its clay-containing nanocomposite membranes with two different clay loadings are presented in **Figure 2.9**.[57] It is clear from the figure that the nanocomposite membranes show dramatic increases in storage modulus. The nanocomposite containing 20 wt% clay shows a 6-time increase at low temperatures and orders of magnitude above 100°C. DMA results indicate that the

nanocomposite membranes are much stiffer and can withstand higher temperatures compared to the neat Nafion membrane. On the other hand, neat Nafion membranes show a high temperature α–transition characteristic of the polar group clusters at around 125°C. In contrast to neat Nafion membranes, the α–transition of the nanocomposite membranes shifts to much higher temperatures. For the nanocomposite membrane containing 20 wt% clay, the transition shifts to 215°C and the membrane becomes much weaker.

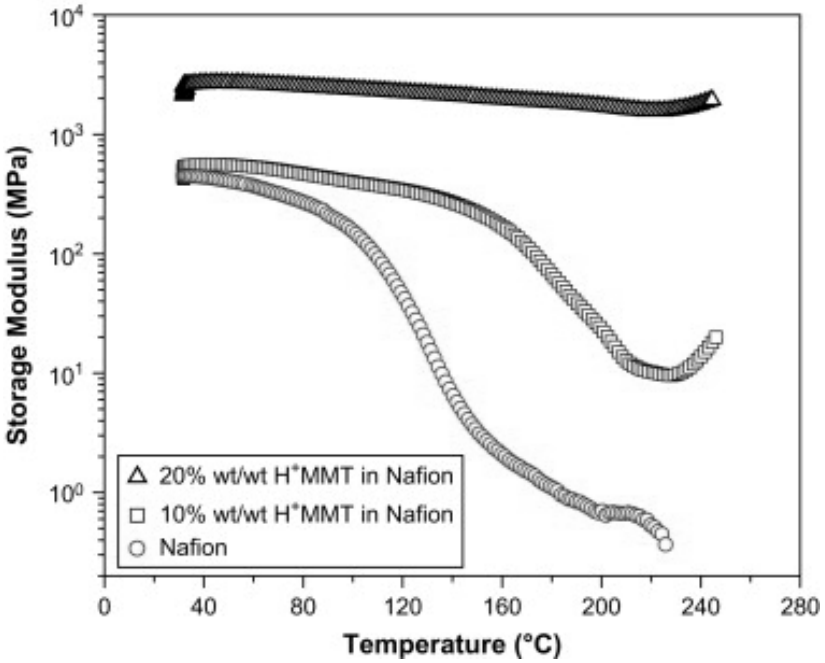

Figure 2.9 Storage modulus as a function of temperature of Nafion and Nafion–clay nanocomposites containing 10 and 20 wt% H^+–MMT. Reproduced from Ref. [57a] with permission from Elsevier Science Ltd.

Kim et al.[96] studied the correlation between modulus and water uptake for the BPSHs [sulphonated poly(arylene ether sulphone) copolymers] and results showed that the former has approximately a seven times higher modulus than Nafion when water uptake was less than 30%, but the difference in modulus decreases as a function of increasing water uptake. This suggests that the higher modulus for the BPSHs after water uptake is a result of the stiffer aromatic backbone structure of the copolymer compared to the flexible perfluorocarbon structure of Nafion. The slow modulus decrease may be related to the semi-crystalline structure in Nafion.

These results are consistent with the previous stress-strain data of both systems under dry and wet conditions. The tensile strength and modulus of BPSHs were generally higher than those of Nafion resin and decreased with water uptake. Moreover, the elongation at break beyond the tensile yield of the copolymers increased with water uptake while a nearly constant elongation was observed in Nafion resin (see **Fig. 2.10**).[86, 87] The relatively small elongation change of Nafion under wet conditions might also be due to its semi-crystalline phase.

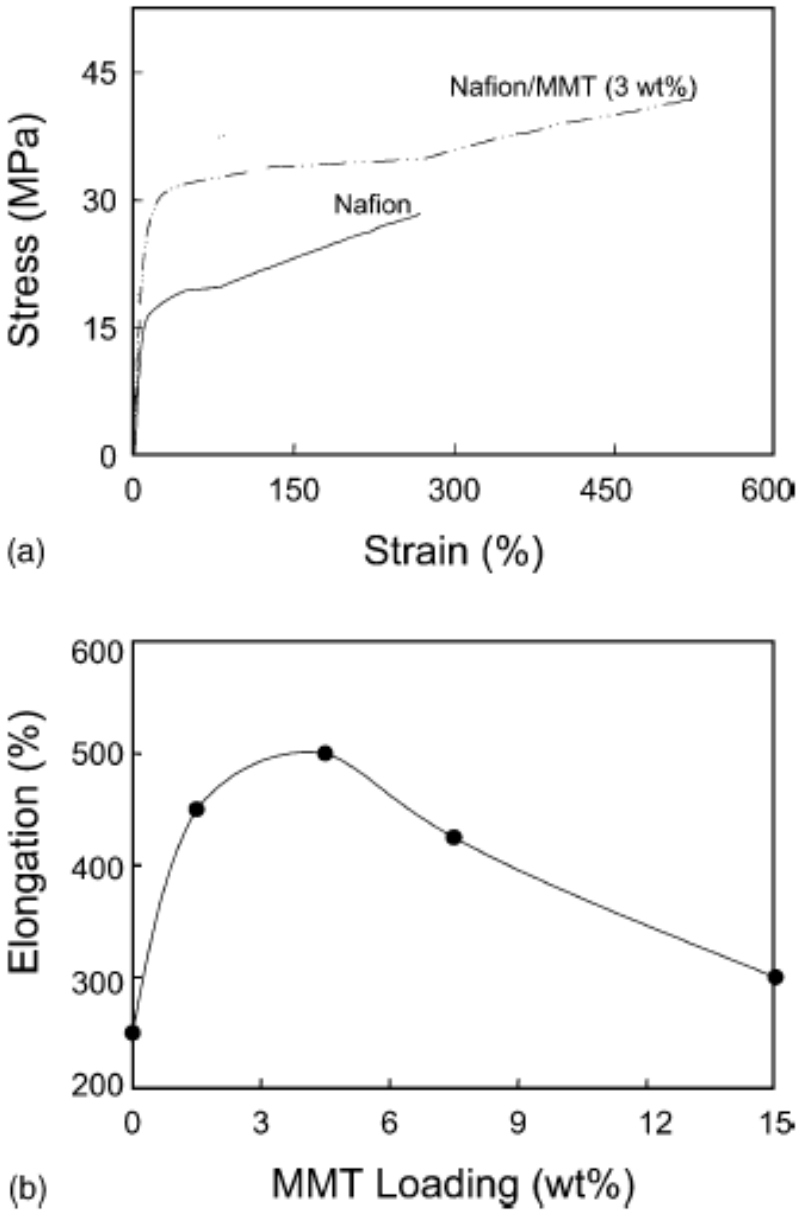

Figure 2.10 Tensile properties of Nafion/MMT nanocomposites: (a) stress–strain curves and (b) tensile elongation. Reproduced from Ref. [53] with permission from Elsevier Science Ltd.

The measurement of tensile properties is an efficient way to estimate the compatibility of Nafion matrix with organo-clays. **Figure 2.10(a)** shows the stress-strain curves of Nafion/MMT nanocomposite membranes.[53] It was reported that once nanolayer exfoliation has been achieved, the polymer/clay nanocomposites exhibit significantly improved properties compared with the neat polymer or the conventional composite.

The maximum strength and elongation at break for extruded Nafion membrane usually exceed 30 MPa and 200%, respectively. In the case of recast Nafion/MMT composite membranes, at a loading of 3 wt% clay, the strength increased more than 35% and the tensile elongation almost doubled than that of neat Nafion membrane. This might also result from the complete dispersion or exfoliation of the clay particles in the polymer matrix. As shown in Figure 2.11(b), the elongation at break of composite membranes reveals a positive deviation until filler content was 15 wt%. This is in good agreement with XRD results.

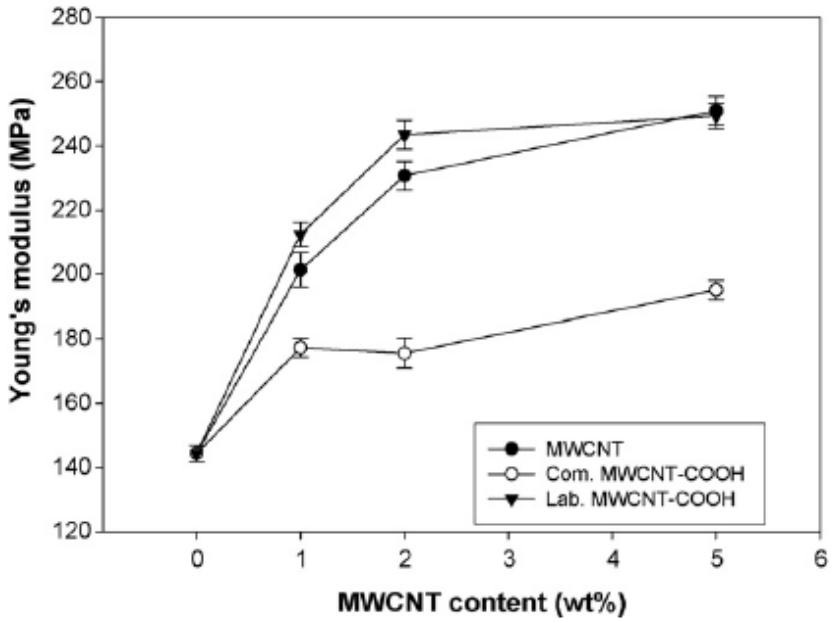

Figure 2.11 Young's modulus of Nafion membranes filled with MWCNT, com. MWCNT–COOH and lab. MWCNT–COOH as a function of the filler content. Reproduced from Ref. [74] with permission from Elsevier Science Ltd.

Thomassin et al. measured the tensile properties of MWCNT-containing Nafion membranes.[74] **Figure 2.11** represents Young's modulus of Nafion membranes filled with MWCNTs, comer. MWCNTs–COOH, and lab MWCNT–COOH were used as a function of the filler content. [100] The modulus was increased by 140% and 160% for MWCNTs contents of 1 and 2 wt% as compared to the neat Nafion, respectively. The reinforcing effect of MWCNTs should delay any membrane failure that occurs rapidly when Nafion is hydrated at a temperature higher than 80°C. The increase in the modulus was slightly higher in the case of lab. MWCNT–COOH, consistent with a better dispersion of MWCNTs in the Nafion matrix. Again, the shorter length of com. MWCNT–COOH accounts for a lower increase in modulus observed in this case. However, in each case, Young's modulus levels off at MWCNTs contents exceeding 2 wt%. This may be due to the increase aggregation of the tubes in the Nafion matrix.

2.5.2 Thermal Stability

The thermal stability of polymeric materials is usually studied by TGA. The weight loss due to the formation of volatile products after degradation at high temperature is monitored as a function of temperature. When the heating occurs under an inert gas flow, a non-oxidative degradation occurs, while the use of air or oxygen allows oxidative degradation of the samples. Generally, the incorporation of inorganic fillers into the polymer matrix is found to enhance thermal stability of the matrix by acting as a superior insulator and mass transport barrier to the volatile products generated during decomposition.

Jung et al. reported the thermal stability for Nafion resin and MMT (pristine) and m-MMT (modified) incorporated Nafion membranes.[20] **Figure 2.12 (a)** shows the TGA thermograms of neat Nafion-based and Nafion/MMT composite membranes. As shown in thermograms of Nafion/MMT composite containing 3 wt% MMT, the weight loss of Nafion/MMT composite in the temperature range from 25–280°C was ~ 6 wt%. A weight loss of 8% was observed in the temperature range of 270–380°C. This may be due to the increase evolution of SO_2 and CO_2 gases in this region and also due to the evolution of others compounds such as SF_4, CO, HF, CF, etc.[102] At a much higher temperature range such as in the temperature range of 355–560°C, 86% of the sample was volatilized. As a result, thermal resistance of Nafion/MMT composite

membrane was lower than that of neat resin membrane in all stages. Another interesting observation was that the thermal stability of composite membranes systematically decreased with increase in MMT loading. This suggests that the stacked and/or agglomerated clay particles behave as a heat source rather than thermal degradation retardant filler in Nafion matrix. Neat MMT works as the defect rather than the retardant filler in polymer matrix.

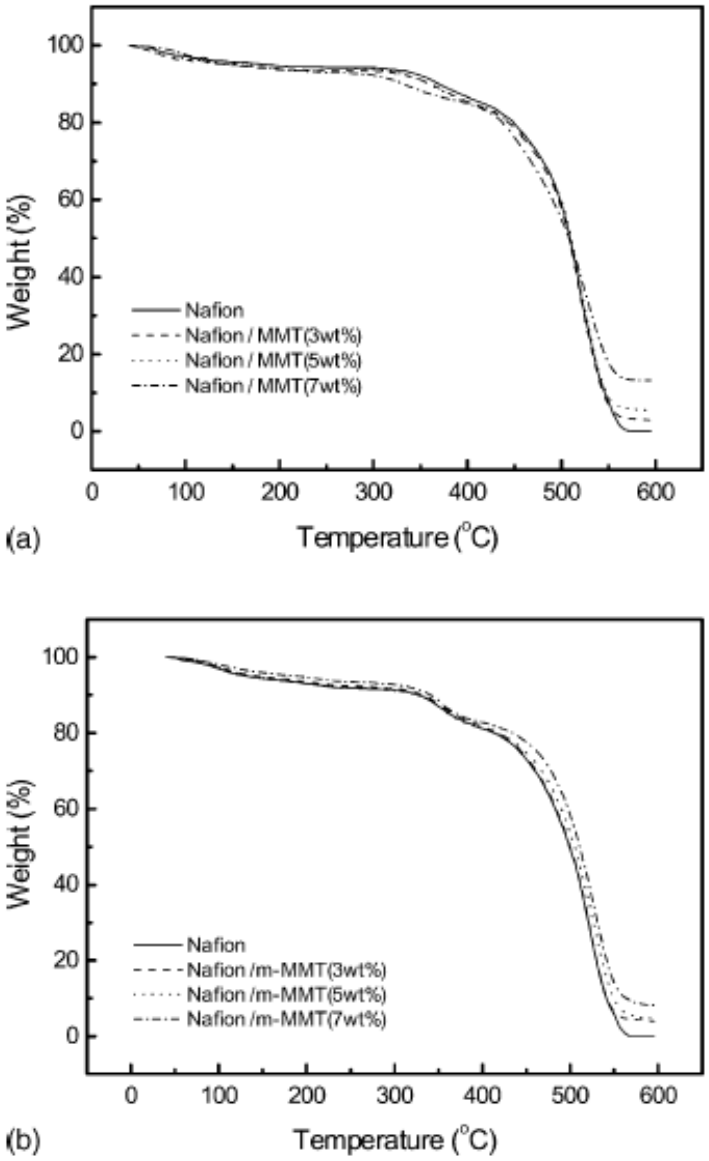

Figure 2.12 Thermogravimetric analysis scans: (a) MMT and (b) Nafion/m–MMT composite membrane with various content of MMT. Reproduced from Ref. [20] with permission from Elsevier Science Ltd.

On the other hand, thermal stability of the Nafion matrix increased after nanocomposite formation with m-MMT and also stability of nanocomposites increased with increase in m-MMT loading. This observation suggests that the homogeneous dispersion of m-MMT particles in Nafion matrix is responsible for the higher thermal stability of the Nafion/m-MMT composite membranes.

Song et al.[53] also studied the thermal stability of Nafion/MMT composite membranes. The membranes were prepared by solvent casting method. The thermal decomposition behavior of Nafion/MMT nanocomposites was similar to that of Nafion itself, but the major decomposition temperature of polymer main chain shifted to a much higher temperature region. This could be attributed to the strong interaction between hydrophobic Nafion backbones and organophilic clay particles.

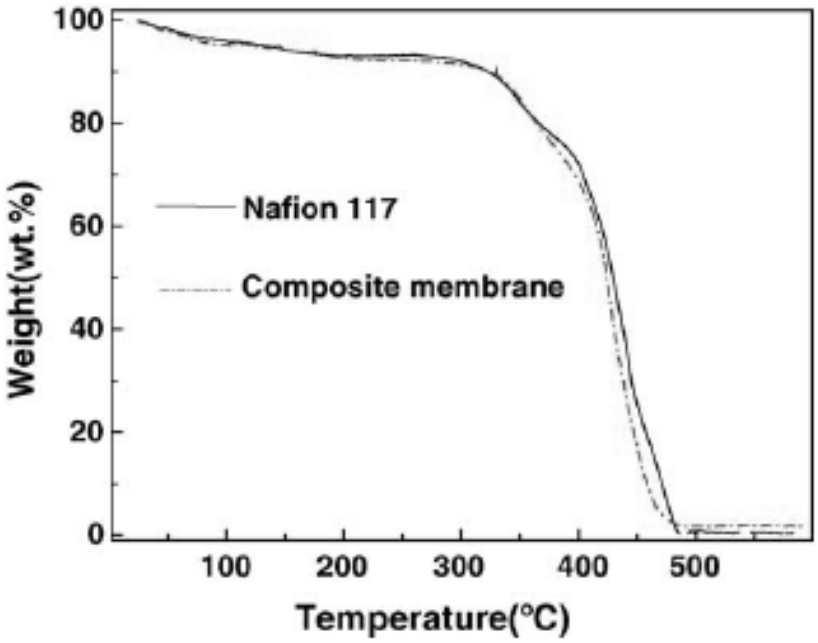

Figure 2.13 Thermogravimetric analysis scans for commercial Nafion without treatment N117 and Nafion/silica/PWA composite membrane with silica content of 38.2 μg/g. Reproduced from Ref. [84] with permission from Elsevier Science Ltd.

On the other hand, Xu et al. [84] have showed that the incorporation of silica and PWA does not deteriorate the thermal stability of Nafion membrane. The TGA thermograms for Nafion/Silica/PWA composite membrane with silica content of 38.2 μg/g and the commercial Nafion without treatment are shown in **Figure 2.13**.[84] It can be seen that the samples retain more than 92 % weights up to a temperature of about 330°C. The lost components mainly are the small molecules such as water, MeOH and ethanol (EtOH).[103–104] After this point, all samples start decomposing rather rapidly.

2.5.3 Methanol Permeability

The methanol permeability is defined as the product of diffusivity and solubility, *DK,* and it is generally calculated by:[105]

$$C_B(t) = \frac{A}{V_B}\frac{DK}{L}C_A(t - t_0) \tag{2.9}$$

$$P = DK = slope \times \left\langle \frac{V_B.L}{A.C_A} \right\rangle \tag{2.10}$$

where C_B and C_A are the methanol concentration of permeated and feed side through the membrane, respectively. A, L, and V_B are the effective area of membrane, the thickness, and the volume of permeated compartment. D, K, and t_0 are the methanol diffusivity, the solubility, and the time lag, respectively.

In recent years, various authors have reported the methanol permeability thus the DK factor, for the Nafion-based membranes in relation to the nature and the amount of filler incorporated. **Figure 2.14** represents the time dependence of methanol permeability of neat Nafion and corresponding MMT containing Nafion membranes with various loading. [20] Gas phase chromatography was used to measure the MeOH permeability of various membranes. It is clear

from the figure that the permeability decreased with increased loading of MMT and this is true for both neat and modified MMT containing Nafion composite membranes, suggesting higher MMT loading leads to the agglomeration of layered silicates particles in Nafion matrix.

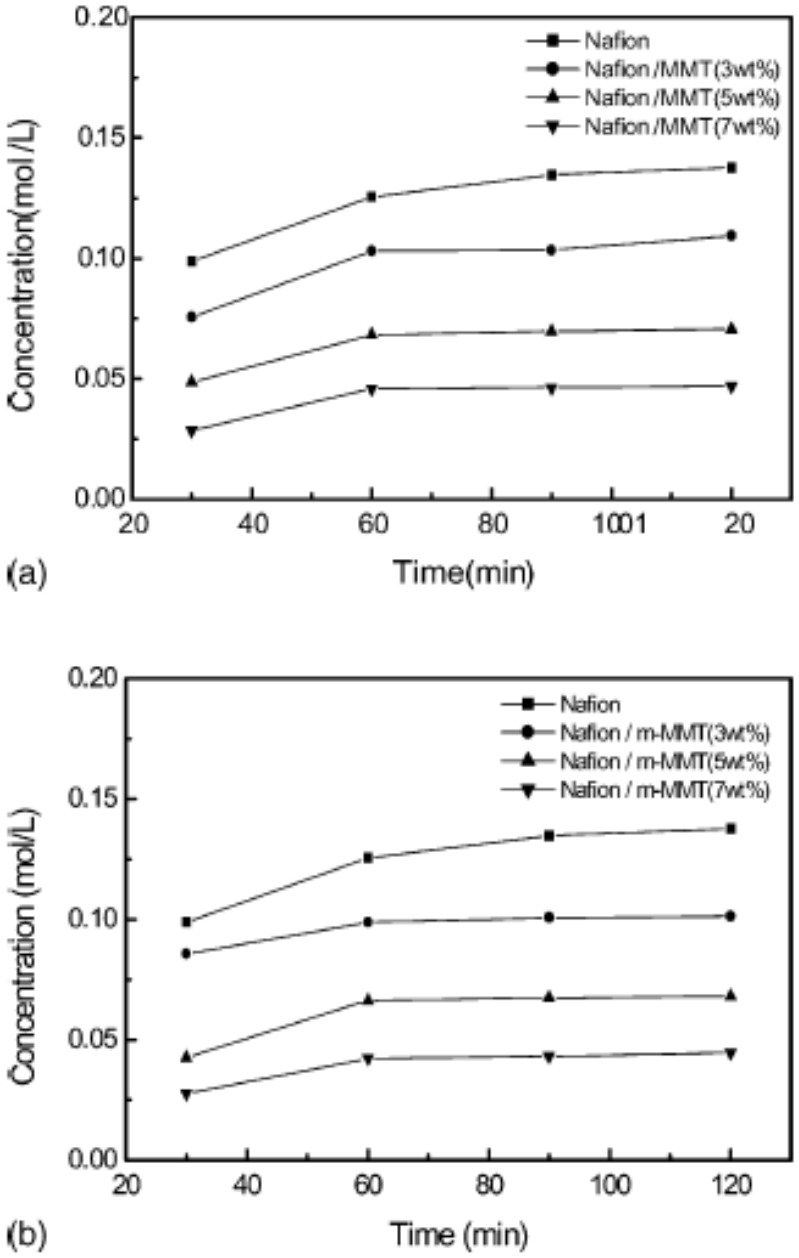

Figure 2.14 Methanol concentration: (a) MMT and (b) Nafion/m–MMT composite membrane with various content of mmt or m–MMT as a function of time. Reproduced from Ref. [20] with permission from Elsevier Science Ltd.

Thomassin et al. [21] reported no improvement in methanol permeability of Nafion membranes upon addition of pristine MMT and Cloisite® ACA clays, while C30B and Cloisite BHB incorporation showed a favorable impact on the methanol permeability of Nafion membranes. The most important effect was observed in the case of the better dispersed Cloisite BHB containing Nafion membrane. On the other hand, in the case of TEOS-containing Nafion membrane, it was found that the methanol permeability decreased with increased loading of silica in the membrane and the value was lower than that of the permeability value of neat Nafion membrane.[80]

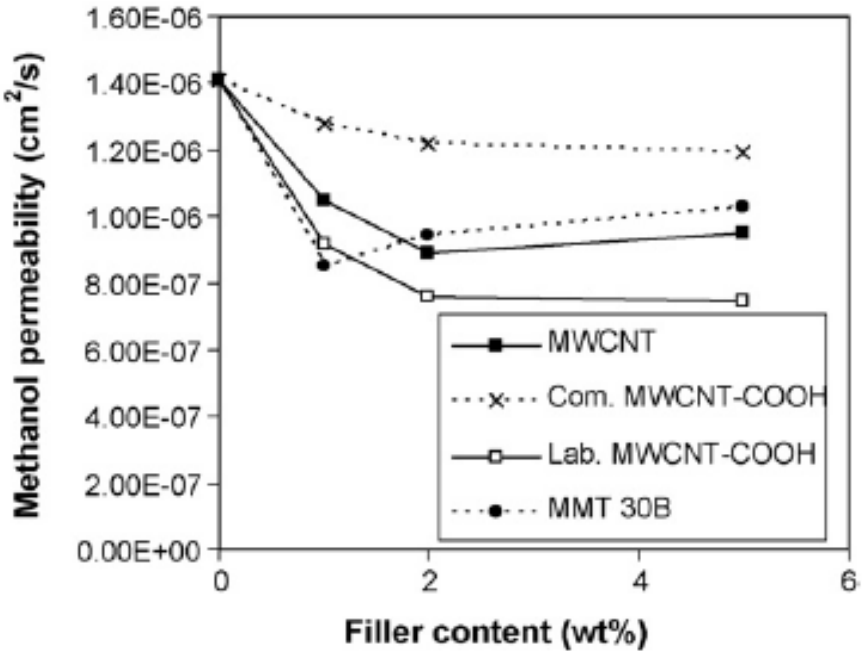

Figure 2.15 The methanol permeability of the MWCNTs containing Nafion membranes. Reproduced from Ref. [74] with permission from Elsevier Science Ltd.

Thomassin et al.[74] measured the methanol permeability of the MWCNTs containing Nafion membranes and the corresponding results are reported in **Figure 2.15**.[74] Upon the addition of 2 wt% of MWCNTs, the permeability value of neat Nafion membrane decreased to 60%, and this value is much higher than that of clay-containing Nafion membrane.[21] This may be due to the fine dispersion of MWCNTs in Nafion matrix, although MWCNTs are expected to be less effective than the platelet-like fillers such as layered silicates. The permeability value further

decreased when lab. MWCNT–COOH dispersed in Nafion matrix, which may reflect a better dispersion of the MWCNTs into Nafion matrix compared to the unfunctionalized MWCNTs. However, beyond 2 wt% MWCNTs incorporation, the permeability did not improve anymore, rather permeability efficiency decreased with the MWCNTs loading. This may be due to the aggregation of MWCNTs in Nafion matrix. On the other hand, the effect of incorporation of com. MWCNT–COOH was lower than in the other two cases, more likely because of the shorter length of these tubes.

A recent report by Alonso et al.[57] showed that the relative permeability of methanol for clay-containing Nafion nanocomposite membranes casted from water showed much less permeability than those casted using low aliphatic alcohols. We believe this is due to the finer distribution of clay particles in the hybrid membranes casted from water as a solvent. The relative permeability of membranes casted from both water and low aliphatic alcohols decreases systematically with an increase in clay loading. However, the decrease is much more in the case of water casted hybrids than low aliphatic alcohol casted membranes. The authors believe this again due to the different degree of dispersion of silicate layers in the Nafion matrix.

By using the well established theories of gas permeability in composite materials,[106] Cussler et. al. also modelled the difference between the methanol-permeability of these two types of membranes by considering the aspect ratio for the clay nanoparticles of 300 and 60 for the nanocomposites casted from water and alcohol, respectively. The results presented in **Figure 2.16** showed that the higher aspect ratio in the case of membranes casted from water is consistent with the better dispersion of the clay in these systems. Membranes cast in low aliphatic alcohols suffer from poor clay dispersion increasing the apparent thickness of the layer nanoparticle and decreasing the aspect ratio. Thus, adding a small volume fraction of well-dispersed clay nanoparticles significantly reduces methanol permeability in Nafion, increasing the fuel efficiency in DM fuel cells and decreasing the potential losses due to the oxidation of methanol in the cathode compartment.

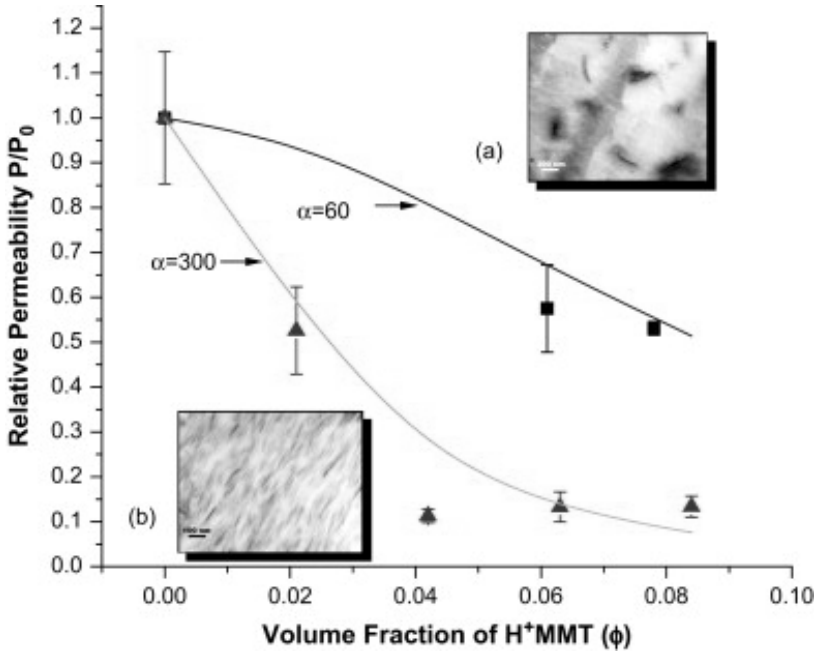

Figure 2.16 Relative methanol permeability for Nafion nanocomposite membranes as a function of volume fraction of clay: (–) Dispersion medium: low aliphatic alcohols and water, solvent cast temperature 80°C; (:) Dispersion medium: water, solvent cast temperature 180°C. Solid lines represent the predictions by considering aspect ratios ~ 300 (light color line) and 60 (deep color line). Insets are bright-field TEM images corresponding to the two nanocomposite membranes. Details can be found in Ref. [57]. Reproduced from Ref. [57] with permission from Elsevier Science Ltd.

2.5.4 Proton Conductivity

High proton conductivity is an important requirement for polymer membranes used as an electrolyte in fuel cell applications. A great challenge in fuel cell technology is to develop polymer membranes with high proton conductivity especially at dry conditions. Proton conductivity of fuel cell membrane is generally measured using a galvanostatic four-point-probe alternative current electrochemical impedance spectroscopy (EIS) technique, which is relatively so insensitive to the contact impedance that it could be adequate to accurately test membranes with high conductivity.[22] A standard conductivity cell is made up of two platinum foils carrying

the current and two platinum wires sensing the potential drop, which is 1 cm apart. The standard cell configuration is illustrated in **Figure 2.17**. The proton conductivity value is calculated by: [29]

$$\sigma = \frac{L}{RWd} \tag{2.11}$$

where σ, L, and R denote the proton conductivity, the distance between the electrodes to measure the potential (1 cm), and the impedance of the membrane, respectively. W and d are the width of the membrane (1 cm) and the thickness of the membrane, respectively, as indicated in Figure 2.17. In a four-point proton conductivity cell, a fixed AC current is passed between two outer electrodes, and the conductance of the material of interest is calculated from the ac potential difference observed between two inner electrodes. In this way, contact resistance, lead resistance, and lead inductance are almost completely eliminated.

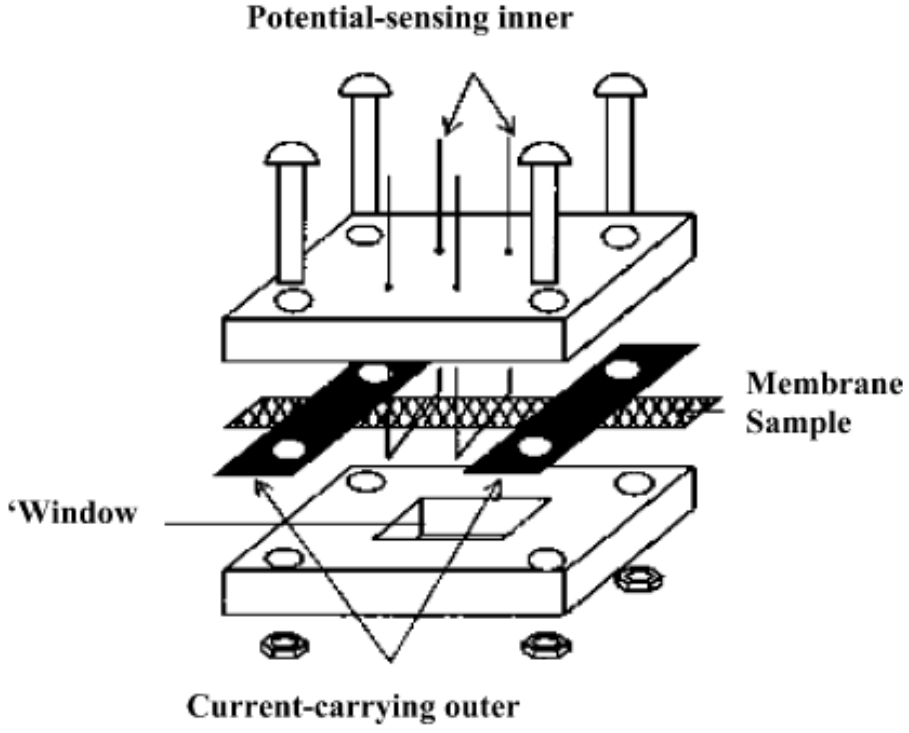

Figure 2.17 Schematic view of proton conductivity cell for four-point-probe electrochemical impedance spectroscopy technique.

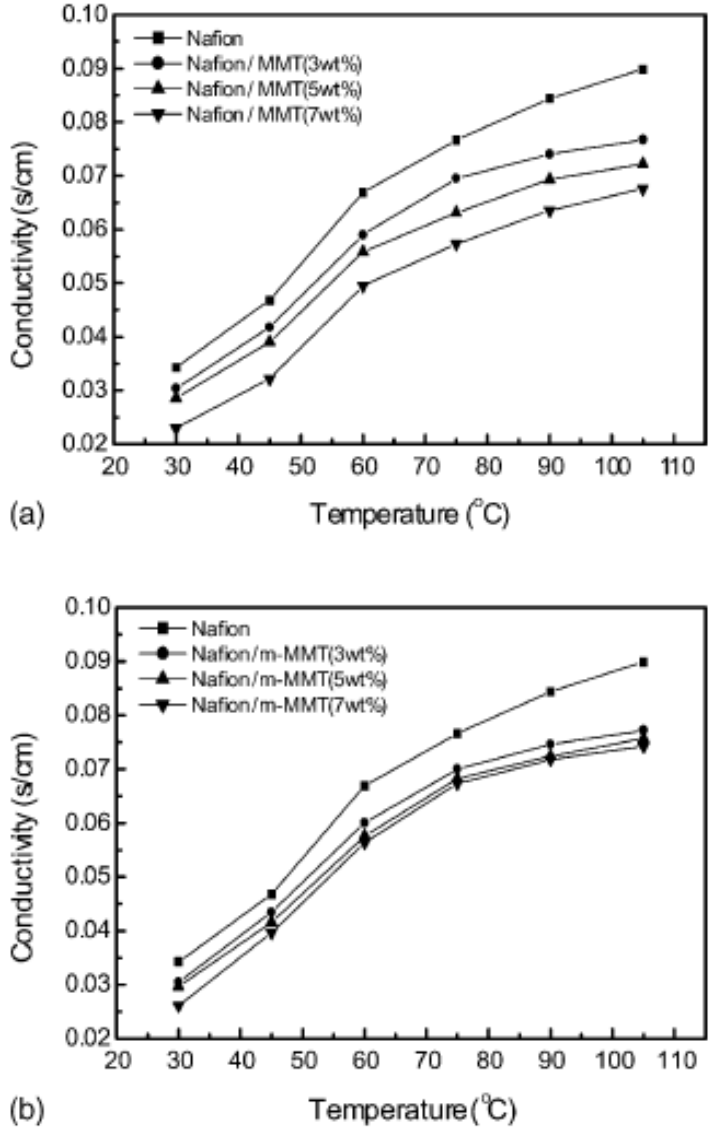

Figure 2.18 Proton conductivity as a function of temperature for: (a) normal membrane and Nafion1 resin/MMT composite membrane, and (b) m-MMT (with 3, 5, and 7 wt% clay loading) at completely humidified stage. Reproduced from Ref. [20] with permission from Elsevier Science Ltd.

Jung et al.[20] measured the ionic conductivities of neat Nafion and MMT containing Nafion nanocomposite membranes at various temperatures. Results are reported in parts (a) and (b) of **Figure 2.18** for Nafion/MMT composite membranes and Nafion/m-MMT composite membranes, respectively. All the membranes exhibited a marked increase in conductivity with

temperature. Such an observation is very normal because temperature plays a vital role in the kinetics of proton motion in the polymeric membrane and the mobility of the polymer chains. However, for a particular temperature, the conductivity value of nanocomposite membrane is lower than the normal neat membrane.

Thomassin et al. [21] also found the same trend; the ionic conductivity of the unfilled membranes was decreased upon the addition of MMT, whether modified or not. This effect was, however, very small except in the case of C30B based nanocomposite membranes, thus MMT modified by a voluminous counter0ion without carboxylic acid attached to it. On the other hand, in the case of Cloisite BHB, where the carboxylic acid was part of the voluminous counter ion, the deleterious impact on the proton transport was restricted.

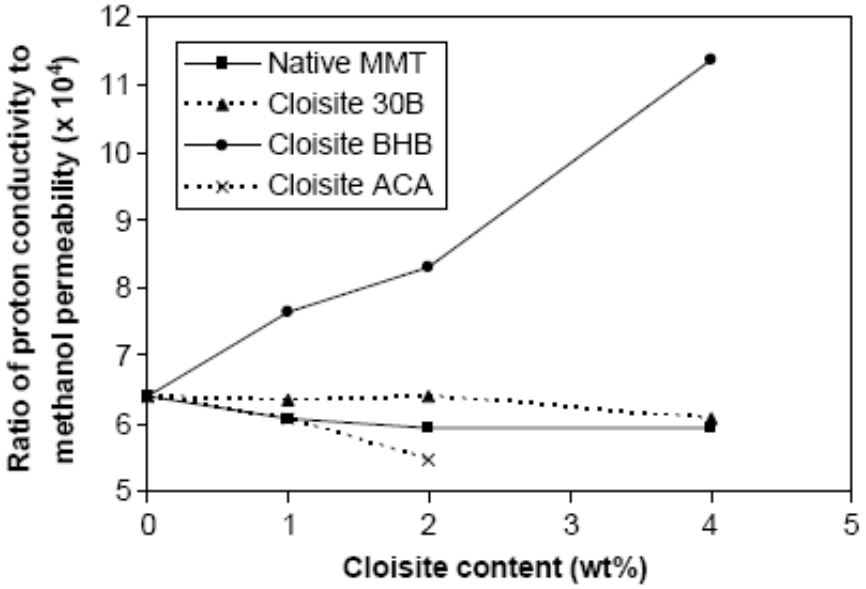

Figure 2.19 Dependence of the C/P ratio on the content of native and modified MMT in Nafion membranes. Reproduced from Ref. [21] with permission from Elsevier Science Ltd.

However, from the experimental data of methanol permeability and the ionic conductivity, it appears that Cloisite BHB containing Nafion membrane was the best compromise as assessed by plotting the conductivity to methanol permeability ratio against the filler loading, as shown in

Figure 2.19. The higher the C/P ratio, the better the performances of Direct Methanol fuel cells. Clearly, Cloisite BHB was the more effective additive with an approximately two-fold increased in C/P ratio compared to the neat Nafion membrane.

Recently, Alonso et al.[57] showed that the ratio of ionic conductivity over permeability of H^+-MMT containing Nafion nanocomposite membranes is higher compared to neat Nafion or hybrids made by incorporation of surface-modified silica nanoparticles. According to the authors, the small decrease of ionic conductivity for H^+-MMT containing Nafion nanocomposite membranes is more than compensated by the large decrease in methanol permeability.

2.5.6. Water Uptake/Hydration

The performance of a proton exchange fuel cell membrane is dependent on proton conductivity, which in turn depends on the hydration. Higher conductivity is supported by the higher level of hydration. However, for operations with wet membranes, there is a possibility of the cathode being flooded, which slows down the oxidation reaction. This is a problem with Nafion-based membranes, which undergo swelling at high water contents and high relative humidity because of the electro-osmotic drag, studied by Zadowzinski et al.[108] The electro-osmotic drag coefficient (EODC), a quantitative measure of hydration, is defined as the number of water molecules transported per protons. Their studies showed that the EODC is mainly a function of water content and is independent of the type of Nafion membrane used. Generally, the water uptake of the membrane determined by measuring the change in the weight before and after the hydration is calculated by the following equation:

$$\text{water uptake (\%)} = \frac{W_{wet} - W_{dry}}{W_{dry}} * 100 \qquad (2.12)$$

where W_{wet} and W_{dry} are the weights of wetted and dried membranes, respectively.

2.6 Fuel Cell Efficiency

Fuel cells with high power density and very low degradation are the state of the art. The main requirement for the future is to achieve high efficiency fuel cell by fabricating alternative membranes with better temperature stability. The fuel cell efficiency is influenced by many properties including: (i) proton conductivity, (ii) mechanical and thermal stability of the membrane, and (iii) methanol permeability of the membrane. The efficiency (η) of any fuel cell is the ratio between the electrical power output and the fuel input. Both must be in the same units (Watts) and is given by the equation:

$$\eta = \frac{\text{electricalpoweroutput}(P_{fc})}{\text{fuelinput}(F_{in})} \qquad (2.13)$$

$$P_{fc} = VI \qquad (2.14)$$

Fuel input is a product of fuel (hydrogen) consumption rate (g/s) and its energy content, usually given as enthalpy (ΔH) or higher heating value. Hydrogen's higher heating value is 142 KJ/g. Hydrogen consumption rate in the chemical reaction:

$$H_2 + \frac{1}{2}O_2 \rightarrow H_2O \qquad (2.15)$$

determined by Faraday's law as:

$$q_{H_2} = \frac{mI}{nF} \qquad (2.16)$$

where m = hydrogen molecular weight (2,016) and Faraday's constant F = $N_A e$ (see appendix A)

I = current (A)
n = number of electrons involved

F = Faraday's constant (96485, 34 C/mol)

Fuel input is therefore:

$$F_{in} = q_{H_2}\Delta H = \frac{m\Delta H}{nf} I \qquad (2.17)$$

For the electrochemical reaction **[Equation (1.15)]**, the expression mΔH/(nF) has a value of 1.482v. This is called the thermo-neutral or revisable potential, which corresponds to the maximum possible energy (both electrical and thermal) resulting from the electrochemical reaction **[see Equation (1.15)]**. Therefore, by combining **Equations (1.13)**, **(1.14)**, **(1.16)**, and **(1.17)**, the fuel cell efficiency is simply the ratio of the actual operating voltage and 1.482v:

$$\eta = \frac{V}{1.482} \qquad (2.18)$$

The free energy part (Δ*G*) of the total enthalpy (ΔH) can be converted into electricity due to irreversible entropy changes (TΔS), i.e.:

$$\Delta G = \Delta H - T\Delta S \qquad (2.19)$$

The theoretical maximum potential of the reaction **[Equation (2.15)]**, corresponds to the free energy (Δ*G*°) at 25°C and atmospheric pressure is 1.229 v. Therefore, the maximum theoretical hydrogen fuel cell efficiency is 1.229/1.482 = 0.83. The theoretical or thermodynamic potential at different conditions is lower than the thermodynamic potential due to various losses such as (a) activation losses, (b) concentration losses, and (c) resistive or ohmic losses.[109] At open circuit, when no load is connected to the fuel cell and consequently no power is being generated, the potential of PEM fuel cell is typically about 1v. When a load is connected to the fuel cell, the cell potential decreases further as more and more current is being generated after the addition of the load. In order to account for mass transport losses that occur when some regions of the electrodes reach the limiting current densities, an empirical equation that fits experimental results very well is considered. [110] The fuel cell efficiency is directly proportional to the cell potential as shown in **Equation (2.15)**, therefore it is also a function of power density. The efficiency at

maximum power is much lower than the efficiency at partial loads, which makes fuel cells very attractive and efficient for applications with highly variable loads, where most of the time a fuel cell is operated at a low load and high efficiency.

Jung et al.[20] found, using Nafion 117 and 2.5 M methanol, an increase in the performance of the cell when operating temperatures increased. They attributed this higher performance to the combined effects of a reduction of ohmic resistance and polarization. In fact, the ionic conductivity of Nafion membranes increases with an increase in temperature. These results are in agreement with those obtained by Surampudi et al.[111] with Nafion 117 membranes and 2 M methanol fuel cell in the range of 30–90°C, and with the results presented in Ref. [60], where it is found that a difference in the operation temperature makes a significant difference in the cell performance. An increase in temperature resulted in an increases in the methanol crossover, as previously mentioned.[60] For this reason, other researchers have studied the possibility of vapor-feed DMFCs.[112] The fuel cell performance is depicted by current vs. voltage plots, known as polarization curves.

2.7 Conclusion

The high temperature proton exchange membranes are very important in the commercialization of fuel cells. Nafion-based nanocomposite membranes are a very important inclusion in the family of proton exchange fuel cell membranes and their history is no longer than five years. The present chapter provides a snapshot of the synthesis and characterization procedures of Nafion and various types of Nafion-based nanocomposite membranes. By changing the nature of the nanofillers and the processing conditions, some of the physical properties of neat Nafion, such as mechanical, thermal, permeability, proton conductivity, etc., have been improved significantly, which was not possible by simple mixing with conventional fillers.

Although a significant amount of work has already been done on various aspects of Nafion-based nanocomposite membranes, much research still remains in order to understand the complex structure-property relationships in various nanocomposite membranes. Particularly, to find out the link between the Nafion semicrystalline morphology and the properties such as transport and

thermo-mechanical properties, relevant to the use of this polymer electrolyte in fuel cells. Another major challenge remains to balance the ratio between the proton conductivity and the methanol permeability, which to date has not been attained. The conclusions drawn are that these nanocomposite membranes should be commercially available once the conductivity/methanol permeability ratio is maximized, and their appropriate utilization will open new directions in alternative energy sources.

2.8 References

[1] H.F. Cui, J.S. Ye, W. D. Zhang, J. Wang, and F.S. Sheu, *J. Electroanal. Chem.* **2005**, *577*, 295–302.

[2] A.V. Anantaraman and C.L. Gardner, *J. Electroanal. Chem.* **1996**, *414*, 115–123.

[3] N. Sugishima, J.T. Hinatsu, and F.R. Foulkes, *J. Electrochem. Soc.* **1994**, *141*, 3325–3333.

[4] V. Plzak and B. Rohland, "Advanced Electrochemical Hydrogen Technologies", in Modern Aspects of Electrochemistry, B.E. Conway, J.O. M. Bockris, and R. E. White, Eds, Plenum Press: New York, **1994**.

[5] K.V. Kordesch and G.R. Simander, *Chem. Rev.* **95**, (1995), 191–207.

[6] Y. Shen, X. Qiu, J. Shen, J. Xi, and W. Zhu, *J. Power Sources* **2006**, *16*, 54–60.

[7] Fuel Cell Basics. (November 2nd, 2**008**) Downloaded from http://americanhistory.si.edu/fuelcells/basics.htm#.

[8] Fuel Cell Handbook, 5th Edition, Report prepared by EG&G Services, Parsons, Inc. and Science Applications International Corporation under contract no. DE–AM26–99FT40575 for the U.S. Department of Energy, National Energy Technology Laboratory, October **2000**.

[9] M. Doyle and G. Rajendran, *Handbook of Fuels Cell Fundamentals*, Vielstich, John Wiley, **2003**.

[10] T. Thampan, S. Malhotra, and R. Datta, *Catalysis Today* **2001**, *67*, 15–32.

[11] A. Katchalsky, R.A. Curran, and F. Peter, *Nonequilibrium Thermodynamics in Biophysics*, Harvard University Press, **1965**.

[12] P. Jannasch, *Curr. Opin. Colloid Interface Sci.* **2003**, *8*, 96–102.

[13] E. Schneider, D. Sagan, and S. Dorion, in "To the Cool Energy Flow", *Thermodynamics and Life*, Chicago, **2005**.

[14] R.B. Gunn, F. Peter, and R.A. Curran, *Biophys. J.* **1971**, *11*, 559–571.

[15] I. Ledneczki, M. Darányi, F. Fülöp, and A. Molnár, *Catalysis Today* **2005**, *100*, 437–440.

[16] N. Miyake, J.S. Wainright, and R.F. Savinell, *J. Electrochem. Soc.* **2001**, *148*, A898–904.

[17] P. Staiti, A.S. Arico, V. Baglio, F. Lufrano, E. Passalacqua, and V. Antonucci, *Solid State Ionics* **2001**, *145*, 101–107.

[18] B. Tazi and O. Savadogo, *Electrochim. Acta* **2000**, *45*, 4329–4339.

[19] K. Tadanaga, H. Yoshida, A. Matsuda, T. Minami, and M. Tatsumisago, *Electrochem. Commun.* **2003**, *5*, 644–646.

[20] D.H. Jung, S.Y. Cho, D.H. Peck, D.R. Shin, and J.S. Kim, *J. Power Sources* **2003**, *118*, 205–211.

[21] J.M. Thomassin, C. Pagnoulle, D. Bizzari, G. Caldarella, A. Germain, and R. Jerome, *Polymer* **2006**, **46**, 11389–11395.

[22] S. Banerjee and D.E. Curtin, *J. Fluorine Chem.* **2004**, *125*, 1211–1216.

[23] D.A. Hounshell and J.K. Smith Jr. DuPont R&D, 1902–**1980**.

[24] K. Johns and G. Stead, *J. Fluorine Chem.* **2000**, *104*, 5–18.

[25] T.D. Gierke, W.Y. Hsu, A. Eisenberg, and H.L. Yeager, Eds., Perfluorinated Ionomer Membranes, *ACS Symp Series*, **1982**.

[26] L. Hong, Y. Zhou, N. Chen, and K. Li, *J. Colloid Interface Sci.* **1999**, *218*, 233– 242.

[27] C. Heitner–Wirguin, *J. Membr. Sci.* **1996**, *120*, 1–33.

[28] W.G. Grot, *Macromol. Symp.* **1994**, *84*, 161–172.

[29] H.R. Zelsmann, M. Pineri, M. Thomas, and M. Escoubes, *J. Appl. Polym. Sci.* **1990**, *41*, 1673–1684.

[30] T. Xue, R.B. Longwell, and K. Osseo-Asare, *J. Membr. Sci.* **1991**, *58*, 175–89.

[31] [31a] S. Sinha Ray, M. Okamoto, *Prog. Polym. Sci.* **2003**, *28*, 1539–1542. [31b] F.F. Fang, H.J. Choi, and J. Joo, *J Nanosci. Nanotechnol.* **2008**, *8*, 1559–1581. [31c] S. Pavlidou and C.D. Papaspyrides, *Prog. Polym. Sci.* **2008**, 33, 1119–1198. [31d] M. Alexandre and P. Dubois, *Mater. Sci. Eng.* **2000**, *R28*, 1–63. [31e] J.H. Park, H.M. Lee,

I.J. Chin, H.J. Choi, H.K. Kim, and W.G. Kang, *J. Phys. Chem. Solids* **2008**, *69*, 1375–1378.

[32] [32a] J. W. Kim, F. Liu, H.J. Choi, S.H. Hong, and J. Joo, *Polymer* **2003**, *44*, 289–293. [32b] H.B. Kim, J.S. Choi, C.H. Lee, S.T. Lim, M.S. Jhon, and H.J. Choi, *Eur. Polym. J.* **2005**, *41*, 679–685. [32c] S.K. Lim, J.W. Kim, I. Chin, Y.K. Kwon, and H. J. Choi, *Chem. Mater.* **2002**, *14*, 1989–1994.

[33] [33a] S. Sinha Ray and M. Bousmina, *Prog. Mater. Sci.* **2005**, *50*, 962–1080. [33b] V. Causin, C. Marega, A. Marigo, G. Ferrara, A. Ferraro, and R. Selleri, *J. Nanosci. Nanotechnol.* **2008**, *8*, 1823–1834.

[34] H. Fischer, *Mater. Sci. Eng.* **2003**, *C23*, 763–772.

[35] G. Lagaly, *Appl. Clay Sci.* **1999**, *15*, 1–9.

[36] E.P. Giannelis, *Adv. Mater.* **1996**, *8*, 29–35.

[37] P.C. LeBaron, Z. Wang, and T. J. Pinnavaia, *Appl. Clay Sci.* **1999**, *15*, 11–29.

[38] R.A. Vaia and H.D. Wagner, *Mater. Today* **2004**, *7*, 32–37.

[39] Q.H. Zeng, A.B. Yu, G.Q. Lu, and D.R. Paul, *J. Nanosci. Nanotechnol.* **2005**, *5*, 1574–1592.

[40] W.E. Gacitua, A.A. Ballerini, and J. Zhang, *Maderas Cienciay Technologia* **2005**, *7*, 159–178.

[41] S. Singh and S. Sinha Ray, *J. Nanosci. Nanotechnol.* **2007**, *7*, 2596–2615.

[42] M.A. Osman, V. Mittal, and H.R. Lusti, *Macromol. Rapid Commun.* **2004**, *25*, 1145–1149.

[43] A.B. Morgan, Polym. *Adv. Technol.* **2006**, *17*, 206–217.

[44] A. Mudaliar**,** Q. Yuan, and R.D.K. Misra, *Poly. Eng. Sci.* **2006**, *46*, 1625–1634.

[45] G. Schmidt and M.M. Malwitz, *Curr. Opin. Colloid Interface Sci.* **2003**, *8*, 103–108.

[46] B. Pascal, A.B. Allen, C. Peter, and W. Andy, *J. Mater. Chem.* **2003**, *13*, 2540–2550.

[47] E. Ruiz–Hitzky, P. Aranda, B. Casal, and J.C. Galvan, *Adv. Mater.* **1995**, *7*, 180–184.

[48] S. Sinha Ray, *J. Indus. Eng. Chem.* **2006**, *6*, 811–842.

[48b] S. Sinha Ray, K. Okamoto, and M. Okamoto, *Macromolecules* **2003**, 36, 2355–2367.

[49] G. Pourcelly and C. Gavach, in *Proton Conductors*, P. Colomban, Ed., Cambridge University Press 1992, p. 45.

[50] [50a] S. Sinha Ray, *Macromol. Mater. Eng.* **2009**, *294*, 281–186. [50b] S. Mehta, F.M. Mirabella, K. Rufener, and A. Bafna, *J. Appl. Polym. Sci.* **2004**, *92*, 928–936. [50c] P.D. Fasulo, W.R. Rodgers, and R.A. Ottaviani, *Polym. Eng. Sci.* **2004**, *44*, 1036–1045. [50d] C. Marega, V. Causin, A. Marigo, and G. Ferrara, *J. Appl. Polym. Sci.* **2009**, *113*, 3920–3928. [50e] K. Masenelli–Varlot, G. Vigier, A. Vermogen, C. Gauthier, and J.Y. Cavaille, *J. Polym. Sci. Part B: Polym. Phys.* **2007**, *45*, 1243–1251. [50f] C. Marega, V. Causin, A. Marigo, G. Ferrara, and H. Tonnaer, *J. Nanosci. Nanotechnol.* **2009**, *9,* 2704–2714.

[51] [51a] J.M. Thomassin, C. Pagnoulle, D. Bizzari, G. Caldarella, A. Germain, and R. Jerome, *e–Polymer* **2004**, *18*, 1–13. [51b] J.M. Thomassin, C. Pagnoulle, D. Bizzari, G. Caldarella, A. Germain, and R. Jerome, *J. Membr. Sci.* **2006**, *270*, 50 – 56.

[52] H. Rhee, H.K. Kim, H. Chang, and J.S. Lee, *Chem. Mater.* **2005**, *17*, 1691–1697.

[53] M.K. Song, S.B. Park, Y.T. Kim, K.H. Kim, S.K. Min, and H.W. Rhee, *Electrochim. Acta.* **2004**, *50*, 639–643.

[54] R.F. Silva, S. Passerini, and A. Pozio, *Electrochim. Acta.* **2005**, *50*, 2639–2645.

[55] T.K. Kim, M. Kanga, Y.S. Choi, H.K. Kim, W. Lee, H. Chang, and D. Seung, *J. Power. Sources* **2007**, *165*, 1–8.

[56] L. Zhang, J. Xu, G. Hou, H. Tang, and F. Deng, *J. Colloid Interface Sci.* **2007**, *311*, 38–44.

[57] R.H. Alonso, L. Estevez, H. Lian, A. Kelarakis, and E.P. Giannelis, *Polymer* **2009**, *50*, 2402–2410.

[58] E. Burgaz, H. Lian, R.H. Alonso, L. Estevez, A. Kelarakis, and E.P. Giannelis, *Polymer* **2009**, *50*, 2384–2392.

[59] [59a] J. Bernholc, C. Roland, and B.I. Yakobson, *Curr. Opinon Solid State Mater. Sci.* **1997**, *2*, 706–715. [59b] C.N.R. Rao, R. Sen, and A. Govindaraj, *Curr. Opin. Solid State Mater. Sci.* **1996**, *1*, 279–284. [59c] J.N. Coleman, U. Khan, W. J. Blau, and Y.K. Guńko, *Carbon* **2006**, *44*, 1624–1652.

[60] X.L. Xie, Y.W. Mai, X.P. Zhou, *Mater. Sci. Eng. R* **2005**, *49*, 89–112.

[61] [61a] K. Zhang, J.Y. Lim, and H.J. Choi, *Diamond Related Mater.* **2009**, *18*, 316–318. [61b] S.T. Kim, H.J. Choi, and S.M. Hong, *Colloid Polym. Sci.* **2007**, *85*, 593–598. [62c] S.J. Park, M.S. Cho, S.T. Lim, and H.J. Choi, *Macromol. Rapid Commun.* **2003**, 24,

1070–1073. [61d] J.N. Coleman, M. Cadek, K.P. Ryan, A. Fonseca, J.B. Nagy, W.J. Blau, and M.S.Ferreira, *Polymer* **2006**, *47*, 8556– 8561.

[62] P.M. Ajayan, L.S. Schadler, and P.V. Braun, *Nanocomposite Science and Technology*. Morlenbach, Germany: Wiley-VCH Verlag, 2003.

[63] J. Qiu, C. Zhang, B. Wang, and R. Liang, *Nanotechnology* **2007**, *18*, 275708 (11pp).

[64] K.I. Winey, T. Kashiwagi, and M. Mu, *Mater. Res. Soc. Bull.* **2007**, *32*, 348–53.

[65] S. Sinha Ray, S. Vaudreuil, A. Maazouz, and M. Bousmina, *J. Nanosci. Nanotechnol.* **2006**, *6*, 2191–2195.

[66] H. Miyagawa, A.K. Mohanty, T.L. Drzal, and M. Misra, *Nanotechnology* **2005**, *16*, 118–24.

[67] [67a] C.S. Choi, B.J. Park, and H.J. Choi, *Diamond Relater. Mater.* **2007**, *16*, 1170–1173. [67b] L.J. Ci and J.B. Bai, *Compos. Sci. Technol.* **2006**, *66*, 599–603. [67c] S. J. Park, M.S. Cho, S.T. Lim, H.J. Choi, and M.S. Jhon, *Macromol. Rapid. Commun.* **2005**, *26*, 1563–1566.

[68] M.S. Dresselhaus, G. Dresselhaus, and P.C. Eklund. Science of Fullerenes and Carbon Nanotubes, Academic Press, San Diego 1996.

[69] J.P. Lu, *Phys. Rev. Lett.* **1997**, *79*, 1297–1300.

[70] P.J.F. Harries. *Carbon Nanotubes and Related Structures*, Cambridge University Press, 1999.

[71] L. Soloviova and M. Marder. Russian Matryoshka. Moscow, Russia: Interbook, 1993.

[72] L.N. Soloviova, Moscow, Russia: Interbook Business, 1997.

[73] Y.H. Liu, B. Yi, Z.G. Shao, D. Xing, and H. Zhang, *Electrochem Solid–State Lett.* **2006**, *9*, 356–359.

[74] J.M. Thomassin, J. Kollar, G. Caldarella, A. Germain, R. Jerome, and C. Detrembleur, *J. Membr. Sci.* **2007**, *303*, 252–257.

[75] N.P. Cele, S. Sinha Ray, and M. Ndwandwe, unpublished results.

[76] K.A. Mauritz and R.M. Warren, *Macromolecules* **1989**, *22*, 1730–1735.

[77] I.D. Stefanithis and K.A. Mauritz, *Macromolecules* **1990**, *23*, 2397–2402.

[78] K.A. Mauritz, *Mater. Sci. Eng.* **1998**, *C6*, 121–33.

[79] P. Dimitrova, K.A. Friedrich, U. Stimming, and B. Vogt, *Solid State Ionics* **2002**, *150*, 115–22.

[80] P.L. Antonucci, A S. Ario, P. Creti, E. Ramunni, and V. Antonucci, *Solid State Ionics* **1999**, *125*, 431–437.

[81] Z.G. Shao, P. Joghee, and I.M. Hsing, *J. Membr. Sci.* **2004**, *229*, 43–51.

[82] K.T. Adjemian, S.J. Lee, S. Srinivasan, J. Benziger, and A.B. Bocarsly, *J. Electrochem. Soc.* **2002**, *149*, 256–261.

[83] D.H. Jung, S.Y. Cho, D.R. Shin, and J.S. Kim, *J. Power Sources* **2002**, *106*, 173–177.

[84] W. Xu, T. Liu, C. Liu, and W. Xing, *Electrochim. Acta* **2005**, *50*, 3280–3285.

[85] C. Li, G. Suna, S. Rena, J. Liu, Q. Wang, Z. Wu, H. Sun, and W. Jin, *J. Membr. Sci.* **2006**, *272*, 50–57.

[86] M. Hickner, Y.S. Kim, F. Wang, J.E. McGrath, and T. Zawodzinski, *Sixteenth Tech. Confer.* **2001**, 323.

[87] Y.S. Kim, M. Hill, F. Wang, M. Hickner, Y.T. Hong, T.A. Zawodzinski, and J.E. McGrath. Eighth International Symposium on Polymer Electrolytes, Santa Fe, May 19–24, **2002**.

[88] M. Watanabe, H. Uchida, and U. Emori. *J. Electrochem. Soc.* **1998**, *145*, 1137– 1141.

[89] E. Chida, Y. Mizuno, L. Agihara, and M. Watanabe, *Chem. Lett.* **2000**, *20*, 1268–1275.

[90] M. Watanabe, H. Uchida, and H. Igarashi, *Macromol. Symp.* **2000**, *156*, 223–230.

[91] C. Yang, C. Srinivasan, A.B. Bocarsly, S. Tulyani, and J.B. Benziger, *J. Membr. Sci.* **2004**, *237*, 145–161.

[92] J.T. Hinatsu, M. Mizuhata, and H. Takenaka, *J. Electrochem. Soc.* **1994**, *141*, 1493–1498.

[93] P. Futerko and I.M. Hsing, *J. Electrochem. Soc.* **1999**, *146*, 2049–2053.

[94] G. Alberti, M. Casciola, S. Cavalaglio, and R. Vivani, *Solid State Ionics* **1999**, *125*, 91–97.

[95] Y.J. Kim, W.C. Choi, S.I. Woo, and W.H. Hong, *Electrochem Acta* **2004**, *29*, 3227–3234.

[96] Y.S. Kima, L. Donga, M.A. Hicknera, B.S. Pivovarb, and J.E. McGrath, *Polymer* **2003**, *44*, 5729–5736.

[97] Y.M. Kim, K.W. Park, J.H. Choi, I.S. Park, and Y.E. Sung, *Electrochem. Commun.* **2003**, *5*, 571–574.

[98] F. Bauer and M. Willert–Porada, *J. Membr. Sci.* **2004**, *233*, 141–149.

[99] V. Ramani, H.R. Kunz, and J.M. Fenton, *J. Membr. Sci.* **2004**, *232*, 31–44.

[100] J-H. Tian, P-F. Gao, Z-Y. Zhang, W-H. Luo, and Z-Q. Shan, *Inter. J. Hydrogen Energy* **2008**, *33*, 5686–5690.

[101] B. Ruffmann, H. Silva, B. Schulte, and S.P. Nunes, *Solid State Ionics* **2003**, *162–163*, 269–275.

[102] C.A. Wilkie, J.R. Thomsen, and M.L. Mittleman, *J. Appl. Polym. Sci.* **1991**, *42*, 901–909.

[103] K.A. Mautritz, R.F. Storey, and C.K. Jones, in: L.K. Utracki and R.A. Weiss (Eds.), ACS Symposium Series 395, American Chemical Society, Washington, DC, 1989, p. 401.

[104] K.A. Mautritz, I.D. Stefanithis, S.V. Davis, R.W. Scheetz, R.K. Pope, G.L. Willes, and H.H. Haung, *J. Appl. Polym. Sci.* **1995**, *55*, 181–190.

[105] V. Tricoli, *J. Electrochem. Soc.* **1998**, *145*, 3798–3801.

[106] [106a] E.L. Cussler, S.E. Hughes, W. J. Ward, and R. Aris. *J. Membr. Sci.* **1988**, *38*, 161–174. [106b] J.P. DeRocher, B.T. Gettelfinger, J.S. Wang, E.E. Nuxoll, and E.L. Cussler, *J. Membr. Sci.* **2005**, *254*, 21–30.

[107] P. Mukoma, B.R. Jooste, and H.C.M. Vosloo, *J. Power Sources* **2004**, *136*, 16–23.

[108] T. Zadowzinski, J. Davey, J. Valerio, and S. Gottesfeld, *Electrochim. Acta* **1995**, *40*, 297–302.

[109] F. Barbir, Hydrogen Energy Systems, NATO ASI295 (1995) 203, J. O'M Bockris and S. Srinivasan, *Fuel Cells, Their electrochemistry*, McGraw–Hill 1969.

[110] J. Kim, S.M. Lee, S. Srinivasan, and C.E. Chamberlain, *J. Electrochem. Soc.* **1995**, *142*, 2670–2674.

[111] S. Surampudi, S.R. Narayanan, E. Vamos, H. Frank, and G. Halpert, Proceedings of the Eighth Annual Battery Conference on Applications and Advances, Long Beach, CA, January 1993.

[112] A.K. Shukla, P.A. Christensen, A. Hamnett, and M.P. Hogarth, *J. Power Sources* **1995**, *55*, 87–91.

3

Experimental Methods

"May $E=mc^2$ be with you"

3.1 Introduction

The energy crisis and its associated greenhouse effect have led to worldwide intensive research in fuel cells. Proton exchange or polymer electrolytes membrane fuel cells (PEMFC) are at the forefront of this research effort because their operation temperature is suitable for home use and automobile applications. PEMFC can play an important role in hydrogen energy. [1] The main hurdles for these applications are the thermo-mechanical properties and water-methanol permeability of fuel cell membrane. Nafion is the most commonly used membrane for PEMFC applications. In this study Nafion was modified to improve such properties, and the composition, structure as well as properties of modified membranes were studied using various characterization methods.

The main objective for this project is to improve fuel cell performance and efficiency by improving thermo-mechanical properties, balancing the ratio of water-methanol permeability and proton conductivity of Nafion membrane. This is achieved by using polymer nanocomposites technology. Polymer nanocomposite is defined as the combination of polymer matrix and filler, which has at least one dimension in the nanometer range with a nanometer d-spacing. [2] This technology is expected to enhance polymer properties without compromising its inherent properties.

3.2 Materials

3.2.1 Nafion

Nafion is a copolymer membrane with polytetraflouroethylene (PTFE) backbone. It is well known for the best ion conductivity and is the leading PEMFC membrane at this moment. The Nafion precursor, i.e. a perfluorosulfonyl fluoride copolymer resin (Nafion R–1100 resin) was purchased from Ion Power Inc., Bear, DE, USA in the sulfonyl fluoride ($–SO_2F$) form. In this form, the polymer does not have the cation-exchange properties, and was chemically treated to make it suitable for cation-exchange applications.

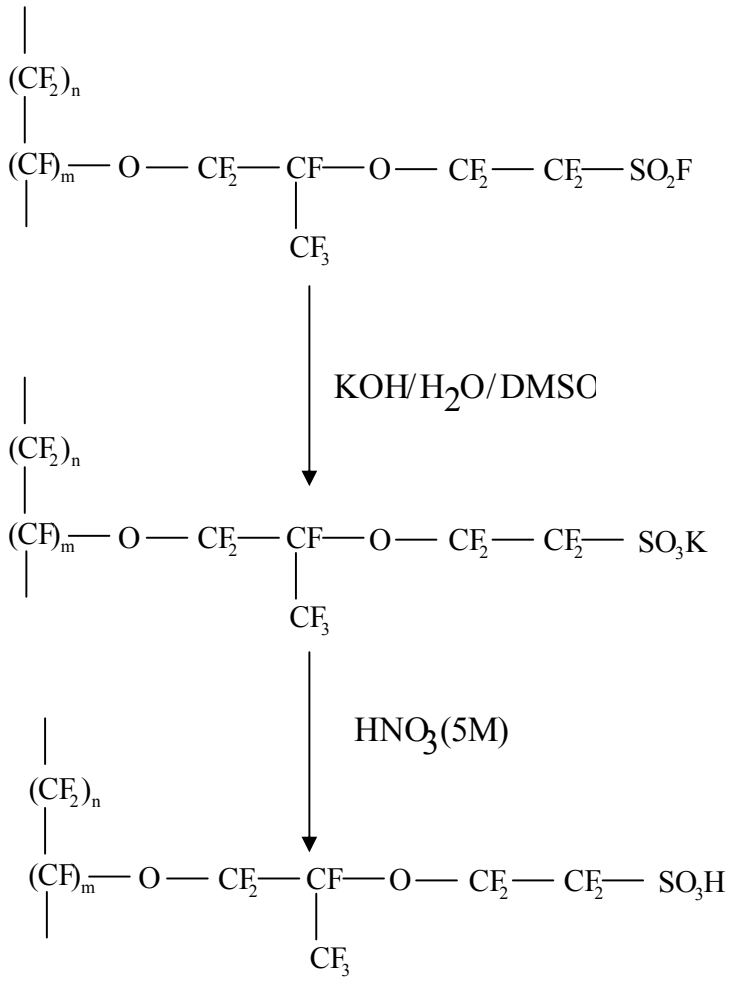

Figure 3.1 Hydrolysis of the Nafion precursor

Nafion resin was converted to the salt form (K^+) and acid form (H^+) using the following processes as shown in **Figure 3.1**. The polymer resins were immersed in a solution containing 15% potassium hydroxide (KOH), 50% deionised water and 35% dimethyl-sulfoxide (wt/wt) at 80°C for 2h. Afterwards the resin was thoroughly washed with deionised water to remove all traces of unreacted KOH. The Nafion resin was now in the K^+ form. The K^+ form Nafion resin was converted to the H^+ form by exchanging K^+ for H^+ ions using a 5 M nitric acid (HNO_3). Since this is an equilibrium exchange, this step was repeated twice with fresh HNO_3 to complete protonation, including a rinse in fresh deionised water after each acid treatment.

3.2.2 Nanofillers

Nanofillers are primary particle compounds used as fillers or reinforcers in polymers with very small particle size (in the nanometer range). There are different materials that are used as fillers. In this study we used carbon nanotubes, titanium dioxide nanotubes, and montmorillonite as fillers as mentioned below.

3.2.2.1 Carbon Nanotubes (CNTs)

CNTs are classified as advanced filler materials with interesting properties and capacity of improving thermo-mechanical properties of a polymer, as reported some years ago. [3–6] This is due to their high aspect ratio, extraordinary mechanical and thermal properties, exceptional strength and flexibility and excellent electrical conductivity. CNTs can be classified as single-walled (consisting of a single graphene sheet rolled up to form a tube) and multi-walled (multiple graphite sheets rolled up to form a tube). Multi-walled CNTs (MWCNTs) were used in this study because they are relatively cheaper and possess more mechanical stability than single-walled CNTs (SWCNTs). Their electrical conductivity is also lower compared to SWCNTs, and this was thought to be an advantage in avoiding short circuiting in PEMFC.

MWCNTs were purchased by Sigma Aldrich with average outer diameter of 10 nm and purity of +95%. The surface of MWCNTs was modified to improve its compatibility and dispersion

within polymer matrix. Modification of carbon nanotubes is based on the previously reported method. [7]

3.2.2.1.1 Surface Modification of CNTs

The as-received neat MWCNTs (pCNTs) were first refluxed in 5 M nitric acid for 1 h to introduce carboxylic acid groups on the surface of MWCNT (COOH–CNTs). Carboxylic acid groups are expected to improve dispersion of CNTs within a polymer matrix. The mixture was then filtered and washed with distilled water until no residual acid was present. The sample was then dried in a vacuum oven at 110°C over night. The as-synthesised COOH–CNTs were then refluxed with hexadecylamine (HAD) for 4 days to attach the amine functional group. Treatment with HDA leads to flexibility and solubility of tubes in organic solvents. The product was first washed with methanol and then extensively washed with deionised water to remove excess amine. Amine functionalized MWCNTs (fCNTs) were then dried in a vacuum oven at 110°C overnight. All pCNTs, COOH–CNTs and fCNTs were then used as fillers and their effect on Nafion properties were compared.

3.2.2.2 Layered Silicates

The most commonly used layered silicate to improve the Nafion membrane properties is montmorillonite (MMT). MMT has been used to improve the properties of Nafion membranes for direct methanol fuel cell applications. [8–15] Most promising layered silicate is a natural MMT modified with methyl tallow bis(2-hydroxylethyl) quaternary ammonium salt (commercially know as Cloisite® 30B, C30B) (**Figure 3.2**). This is an additive for plastics to improve various plastic physical properties, such as reinforcement and barrier. C30B has shown much improvement on methanol permeability compared to other types of multi-layered silicates. However this improvement was achieved at the expense of proton conductivity of Nafion membranes. In this study, a different method (melt-mixing) will be used to prepare nanocomposite membranes with C30B (purchased from Southern Clay Products, USA) as filler. This method is expected to improve dispersion of clay within polymer matrix. This might balance both methanol permeability and proton conductivity properties of Nafion.

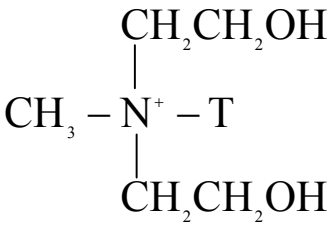

Figure 3.2 Chemical structure of **methyl tallow bis(2-hydroxylethyl) quaternary ammonium salt used to modify MMT**, where T is Tallow (~65% C18; ~30% C16; ~5% C14)

3.2.2.3 Titanium Dioxide Nanotubes (TNTs)

Beginning with the discovery of carbon nanotubes,[16–18] a series of approaches to produce nanotubular structures other than carbon, such as the well–known cases of alumina or Titania, have been explored. Among them special attention has been directed to TiO_2 due to its unique functional properties. Their photo-corrosion resistance, high photo-conversion efficiency, and the suitability as a material for purification of water and air have attracted more attention in many research fields. In this study, a new application for TiO_2 nanotubes is investigated. TiO_2 is used as filler in Nafion membranes and its photo-corrosion resistance property is expected to improve Nafion mechanical stability at high temperatures.

3.2.2.3.1 Synthesis of TNTs

TNTs were synthesised using steel reactors with conventional heating, reported previously.[19–20] TiO_2 was mixed with potassium hydroxide (KOH) and the mixture was synthesised in the Teflon underlined steel reactor at 150°C for 24 h. The reaction product was then washed with deionised water by means of centrifugation. Washing was repeated several times to remove excess waste. The sample was then dried in vacuum oven and calcined at 300°C for 4 h.

3.3 Preparation of Polymer Nanocomposites Membranes

A polymer nanocomposite can be defined as an interacting mixture of two or more phases, one of which, at least one dimension, is in the nanometer size range. The presence of the nanoscopic component is believed to give rise to unique properties and technological opportunities. Polymer nanocomposites were prepared using the melt-mixing method

3.3.1 Solvent Casting Method

In solvent casting, a polymer is dissolved in an organic solvent. Particles or fillers with specific dimensions are then added to the solution. The mixture is shaped into its final geometry. For example, it can be casted onto a glass plate to produce a membrane. When the solvent evaporates it creates a structure of composite material consisting of the particles together with the polymer. This method is used for the production of engineering plastics, optical films, medical films and sheet forming for electronic applications. The advantage of this technology includes uniform thickness distribution.

In this study, this method was employed using a mixture of Nafion in low aliphatic alcohol and water with required amounts of desired nanofillers. The solution was ultrasonicated before casting in a glass petri dish and evaporated at high temperatures (130°C). The casted Nafion nanocomposite was pulled off the petri dish by adding a small amount of deionised water. Before characterization, samples were pretreated with hydrogen peroxide aqueous solution and in sulphuric acid solution.

3.3.2 Melt–Blending Method

The melt-extrusion method is carried out using a melt-mixer when the base polymer is soft and flexible. This method is carried out at relatively low temperatures to keep the polymer viscosity high so as to increase the shear input. This method is commonly used in industries as it gives a good dispersion and repeatability output.[21] In this study, this method was used to disperse fillers such as CNTs, MMTs, and TNTs into the Nafion matrix. It is the preferred method over others due to low impurity content from solvents like solvent casting method.

Nafion nanocomposite membranes were prepared using both melt-blending and melt-extrusion methods. The most advanced Thermo Haake PolyLab Rheomix OS (HAAKE) from Thermo Scientific instruments was used for the melt-blending process. Prepared samples were then converted into sheets by compression molding using a Caver Laboratory Press. Polymer nanocomposites were prepared at different blending ratios of filler to polymer under the same processing conditions. Samples were then pretreated using a standard procedure reported elsewhere.[22] This was done by boiling samples in hydrogen peroxide solution to remove organic impurities, followed by washing in deionised water. Nanocomposite membranes were then boiled in sulphuric acid solution to remove inorganic impurities and also to complete protonation followed by washing in deionised water. Washing with water was repeated several times to remove any traces of acid as checked by pH paper. The membranes were kept in deionised water prior to measurements and characterizations.

3.4 Characterization Techniques

Characterization techniques produce quantitative information and comparisons in materials such as polymers, thin films, and powders. This section summarizes various techniques such as SEM, TEM, XRD, SAXS, BET, FT-IR, TGA, and DMA. These techniques were used to characterize detailed structure and properties of nanocomposites material. In situ electrical characterization techniques, such as cyclic voltammetry (CV) and electrochemical impedance spectroscopy (EIS), will also be discussed. These techniques provide a wealth of information about the actual behavior of the nanocomposite membranes in fuel cell operation

3.4.1 FT-IR Spectroscopy

In IR spectroscopy, IR radiation is passed through a sample. Some of the IR radiation is absorbed by the sample and some of it is transmitted or reflected. The resulting spectrum represents the molecular absorption and transmission, creating a molecular fingerprint of the sample. Like a fingerprint no two unique molecular structures produce the same IR spectrum. This makes IR spectroscopy useful for several types of analysis such as identifying unknown materials. It is used to determine the quality and composition of the sample.

FT-IR spectrometry was developed in order to overcome the limitations encountered with dispersive instruments. The main difficulty was the slow scanning process. A method for measuring all of the infrared frequencies simultaneously, rather than individually, was needed. A solution was developed that employed a very simple optical device called an interferometer. The interferometer produces a unique type of signal that has all of the IR frequencies "encoded" into it. FT-IR spectroscopy is a measurement technique for collecting IR spectra. Instead of recording the amount of energy absorbed when the frequency of the IR light is varied (monochromator), the IR light is guided through an interferometer. After passing through the sample, the measured signal is the interferogram. Performing a mathematical Fourier transform on this signal results in a spectrum identical to that of conventional (dispersive) IR spectroscopy.[23]

IR energy is emitted from a glowing black-body source. This beam passes through an aperture that controls the amount of energy presented to the sample (and, ultimately, to the detector). The beam enters the interferometer where the "spectral encoding" takes place. The resulting interferogram signal then exits the interferometer. The beam enters the sample compartment where it is transmitted through or reflected off of the surface of the sample, depending on the type of analysis being accomplished. This is where specific frequencies of energy, which are uniquely characteristic of the sample, are absorbed. The beam finally passes through to the detector for final measurement. The detectors used are specially designed to measure the special interferogram signal. The measured signal is digitized and sent to the computer where the Fourier transformation takes place. The final infrared spectrum is then presented to the user for interpretation and any further manipulation. In this study, FT-IR spectroscopy 800 from Perkin Elmer was used to investigate elementary composition of CNTs and nanocomposites membranes. This information is extremely important when developing new electrolyte materials.

3.4.2 Raman Spectroscopy

Raman spectroscopy is a very useful technique for material identification. It is a straightforward, non-destructive technique requiring no sample preparation. Raman spectroscopy involves illuminating a sample with monochromatic light and using a spectrometer to examine light

scattered by the sample. When a beam of light is incident on a molecule most of the light is elastically scattered in random directions. The elastic process is termed Rayleigh scattering and is illustrated in **Figure 3.3 a**, while the inelastic process is termed Raman scattering, as shown in **Figure 3.3 b** and **Figure 3.3 c**.

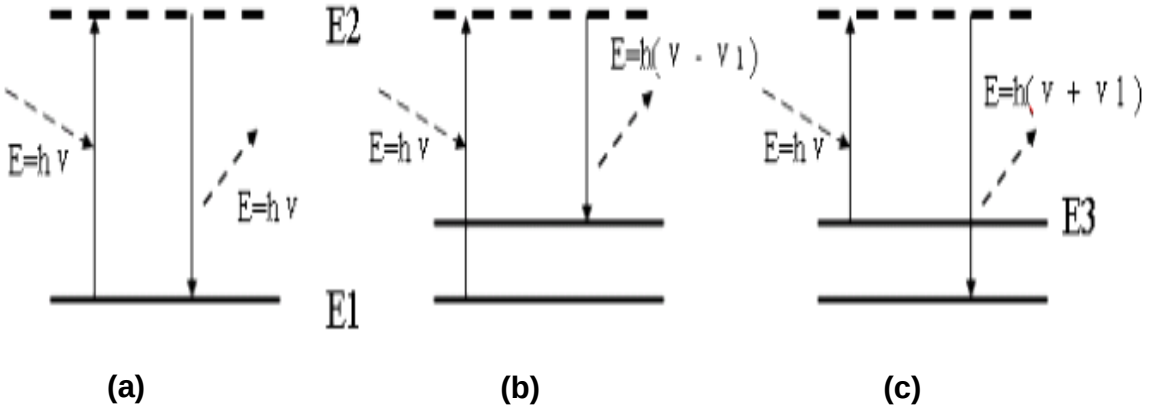

Figure 3.3 Three different possible scattering scenarios are shown here. E1 is the lowest vibrational energy level while E3 is an excited higher energy level. E2 is a metastable state. Reproduced from Ref [24] with permission from Wiley and Sons Ltd.

The electric field component of the scattering photon perturbs the electron cloud of the molecule and may be regarded as exciting the system to a 'virtual' state. Raman scattering occurs when the system exchanges energy with the photon and the system subsequently decays to vibrational energy levels above or below that of the initial state. The frequency shift corresponding to the energy difference between the incident and scattered photon is termed the Raman shift. Depending on whether the system has lost or gained vibrational energy, the Raman shift occurs either as an up- or down-shift of the scattered photon frequency relative to that of the incident photon. The down-shifted and up-shifted components are called the Stokes and anti-Stokes lines, respectively. The Raman spectrum is formed as a result of the energy difference between an incoming and outgoing photon.

3.4.2.1 Setup of Raman

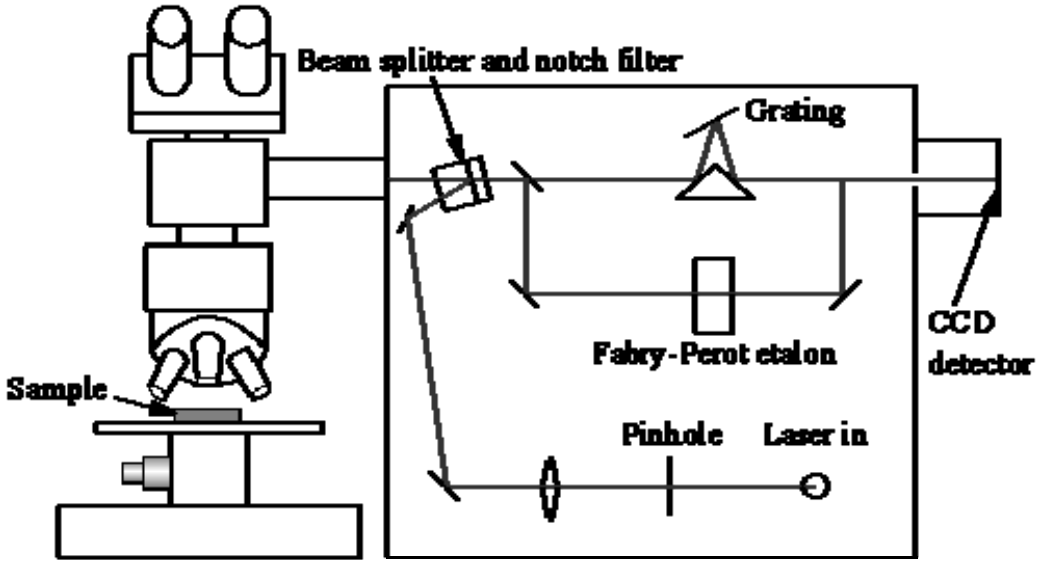

Figure 3.4 Schematic diagram of a Raman spectrometer.

Figure 3.4 is a schematic diagram of a typical Raman spectrometer. Lasers are used as a photon source due to their highly monochromatic nature and high beam fluxes. This is necessary as the Raman effect is weak, typically the Stokes lines are ~10^5 times weaker than the Rayleigh scattered component. In the system used in this study, a laser is passed into the spectrometer and directed into the microscope by a series of mirrors. The laser is then focused onto the surface of the sample. Light reflects off the sample. This Rayleigh radiation is filtered out at the holographic notch filter. The light is then passed through a lens and a slit to filter the light. The filtered light is passed through another lens, onto a mirror and then onto a grating. The resulting beam of light is then captured on a charge-coupled device (CCD) detector. A computer then interprets the CCD information and displays a spectrum.

The laser Raman spectrometer used in this study was a Dilor XY-multi-channel Raman spectrometer, with a 514.5 nm Argon ion excitation laser. In order to reduce heating effects and degradation of the samples, the laser power was set at 100 mW, thereby only probing at about 100 nm depth of the sample surface.

3.4.3 BET

BET surface area is an important property for many types of advanced materials such as nanomaterials, thin films, powder metallurgy materials, battery active materials, fibers, pigments, thermal spray powders, minerals, and additives. The BET surface area instrument is used to determine information such as gas uptake, micropore volume (t–plot method), and pore size distribution via adsorption and desorption isotherms. In a BET surface area analysis, a dry sample is evacuated of all gas and cooled to 77K, using liquid nitrogen. A layer of inert gas physically adheres to the sample surface, lowering pressure in the analysis chamber. Surface area is then calculated from the measured absorption isotherm of the experiment. The BET TriStar II model from Micromeritics was used in this study.

3.4.4 TGA

TGA is an analytical technique used to determine a material's thermal stability and its fraction of volatile components by monitoring the weight change that occurs as a specimen is heated. The measurement is normally carried out in air or in an inert atmosphere, such as Helium or Nitrogen, and the weight is recorded as a function of increasing temperature. Sometimes, the measurement is performed in a lean oxygen atmosphere (1 to 5 vol% O_2 balanced in N_2 or He) to slow down oxidation. In the particular case of CNTs, the weight change in an air atmosphere is typically a superposition of the weight loss due to the oxidation of carbon into gaseous carbon dioxide and the weight gain due to the oxidation of residual metal catalyst into solid oxides.

TGA measurements were carried out using a vertical balance instrument TA 2000 TGA, where a sample pan hangs from the balance. Prior to measurements aluminium pans were cleaned with acetone and thermally treated to remove excess impurities. About 5–10 mg of polymer film samples were then loaded into the pans. The results were analysed using TA Universal analysis software. The measurements were repeated several times to confirm reproducibility

3.4.5 DMA

DMA provides information about the mechanical properties of a material placed in a negligible, sinusoidal, oscillation as a function of time and temperature by subjecting it to a small, sinusoidal, oscillating force. The applied mechanical load, that is, stress, brings out a corresponding strain of deformation whose amplitude and phase shift can be determined. The mode of deformation is governed by the complex modulus. The complex modulus is composed of the storage modulus E' (real part) and the loss modulus E" (imaginary part). These are dynamic elastic characteristics and their magnitude depends critically on the frequency as well as the measuring conditions and nature of the samples. The real part of the modulus E' may be used for assessing the elastic properties and E" for the viscous properties. The phase angle (δ) is the phase difference between the dynamic stress and the dynamic strain in a viscoelastic material subjected to a sinusoidal oscillation and is expressed in radians. The loss factor is given by tan δ = E"/E'. It is a measure of energy loss, expressed in terms of the recoverable energy and represents internal friction in a viscoelastic system. A high tan δ value is indicative of a material that has high glass transition temperature and high mechanical properties. [25]

DMA 8000 from Perkin Elmer was used to conduct force-controlled tests by applying a sinusoidal stress and measure deformation. The dual cantilever mode was used to investigate the frequency dependence of T_g.

3.4.6 Electron Microscopy

When a high energy electron beam (e^- beam) interacts with a specimen, a variety of signals may be detected in an electron microscope (see **Fig. 3.5**).[26] In a scanning electron microscope (SEM) mainly the secondary electrons (SE), backscattered electrons and characteristic X-rays (EDX) are analyzed. The first two types of electrons provide visual information about the specimen. Information regarding specimen composition can be determined using EDX, Cathodoluminescence and Auger electron signals. Some of these signals are used in TEM.[26–27]

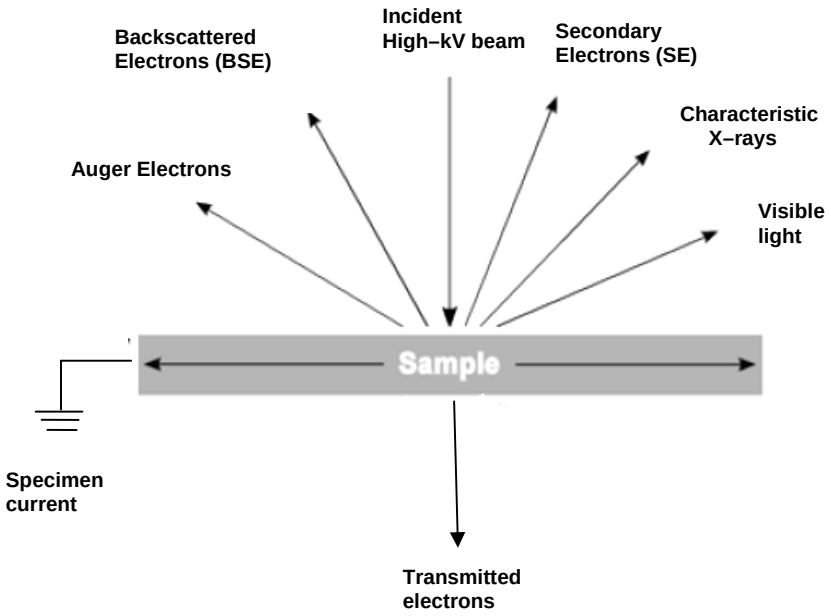

Figure 3.5 Illustration of possible signals generated when a high beam interacts with a thin specimen [27].

3.4.6.1 SEM

In SEM the e^-– beam is generated within an electron gun and accelerated by a high voltage. It is then transformed into a fine probe by electromagnetic lenses. The first lens that influences the electron beam is the condenser lens, which causes the e^-– beam to converge and pass through a focal point that is produced above a condenser aperture. Condenser lens with accelerating voltage is responsible for determining the intensity of e–beam when it scans at a given specimen. The final lens (objective lens) is used to bring the beam into focus at the specimen by demagnifying it into a focal point at the specimen surface. An image is formed from the interaction of the electrons scanning through the specimen.

All samples must be of an appropriate size to fit in the specimen chamber and are generally mounted rigidly on a specimen holder called a specimen stub. Several models of SEM can

examine any part of a 6-inch (15 cm) semiconductor wafer, and some can tilt an object of that size to 45 degrees. For conventional imaging in the SEM, specimens must be electrically conductive, at least at the surface, and electrically grounded to prevent the accumulation of electrostatic charge at the surface. Nonconductive specimens tend to charge when scanned by the electron beam, and especially in secondary electron imaging mode, which causes scanning faults and other image artifacts. The nonconducting materials are therefore usually coated with an ultrathin coating of electrically conducting material, such as gold, deposited on the sample either by low vacuum sputter coating or by high vacuum evaporation.[28]

The SEM, model LEO 1525 Field Emission, was used to generate data on the morphology of the samples. The polymer samples were placed in liquid nitrogen for 10 m, removed and quickly fractured to expose the cross-sectional surface area of the membranes. Polymer samples were non-conducting, therefore, they were coated with carbon (via electric arc deposition process) to prevent accumulation of electro-static charge. Denton desk sputtering system was used with 40 mA for 1 min. Samples were loaded into SEM and a vacuum was applied. Imaging commenced at 10 kV once 1.4×10^{-5} mm Hg pressure was attained in the SEM chamber.

3.4.6.2 TEM

TEM is a microscopy technique whereby a beam of electrons is transmitted through an ultra thin specimen, interacting with the specimen as it passes through. An image is formed from the interaction of the electrons transmitted through the specimen. The image is magnified and focused onto an imaging device, such as a fluorescent screen, on a layer of photographic film, or detected by a sensor such as a CCD camera. Conventional TEM uses only the transmitted beams or some of the forward scattered beams to create a diffraction contrast image. High resolution TEM uses the transmitted and the scattered beams to create an interference image. A TEM microscope must have a high performance (low spherical deviation and high stability of the high tension of the lens currents and of the energy of the electron beam).

TEM specimens are required to be at the most hundreds of nanometers thick, as unlike neutron or X-ray radiation the electron beam interacts readily with the sample an effect that increases

roughly with the square of the atomic number.[29] High quality samples will have a thickness that is comparable to the mean free path of the electrons that travel through the samples, which may be only a few tens of nanometers. Preparation of TEM specimens is specific to the material under analysis and the desired information to obtain from the specimen. As such, many generic techniques have been used for the preparation of the required thin sections. Powder samples are typically placed in copper (Cu) grids and polymers are cut using a microtome. [30–31] The high-resolution TEM from JEOL (JEM 2100 model) was used to investigate the morphology and dispersion of MWCNTs, TiO_2 nanotubes, and MMT into polymer matrix.

3.4.7 AFM

AFM is a powerful technique that allows imaging of almost any type of surface, including polymers, ceramics, composites, glass, and biological samples. It is used to measure and localize many different forces including adhesion strength, magnetic forces, and mechanical properties. AFM consists of a sharp tip of about 10–20 nm in diameter, which is attached to a cantilever (see **Fig. 3.6**). AFM tips and cantilevers are microfabricated from Si or Si_3N_4. The tip moves in response to tip-surface interactions, and this movement is measured by focusing a laser beam with a photodiode.

AFM is operated in two basic modes, i.e., contact and tapping modes. In contact mode the AFM tip is in contact with the surface continuously. Whereas in tapping mode the AFM cantilever is vibrated above the sample surface so that the tip is only in contact with the surface intermittently. This helps to reduce shear forces associated with the tip movement. AFM tapping mode is the recommended mode commonly used for imaging. Contact mode is only used for specific applications such as force curve measurements.[32] The AFM is used to image and manipulate atoms and structures on a variety of surfaces. The atom at the apex of the tip "senses" individual atoms on the underlying surface when it forms incipient chemical bonds with each atom. Because these chemical interactions delicately alter the tip's vibration frequency, they can be detected and mapped.

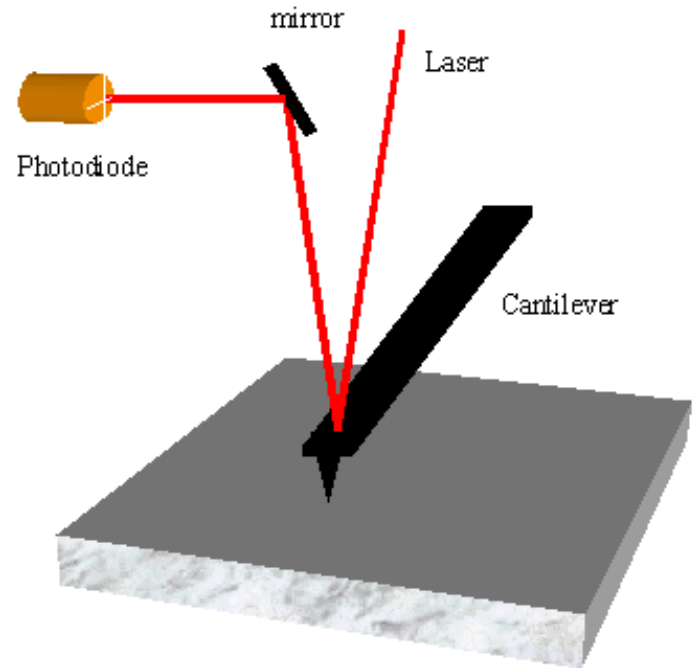

Figure 3.6 The vertical deflection of the cantilever is detected by reflecting a laser beam onto a two-segment photodiode.

Unlike the electron microscope, which provides a two-dimensional projection or a two-dimensional image of a sample, the AFM provides a true three-dimensional surface profile. Additionally, samples viewed by AFM do not require any special treatments (such as metal/carbon coatings) that would irreversibly change or damage the sample. While an electron microscope needs an expensive vacuum environment for proper operation, most AFM modes can work perfectly well in ambient air. In principle, AFM can provide higher resolution than SEM. It has been shown to give true atomic resolution in ultra-high vacuum (UHV) and, more recently, in liquid environments. High resolution AFM is comparable in resolution to scanning tunnelling microscopy and TEM. A disadvantage of AFM compared with the SEM is the image size. The SEM can image an area on the order of millimeters by millimeters with a depth of field on the order of millimeters. The AFM can only image a maximum height on the order of micrometers and a maximum scanning area of around 150 by 150 micrometers. That is the reason both AFM and SEM were used in this study. AFM Vicco model was used in a contact mode with a spring constant of 1N/m to investigate the topography of nanocomposites membranes.

3.4.8 XRD

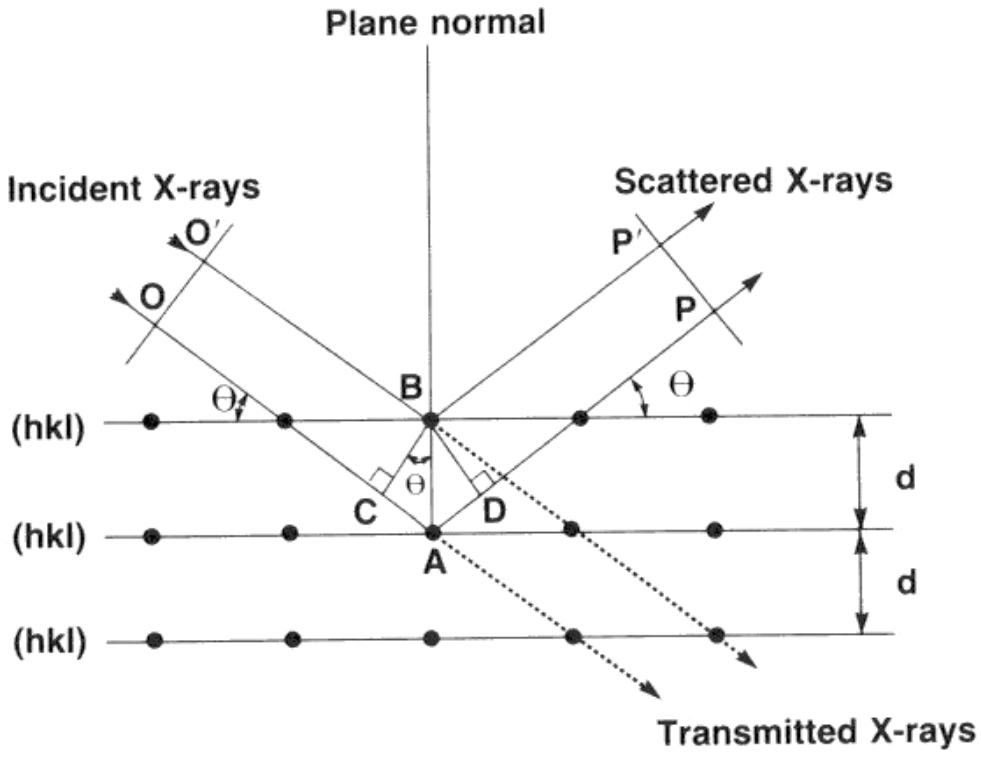

Figure 3.7 Interference of radiation between atomic planes in a crystal. Reproduced from Ref. [31] with permission from John Wiley & Sons.

All diffraction methods are based on the generation of X-rays in an X-ray tube. These X-rays are directed to the sample, and the diffracted rays are collected. A key component of all diffraction is the angle between the incident and diffracted rays (see **Fig. 3.7**). X-rays are generated in a cathode ray tube by heating a filament to produce electrons, accelerating the electrons toward a target by applying a voltage and bombarding the target material with electrons. [33] As shown in **Figure 3.7**, X-rays can either be scattered or transmitted through the plane of atoms (hkl). Parallel planes of atoms are separated by d-spacing. The X-ray beam makes the angle of incidence (θ) with the plane of atoms

The basis for X-ray diffraction is described by the Bragg's equation, which describes the condition of constructive interference of X-rays, scattered from atomic planes of a crystal by this equation:

$$n\lambda = 2d\sin\theta \qquad (3.1)$$

where n is an integer, λ is the wavelength of the radiation, d is the spacing between atomic planes and θ the angle between the radiation and the atomic planes, known as the Bragg angle. [34] This relation demonstrates that interference effects are observable only when radiation interacts with physical dimensions that are approximately the same size as the wavelength of the radiation.

3.4.8.1 Wide Angle XRD (WAXRD)

XRD is a rapid analytical technique primarily used for phase identification of a crystalline material and can provide information on unit cell dimensions. Usually samples are measured in reflection mode and one experiment is sufficient. The analyzed material is finely ground, homogenized, and average bulk composition is determined.

X-ray diffraction is based on constructive interference of monochromatic X-rays and a crystalline sample. These X-rays are generated by a cathode ray tube, filtered to produce monochromatic radiation, collimated to concentrate, and directed toward the sample. The interaction of the incident rays with the sample produces constructive interference (and a diffracted ray) when conditions satisfy Bragg's Law ($n\lambda=2d$ sin θ). This law relates the wavelength of electromagnetic radiation to the diffraction angle and the lattice spacing in a crystalline sample. These diffracted X-rays are then detected, processed, and counted. By scanning the sample through a range of 2θ angles, all possible diffraction directions of the lattice should be attained due to the random orientation of the powdered material. Conversion of the diffraction peaks to *d*-spacing allows identification of the mineral because each mineral has a set of unique *d*-spacing. Typically, this is achieved by comparison of *d*-spacing with standard reference patterns. The geometry of an X-ray diffractometer is such that the sample rotates in the path of the collimated X-ray beam at an angle θ while the X-ray detector is mounted on an arm to

collect the diffracted X-rays and rotates at an angle of 2θ. The instrument used to maintain the angle and rotate the sample is termed a goniometer. [35–36]

XRD experiments were carried out on a Phillips PW 1830 generator X-ray diffractometer with Cu (0.154 nm) irradiation at 45 kV and 40 mA using a Ni filter. Samples were placed into a sample holder, making sure that the upper surface is kept flat to achieve a random distribution of lattice orientations for typical powder patterns. Data was collected at 2θ from ~5° to 70°. X-ray scans were then analysed using X–Pert software.

3.4.8.2 SAXS

SAXS is an analytical method to determine the particle system in terms of its shape, size, and structure. The material can be solid or liquid and they can contain solid, liquid, or gaseous domains (so-called particles) of the same or another material in any combination.

X-rays are either scattered or absorbed and then scattered waves are processed into a picture by a lens. In SAXS, the scattered intensity is recorded by a detector and is processed mathematically, as a replacement for the action of a lens. With scattering techniques the whole illumination sample volume is investigated. As a consequence, average values of the structure parameters can be obtained with SAXS. The average is taken over all objects and all orientations of the objects. Therefore, structure details of the object will not become visible unless they are pronounced enough and representative for the whole sample.

In SAXS, X-rays produced by a source irradiate a sample. In most cases the source is an X-ray tube, but in some cases the source can also be a synchrotron, especially when high beam intensities or unusual wavelengths are required. The atoms inside the sample will scatter the incident radiation into all directions, which gives a background radiation that is almost constant at small angles. The particles (clusters of atoms) inside the sample will produce additional scattering that is characteristic to the average particle's structure. By measuring the angle-dependent distribution of the scattered radiation (intensity) it is possible to conclude about the average structure of the particles. Small Angle X-rays diffraction (SAXS) experiments were carried out using Anton Paar SAXSess with Nickel filter CuKα radiation (λ = 0.1542nm).

3.4.9 Electrochemical Characterization Techniques

These techniques use the electrochemical variables of voltage, current, and time to characterize the performance and ionic conductivity of the fuel cell membranes.

3.4.9.1 CV

This technique is typically used to characterize a material's activity in more details. In a CV measurement, the voltage sweep is applied to a system with time back and forth across a voltage window of interest. The resulting cyclic current response is measured as a function of the cyclic voltage sweep. The voltage sweep is generally linear with time and the plot of the resulting voltage is called a cyclic voltammogram. Cyclic voltammetry is generally used to study the electrochemical properties of a material in solution.[37–38] An autolab 4.90006 potentiostat GIS, connected to a homemade electrochemical cell, was used for CV measurements. GIS software was used to analyze cyclic voltammogram data.

3.4.9.2 EIS

In this technique, a sinusoidal perturbation (usually a voltage perturbation) is applied to a system and the amplitude and phase shift of the resulting current response are measured. Measurements can be conducted over a wide range of frequencies, resulting in the construction of an impedance spectrum. EIS is the most widely used technique for differentiating between major sources of losses in a fuel cell and is also used to measure the proton/ion conductivity of the electrolytes.

3.4.9.2.1 EIS Fundamentals

Like resistance, impedance is the ability of a circuit element to impede the flow of electrical current. Recall how resistance R is defined from Ohm's law **(Equation 3.2)** as the ratio between voltage (V) and current (I).

$$R = \frac{V}{I} \qquad (3.2)$$

Unlike resistance, impedance includes time and frequency dependence phenomena. In an analogous manner impedance (Z) is given by the ratio between a time-dependent voltage and a time-dependent current, see **Equation 3.3**:

$$Z = \frac{E(t)}{I(t)} \tag{3.3}$$

The real world contains circuit elements that exhibit much more complex behavior. These elements force us to abandon the simple concept of resistance. In its place we use impedance, which is a more general circuit parameter. Like resistance, impedance is a measure of the ability of a circuit to resist the flow of electrical current. However, impedance is not limited by the simplifying properties listed above.[39]

Electrochemical impedance measurements are usually carried out by applying an alternating current potential to an electrochemical cell and measuring the current through the cell. Suppose that we apply a sinusoidal potential excitation, the response to this potential is an AC current signal, containing the excitation frequency and its harmonics. This current signal can be analyzed as a sum of sinusoidal functions (a Fourier series). The excitation signal is expressed as a function of time and has the form:

$$E(t) = E_0 \cos(\omega t) \tag{3.4}$$

E(t) is the potential at time t_r, E_o is the amplitude of the signal, and ω is the radial frequency. The relationship between radial frequency ω (expressed in radians/second) and frequency, f (expressed in hertz) is:

$$\omega = 2\pi f \tag{3.5}$$

In a linear system, the response signal, I_t is shifted in phase angle and has a different amplitude, I_0:

$$I(t) = I_0 \cos(\omega t - \phi) \quad (3.6)$$

An expression analogous to Ohm's Law allows us to calculate the impedance of the system as:

$$Z = \frac{E(t)}{I(t)} = \frac{E_0 \cos(\omega t)}{I_0 \cos(\omega t - \phi)} = Z_0 \frac{\cos(\omega t)}{\cos(\omega t - \phi)} \quad (3.7)$$

The impedance is therefore expressed in terms of a magnitude, Z_0, and a phase shift, f.
Using Euler's relationship,

$$\exp(j\phi) = \cos\phi + j\sin\phi \quad (3.8)$$

it is possible to express the impedance as a complex function. The potential is described as,

$$E(t) = E_0 \exp(j\omega t) \quad (3.9)$$

and the current response as,

$$I(t) = I_0 \exp(j\omega t - j\phi) \quad (3.10)$$

The impedance is then represented as a complex number,

$$Z = \frac{E}{I} = Z_0 \exp(j\phi) = Z_0(\cos\phi + j\sin\phi) \quad (3.11)$$

3.4.9.2.2 Data Presentation

Look at **Equation 3.11** in the previous section. The expression for Z is composed of a real and an imaginary part. If the real part is plotted on the X axis and the imaginary part on the Y axis of a chart, we get a "Nyquist plot" (refer to **Figure 3.8**). Notice that in this plot the Y axis is negative and that each point on the Nyquist plot is the impedance at one frequency.

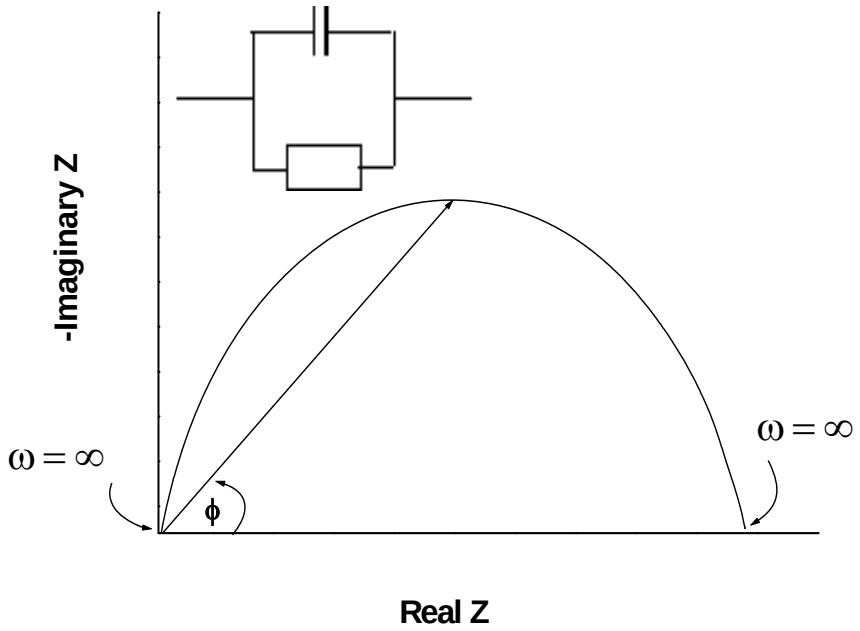

Figure 3.8 Nyquist plot with impedance vector and its equivalent circuit.

Figure 3.8 has been annotated to show that low frequency data are on the right side of the plot and higher frequencies are on the left. On the Nyquist plot, the impedance can be represented as a vector of length |Z|. The angle between this vector and the X axis is f. The semicircle is characteristic of a single "time constant". Electrochemical impedance plots often contain several time constants. Often only a portion of one or more of their semicircles is seen.[39]

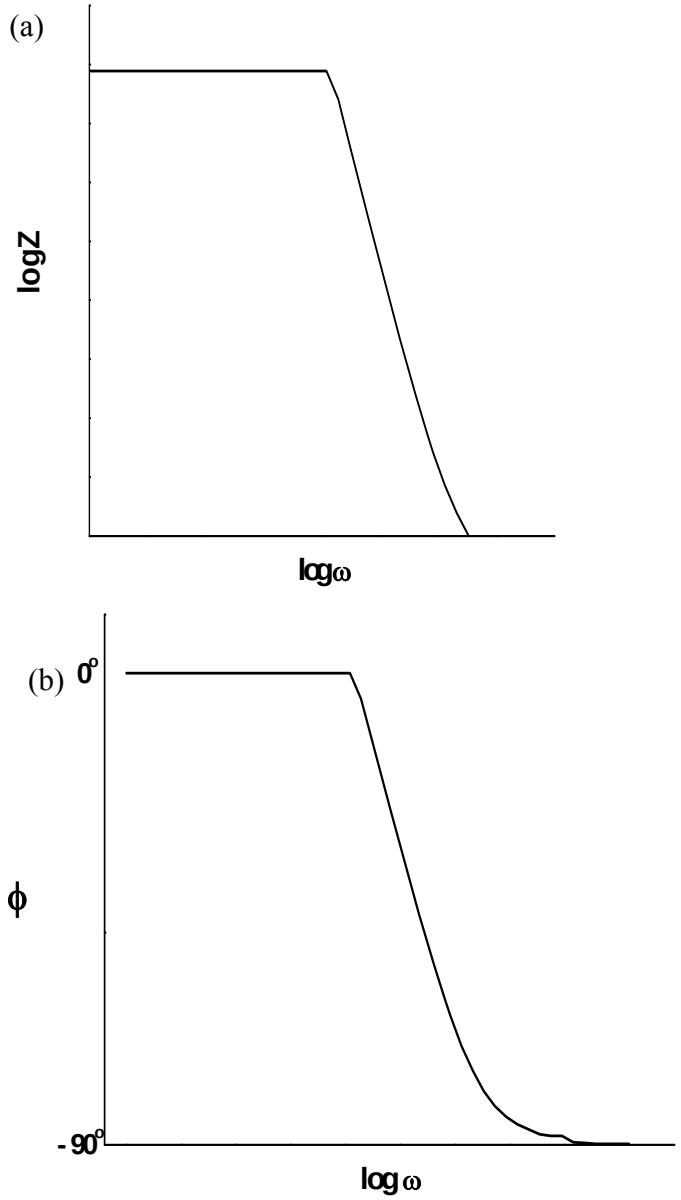

Figure 3.9 Bode Plots with one time constant: (a) frequency vs. Z and (b) frequency vs. phase angle.

Another popular presentation method is the "Bode plot". The impedance is plotted with log frequency on the X axis and both the absolute value of the impedance ($|Z| = Z_0$) and phase-shift on the Y axis. The Bode plot for the electric circuit of Figure 3.4 is shown in Figure 3.9. Unlike the Nyquist plot, the Bode plot explicitly shows frequency information.

3.4.9.2.3 EIS and Electrical circuit modelling

EIS data is commonly analyzed by fitting it to an equivalent electrical circuit model. Most of the circuit elements in the model are common electrical elements such as resistors, capacitors, and inductors. To be useful, the elements in the model should have a basis in the physical electrochemistry of the system. As an example, most models contain a resistor that models the cell's solution resistance. By using a good equivalent circuit model, it is then possible to extract information about reaction kinetics, mass transport and conduction processes of a fuel cell membrane. Knowledge of the impedance of the standard circuit components is therefore quite useful.[39] **Table 3.1** lists the common circuit elements, the equation for their current versus voltage relationship, and their impedance.

Table 3.1 Common electrical elements for electrochemical impedance measurements

Component	Current vs.Voltage	Impedance
resistor	E= IR	Z = R
inductor	E = L di/dt	Z = j**w**L
capacitor	I = C dE/dt	Z = 1/j**w**C

The impedance of a resistor is independent of frequency and has only a real component. Because there is no imaginary impedance, the current through a resistor is always in phase with the voltage. The impedance of an inductor increases as frequency increases. Inductors have only an imaginary impedance component. As a result, an inductor's current is phase-shifted 90 degrees with respect to the voltage. The impedance versus frequency behavior of a capacitor is opposite to that of an inductor. A capacitor's impedance decreases as the frequency is raised. Capacitors also have only an imaginary impedance component. The current through a capacitor is phase shifted –90 degrees with respect to the voltage.

3.4.9.2.4 EIS and Proton Conductivity

Proton conductivity of fuel cell membranes is generally measured using a galvanostatic four-point-probe AC EIS technique, which is relatively so insensitive to the contact impedance that it could be adequate to accurately test membranes with high conductivity.[40–41] A standard electrochemical conductivity cell is used. The proton conductivity (σ) is calculated by:[42]

$$\sigma = \frac{L}{RWd} \qquad (3.12)$$

where σ, L, and R denote the proton conductivity, the distance between the electrodes and the electrolyte resistance, respectively. W and d are the width and thickness of the membrane, respectively. The electrochemical cell was connected using a two-point probe technique to an Auto lab model 4.90006 potentiostat and frequency response analyser (FRA). The FRA electrochemical impedance software was used for the impedance measurements and analysis.

3.5 Water/Methanol Uptake

Nanocomposite films were completely dried under vacuum at 100°C for 24 h and weighed (W_{dry}) and then placed in water/methanol (50/50) by volume solution at 25°C for 24 h. The nanocomposite films were then wiped dry quickly with filter paper and weighed (W_{wet}). The water/methanol uptake was then calculated as:

$$\text{Water/methanol uptake (\%)} = \frac{W_{wet} - W_{dry}}{W_{dry}} * 100 \qquad (3.13)$$

3.6 Methanol Permeability Measurement

A methanol diffusion homemade cell was used based on previous reports. [43] Compartment A was filled with methanol solution and compartment B was filled with the same volume of deionised water. The membrane was clamped between the two compartments and these were stirred continually during the experiment to avoid any concentration build-up in the two compartments. Methanol concentration profiles were determined over a period of time at different operating temperatures. Samples were kept for about 30 m between compartments. The concentration of methanol was determined by gas chromatography (GC). Methanol permeability was modelled on the basis of Fick's law expression for diaphragm-cell diffusion. In order for this model to hold, certain assumptions are made.[44]

3.7 Electrical Conductivity Measurements

The electrical resistivity was measured at room temperature using the four-point collinear probe method. [45] The equidistant tungsten carbide probes have a separation distance (s) and probe radius of 0.127 cm and 0.005 cm, respectively. The 1 x 1 cm^2 samples were prepared with a thickness of about 0.2 cm. The Keithley 4200-SCS Semiconductor Characterization System, equipped with four supply-and-measure units (SMUs) and a pre-amplifier, was used to perform high precision direct-current characterization by supplying currents ranging from 1 fA – 1 mA. The resistivity changes as a function of probe spacing (0.127 cm) and is given by:

$$\rho = 2\Pi s \left(\frac{V}{I}\right) \qquad \text{for } t>>s \qquad (3.14)$$

where t is the thickness of the films [19]. The electrical conductivity is then given by:

$$\sigma = 1/\rho \qquad (3.15)$$

3.8 References

[1] F. Kreith, *J. Energy Resour. Technol.* **2004**, *126*, 249–257.

[2] S. Sinha Ray, M. Okamoto, *Prog. Polym. Sci.* **2003**, *28*, 1539–1641.

[3] P.M. Ajayan, O. Stephan, C. Colliex, and D. Trauth, *Science* 1994, *265*, 1212–1224.

[4] H.D. Wagner, O. Lourie, Y. Feldman, and R. Tenne. *Appl. Phys. Lett.* **1998**, *72*, 188–91.

[5] S.A. Curran, P.M. Ajayan, W.J. Blau, D.L. Carroll, J.N. Coleman, and A.B. Dalton, *Adv. Mater.* **1998**, *10*, 1091–1098.

[6] L.S. Schadler, S.C. Giannaris, and P.M. Ajayan, *Appl. Phys. Lett.* 73 (1998) 3842–5

[7] J. Chen, *J. Phys. Chem.* **2001**, *B 105*, 2525–2532.

[8] C.H. Rhee, H.K. Kim, H. Chang, and J.S. Lee, *Chem. Mater.* **2005**, *17*, 1691–1697.

[9] D.H. Jung, S.Y. Cho, D.H. Peck, D.R. Shin, and J.S. Kim, *J. Power Sources* **2003**, *118*, 205–211.

[10] R.F. Silva, M. De Francesco, and A. Pozio, *Electrochim. Acta* **2004**, *49*, 3211–3219.

[11] C.R. Martin, T.A. Rhoades, and J.A. Ferguson, *Anal. Chem.* **1982**, *54*, 1639–1645.

[12] R.F. Silva, S. Passerini, and A. Pozio, *Electrochimica Acta* **2005**, *50,* 2639–2645.

[13] Y. Kim, J.S. Lee, C.H. Rhee, Hae Kyung Kimd, Hyuk Chang. *J. Power Sources* **2006**, *162*, 180–185.

[14] C. Li, G. Sun, S. Ren, J. Liu, Q. Wang, Z. Wu, H. Sun, W. Jin, *J. Membr. Sci.* **2006**, *272*, 50–57.

[15] V.K. Nguyena, Y. Yoo, *Sensors and Actuators* **2007**, *B 123*, 183–190.

[16] A. Oberlin, M. Endo, and T. Koyama, *J. Cryst. Growth.* **1976**, *32*, 335–349.

[17] R. Bacon and J.C. Bowman, *Amer. Phys. Soc.* **1957**, *2,* 131–338.

[18] S. Iijima, *Nature* **1991**, *354*, 56–58.

[19] L.M. Sikhwivhilu, N. Coville, and S. Sinha Ray, *Appl. Phys.* **2009**, *A 94,* 963–973.

[20] Q. Chen, W.Z. Zhou, G.H. Du, and L.M. Peng, *Adv. Mater*. **2002**, *14*, 1208–1216.

[21] T. Gcwabaza, S. Sinha Ray, W.W. Focke, and A. Maity, *Euro. Polym. J.* **2009**, *45*, 353–367.

[22] R.F. Silva, S. Passerini, and A. Pozio, *Electrochim. Acta* **2005**, *50*, 2639–2645.

[23] N. Demirdöven, C.M. Cheatum, H.S. Chung, M. Khalil, J. Knoester, and A. Tokmakoff, *J. Am.Chem.Soc.* **2004**, *126*, 7981–7989.

[24] E. Smith and G. Dent, *Modern Raman Spectroscopy: A Practical Approach*, Wiley and Sons Ltd., Great Britain **2005**

[25] H.A. Sharifah, P.A. Martin, J.C. Simon, and R.P. Simon*, Comp. Sci. Technol.* **2005**, *65*, 525–535.

[26] M.T. Postek, Jr. & Ladd Research Industries, Inc., *Scanning Electron Microscopy – A Students Handbook* **1980**.

[27] P.J. Goodhew and F.J. Humphreys, *Electron Microscopy and Analysis*, 2nd Edition, Taylor & Francis, London **1988**.

[28] E. Suzuki, "High–resolution scanning electron microscopy of immunogold–labelled cells by the use of thin plasma coating of osmium". *J. Micros.* **2002**, *208*, 153–157.

[29] B. Fultz, J. Howe, *Transmission Electron Microscopy and Diffractometry of Materials*. Springer. **2007**. ISBN 3540738851

[30] K. Porter and J. Blum, *The anatomical record* **1953**, *117*, 685–693.

[31] Phillips, *B. J. Appl. Phys.* **1961**, 12, 554–561.

[32] A.D.L. Humphris, M.J. Miles, and J.K. Hobbs, *Appl. Phys. Lett.* **2005**, *86*, 034106–034112.

[33] D.L. Bish, J.E. Post, and B.D. Cullity, 2nd ed. Addison-Wesley, *Mineralogical Society of America*, **1978**, *20*.

[34] M.S. Gordon, D.R. Gano, J. Stephen Binkley, and M.J. Frisch, *J. Am. Chem. Soc.* **1986**, *108*, 2191–2197.

[35] H.P. Klug and L.E. Alexander, 2nd ed. Wiley, New York, **1974**.

[36] R.C. Reynolds, 2nd Ed. Oxford University Press, New York **1997**.

[37] Bard, Allen J.; Larry R. Faulkner, 2nd ed. Wiley. ISBN 0471043729, **2000**, 12–18.

[38] Fuel Cells Fundamentals 2nd Ed. **2008**

[39] F. Mansfeld, *Electrochimica Acta*, **1990**, 135, 1533–1542.

[40] D.H. Jung, S.Y. Cho, D.H. Peck, D.R. Shin, and J.S. Kim, *J. Power Sources* **2003**, 118, 205–213.

[41] P. Agarwal, M.E. Orazem, and L.H. Garcia–Rubio, *J. Electrochem. Soc*, **1992**, *139*, 1917–1922.

[42] M. Doyle and G. Rajendran, Handbook of Fuel Cells—Fundamentals,Technology and Applications, Part 3, vol. **3**, Wiley **2005**.

[43] P. Mukoma, *J. Membr. Sci.* **2004**, *243*, 293–299.

[44] E.L. Cussler, Diffusion: Mass transfer in fluid systems, Cambridge University Press, Cambridge, USA, **1997**.

[45] P. Jannasch, *Curr Opin Colloid Interface Sci.* **2003**, *8*, 96–102.

4

Modification of Multi-Walled Carbon Nanotube Surface for Binding with Nafion Matrix

Abstract

Multi–walled Carbon nanotubes seem to be a solution to many challenges associated with drug delivery systems, sensors, imaging, and hydrogen fuel cell development. The main challenge is the poor dispersion and compatibility, solubility of carbon nanotubes within polymer matrix. Carbon nanotubeswere rendered soluble in common solvents, such as dimethyl sulfoxide by chemical functionalization of carboxylic acid groups attached on carbon nanotubes (by refluxing in nitric acid for 1 h). Fourier transform Infrared spectroscopy and X-ray diffraction confirm that amine groups are attached to the sidewalls of tubes and the alignment of the tubes, respectively.

4.1. Introduction

CNTshave attracted much attention since their discovery because they exhibit exceptional electrical, thermal, and mechanical properties.[1] Due to their high aspect ratio, small diameter, light weight, and high strength, CNTs are recognized as the ultimate carbon fibers for nanostructured materials.[1–5] They have various potential applications such as electronics, sensing, gas storage, catalyst support; probes for scanning probe microscopy and components in high performance composites.[6–8] The effective utilization of CNTs depends strongly on the ability to homogenously disperse them through the matrix without destroying or affecting their excellent properties. CNT surface modification has shown promise to overcome this challenge especially for the preparation of CNT-polymer composites materials. CNT-polymer composites materials have many potential applications,[9–12] due to the fact that individual properties of the two materials combine to give good mechanical strength, high thermal properties, and excellent conductivity. The CNTs can act as nanofillers to improve properties of a polymer. Hence, significant effort has been made in the fabrication of polymer nanocomposites material. However, different applications of CNTs require various modifications to improve nanotubes processability, accessibility, and performance.

A common technique to incorporate CNTs into polymers is through chemical functionalization of the SWCNTs, which enables chemical covalent bonding between the CNTs and the polymer material of interest.[13–17] Examples of such covalent linkages achieved through chemical functionalization have been utilized in CNT reinforced polymer composites.[18–20] In CNT-polymer composites, the chemical functionalization is used to enhance the nanotubes-polymer interfacial interaction. Increasing the interfacial binding between CNTs and the polymer will improve the interfacial strength and thus load transfer from CNTs to polymer and polymer to CNTs, with the aim of improving the mechanical properties of the composite. Functionalized nanotubes are also typically easier to disperse in organic solvents that can improve the dispersion and homogeneity of the CNTs within the polymer.[16–21] While property improvements based on carboxylated functionalized MWCNTs in a polymer has been obtained. [21–22]

The preparation of amino-functionalized CNTs is described based on previously reported methods.[10–23] This approach involves a direct coupling of carboxylic groups in CNTs to

introduce amino groups via amide formation. The effect of surface modification on CNTs' properties was studied.

4.2. Experimental Procedure

4.2.1 Materials

Pure MWCNTs (from now abbreviated as pCNTs) with the outside diameter of 40–60 nm, inside diameter of about 5–10 nm and a length of about 0.5–500 μm were purchased from Sigma Aldrich. Other chemicals were also purchased from Sigma Aldrich and used as received.

4.2.2.1 Oxidation of CNTs

Following a reported procedure, the as-received CNTs were first treated with 5 M nitric acid by refluxing mixture for 1 h at 40°C to introduce carboxylic acid groups on the CNT surface. Upon completion, the mixture was then filtered through a 0.45 μm pore size nylon filters. The filtrate was then washed with distilled water until no residual acid was present. The sample was then dried in a vacuum oven at 110°C over night.

4.2.2.2 Fictionalization of CNTs with Hexadecylamine

Two hundred milligrams of the oxidized nanotubes (oCNTs) was refluxed in 2 g of hexadecylamine (HAD) for 4 days at 120°C as shown in **Scheme 4.1**. The product was then diluted with 200 ml of methanol and filtered using 0.45 μm pore size nylon filter paper, after which the filtrant was washed extensively with deionised water. The functionalized MWCNTs were then dried in a vacuum oven at 110°C overnight.

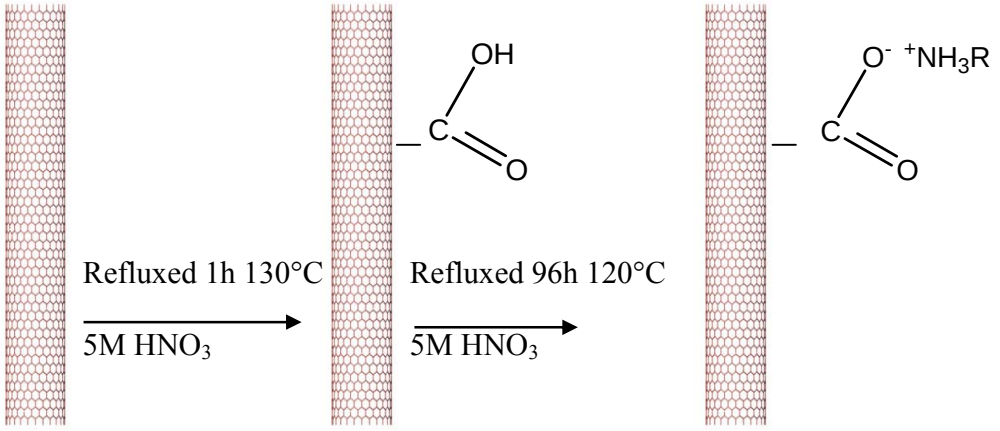

Scheme 4.1 Schematic representation of grafting of MWCNTs surfaces by carboxylic acid, and then functionalization by hexadecylamine group.

4.2.2 Characterization Techniques

The FT-IR measurements were conducted on a Perkin-Elmer Paragon 1000 Fourier transform infrared spectrometer at room temperature (25°C). The specimens were sufficiently thin to be within a range where the Beer-Lambert law is obeyed. A spectrum collected as the average of 64 scans with a resolution of 4 cm^{-1}, was recorded from 4000 to 550 cm^{-1} for the transmission mode. The pressure was equal in all measurements to avoid differences brought by the pressure and penetrating depth.

Dry membranes were manually fractured after cooling in liquid nitrogen (77K) to expose their cross section. The morphology of the samples was analyzed using SEM LEO 1525 Field Emission model.

TGA were conducted on a TGA Q500 (TA Instruments) at a heating rate of 10°C/min under oxygen from room temperature to 800°C. XRD experiments were carried out on a Phillips PW 1830 generator X-ray diffractometer with Cu (0.154 nm) irradiation at 45 kV and 40 mA using a Ni filter. Data were recorded at the scanning rate and step size of 1.0 (degree)/min and 0.02°, respectively. A Perkin Elmer DMA 8000 in the dual cantilever bending geometry measured

mechanical properties of Nafion and its CNTs-containing composites. The temperature dependence of storage modulus (G') and tan delta of Nafion and nanocomposites were measured at a constant frequency of 1 Hz with the strain amplitude of 0.02% from room temperature to 180°C with a heating rate of 5°C/min.

The conductivity of the films was measured at room temperature by pressing the probe on the surface of CNTs. The Keithley 4200-SCS Semiconductor Characterisation System, equipped with four supply-and-measure units (SMUs) and a pre-amplifier, was used to perform high precision direct-current characterization by supplying currents ranging from 1 fA – 1 mA with a resolution of 0.1 fA.

4.3 Results and Discussions

4.3.1 FT-IR Spectroscopy

The resultant oCNTs and fCNTs were characterized with FT-IR, which is an effective technique for the investigation of CNTs surface modification. The FT-IR spectra are shown in **Figure 4.1**, pCNTs and oCNTs show similar peaks. However, for oCNTs the peak at about 2300 cm^{-1} is broader confirming the presence of O-H vibrations. The FT-IR spectra of fCNTs indicate the appearance of some new peaks and these are due to the grafting of amine groups on CNTs outré surfaces. The peaks centering around 2900–2600 cm^{-1} are contributed by the N-H stretching vibrations.[23] The broad peaks at around 1650–1590 cm^{-1} are assigned to the N-H deformation of the amine group.[24] This confirms that the amino groups have been grafted into CNTs.

4.3.2 Raman

Figure 4.2 presents Raman spectra of pCNTs, oCNTs, and fCNTs. Three Raman bands of CNTs are strongly resonance enhanced. *D*, *G,* and *G*" bands at about 1350, 1580 and 2700 cm^{-1}, respectively. *D*-bands in the spectra are assigned to A_{1g} modes or intermediate modes, which is attributed to disorder forms of carbon. Peaks appearing around 1580–2800 cm^{-1}, correspond to the characteristic, E_{1g}, and E_{2g} modes or tangential modes of the graphite sheet.[25] The ratio of

the intensities of the *G*- and *D*- bands (I_G/I_D) gives a better understanding of the quality or purity of the tubes. The intensity ratio I_G/I_D of oCNTs decreased, this is attributable to the extent of the destruction of CNTs by strong oxidation. The C=C bond may be broken to yield a C-C bond, generating defects in the CNTs. For fCNTs the I_G/I_D ratio increased (this has never been seen before), as we expected the existence of grafted amine chemical groups in the tubes. However it can be due to the amine covering all the CNTs impurities. There is no observable frequency shift in the *G* and *D* bands. This suggests that amine participated in the fictionalization otherwise; the intertube connection would show a frequency shift on the G band.[26]

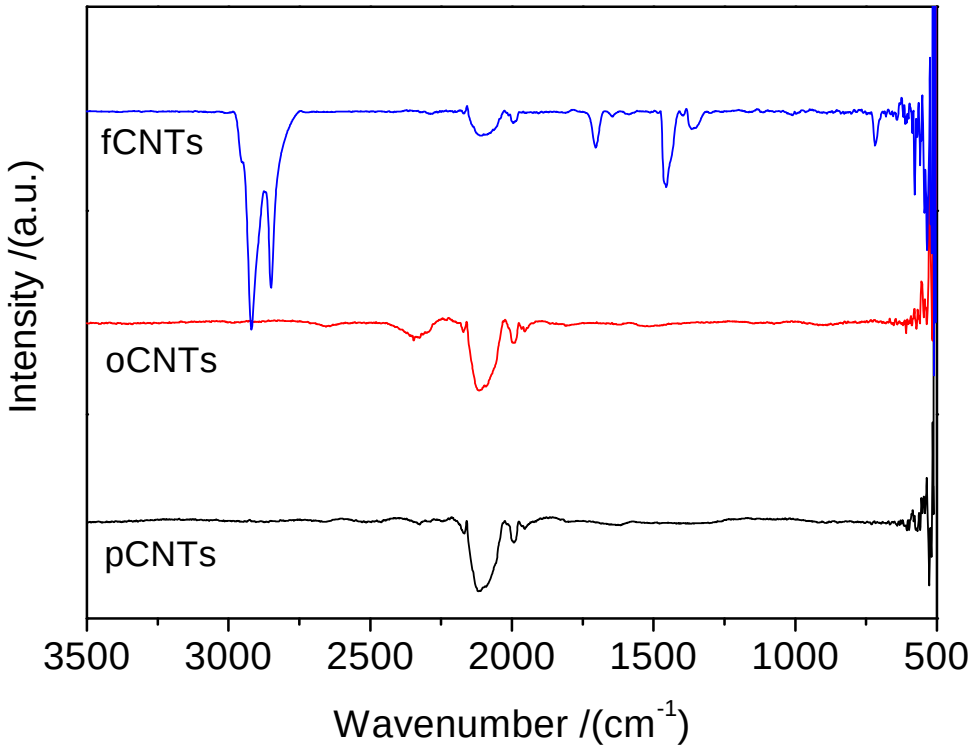

Figure 4.1 FT-IR spectra of neat-MWCNTs (pCNTs), oxidized MWCNTs (oCNTs), and amine functionalized MWCNTs (fCNTs).

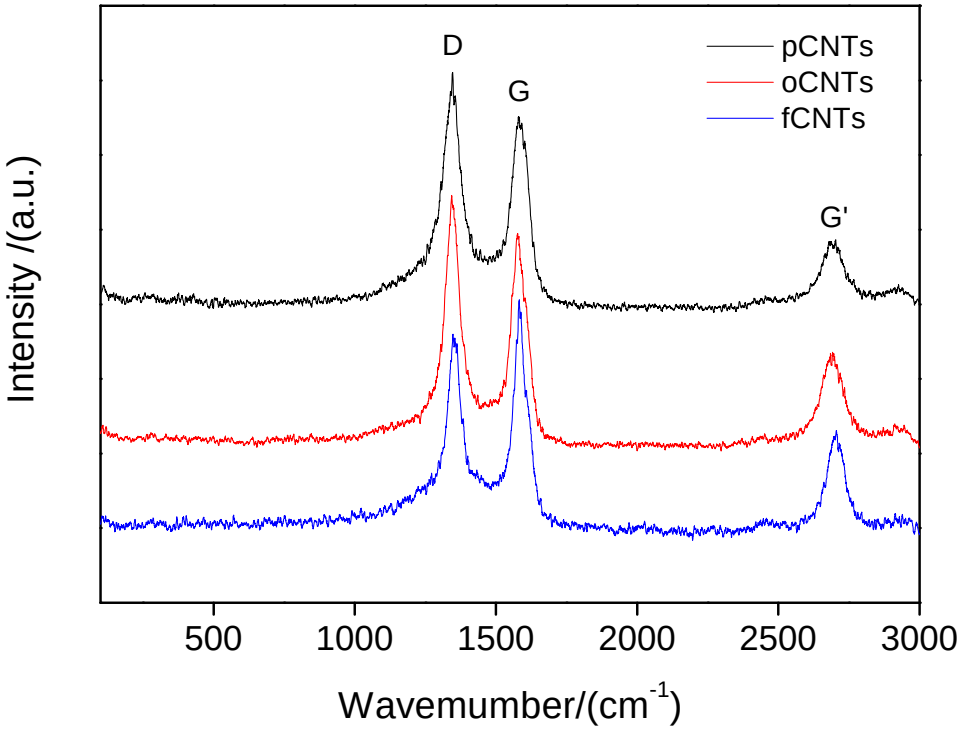

Figure 4.2 Raman spectra of pure-CNTs (pCNTs), oxidized CNTs (oCNTs), and amine functionalized CNTs (fCNTs).

4.3.3 Morphology

Figure 4.3 shows SEM images of (a) pCNTs, (b) oCNTs, and (c) fCNTs. All micrographs show bundles of CNTs with different morphologies. pCNTs are loosely bound to one another and aligned in one direction and oCNTs are loosely bound and randomly distributed. This suggests that carboxylic acid groups promote electrostatic repulsion. Whereas, fCNTs are densely packed forming aligned bundles, which are covered by the amine. This can be attributed to the electrostatic attraction between the tubes in the presence of amine groups. The effect of oxidation and fictionalization was also studied by TEM [see **Figure 4.3** (d-e)]. TEM imaging of the sample (see **Figure 4.3**) reveals the presence of hollow CNTs with catalyst (iron) on the tips of the tubes. This was verified by EDX analysis (see insertion). TEM results suggest that the structure of multi-walled carbon nanotubes remain intact after oxidation and functionalization.

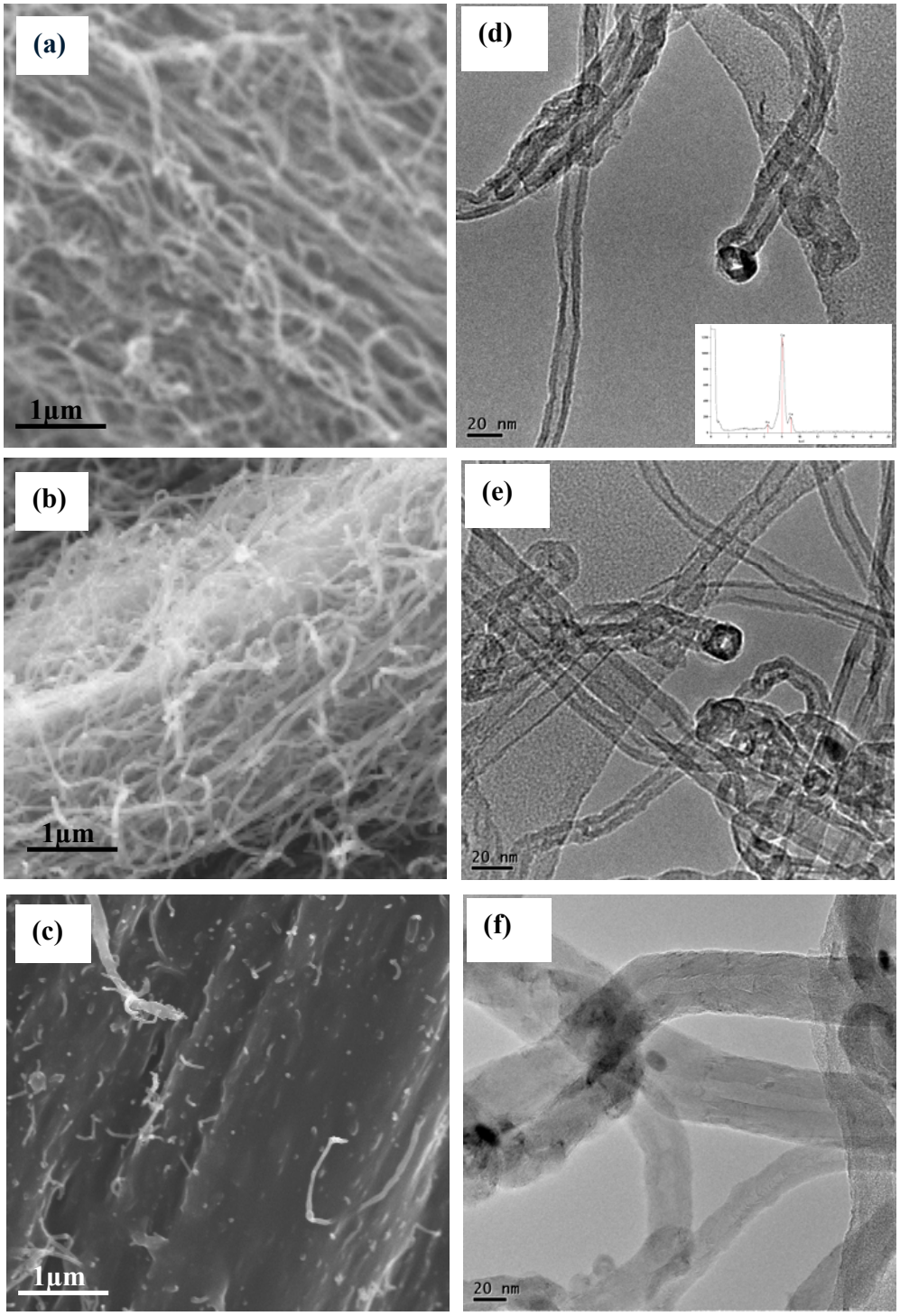

Figure 4.3 The scanning electron microscopy images: (a) pCNTs, (b) oCNTs, (c) fCNTs; and transmission electron microscopy images: (d) pCNTs, (e) oCNTs, (f) fCNTs.

4.3.4 XRD

XRD measurements were carried out using Cu Kα, λ = 0.154nm radiation. XRD peak patterns of pCNTs, oCNTs, fCNTs are shown in Figure 4.4. XRD pattern shows typical (002) peak at 26˚ and (100) peak at 42.5°, corresponding to the inter-plannar spacing of 0.34 and 0.22 nm, respectively. For fCNT sample, the (002) peak is relatively strong, indicating an increase in crystallinity when amine functional groups were attached on CNTs. Furthermore, other peaks (23˚ and 54˚) emerge corresponding to the crystalline nature of amine. Consequently, (002) peaks intensity sharply decreases with COOH grafted CNTs.

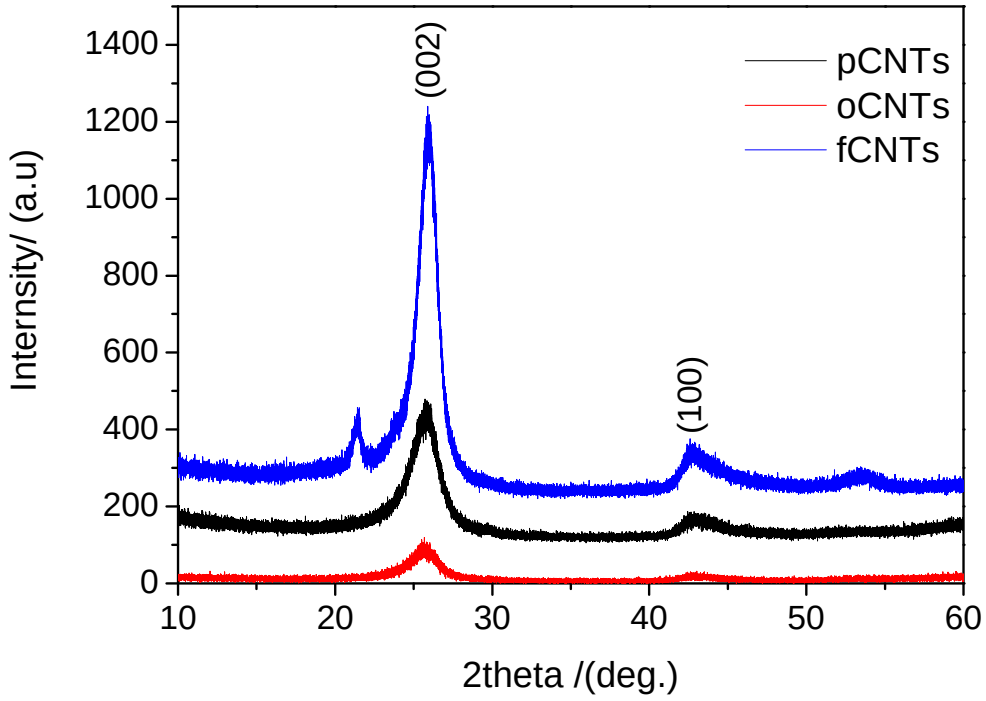

Figure 4.4 X-ray diffraction patterns of pCNTs, oCNTs, and fCNTs samples.

This difference in the intensity of the (002) peak can be explained by the alignment or orientation of the tubes with respect to the incident and scattered beams, incident beam, and the symmetry axis between them. [27] Only the Bragg diffraction from those crystalline faces parallel to the sample surface that is normal to the symmetric axis can be detected by the collector. This

suggests that oCNTs are vertically aligned but also a little curled (as observed in SEM image **Figure 4.3**), changing the direction of (002) fringes and weak (002) peak is observed. For pCNTs sample, tubes are more disordered (see **Fig. 4.2 a**) than oCNTs and the intensity increases accordingly. However, for fCNT sample, there is a considerable amount of nanotubes whose axis is perpendicular to the symmetric axis. This is in agreement with SEM results.

4.3.5 Thermal Stability

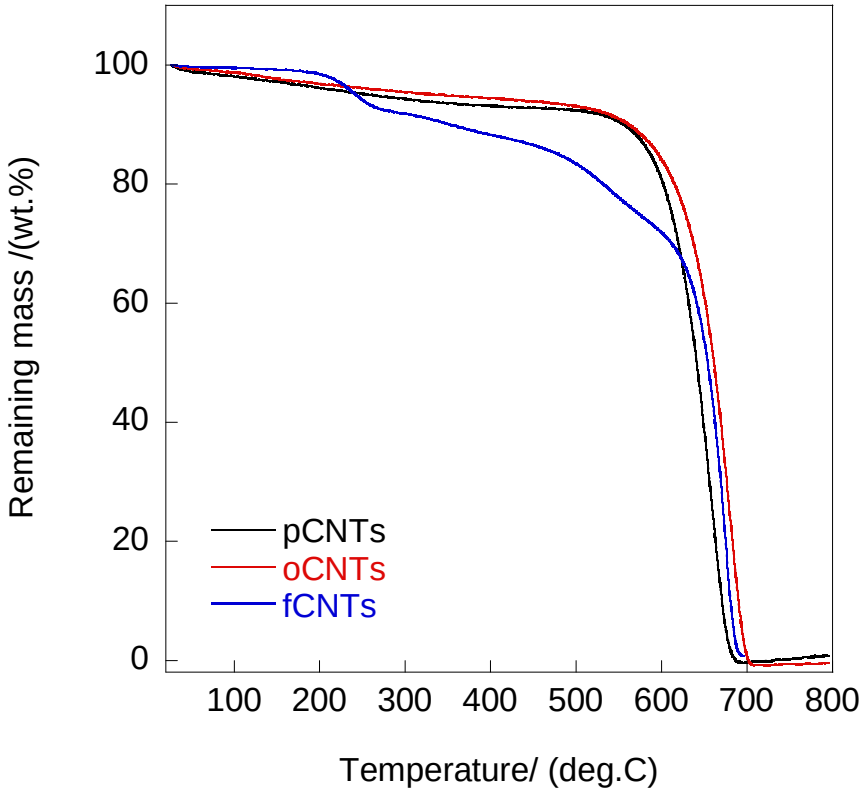

Figure 4.5 Thermogravimetric analysis of pCNTs, oCNTs, and fCNTs samples.

Figure 4.5 illustrates TGA curves of pCNTs, oCNTs, and fCNTs. Two thermal degradation stages are observed with fCNTs. The first thermal decomposition at about 300°C is due to decomposition of amine functional groups and the second one at 550°C is due to CNT combustion. pCNTs and oCNTs decomposed linearly with an increase in temperature. The

oCNTs maintained a weight loss of about 5% up to 650°C, which indicate more thermal stability when carboxylic acid groups are attached to the tubes.

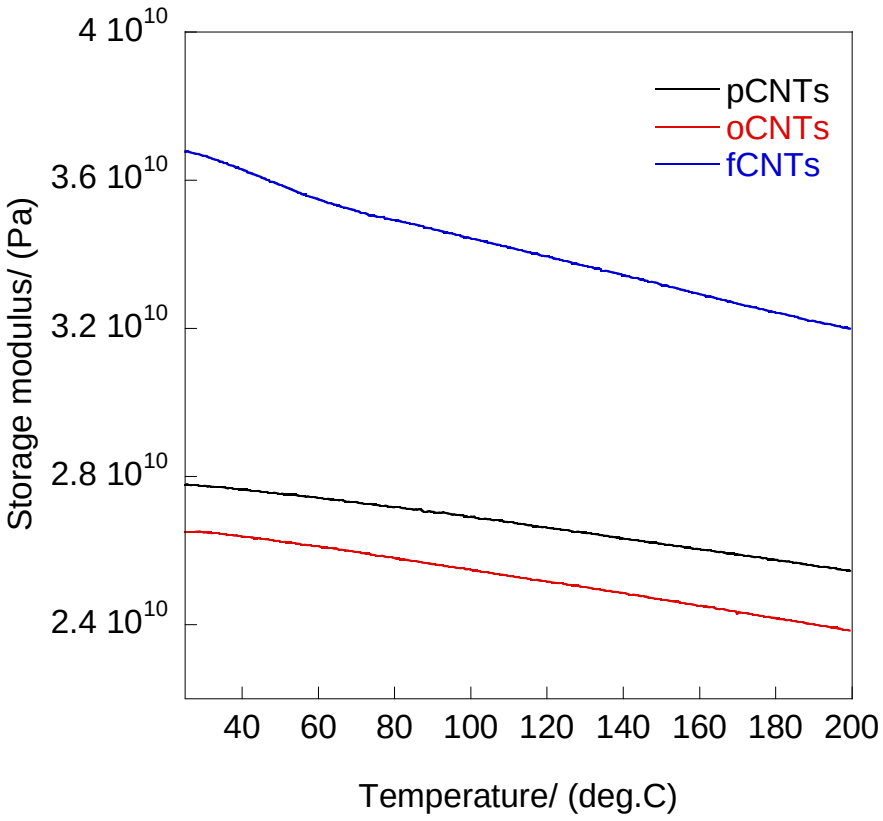

Figure 4.6 Dynamic mechanical analysis of pCNTs, oCNTs and fCNTs samples.

Since mechanical properties depend on the compatibility between polymer and filler, fCNTs are expected to have higher mechanical properties compared to pCNTs due to their ability to dissolve in some solvents. Typical DMA curves are shown in **Figure 4.6**. The storage modulus indicates the amount of energy stored in CNTs as elastic energy, which is highly affected by geometric characteristics and the interfacial bonding strength between the tubes. At room temperature, fCNTs demonstrate a significant higher storage modulus (36 GPa) compared to pCNTs (28 GPa) and oCNTs (26 GPa). This improvement might be attributed to the higher crystallinity observed with XRD and is in agreement with Raman results.

4.4. Conclusion

Modification of multi-walled carbon nanotubes outer surfaces was obtained in a two-step process comprising oxidation of tubes with nitric acid followed by a surface grafting with a hexadecylamine. Acid and amine modification of these unique structures provides the potential to manipulate its properties. Functionalized tubes were highly dispersible and soluble in organic solvent. The surface modification of carbon nanotubes can lead to important platforms and potential applications such as drug delivery systems, vaccines, bio-sensors, polymer nanocomposites, photo catalysis, and energy storage.

4.5 References

[1] M.S. Dresselhaus, G. Dresselhaus, and P. Eklund, Science of fullerence and carbon nanotubes, Academic *Press:* New York, **1996**, 123-500.

[2] P. Calvert, *Nature* **1992,** *357*, 365-372.

[3] P. Calvert, *Nature* **1999,** *399*, 210-218.

[4] R. Dagani, *Chem. Eng. News* **1999,** *77*, 25-32.

[5] P.M. Ajayan, L.S. Schandler, C. Giannaris, and A. Rubio, *Adv.Mater.* **2000,** *12*, 50-62.

[6] M.S. Dressehaus, G. Dresselhaus, and P Avouris, Carbon nanotubes: Synthesis, Structure, Properties and Applications, *Springer Berlin*, Germany **2001**

[7] R.H. Baugham, A.A. Zakhidov, and W.A. de Heer, *Science* **2002,** *297*, 787-795.

[8] G. Malgas, C. Arendse, N.P. Cele, and F. Cummings, *J. Mater. Sci*. **2008,** *26*, 322-331.

[9] S. Pekker, J.P. Salvetat, E. Jakab, J.M. Bonard, and L. Forro, *J. Phys. Chem. B* **2001**, *10*, 7938-7946.

[10] E.T. Mickelson, C.B. Huffman, A.G. Rinzler, R.E. Smalley, R.H. Hauge, and J.L. Margrave, *Chem. Phys. Lett.* **1998**, *296,* 188-195.

[11] M.A. Hamon, H. Hu, P. Bhowmik, S. Niyogi, B. Zhao, M.E. Itkis, and R.C. Haddon, *Chem. Phys. Lett.* **2001**, *347,* 8-15.

[12] Y.P. Sun, W.J. Huang, Y. Lin, K.F. Fu, A. Kitaygorodskiy, L.A. Riddle, Y.J. Yu, and D.L. Carroll, *Chem. Mater.* **2001**, *13*, 2864-2873.

[13] S.B. Sinnott, *J. Nanosci. Nanotechnol.* **2002**, *2*, 113-121.

[14] J.L. Stevens, A.Y. Huang, H.Q. Peng, L.W. Chiang, V.N. Khabashesku, and J.L. Margrave, *Nano Lett.* **2003**, *3,* 331-338.

[15] Y.P. Sun, K.F. Fu, Y. Lin, and W.J. Huang, *Acc. Chem. Res.* **2002**, *35*, 1096.

[16] S. Banerjee, T. Hemraj-Benny, and S. Wong, *Adv. Mater.* **2005,** 1, 17-25.

[17] J. Chen, *J. Phys. Chem. B* **2001,** *105*, 2525-2531.

[18] A. Eitan, K. Jiang, R. Andrews, and L.S. Schadler, *Chem. Mater.* **2003**, *15* (16), 3198.

[19] D.E. Hill, Y. Lin, A.M. Rao, L.F. Allard, and Y.P. Sun, *Macromolecules* **2002**, *35*, 9466-9472.

[20] T.L. Wang and C.G. Tseng, *J. Appl. Polym*. Sci. **2007**, *105*, 1642-1649.

[21] A. Eitan, K. Jiang, R. Andrews, and L.S. Schadler, *Chem. Mater.* **2003**, *15,* 1624-1630.

[22] J.Y. Kim, Y.G. Kim, and J.L. Stickney, *J. Electrochem. Soc*. **2007**, *154*, 260-271.

[23] S. Wang, Z. Liang, T. Liu, B. Wang, and C. Zhaung, *Nanotechnology* **2006**, *17*, 1551-1558.

[24] A. Sasa and M. Jovan, *Macromolecules* **2003,** 31, 8463-8471.

[25] J. Zhang, *J. Phys. Chem. B* **2003**, *107*, 3712-3718.

[26] P.W. Chiu, G. S. Duesberg, U. Dettlaff Weglikowska, and S. Rotha, *Appl. Phys. Lett.* **2002,** *80*, 3811-3818.

[27] A. Cao, C. Xu, J. Liang, D. Wu, and B. Wei, *Chem. Phys. Lett.* **2001,** 344, 13-22.

5

Effect of Multi-walled Carbon Nanotubes Loading on the Properties of Nafion Membranes

Abstract

The dispersion of carbon nanotubes is one of the problems in the application of polymer nanocomposites. In this study, the effect of chemical fuctionalization of carbon nanotube surface on the dispersion of the tubes within a polymer is reported. The effect of carbon nanotube weight loading on the properties of polymer membranes was also studied. Multi-walled carbon nanotubes were dispersed in Nafion matrix by melt-processing techniques to form nanocomposites membranes. The morphology, direct current electrical conductivity, thermal stability, mechanical properties, and proton conductivity of these nanocomposites were investigated. Nitric acid functionalized carbon nanotubes were evenly dispersed with Nafion as observed by scanning electron microscopy. The measurements of mechanical properties indicate that this processing method and carbon nanotube loading can improve the modulus of the nanocomposites.

5.1 Introduction

Polymer electrolyte membrane (PEM) fuel cells based on perfluorinated membranes have typically been operated in a temperature range of 50–80°C.[1–2] Increasing the operating temperature of fuel cells improves the electrode kinetics of the oxygen reduction reaction. [3–4] The ceiling temperature results from difficulty in maintaining membrane water content at temperatures above 100°C. Temperatures above the glass transition temperature (110°C) for protonated Nafion can cause polymer chains rearrangement, which can lead to the structural changes in the membrane and lower the membrane stability, performance, and lifetime.[1–6] Those are all the hurdles for operating fuel cells at higher temperatures.

However, polymer membranes that can be operated at elevated temperatures of about 120°C could benefit from enhancing carbon monoxide (CO) tolerance.[7–8] The most significant barrier to operating a PEM fuel cell at that temperature is maintaining the proton conductivity of the membrane.[6–9] Higher temperatures increase the water vapor pressure required to keep a given amount of water in the membrane, thereby increasing the possibility of water loss and significantly reducing proton conductivity. There are different approaches to improve performance of PEM used in fuel cells. Three strategies are commonly used to tackle these problems:[1–18]

1. Replace Nafion with alternative polymers such as sulfonated polyetherketone, sulfonated polyaromatics and polyheterocyclic, etc.
2. Use acid-based polymers such as phosphoric acid doped polybenzimidazole (PBI).
3. Modify ionic conducting polymers with inorganic filler such as silica, zirconium phosphate, multi-layered silicates, etc.

The addition of an inorganic material into a polymer matrix can alter and improve the physical and chemical properties of interest such as elastic modulus, proton conductivity, permeability, tensile strength, etc. The main reason for addition of inorganic fillers in fuel cell membranes is to reduce methanol permeability while keeping proton conductivity as high as possible. Many researchers have not been able to achieve a counter balance in those properties. In this study, the

filler material of interest is CNTs. This is because of their very interesting properties and capacity of improving the mechanical properties of polymer matrices.[18–20] There are problems associated with CNTs incorporated into PEM such as risk of short circuiting and their cylindrically shape. These make it difficult for CNTs to be evenly dispersed in a polymer as mentioned in previous chapters.[21] In this study such problems can be limited by modifying the surface of carbon nanotubes with carboxylic acid groups and amine functional groups.[22]

5.2 Experimental Part

5.2.1 Membrane Preparation

Nafion nanocomposite membranes were prepared by melt-mixing the Nafion precursor with CNTs at 250°C in a Reomix OS (HAAKE) instrument, at a rotor speed of 60 rpm for 10 m. The CNTs were added after two minutes of melting Nafion inside the extruder. For each nanocomposite, the amount of CNTs loaded was varied from 0.2 to 1 wt% to study the effect of CNTs loading on the properties of Nafion. Nanocomposites were prepared with pCNTs, oCNTs and fCNTs. The nanocomposites samples were then converted into sheets or films with a thickness range of about 0.12–0.2 mm using a Carver laboratory press at 2 MPa and 250°C. The nanocomposites were then hydrolyzed, to allow cation exchange. These nanocomposites were immersed in a mixture of 15 wt% potassium hydroxide, 50 wt% of deionised water and 35 wt% of dimethyl-sulfoxide at 80°C for 2 h, followed by the repeated immersion (three times) in a fresh 5M HNO_3 for 1 h to complete protonation. A series of nanocomposites samples were prepared to study the effect of CNT loading on Nafion properties as shown in Table 1.

Table 5.1 Processing parameters for Nafion nanocomposites preparation

Series	CNTs type	Loading /wt%	Processing temperature /°C
A	pCNTs	0.2– 1	250
B	oCNTs	0.2–1	250
C	fCNTs	0.2–1	250

5.2.2 Characterization and Property Measurements

The bulk DC resistivity of various membranes was measured at room temperature using the four-point collinear probe method. The equidistant tungsten carbide probes have a separation distance (s) and probe radius of 0.127 cm and 0.005 cm, respectively. The 1 x 1 cm^2 samples were prepared with a thickness of about 0.2 cm. The Keithley 4200-SCS Semiconductor Characterization System, equipped with a four supply-and-measure unit (SMUs) and a pre-amplifier, was used to perform the high precision direct-current characterization by supplying currents ranging from 1 fA to 1 mA with a resolution of 0.1 fA. Impedance measurements were carried out at 100% humidity and 26°C in a frequency range 1 Hz to1 MHz. The amplitude of the AC voltage was 5 mV. It is assumed that the resistance of the Nafion membrane is given by the high frequency extrapolation of the Nyquist plot to the real axis (Z'). At the lowest frequency values the impedance changes are dominated by the frequency response of the electrode-membrane interface. Using the membrane resistance values determined from the Nyquist plots and cell constants. The proton conductivity was calculated using **Equation (3.12)**. The nanocomposites films were completely dried under vacuum at 90°C for 24 h weighed (W_{dry}) and then placed in water at 25°C for 24 h. The nanocomposites films were then wiped quickly with filter paper and weighed (W_{wet}). The water uptake was then calculated using **Equation 3.13.**

5.3. Results and Discussions

5.3.1 Morphology

Figure 5.1 shows the cross sectional surface morphology of the Nafion-pCNTs composites with different nanotube loadings. In Figure 5.1 a, N-0.2 wt% pCNTs, tubes are clearly distinguished in the micrograph as network like-structures within polymer matrix. Some pCNTs form bundles as shown in **Figure 5.1 a**. N-0.5 wt% pCNTs composite membrane shows CNTs concentrated in one area. This is due to the poor dispersion of pCNTs in Nafion polymer. In **Figure 5.1 c**, white dots attributed to CNTs are evenly dispersed in the polymer. This suggests a good dispersion of

pCNTs in a polymer matrix and that 1 wt% of pCNTs is adequate to be evenly dispersed within Nafion matrix compared to lower weight percentages.

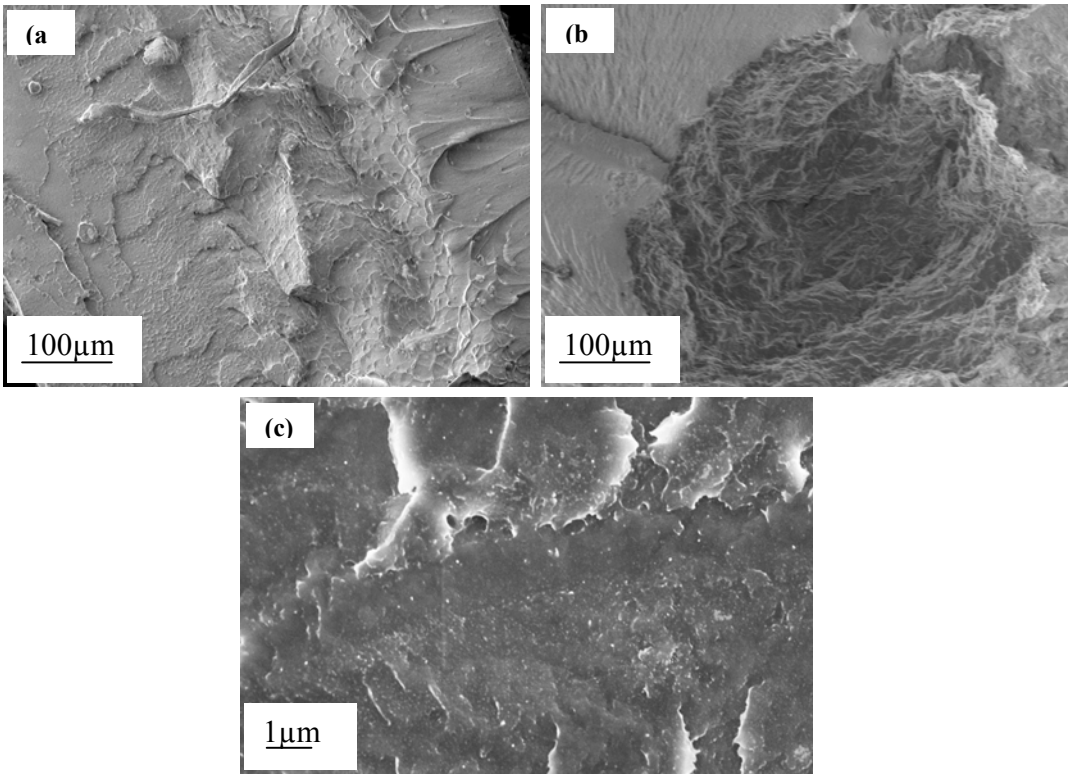

Figure 5.1 SEM micrographs of the cross sectional surface morphology for Nafion pCNTs nanocomposites with different pCNTs loadings: (a) 0.2 wt%, (b) 0.5 wt%, and (c) 1.0 wt%

Figure 5.2 shows SEM images of Nafion-oCNT composites with different weight loadings of the oCNTs. **Figure 5.2 a**, oCNTs are observed as interconnecting structures within the polymer matrix. They are loosely bound and well dispersed within the polymer. As the oCNTs loading is increased to 0.5 wt% within polymer, oCNTs form interconnected structures in the polymer matrix. Tubes are evenly dispersed but stacked compared to 0.2 wt% loading. In **Figure 5.2 c** oCNTs are well dispersed and stacked together in a polymer. This good dispersion observed with N-oCNTs composites films is attributed to the compatibility of –COOH functional groups to the $–SO_2H$ groups of Nafion.[21–23a] This is also due to the Van der Waals forces with carbon nanotubes, which cause the CNTs to easily slide or rotate with respect to one another, forming

near-ideal linear nano-bearings.[23b] This suggests that –COOH acid groups promote such motion in the CNTs.

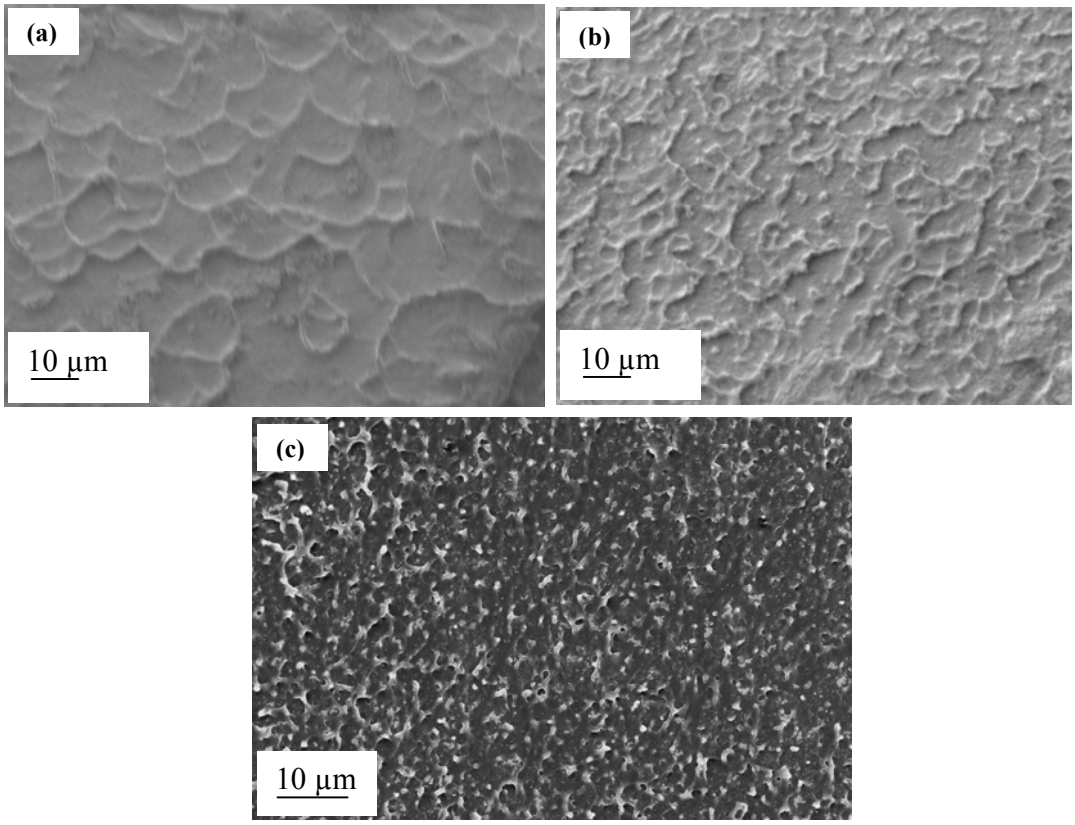

Figure 5.2 Scanning electron microscopy images of the cross sectional surface morphology for Nafion–oCNTs nanocomposites with different weight loadings of the oCNTs: (a) 0.2 wt%, (b) 0.5 wt%, and (c) 1.0 wt%

Figure 5.3 shows SEM micrographs of Nafion-fCNT nanocomposite membranes. In Figure 3 a, a bundle of fCNTs is observed in some part of Nafion membrane. The similar type of morphology is observed with N-0.5 wt% fCNTs sample. This poor dispersion is associated with the NH_2 functional groups, which promote electrostatic attraction forces between the tubes. This makes it difficult to disperse fCNTs within a polymer via melt-extrusion even though these tubes are soluble in some solvents. When 1 wt% of fCNTs is incorporated with a polymer matrix, tubes are hardly observed, they are imbedded within a polymer. This suggests that NH_2 functional groups do not favor dispersion of CNTs within Nafion due to the poor compatibility with sulfonic acid groups of Nafion membrane.

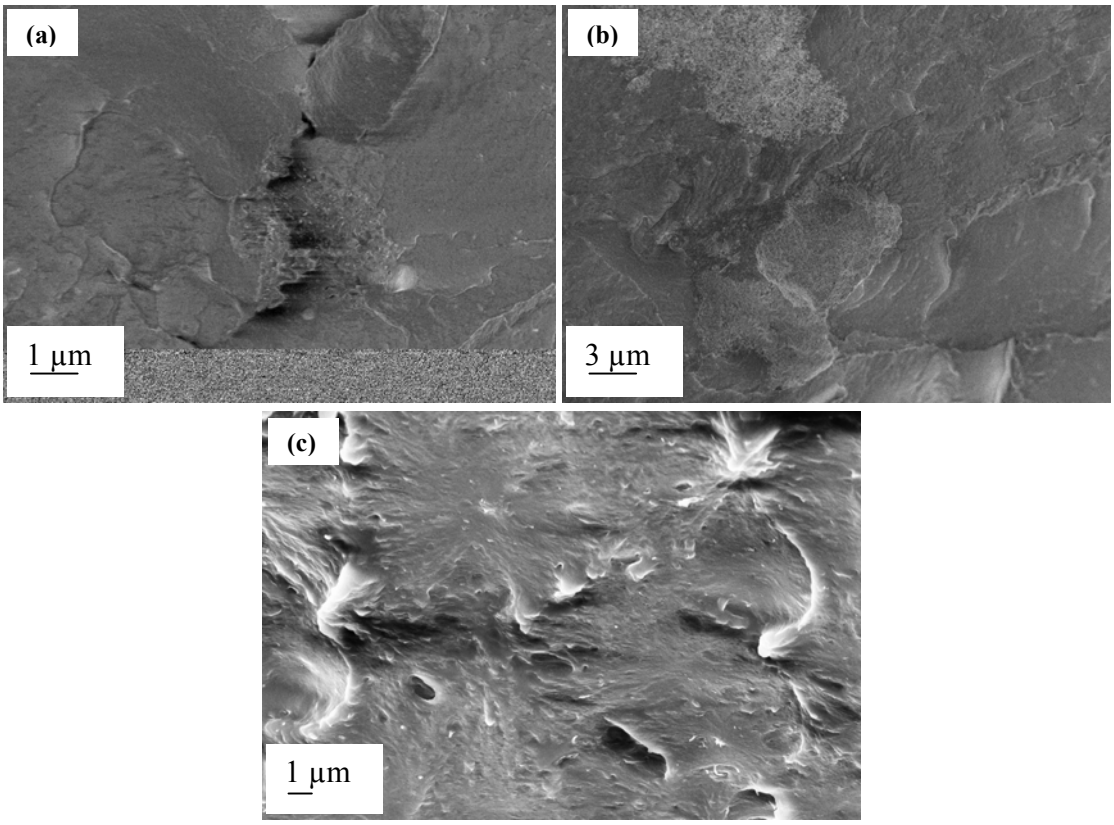

Figure 5.3 Scanning electron microscopy images of the cross sectional surface morphology for Nafion-fCNTs nanocomposites with different weight loadings of the fCNTs: (a) 0.2 wt%, (b) 0.5 wt%, and (c) 1.0 wt%.

Levels of dispersion were further quantified using optical microscopy (OM). **Figure 5.4** exhibits the high resolution optical micrographs (OMS) of the nanocomposites films with different weight loadings of pCNTs. There are a few black spots in **Figure 5.4 a**, which are attributed to pCNTs. This indicates that nanotubes are evenly distributed within Nafion matrix containing 0.2 wt% of pCNTs. As weight percentage in polymer increases to 0.5 pCNTs clusters of about 20 µm are observed. This is due to the nanotubes poor dispersion as observed with SEM. N-1 wt% pCNT nanocomposite contains evenly dispersed CNTs of about 1 µm. This was ascribed to the specific surface area of a polymer, which is much less than that of the nanotubes. Therefore, polymer can merely adsorb a certain amount of pCNTs and more tubes leads to poor dispersion and agglomeration.

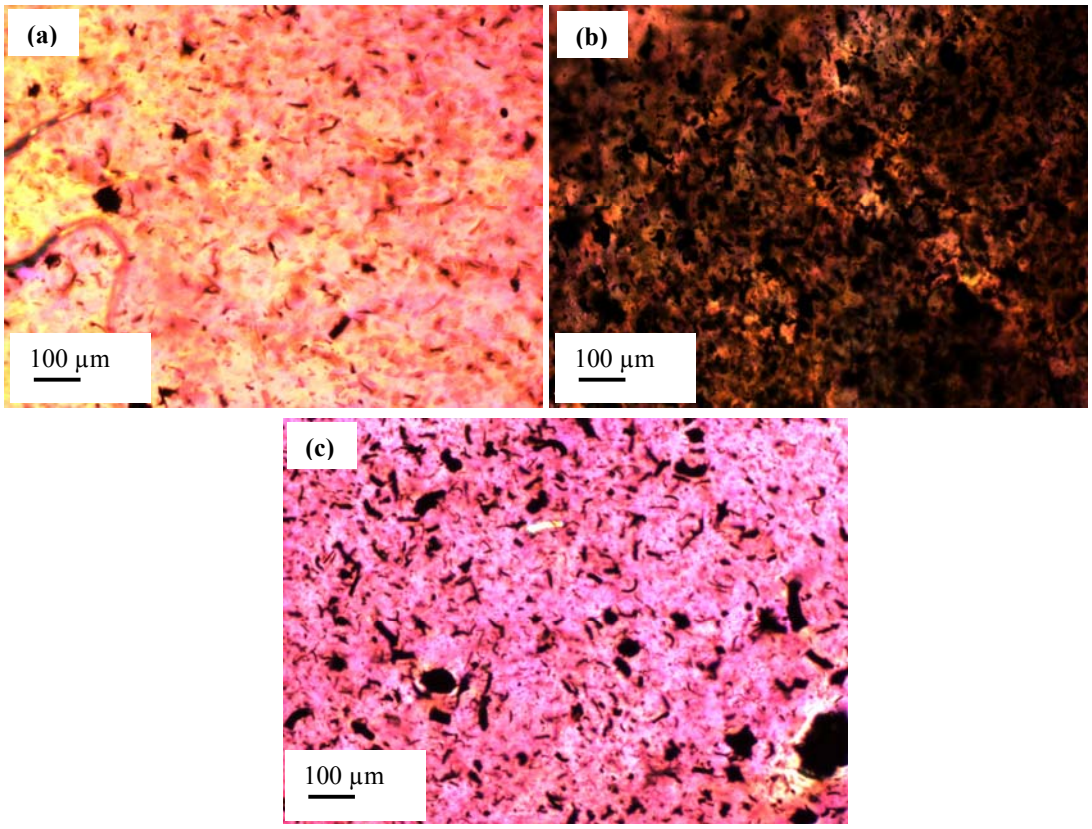

Figure 5.4 High resolution optical micrographs of Nafion nanocomposite films with different weight loadings of pCNTs (a) 0.2 wt% , (b) 0.5 wt%, and (c) 1.0 wt%.

Figure 5.5 shows the optical images of Nafion-oCNTs nanocomposite films. In all nanocomposites, oCNTs are well dispersed. These tubes bundle-up as the weight percentage increases. This is in good agreement with SEM observations. The morphology of N-fCNTs composite membranes was also studied (see **Figure 5.6**). It was observed that as the fCNTs content increases the tubes are poorly dispersed within Nafion matrix. This is due to the amine functional groups, which promote the electrostatic attraction between the tubes.

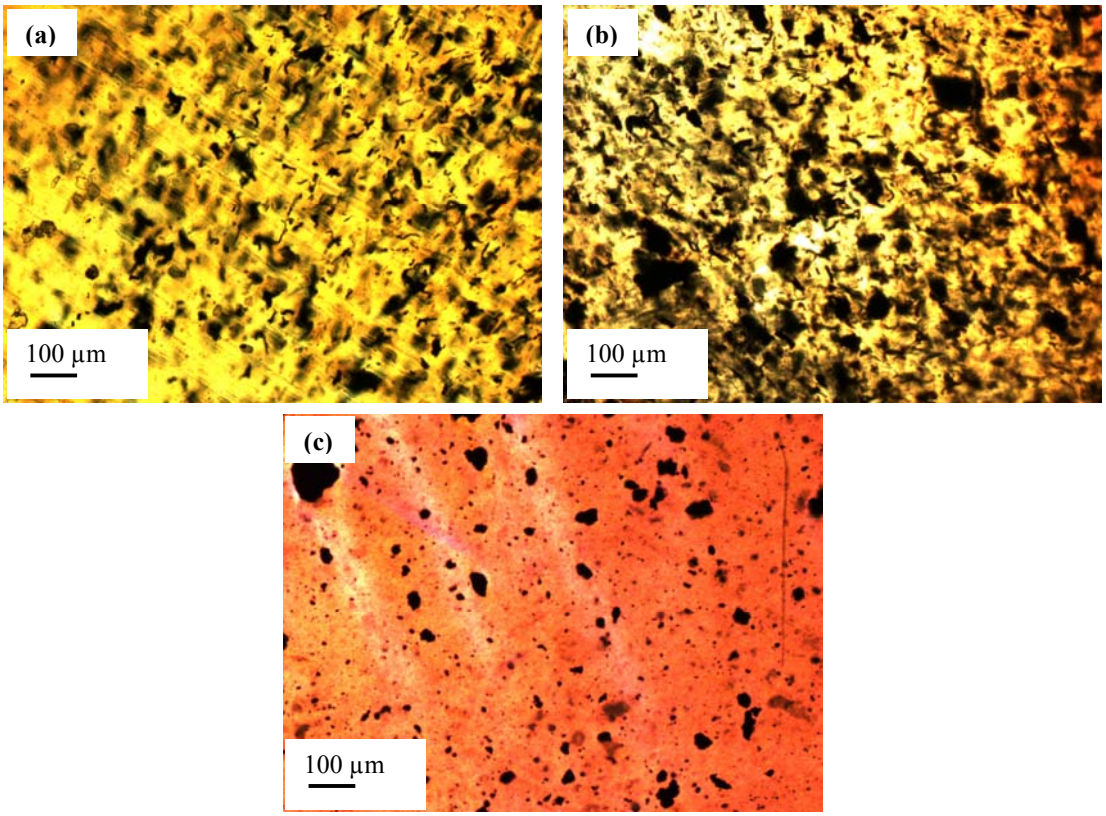

Figure 5.5 Optical microscopy images of Nafion nanocomposite films with different weight loadings of oCNTs: (a) 0.2 wt%, (b) 0.5 wt%, and (c) 1.0 wt%.

5.3.2 Electrical Conductivity and Water Uptake of the Membranes

Figure 5.7 a-c shows the relationship between both water uptake and electrical conductivity versus the weight fraction of pCNTs in the nanocomposites membranes. The water uptake increases with 0.2 wt% pCNTs nanocomposite membrane. This might be due to the surface modification of Nafion with higher surface area carbon nanotubes making the surface more hydrophilic compared to neat Nafion. With an increase of pCNTs to 0.5 wt% within polymer matrix, the water uptake of nanocomposites sharply decreased to about 4%. This is due to the pCNTs bundles observed with SEM and OM images, which hinder most of the Nafion matrix surface to take up water. As the weight fraction of pCNTs within Nafion increases to 1 wt%, the

water uptake of nanocomposites slightly increases to about 10%. As shown in **Figure 5.7 a**, the bulk electrical conductivity remains at zero after incorporation of 0.2 wt% pCNTs.

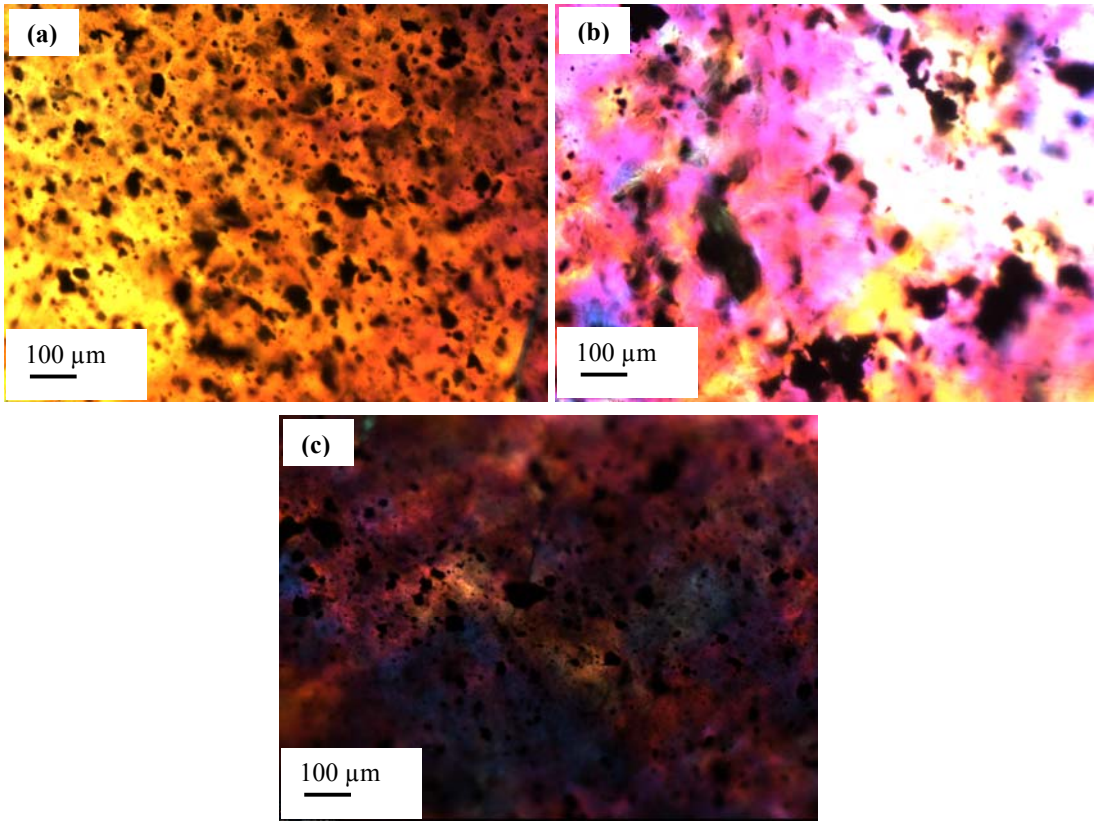

Figure 5.6 Optical microscopy images of nanocomposites films with different weight loadings of fCNTs: (a) N-0.2 wt% fCNTs, (b) N-0.5 wt% fCNTs, and (c) N-1.0 wt% fCNTs.

This suggests that 0.2 wt% of pCNTs does not have an effect on the electrical conductivity of Nafion. The electrical conductivity increases with 0.5 wt% pCNTs nanocomposites to about $2.5x10^{-4}$ S/cm. The electrical conductivity of 1 wt% pCNTs slightly decreases to about $2x10^{-4}$ S/cm compared to that of 0.5 wt% pCNTs nanocomposites. This is attributed to electrical percolation threshold of CNTs. The lower percolation threshold compared to the previously reported values of about 4 wt% by Zhang et al.[23c] is due to the dispersion of the tubes in polymer matrix. Nanocomposites preparation methods play a huge role in the morphology.

In **Figure 5.7 b**, the water uptake and electrical conductivity of Nafion increase with an incorporation of 0.2 wt% oCNTs. This electrical conductivity improvement is associated with the interconnected structures of the tubes observed in SEM micrographs. The water uptake increase is associated with the hydrophilic nature of COOH functional groups attached to the tubes. As the oCNTs content increases to 0.5 wt% within polymer, both electrical conductivity and water uptake decrease comparable to neat Nafion. However, for N-1 wt% oCNTs water uptake further decreases and electrical conductivity slightly increases. A decrease in water uptake with an increase in oCNTs loading associated with water uptake threshold of Nafion and barrier effect of CNTs. More CNTs in nanocomposites hinders absorbance of water molecules within the polymer. The higher electrical conductivity is also due to the higher content of the tubes in a polymer composite.

Nafion-fCNTs composites show an increase in water uptake to about 35% with N-0.2 wt% and N-0.5 wt% fCNTs as shown in **Figure 5.7 c**. This is due to the hydrophilic nature of amine functional groups present in the composites membranes. However, water uptake tends to decrease as the fCNTs content increases to 1 wt%. This is due to the water uptake percolation of the composite membranes. The electrical conductivity remains zero with N-0.2 wt% fCNTs and decreases below zero with N-0.5 wt% fCNTs nanocomposites. This decrease in electrical conductivity might be due to the amine that covers the tubes and the polymer surface. However, N-1 wt% fCNTs has electrical conductivity of zero, the same as Nafion and N-0.2 wt% fCNTs nanocomposites. This suggests that fCNTs have no effect on the electrical conductivity of Nafion.

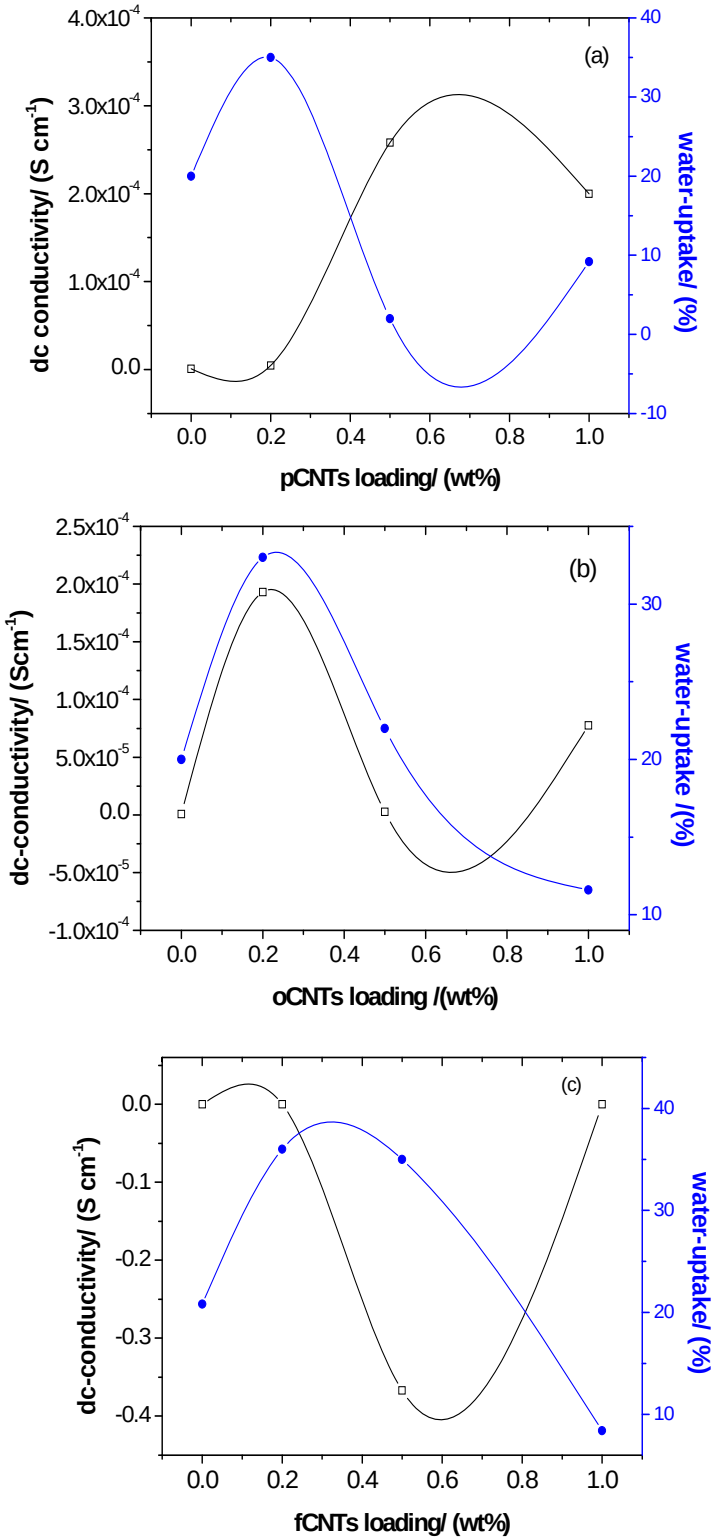

Figure 5.7 Electrical conductivity and water uptake measurements of Nafion and its nanocomposites with different filler loadings: (a) pCNTs, (b) oCNTs, and (c) fCNTs**.**

5.3.3 Thermal Properties

Thermal analysis was used to determine the degradation temperature of the nanocomposites membranes. **Figure 5.8** shows thermogravimetric analysis (TGA) results of Nafion and CNTs based Nafion composites membranes with various CNTs content. All membranes decompose in three degradation stages. **Figure 5.8 a**, shows that Nafion and pCNTs composites of 0.2 wt%, 0.5 wt% and 1.0 wt% have the initial weight loss (1st stage) of 7.5, 6.2, 7.8 and 5.0%, respectively at 30–300°C. This is attributed to the loss of residual water within the membranes. The second degradation stage (300–430°C) is associated with to the desulfonation of sulfonic acid groups of Nafion.[22, 24] The third stage (430–550°C) is related to polytetrafluoroethylene (PTFE) backbone decomposition.[22–26] The degradation profiles for all samples are similar. However, the onset degradation temperature is different. Nafion, 0.2 wt%, 0.5 wt%, and 1 wt% have degradation temperatures of 400, 410, 380, and 410°C, respectively. The difference in the onset temperature is associated with the sample's thermal stability. Poor thermal stability of N-0.5 wt% pCNTs nanocomposites is attributed to the poor dispersion of CNTs within a polymer observed with SEM. This might also be due to the poor compatibility leading to the weaker interaction between filler and polymer chains. These aggregates absorb heat and act as a secondary heat source, therefore decomposing nanocomposites much quicker. A slight increase in thermal stability is observed with 0.2 and 1 wt% polymer nanocomposites. This is attributed to the good dispersion of pCNTs within a polymer observed with SEM results.

Figure 5.8 b shows TGA profiles of N-oCNTs composite membranes. In this case, the temperatures corresponding to the onset thermal degradation (T_d) for Nafion, N-0.2 wt% oCNTs, N-0.5 wt% oCNTs and N-1 wt% oCNTs are 400, 375, 390 and 410°C, respectively. This shows an increase in thermal stability of Nafion with an increase in oCNTs content. This is associated with ion exchange that occurs when COOH groups of CNTs interact with protons and sulfonate groups of Nafion and the intermolecular interaction between polymer and oCNTs. From the comparison of the curves, it is noted that the thermal decomposition of nanocomposites is dependent on the weight percentage of CNTs.

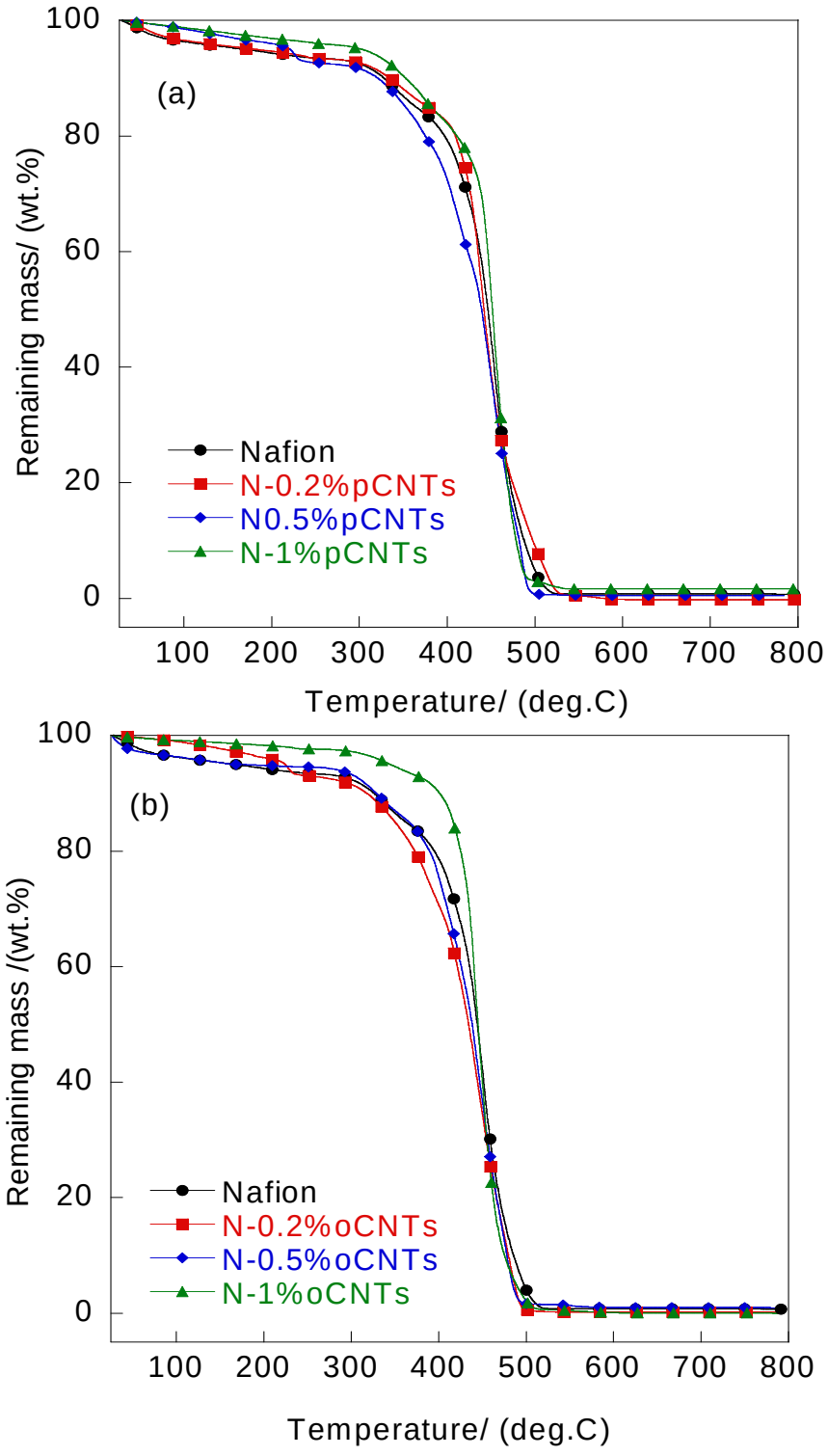

Figure 5.8 Thermogravimetric analysis scans of Nafion and CNTs based Nafion nanocomposites membranes with different filler loadings: (a) pCNTs and (b) oCNTs.

5.3.4 Dynamic Mechanical Measurements

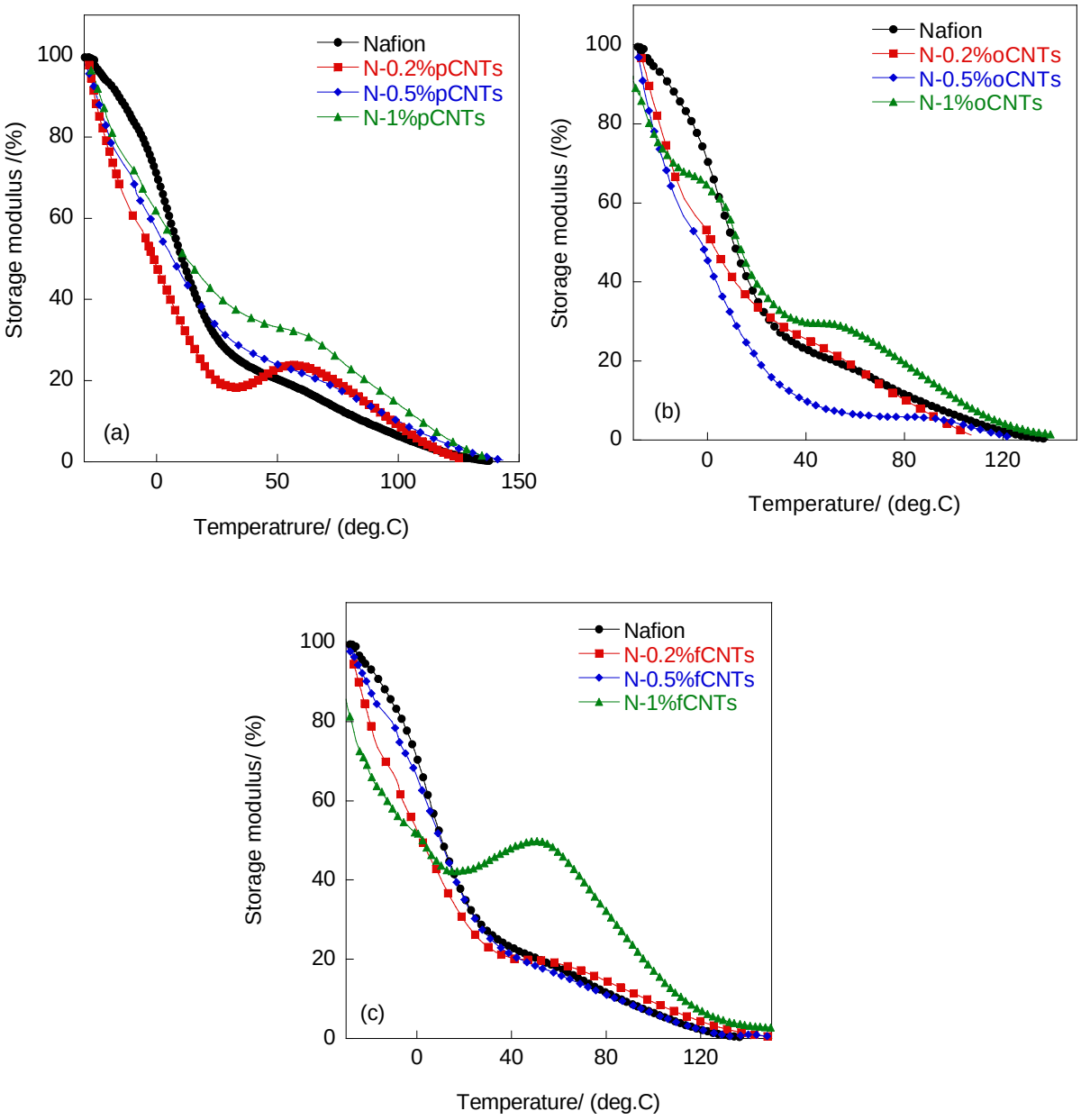

Figure 5.9 Temperature dependence of storage modulus for Nafion and its CNT-based nanocomposites with different CNT loadings: (a) pCNTs, (b) oCNTs, and (c) fCNTs.

Operating the fuel cell at temperatures closer to the α-transition of Nafion matrix would be beneficial to its performance. This is because the ionic domains of the membranes will be more mobile and will reduce resistance. It is, therefore, important to understand the mechanical behavior of these membranes in such temperatures. **Figure 5.9** shows the normalized plots of storage modulus as a function of temperature for Nafion and its nanocomposite with different CNT loadings (a) pCNTs, (b) oCNTs, and (c) fCNTs. The actual values of the storage modulus for all the membranes are listed in Table 2. The moduli for all samples decrease with an increase in temperature.

In **Figure 5.9 a** neat Nafion showed the highest storage modulus at lower temperatures compared to N-pCNTs composites and N-fCNTs (see **Fig. 8 c**). N-0.5 wt% pCNTs has the lowest E' at low temperature but the E' decreases slowly as the temperature increases. At temperatures > 50°C, the percentage of E' increases with an increase in pCNTs content. This increase in resistance to deformation or stiffness is associated with immobilization of side chains in nanocomposites as content of pCNTs are imbedded in polymer increases. This property is related to the thermal stability of these nanocomposites represented in the thermal stability section. Interestingly, unmodified Nafion has the highest storage modulus at lower temperatures. This suggests that all nanocomposites are softer than Nafion at the lower temperatures, while possessing superior resistance to deformation at higher temperatures. The E' plots of N-0.2 wt% pCNTs shows a peak at about 60°C. This is due to the thermal condensation reaction between clustered tubes and Nafion.[27] This feature is also observed with N-1 wt% pCNTs but not prominent.

Figure 5.9 b shows E' plot of N-oCNTs nanocomposite membranes. N-0.5 wt% shows the highest E' at lower temperatures and the highest decrease in modulus. N-1 wt% shows the lowest decrease in storage modulus and remains stable at temperatures above 120°C. This suggests that oCNTs enhances the stiffness of Nafion and there is greater interaction between the tubes and polymer. Nafion-fCNTs nanocomposite membranes show a decrease in E' compared to neat Nafion. However, N-1 wt% fCNTs shows a higher E' at higher temperatures. This might be due to the stiffness of nanocomposites due to the amine functional groups on the outer surface of the tubes. This is related to the deformation resistance of the side chains.

All the samples show a continuous loss of storage modulus as temperatures increase. Some transitions are happening between 40–80°C. This transition might represent the change in elastic behavior of these composite membranes. Crum et al. reported this transition peak as the glass transition temperature of the membranes. [28] This is a major transition for polymers as physical properties change dramatically from a glassy state to a rubbery one.

Table 5.2 Average storage modulus (E') values of membranes at different temperatures

Sample	E'(–30°C) /MPa	E' (30 °C) /MPa	E' (60 °C) /MPa	E' (90 °C) /MPa	E' (120 °C) /MPa
Nafion	8.7	2.3	1.5	0.8	0.20
N-0.2% pCNTs	6.5	1.3	1.6	0.9	0.10
N-0.5% pCNTs	1.3	0.4	0.3	0.2	0.10
N-1.0% pCNTs	7.6	3.0	2.5	1.4	0.50
N-0.2% oCNTs	6.5	1.9	1.2	0.5	–
N-0.5% oCNTs	10	1.5	0.7	0.6	0.10
N-1.0% oCNTs	6.8	2.5	2.2	1.3	0.50
N-0.2% fCNTs	2.0	0.5	0.4	0.2	0.06
N-0.5% fCNTs	3.7	1.0	0.6	0.4	0.06
N-1.0% fCNTs	3.8	2.0	2.1	1.0	0.30

5.3.5 EIS Measurements

The equivalent circuit for all the membranes is shown in **Figure 5.10** and the fitting parameters and conductivity values are tabulated in **Table 5.3**. **Figure 5.11** shows the Nyquist plots for Nafion and its nanocomposite membranes. It can be observed that the position of the high frequency portion of the Nyquist plots stays nearly unaltered for all samples. Correspondingly, the membrane conductivity values range from 0.07 $S.cm^{-1}$ to a final value of 0.10 $S.cm^{-1}$ for Nafion, N-pCNTs and N-oCNTs composite membranes. This suggests that the CNT content has not much effect on the ionic conductivity of Nafion membranes. For N-fCNTs composite membranes, the proton conductivity sharply decreases to about $0.8x10^{-3}$ $S.cm^{-1}$. The higher ionic resistance is associated with the amine treated CNTs within a polymer hindering the flow of

protons. However, as the content of fCNTs within Nafion increases the proton conductivity increases to about $4x10^{-3}$ $S.cm^{-1}$.

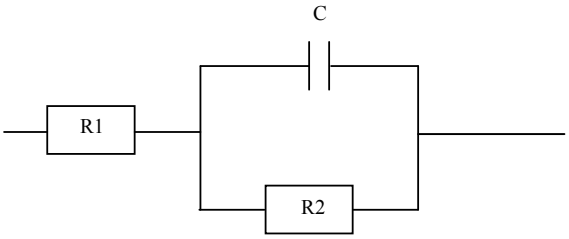

Figure 5.10 The equivalent circuits for all membranes, where R1 is the electrolytes resistance, R2 is the charge transfer resistance and C is the capacitance.

Table 5.3 Proton conductivity of Nafion and its various multi-walled carbon nanotubes-containing nanocomposite membranes.

Sample	**Thickness /cm**	**R /Ω**	$\sigma = d/RA$ **/S.cm^{-1}**
Nafion	0.020	226.6	0.07
N-0.2% pCNTs	0.016	217.8	0.10
N-0.5% pCNTs	0.020	217.7	0.08
N-1.0% pCNTs	0.017	263.6	0.07
N-0.2% oCNTs	0.018	204.1	0. 09
N-0.5% oCNTs	0.020	204.7	0.08
N-1.0% oCNTs	0.020	235.8	0.07
N-0.2% fCNTs	0.010	40.9k	$0.8x10^{-3}$
N-0.5% fCNTs	0.015	16.6k	$1.0x10^{-3}$
N-1.0% fCNTs	0.012	26.7k	$4.0x10^{-3}$

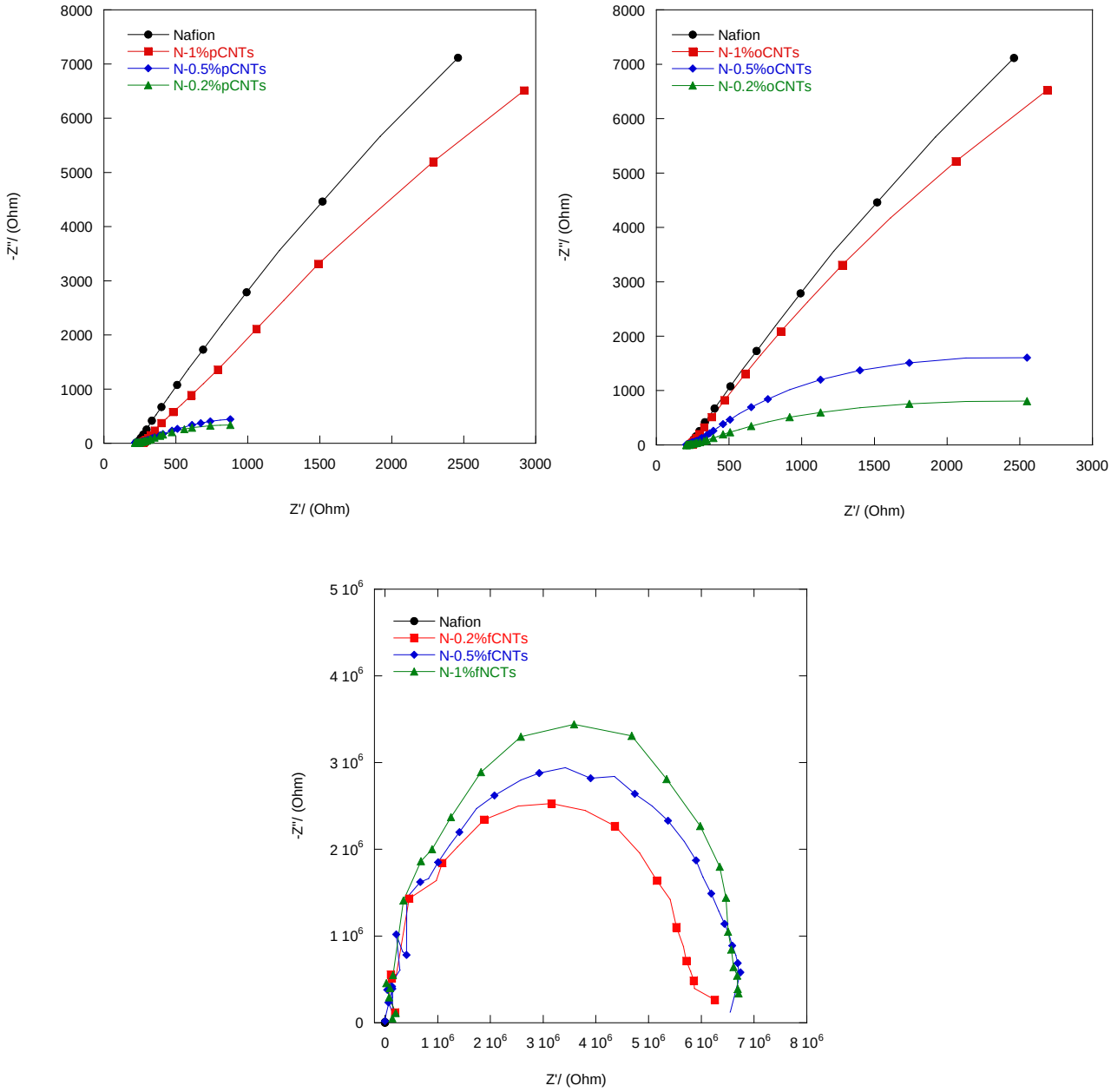

Figure 5.11 Nyquistry impedance plots of Nafion and various multi-walled carbon nanotubes-containing nanocomposite membranes with different filler loadings: (a) pCNTs, (b) oCNTs, and (c) fCNTs.

5.4 Conclusion

The results indicate that nitric acid functionalized tubes can be uniformly dispersed in Nafion by the melt-extrusion method. The nanocomposites exhibit a very low electrical percolation threshold of about 0.5 wt% CNT loading. This very low percolation threshold is indicative of good dispersion and the tube-tube distance required for electrical conductivity. The mechanical properties of nanocomposites show dependence on the loading of the tubes. At 120°C, higher mechanical stability of nanocomposites was observed with 1 wt% CNT loading for all different types of the tubes. The proton conductivity does not depend heavily on the carbon nanotube loading, rather the chemical modification of the tubes. The average proton conductivity of about 0.09 S/cm was measured for N-pCNTs and N-oCNTs composite membranes. While N-fCNTs show very poor proton conductivity. N-pCNT and N-oCNTs show better dispersion and good proton conductivity compared to the N-fCNTs nanocomposite membranes. N-1 wt% pCNTs and N-1 wt% oCNTs show balance in water uptake and proton conductivity, good thermal stability and excellent mechanical properties.

5.5 References

[1] F. Bauer and M. Willert-Porada, *J. Membr. Sci.* **2004**, *233*, 141–153.

[2] A. Collier, H. Wang, X.Z. Yuan, J. Zhang, and D.P. Wilkinson, *International J. Hydrogen Energy* **2006**, *31*, 1838–1854.

[3] D.H. Jung, S.Y. Cho, D.H. Peck, D.R. Shin, and J.S. Kim, *J. Power Sources* **2003,** *118*, 205–213.

[4] J.Jaafar, A.F. Ismail, and T. Matsuura, *J. Membr. Sci.* **2009**, *345,* 119–127

[5] T.Vernersson, B. Lafitte, G. Lindbergh, and P. Jannasch, *Fuel Cells* **2006,** 6, 340–346.

[6] A.M. Elmér and P. Jannasch, *J. Polym. Sci*. **2007**, *45*, 79–90.

[7] T. Thampan, S. malhotra, and R. Datta, *Catalysis Today* **2001**, *67*, 15–32.

[8] M. H. Yildirim, A.R. Curòs, J. Motuzas, A. Julbe, D.F. Stamatialis, and M. Wessling, *J. Membr. Sci.* **2009**, *338*, 75–83.

[9] W. Xu, T. Lu, C. Liu, and W. Xing, *Electrochim. Acta* **2005,** *50*, 3280–3285.

[10] K.D. Krwuer, *J. Mebr. Sci.* **2001**, *185*, 29–39.

[11] Q.F. Li, R.H. He, O.J. Jensen, and N. Bjerrum, *J. Chem Mater Eng* **2000**, *279*, 1–9.

[12] V. Ramani, H.R. Kunz, and J.M. Fenton, *J. Membr. Sci.* **2004**, *232*, 31–37.

[13] Z.G. Shao, H. Xu, M. Li, and I.M. Hsing, *Solid State Ionics* **2006**, *177*, 779

[14] R.F. Silva, S. Passerini, and A. Pozio, *Electrochim. Acta* **2005**, *50*, 2639–2644.

[15] M.K. Song, S.B. Park, Y.T. Kim, K.H. Kim, S.K. Min, and H.W. Rhee, *Electrochim. Acta* **2004**, *50*, 639–646.

[16] C.H. Rhee, H.K. Kim, H. Chang, and J.S. Lee, *Chem. Mater.* **2005,** *17*, 1691–1698.

[17] J.M. Thomassin, C. Pagnoulle, G. Caldarella, A. Germain, and R. Jerome, *Polymer* **2005**, *46*, 11389–11398.

[18] J.M. Thomassin, C. Pagnoulle, G. Caldarella, A. Germain, and R. Jerome, *J. Membr. Sci.* **2006,** *270*, 50–58.

[19] T. McNallya, P. Potschke, P. Halley, M. Murphy, D. Martin, S.E. Bell, G.P.Brennan, D. Bein, P. Lemoine, and J.P. Quinn, Polyethylene multiwalled carbon nanotube composites, *Polymer* **2005**, *46*, 8222–8233.

[20] S. Sinha Ray, S. Vaudreuil, A. Maazouz, and M. Bousmina, *J. Nanosci. Nanotechnol.* **2006**, *6*, 2191–2195.

[21] J.M. Thomassin, J. Kollar, G. Caldarella, A. Germain, R. Jerome, and C. Detrembleur, *J. Mebr. Sci.* **2007**, *303*, 252–257.

[22] C. de Bonis, A. D'Epifanio, M.L. Di Vona, C. D'Ottavi, B. Mecheri, E. Traversa, M. Trombetta, and S. Licoccia, *Fuel Cells* **2009,** *9*, 387–393.

[23] [23a] J. Wang, M. Musameh, and Y. Lin, *J. Am. Chem. Soc.*, **2003**, *125*, 2408–2409. [23b] S.V. Rotkin, S. Subramoney, Applied physics of carbon nanotubes: fundamentals and theory Wiley **2008**, 156–239. [23c] Q. Zhang, S. Rastogi, D. Chen, D. Lippits, and P.J. Lemstra, *Carbon* **2006**, *44*, 778–785.

[24] K.T. Adjemian, R. Dominey, L. Krishnan, H. Ota, P. Majsztrik, T. Zhang, J. Mann, B. Kirby, L. Gatto, M. Velo–Simpson, S. Srinivasan, J.B. Benziger, and A.B. Bocarsly, *Chem. Mater.***2006***, 18*, 2238–2248.

[25] H.S. Park, Y.J. Kim, W.H. Hong, Y.S. Choi, and H.K. Lee, *Macromolecules* **2005**, *38*, 2289–2296.

[26] D. Bikiaris, A. Vassiliou, K. Chrissafis, K.M. Paraskevopoulos, A. Jannakoudakis, and A. Docoslis, *Polymer degradation stability* **2008**, *93*, 952–959.

[27] S.K. Young and K.A. Mauritz, *J. Polymer Sci.* **2001,** *B39*, 1282–1295.

[28] N.G. Crum, C.P. Buckley, and C.B. Bucknall, *Principles of polymer engineering, 2nd Ed, New York: Oxford Science* **1999**.

6

Carbon Nanotube-based Nafion Composite Membranes for Fuel Cell Applications

Abstract

Carbon nanotubes containing Nafion composite membranes were prepared via melt-blending at 250°C. Using three different types of multi-walled carbon nanotubes such as pCNTs, oCNTs, and fCNTs, the effect of tubes surface oxidation as well as functionalization in composite membranes was investigated by focusing on three aspects: thermo-mechanical stability, thermal degradation, and proton conductivity. The oCNTs containing Nafion composite membrane exhibited concurrent improvement in most of the properties as compared to that of neat Nafion or other CNTs containing Nafion composite membranes. However, pCNTs containing Nafion membrane show higher fuel cell performance.

6.1 Introduction

The main objective of this work is to investigate the effect of CNT surface functionalization on the thermal and the thermo-mechanical stability and conductivity of CNT-based composite membranes. The composite membranes were prepared by a melt-blending-compression-molding technique. The degree of dispersion of CNTs in the Nafion matrix was studied by SEM. Thermogravimetric and dynamic mechanical analyzers were used to study thermal and mechanical properties of neat Nafion and nanocomposite membranes, respectively. The effect of incorporation of CNTs on the DC resistivity and alternating-current (AC) impedence of Nafion membrane are also reported.

6.2 Experimental procedure

6.2.1 Membrane Preparation

Nafion composite membranes were prepared by melt-mixing the Nafion precursor with CNTs at 250°C in a Reomix OS (HAAKE) instrument, at a rotor speed of 60 rpm for 10 m. The filler was added after two minutes of melting of Nafion inside the mixer. For each composite, the amount of CNT loading was fixed to 1 wt% to avoid short circuiting in the fuel cell. Composites were prepared with neat pCNTs, oCNTs and fCNTs (HDA functionalized CNTs), and were correspondingly abbreviated as N-pCNTs, N-oCNTs, and N-fCNTs, respectively. The dried composite strands were then converted into sheets with a thickness of 0.12–0.2 mm by pressing with 2 MPa pressure at 250°C for 5 m. The compression molded sheets were then hydrolyzed to have cation exchange properties as follows: compression molded sheets were immersed in a solution of 15% potassium hydroxide, 50% of deionised water, and 35% of dimethyl sulfoxide at 80°C for 2 h, followed by the repeated immersion (three times) in a fresh 5 M HNO_3 for 1 h.

The membranes were then treated according to the standard procedure by boiling in 5% H_2O_2 (hydrogen peroxide) aqueous solution for 1 h, to remove organic impurities, followed by washing with boiling deionised water for 30 m. The membranes were then boiled in 1 M H_2SO_4

for 1 h to remove inorganic impurities and also to complete protonation before washing with deionised water for 30 m. Washing with deionised water was repeated several times to remove any traces of acids, as checked by pH paper. Finally, all membranes were kept in deionised water prior to measurements.

6.2.2 Characterization and Property Measurements

The bulk DC resistivity of various membranes was measured at room temperature using the four-point collinear probe method.[9] The equidistant tungsten carbide probes have a separation distance(s) and probe radius of 0.127 cm and 0.005 cm, respectively. The 1 x 1 cm^2 samples were prepared with a thickness of about 0.2 cm. The Keithley 4200-SCS Semiconductor Characterisation System, equipped with a four SMUs and a pre-amplifier, was used to perform the high precision DC resistivity characterization by supplying currents ranging from 1 fA – 1 mA with a resolution of 0.1 fA. The AC impedance measurements of neat Nafion and CNT-containing composite membranes were performed on films with thickness of about 0.1–0.3 mm at 26°C and 100% relative humidity. Conductivity measurements were performed on membranes using a homemade cell. The cell geometry was chosen based on previously reported experiments to ensure that the membranes resistance dominates the response of the system.[27] The four-point-probe conductivity cell was made of two perplex blocks, with area of 5x5 cm^2 and an open groove on the top one, to keep membranes fully hydrated. Two copper wire electrodes were used to apply current to the ends of the membrane sample, while another pair of electrodes (1 cm apart) was used to measure the voltage drop across the sample. The membrane samples were sandwiched between two blocks that were pressed together by four screws fastened with approximately the same force to ensure good electrode-membrane contact (see **Figure6.1**). The electrochemical cell was connected using a four-point probe technique at an Auto lab model 4.90006 Potentiostat and FRA. The FRA electrochemical impedance software was used for the impedance measurements from 1 MHz to 1 Hz. The amplitude of the AC voltage was 5 mV.

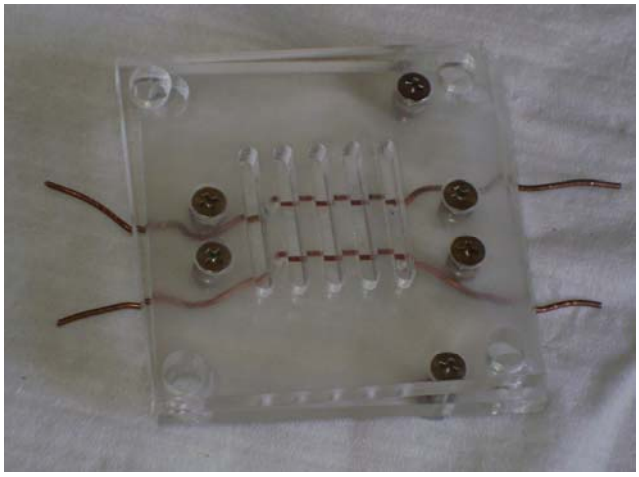

Figure 6.1 Four-point probe cell used for the measurements of proton conductivity.

6.3 Results and Discussion

6.3.1 Studies on CNTs and Composites Morphology

The degree of dispersion of CNTs in the Nafion matrix was studied by SEM. The freeze-fractured surface was used for the morphological study, and results are presented in **Figure 6.2**. A good dispersion is observed when pCNTs (see **Figure 6.2 a**) were incorporated into the Nafion matrix. Although pCNTs are covered with polymer chains, homogeneous dispersion of aggregated CNTs is more discernible at a high magnification SEM image (see inset of Figure 3 a). A much higher level of dispersion of CNTs with less aggregation into Nafion matrix is obtained when oCNTs were used for composite preparation (see **Fig. 6.2 b**). This was also observed with a small angle X-ray as shown in Appendix C. This can be attributed to the high level of compatibility between the sulfonic acid groups of the Nafion and the COOH groups of oCNTs. Another reason may be due to the small amount of Van-der-Waals interactions among the tubes after oxidation, which actually helps to disperse tubes nicely and homogeneously into the Nafion matrix. The poor dispersion of CNTs in the case of fCNTs-containing Nafion composite (**Figure 6.2 c**) is due to the high degree of covering of CNTs outer surfaces by HDA

group, as shown in Chapter 4, **Figure 4.3 c**, where it is not compatible with the Nafion matrix. This is also observed on AFM images of Nafion and N-fCNTs composites (see **Figure 6.3**).

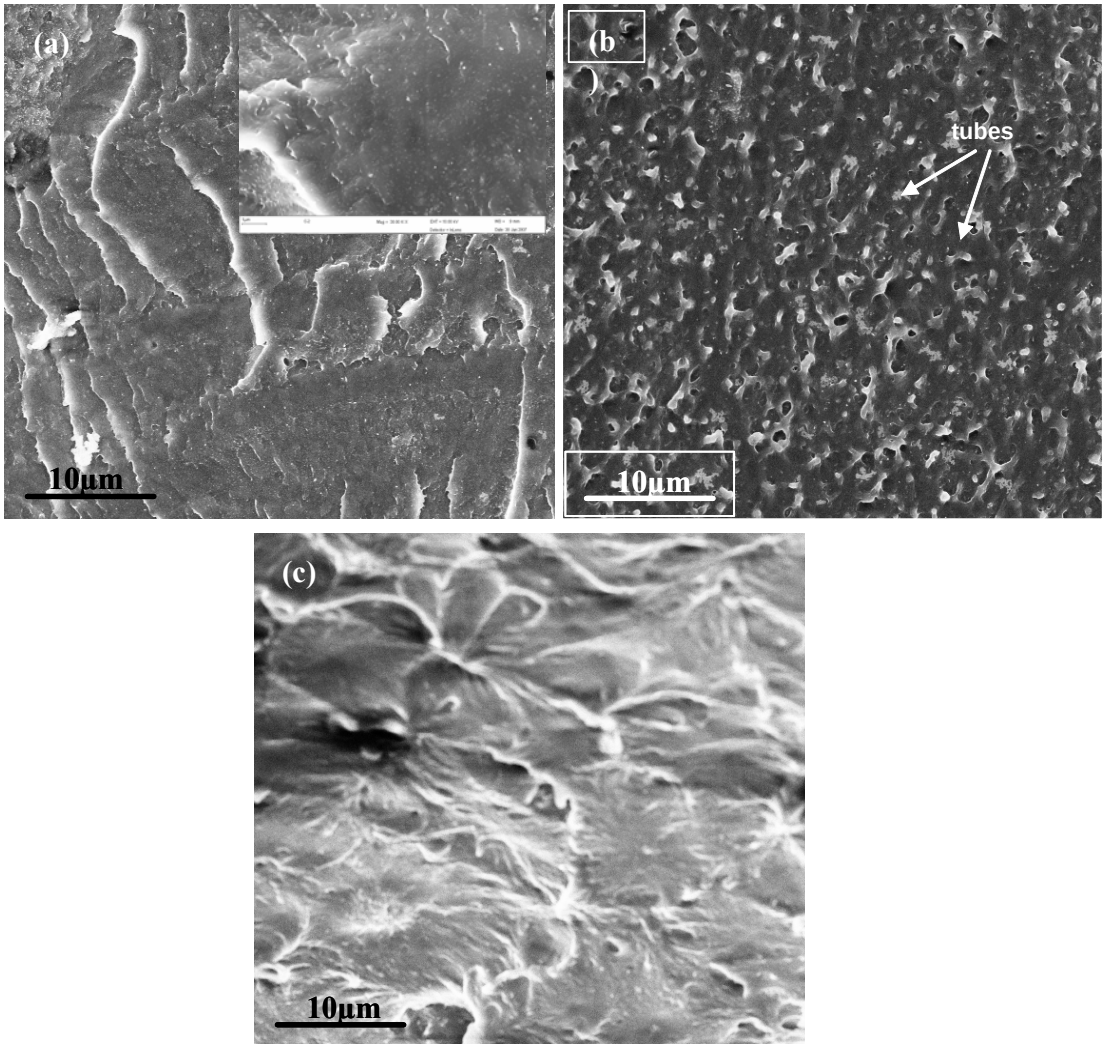

Figure 6.2 Scanning electron microscopy images of the freeze-fractured surface of CNT-containing Nafion composite membranes: (a) pCNTs, (b) oCNTs, and (d) fCNTs.

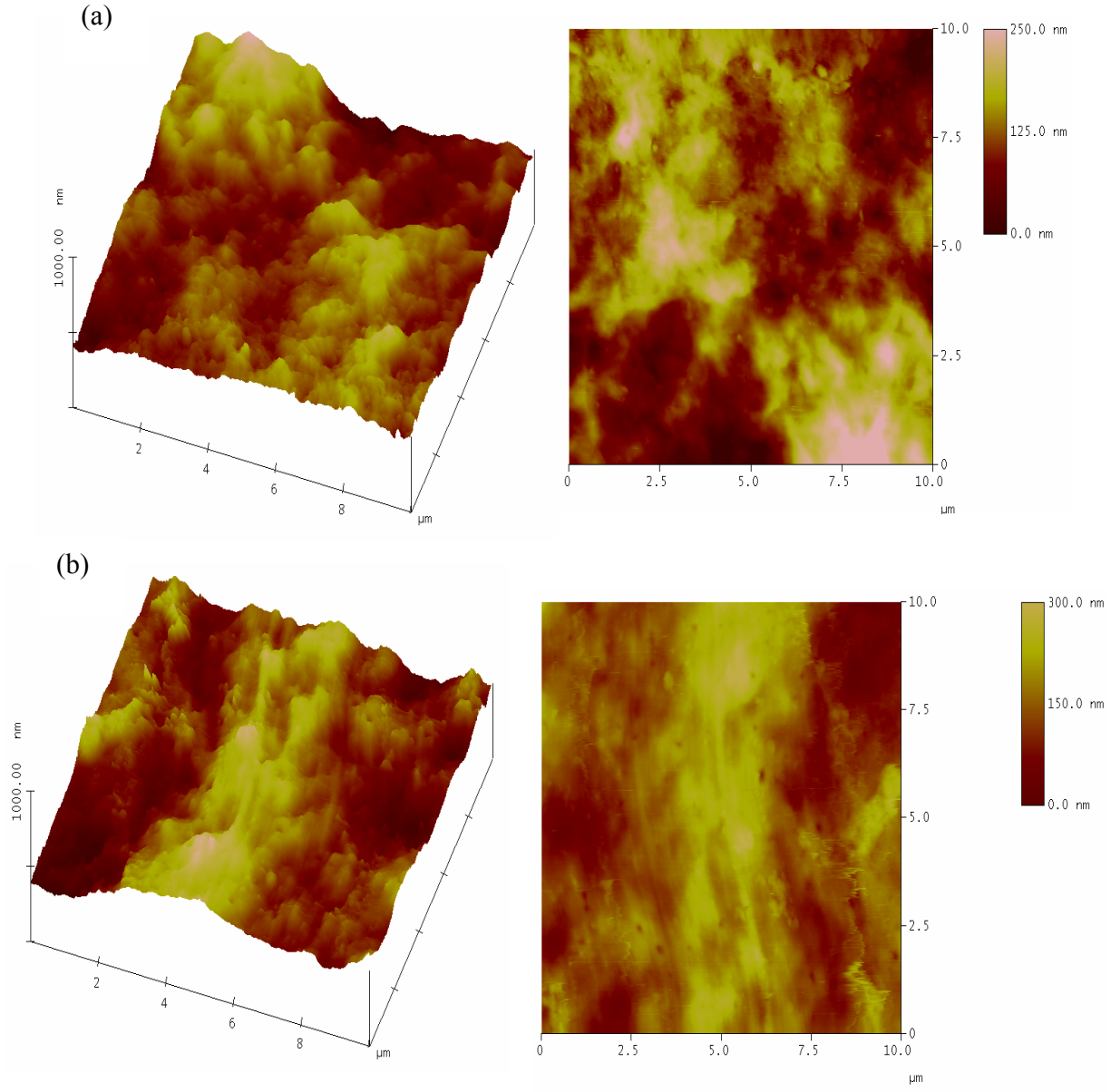

Figure 6.3 Atomic force microscopy images: (a) Nafion and (b) amine functionilized CNT composite

6.3.2 Thermogravimetric Analysis

The TGA scans of neat polymer and composite membranes in air atmosphere are illustrated in **Figure 6.4**. It is apparent that the thermal degradation is very similar for all the samples. However, the temperature corresponding to the onset thermal degradation (T_{on}) and the slope of mass loss (wt%) are different for different composite membranes. The weight losses observed at 30–300°C for neat Nafion, N-pCNTs, N-oCNTs, and N-fCNTs membranes are 7.5, 4.2, 2.5, and 3.4%, respectively. This is due to the boundary water loss, and this water could not be completely removed at 100°C. The evaporation temperature of bulk water is higher due to the interaction of water molecules with the sulfonic acid groups of the Nafion resin. The second degradation stage around 380–430°C is related to the desulfonation process, and the third stage around 430–530°C is associated with the polytetrafluoroethylene (PTFE) backbone decomposition.[28–30] It is clear from TGA scans that the thermal stability of polymer matrix increases after composite formation with CNTs, however, the N-oCNT composite shows higher thermal stability up to 430°C.

Similar behavior in terms of thermal stability of polymer nanocomposites containing CNTs has been reported in the literature.[31–32] Furthermore, Marosfoi et al. [33] reported that the thermal stabilization effect of CNTs could be attributed to the increased interfacial interactions between the CNTs and polymer, which leads to an increase of the thermal degradation activation energy. In the case of N-oCNT composite membrane, because of the strong interfacial interactions between the CNT surface'-COOH' groups and Nafion polymer chains, CNTs are homogeneously dispersed in the Nafion matrix. Such homogeneous dispersion of oCNTs enhances the performance towards thermal stability by increasing the degradation activation energy and also by acting as a superior insulator and mass-transport barrier to the volatile products generated during thermal decomposition.[34, 35] On the other hand, the higher thermal stability of N-pCNTs composite in the temperature range of 430–550°C is due to the presence of pCNT, which by nature has higher thermal stability in the high temperature region compared to oCNT or fCNT, used for this study.[36]

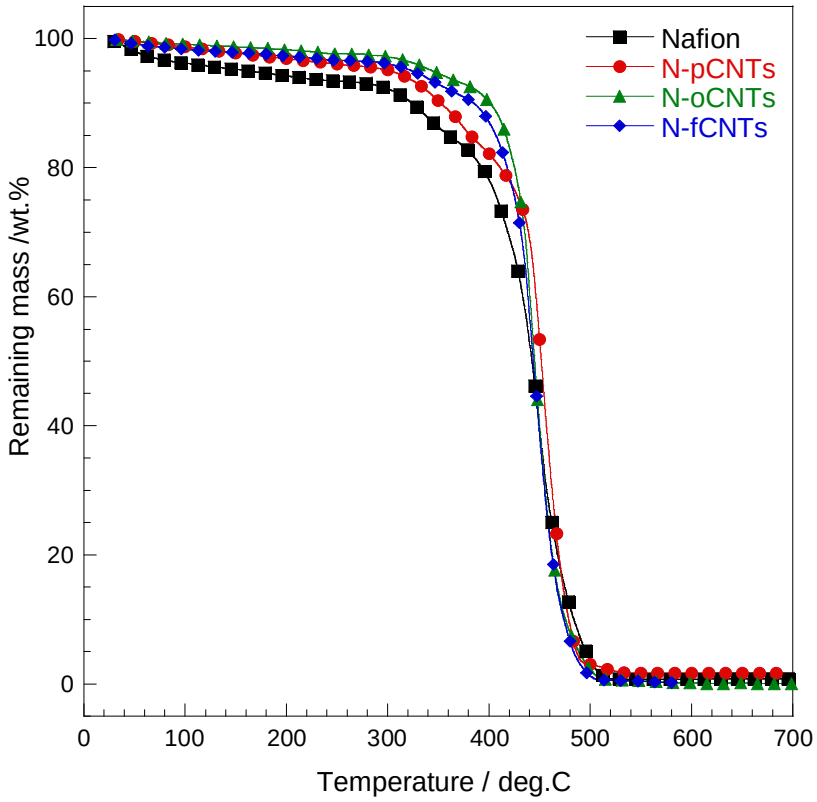

Figure 6.4 Thermogravimetric analysis scans of various samples under air atmosphere and heating rate 10°C/min.

6.3.3 Mechanical Properties

DMA results in **Figure 6.5** show the temperature dependence of tan δ curve of the neat Nafion resin and various CNT-containing composite membranes. There is only one peak observed in the temperature range examined here (25–180°C). This peak is attributed to the α-relaxation, which is close to the glass transition temperature (T_g) of the ionic clusters of the Nafion resin. [37] For neat polymer membranes the maximum tan δ or T_g peak appears at about 140°C; and when pCNTs and oCNTs were incorporated into the Nafion matrix, the T_g of Nafion matrix shifts to the higher temperature range. The highest T_g of about 160°C is observed in the case of N-oCNTs composite membrane. This confirms that the N-oCNTs composite membrane has an excellent

thermo-mechanical stability compared to other membranes. This dramatic improvement in thermo-mechanical stability is due to the homogeneous dispersion of o-CNTs into the Nafion matrix, as a result of the possible strong interaction between the COOH groups on oCNTs outer surfaces and sulfonic groups of Nafion matrix. However, in the case of N-fCNTs composite membrane, the T_g of matrix shifts to the lower temperature region, indicating poor thermo-mechanical stability that is associated with the poor dispersion of fCNTs in the Nafion matrix. Presence of HDA in the composite membrane, which acts as a plasticizer for the Nafion matrix, can be another reason for the observed T_g shift.

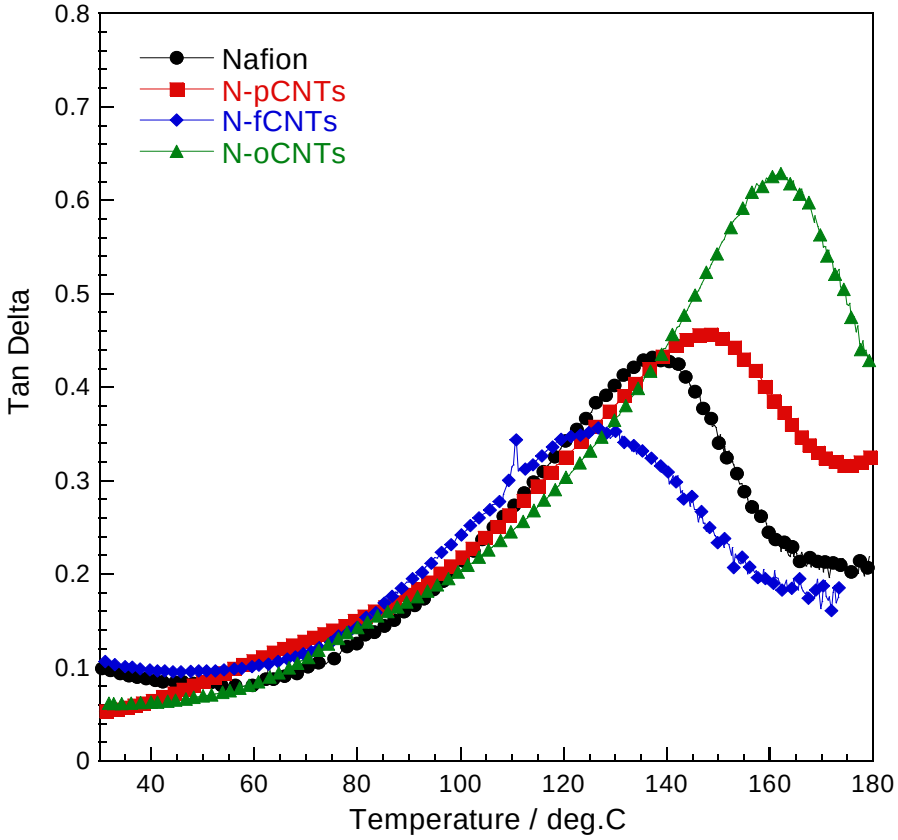

Figure 6.5 Temperature dependence of tan delta (tanδ) of neat Nafion and its CNT-containing composite membranes.

6.3.4 Bulk DC Electrical Resistivity Measurements

The DC electrical resistance of the membranes was measured using a four-point probe method. The current (I) was supplied in a range of 1 mA to 1 μA through the two outer probes and the voltage drop (V) was measured by the inner probes. The resistance changes as a function of probe spacing (0.127 cm) and is given by **Equation 3.14**. The conductivity is then calculated by **Equation 3.15.**

The resistivity and conductivity values of various membranes are presented in **Table 6.1**. The conductivities of N-pCNT and N-oCNT composite membranes are in the range of 10^{-4} S/cm, which is 1000 times higher than that of neat Nafion and N-fCNT composite membranes. This could be due to the excellent electrical properties of CNTs and not advantageous for fuel cell application because for fuel application, the DC electrical conductivity should be as low as possible.

Table 6.1 Electrical conductivity measurements of Nafion and its CNT nanocomposites

Sample	I^a /A	R^b/Ω	σ^c /S.cm^{-1}
Nafion	10 x 10^{-6}	10^{6}	10^{-7}
N-pCNTs	10 x 10^{-3}	10^{3}	10^{-4}
N-oCNTs	1.0 x 10^{-3}	10^{3}	10^{-4}
N-fCNTs	10 x 10^{-6}	10^{6}	10^{-7}

[a]Current supplied through the two outer probes; [b]resistance calculated from the voltage drop measured by inner probes and supplied current; [c]electrical conductivity range calculated using equation 3.15.

6.3.5 Proton Conductivity

In order to understand the proton conductivity of prepared composite membranes, electrochemical impedance spectroscopy (EIS) analysis was performed. The impedance plots

(Nyquist plots) and Bode plots for neat polymer and composite membranes are shown in **Figures 6.6** and **6.7**, respectively. The experimental data was fitted to the equivalent circuits R1(C[R2W]) for the neat Nafion resin, N-pCNTs and N-oCNTs composite membranes, whereas the N-fCNT composite membrane was fitted with R1(R2C) circuit. The electrolyte resistance (R1) was estimated from the fitting procedure and proton conductivity of membranes was then calculated using the **Equation 3.12**. The active length for all membranes was 3 cm. The fitting parameters and conductivity values are tabulated in **Table 6.2**.

In a Nyquist plots (Z'' vs. Z'), where Z'' = imaginary part of impedance and Z' = real part of impedance, frequencies decrease from the left to the right. The frequency range at which either the semicircle or straight line is observed depends strongly on the ionic conductivity of the material. For neat Nafion, N-pCNTs, and N-oCNT composite membranes, impedance appears as a straight line. This is called Warburg impedance, which is associated with the Warburg infinite behavior at an electrolytes interface [38] and this depends on the thickness of a material. For N-fCNTs composite membrane, a semicircular arc is observed. This is attributed to the bulk properties of mixed kinetics and diffusion control of a material. The diameter of a semicircle is about 6.5 MOhm, which is equal to the charge transfer resistance (R2). The electrolyte resistance (R1) strongly influences proton conductivity and can be obtained by extrapolation at the high frequency intercept. A slight increase in electrolyte resistance is observed when CNTs were incorporated into the Nafion matrix, indicative of a decrease in ionic conduction. However, the poorest ionic conduction is observed with N-fCNTs composite membrane. This might be due to the presence of amine functional surfactant chains on the tubes' outer surfaces that hinder the ionic conduction through the composite membranes. The poor dispersion of fCNTs in the Nafion matrix also contributes to the very low ionic conductivity of N-fCNTs containing composite membrane.

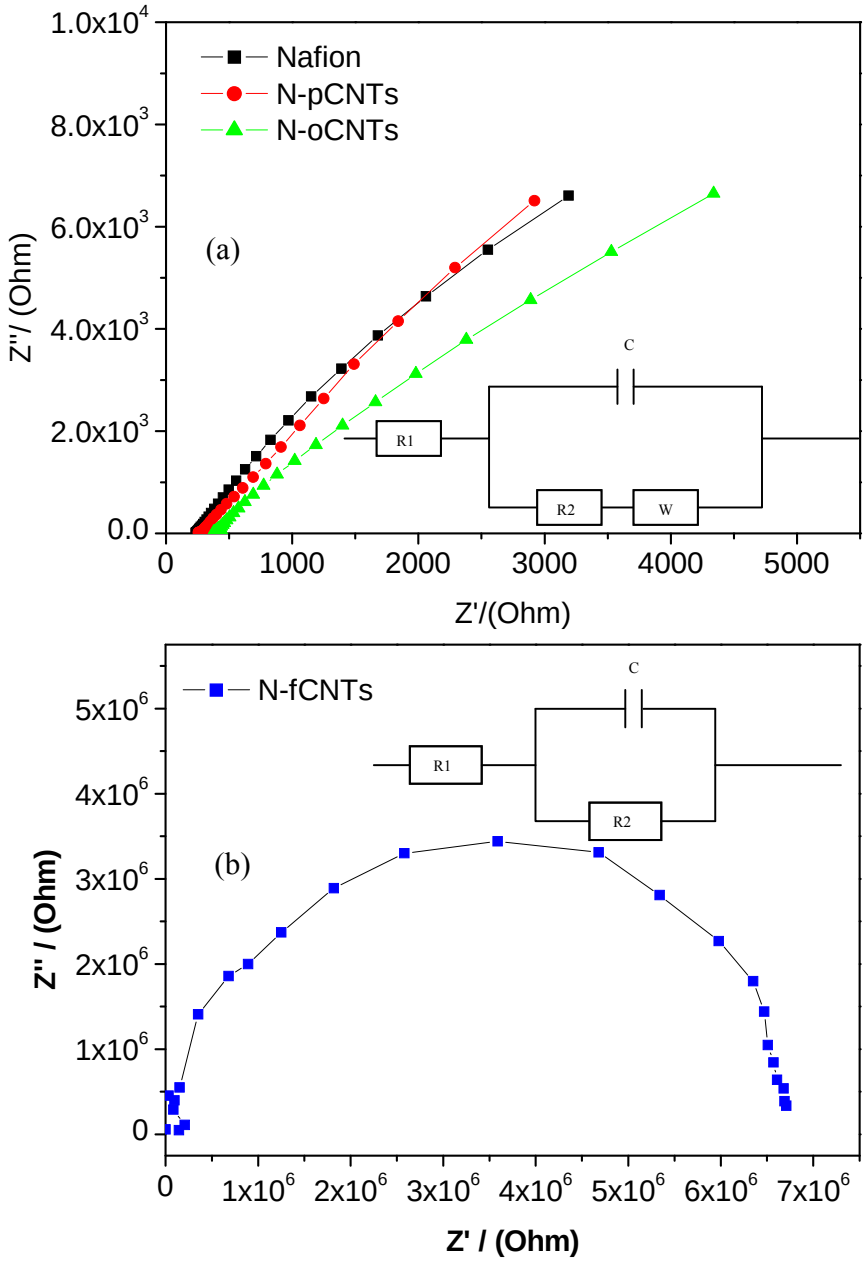

Figure 6.6 Nyquist impedance plots and their equivalent circuits for: (a) neat Nafion membrane and N-pCNT and N-oCNTs composite membranes and (b) N-fCNTs composite membranes measured at room temperature.

The same data was plotted in Bode format (see **Figure 6.7**). Bode plots were interpreted using information in Appendix B. The phase angle at lower frequencies approaches 65° for neat Nafion, N-pCNT, and N-oCNT composite membranes, whereas phase angle approaches 75° for

N-fCNT composite membrane, indicative of mixed kinetics and adsorption processes. The slope of Z vs. log f plots indicates the pseudo-capacitive behavior, which is a good indication of ionic transfer through the membranes. The water uptake in the PEM fuel cell is essential as membrane hydration, required for high proton conductivity. However, the uptake of both water and MeOH must be as low as possible to avoid the flooding and poisoning of the catalyst layer.

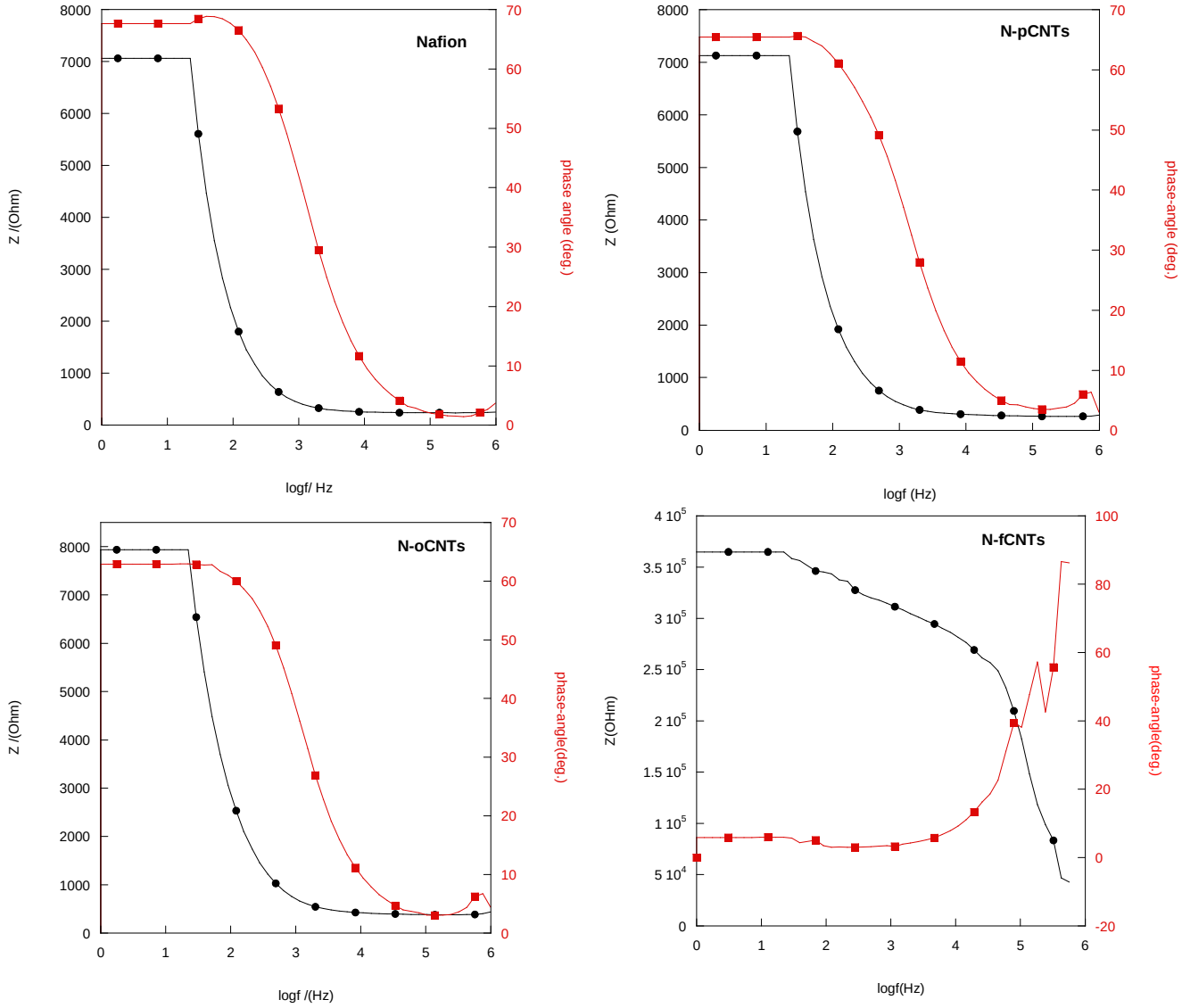

Figure 6.7 Bode plots of impedance spectra of neat Nafion and three different composite membranes. The red plot represents the phase angle and the black one represents the impedance.

Table 6.2 Parameters for circuit elements evaluated by fitting data to the equivalent circuit and calculated conductivity for prepared composite membranes. The average calculated error is about 8%.

Sample	Water/MeOH uptake /%	Slope of Z^a *vs.* log f^b	t^c /cm	σ^d /S.cm^{-1}	$(C)^e/(P)^f$
Nafion	22.0	0.3	2.0×10^{-2}	2.04×10^{-4}	7.5×10^{-2}
N-pCNTs	9.5	0.2	3.0×10^{-2}	2.45×10^{-4}	4.5×10^{-2}
N-oCNTs	6.5	0.157	2.3×10^{-2}	1.01×10^{-4}	3.8×10^{-2}
N-fCNTs	8.0	0.001	1.5×10^{-2}	3.02×10^{-5}	1.8×10^{-2}

[a]*absolute impedance;* [b]*frequency;* [c]*thickness of the membrane;* [d]*proton conductivity of nanocomposites membranes;* [e]*change in proton conductivity;* [f]*change in water/MeOH uptake measurements*

6.4 Conclusion

In summary, CNT-containing Nafion composite membranes were prepared using a melt-mixing - compression-molding process. Thermal stability of all composite membranes was improved with the addition of only 1 wt% of CNTs. The Nafion composite membrane containing 1 wt% of oCNTs shows dramatic improvement in thermo-mechanical stability compared to the neat Nafion and other composite membranes. This is due to the high level of compatibility between the oCNTs outer surfaces and the Nafion matrix. The DC electrical conductivity of the Nafion-based composites was improved when pCNTs were used as filler. The proton conductivity decreases with the incorporation of CNTs. Such observations suggest that the filler amount must be reduced to maintain a higher resistivity and increased proton conductivity. On the basis of thermal and thermo-mechanical stability and proton conductivity, the oCNT-containing Nafion composite membrane will be the best membrane for fuel cell applications. Further investigation to optimize the oCNT concentration in the Nafion matrix and therefore, next challenge is to get a membrane with a balance of all properties.

6.5 References

[1] H.-F. Cui, J.-S. Ye, W.-D. Zhang, J. Wang, and F.-S. Sheu, *J. Electroanal. Chem.* **2005**, *577*, 295–302.

[2] M. Watanabe, H. Uchida, Y. Seki, and M. Emori, *J. Electrochem. Soc.* **1996**, *143*, 3847–3851.

[3] G. Cacciola, V. Antonucci, and S. Freni, *J. Power Sources* **2001**, *100*, 67–75.

[4] R.F. Silva, S. Passerini, and A. Pozio, *Electrochim. Acta* **2005**, *50*, 2639–2646.

[5] X. Ren, P. Zelenay, S. Thomas, J. Davey, S. Gottesfeld, V. Plzak, and B. Rohland, *J. Power Sources* **2001,** *86*, 111–118.

[6] K.V. Kordesch and G.R. Simander, *Chem. Rev*. **1995**, *95*, 191–199.

[7] C. Heitner-Wirguin, *J. Membr. Sci.* **1996**, *120*, 1–15.

[8] A.V. Anantaraman and, C.L. Gardner, *J. Electroanal. Chem.* **1996**, *414*, 115A.

[9] P. Jannasch, *Curr. Opinion Colloid Interface Sci.* **2003**, *8*, 96–102.

[10] F. Barbir and S. Yazici, *Int. J. Energy Res*. **2008**, *32*, 369–374.

[11] M.F. Mathias, J. Roth, J. Fleming, and W. Lehnert, Handbook of Fuel Cells, Fundamentals, Technology and Applications, *Vol 3*, (Eds. W. Vielstich, A. Lamm, H. A. Gastegier), WILEY–5, **2003**, pp 517.

[12] M. Doyle and G. Rajendran, Handbook of Fuels Cell Fundamentals, (Eds. W. Vielstich), WILEY– 3, **2003**, pp 351.

[13] R.B. Gunn, F. Peter, and R.A. Curran, *Biophys. J.* **1971**, *11*, 559–567.

[14] M. Watanabe, Y. Seki , and M. Emori, *J. Phys. Chem.* **1998**, *B102*, 3129–3136.

[15] E. Chida, Y. Seki, L. Agihara, and M. Watanabe, *Electrochem. Soc.* **2003**, *150*, 957–962.

[16] J.M. Thomassin, C. Pagnoulle, D. Bizzari, G. Caldarella, A. Germain, and R. Jerome, *e-Polymers* **2004** , *18*, 19–25.

[17] D.H. Jung, S.Y. Cho, D.H. Peck, D.R. Shin, and J.S. Kim, *J. Power Sources,* **2003,** *128*, 215–221.

[18] Y. Deyrail, F. Mighri, M. Bousmina, and S. Kaliaguine, *Fuel Cells* **2007**, *6*, 447–453.

[19] D.H. Jung, S.Y. Cho, D.H. Peck, D.R. Shin, and J.S. Kim, *J. Power Sources* **2003**, *118*, 205–213.

[20] B. Pascal, A.B. Allen, C. Peter, and W. Andy, *J. Mater. Chem.* **2003**, *13*, 2540–2547.

[21] S. Bouatia, F. Mighri, and M. Bousmina, *Fuel Cells* **2008**, *2*, 120–127.

[22] S. Sinha Ray and M. Okamoto, *Prog. Polym. Sci.* **2003,** *28*, 1529–1536.

[23] H. Xu, K. Chen, X. Guo, J. Fang, and J. Yin, *J. Membr. Sci.* **2007**, *288*, 255–261.

[24] S. Sinha Ray, S. Vaudreuil, A. Maazouz, and M. Bousmina, *J. Nanosci. Nanotechnol.* **2006**, *6*, 2191–2198.

[25] Y.H. Liu, B. Yi, Z.G. Shao, D. Xing, and H. Zhang, *Electrochem. Solid–State Lett.* **2006**, *9*, 356–361.

[26] J.M. Thomassin, J. Kollar, G. Caldarella, A. Germain, R. Jerome, and C. Detrembleur, *J. Membr. Sci.* **2007**, *303*, 252–259.

[27] P. Mukoma, B.R. Jooste, and H.C.M. Vosloo, *J. Power Sources* **2004**, *136*, 16–23.

[28] Q. Deng, C.A. Wilkie, R.B. Moore, and K.A. Mauritz, *Polymer* **1998**, *39*, 5961–5967.

[29] F.J. Fernandez–Carretero, V. Compan, and E. Riande, *J. Power Sources* **2007**, *173*, 68–76.

[30] H.S. Park, Y.J. Kim, W.H. Hong, Y.S. Choi, and H.K. Lee, *Macromolecules* **2005**, *38*, 2289–2295.

[31] M. Zanetti, G. Camino, P. Reichert, and R. Mulhaupt, *Macromol Rapid Commun* **2001**, *22*, 176–182.

[32] Y. Tang, Y. Hu, L. Song, R. Zong, Z. Gui, and Z. Chen, *Polym Degrad Stab* **2003**, *82*, 127–135.

[33] B.B. Marosfői, A. Szabó, G. Marosi, D. Tabuani, G. Camino, and S. Pagliari, *J. Therm Anal Calorim* **2006**, *86*, 669–673.

[34] X-L. Xi, Y-W. Mai, and X-P. Zhou, *Mater. Sci. Eng.* **2005**, *R49*, 89–96.

[35] T. Kashiwagi, E. Grulke, J. Hilding, R. Harris, W. Awad, and J. Douglas, *Macromol. Rapid. Commun.* **2002**, *232*, 761–767.

[36] S.K. Pillai, S. Sinha Ray, and M. Moodley, *J. Nanosci. Nanotechnol.* **2008**, *8*, 6187–6193.

[37] F. Bauer, S. Denneler, and M. Willert-Porada, *J. Polym. Sci. Part B: Polym. Phys.* **2005**, *43*, 786–791.

[38] Y. Zhang and Y. Huang, *Solid States Ionics* **2006,** *177*, 65–74.

7

Low Methanol Permeable Nafion-Organically Modified Montmorrilonite Nanocomposite Membranes

Abstract

Montmorrilonite containing Nafion nanocomposite membranes were prepared via melt-blending at 250°C. Using the methyl tallow bis(2-hydroxylethyl) quaternary ammonium modified montmorrilonite, commercially know as Cloisite® 30B in different loadings. The effect of organoclay loading in the Nafion properties, such as methanol permeability and thermo-mechanical stability, was investigated. The organoclay-containing Nafion composite membrane exhibited improvement in thermo-mechanical properties as compared to that of neat Nafion. The ionic conductivity and methanol permeability ratio is maximized when 0.5 wt% organoclay was incorporated. This suggests an improvement in fuel cell performance.

7.1 Introduction

MMT has been commonly used to improve Nafion membrane properties.[1–15] MMT has the ability to disperse into individual layers and also their surface chemistry can be fine-tuned through ion exchange reactions.[16–25] These two characteristics make MMT more suitable for Nafion-based nanocomposite membranes since the dispersion is a crucial issue in electrolytes membranes. The main challenge in Nafion-MMT nanocomposite membranes so far, is to improve methanol permeability without compromising proton conductivity. However, MMT that is organically modified with a quaternary ammonium salt is promising to solve such a challenge. The MMT consists of stacks of negatively charged alumino-silicate layers, with positive counter ions in the interlamellar gallery (see **Scheme 7.1**). This nanofiller is then made organophilic by exchanging the native inorganic counter ions with methyl tallow bis(2-hydroxylethyl) alkyl ammonium cations forming .This is done to improve its compatibility and interactions in a polymer matrix to achieve its maximum impact on polymer properties.

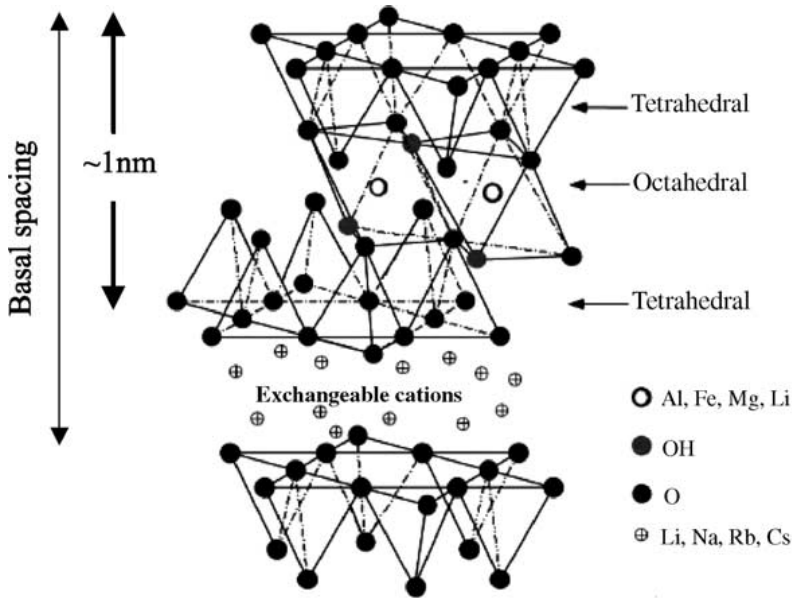

Scheme 7.1 Schematic representation of the structure of 2:1 montmorillonite, with a layer thickness of about 1 nm. The lateral dimensions of these layers may vary form 30 nm to several microns. Reproduced from Ref [25] with permission from Springer.

In 2003 Jung et al. were first to report the preparation of Nafion/MMT composite membranes by direct melt injection method.[12] They managed to decrease MeOH permeability at the expense of proton conductivity. Silva et al.[13] used the solution casting method to prepare MMT-containing Nafion membranes, and their results showed that the addition of 1 wt% MMT did not alter the ionic conductivity, but rather resulted in reduced MeOH permeability. This is an important improvement for applications in fuel cells.

The dispersion of MMT layers into Nafion is expected to improve the barrier properties of the polymer, particularly towards MeOHpermeability. This could be possible due to the high aspect ratio (length-to-width). This study aims at dispersion C30B within the Nafion matrix using the melt-mixing method to reduce methanol permeability without compromising proton conductivity of the membranes.

7.2 Experimental Details

7.2.1 Membrane Preparation

Nafion composite membranes were prepared by melt-mixing the Nafion precursor (R1100) with MMT at 250°C in a micro-extruder Reomix OS (HAAKE) instrument, at a rotor speed of 60 rpm for 10 m as shown in **Table 7.1**.

Table 7.1 Processing parameters for Nafion nanocomposites preparation

Nafion	MMT	Processing temperature /°C
99.5	0.5	250
99.0	1.0	250
98.0	2.0	250

MeOH permeability measurements were carried out using a testing device constructed in our laboratories. The polymer membranes with surface area of 12 cm^2 were inserted between vessels A and B. A 250 ml solution of MeOH (2M) was transferred to vessel A while vessel B was filled

with 250 ml of deionized water (H_2O). After 24 h, the amount of methanol that crossed through the membrane to vessel B was determined by gas chromatography (GC 17A, Shimadzu model). The gas chromatograph equipped with a capillary column (14% cyano propyl phenyl methyl poly siloxane, 30 m x 0.25 mm x 1.0 μm) and a flame ionization detector (FID). The permeability of methanol through the membrane can be expressed with diffusion coeffient, P ($cm^2.s^{-1}$) using **Equation 7.1**.[15]

$$P = \frac{kVL}{A\Delta C} \qquad (7.1)$$

where *k* is the slope of the concentration profile (mol/cm^3s), *V* is the volume of a solution in compartment (cm^3), *L* is thickness of the membrane (cm), *A* is the active surface area of the membrane (cm^2) and ΔC is the difference of methanol concentration between two compartments (mol/cm^3).

7.3 Results and Discussions

7.3.1 Morphology

Figure 7.1 shows the high-resolution optical micrographs of Nafion nanocomposite films with different C30B contents. The highly anisotropic black spots in **Figure 7.1 a-c** are attributed to MMT particles dispersed in Nafion. The micrographs show the even distribution of C30B when 0.5 and 2 wt% were incorporated. This dispersion impacts anisotropic properties to the polymer matrix, which should improve barrier properties. This suggests that the hydroxyl groups available in the interlamellar space of C30B interact favorably with Nafion. This contributes to the polymer penetrating the clay galleries and the delaminating of the alumino-silicate stacks by the shearing forces during melt blending. However, large alumino-silicate stacks are observed with the 1 wt% C30B-containing nanocomposites. This suggests that polymer chains could not penetrate the clay galleries properly.

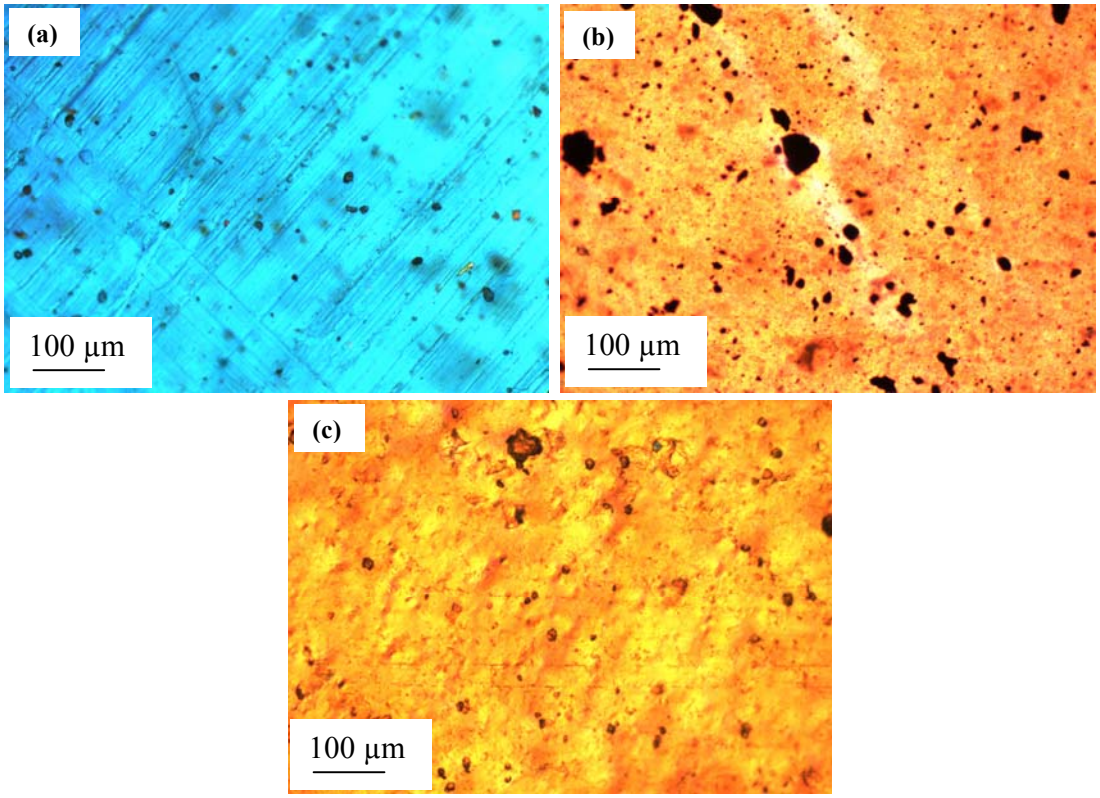

Figure 7.1 Optical miscropcopy images of Nafion nanocomposite films with different C30B loadings: (a) 0.5 wt%, (b) 1.0 wt%, and (c) 2.0 wt%.

7.3.2 FT-IR Spectral Analyses

FT-IR spectra shown in **Figure 7.2** of C30B showed absorption bands at 1065 cm^{-1} and 520 cm^{-1}. These are attributed to water in the interlays, hydroxyl bending of adsorbed water, and bending of Si–O–Si and Si–O–Al. Nafion showed adsorption bands at 600, 950, 1150–1200 cm^{-1} and these are ascribed to CF–CF_2 and SO_2–O stretching, respectively.[15–16] FTIR spectra showed that the incorporation of C30B, in different proportions into Nafion leads to a decrease in the intensity of the bands (OCF–CF_2 and CF_2–S_2–O). This suggests that side chains of Nafion resin may be involved in the interactions with C30B. However, the position of Nafion bands remains unchanged. This indicates that the molecular motions of the OCF_2 and SCF_2 are considerably restricted, probably due to the interactions with C30B. This is consistent with previous observations.[17–19]

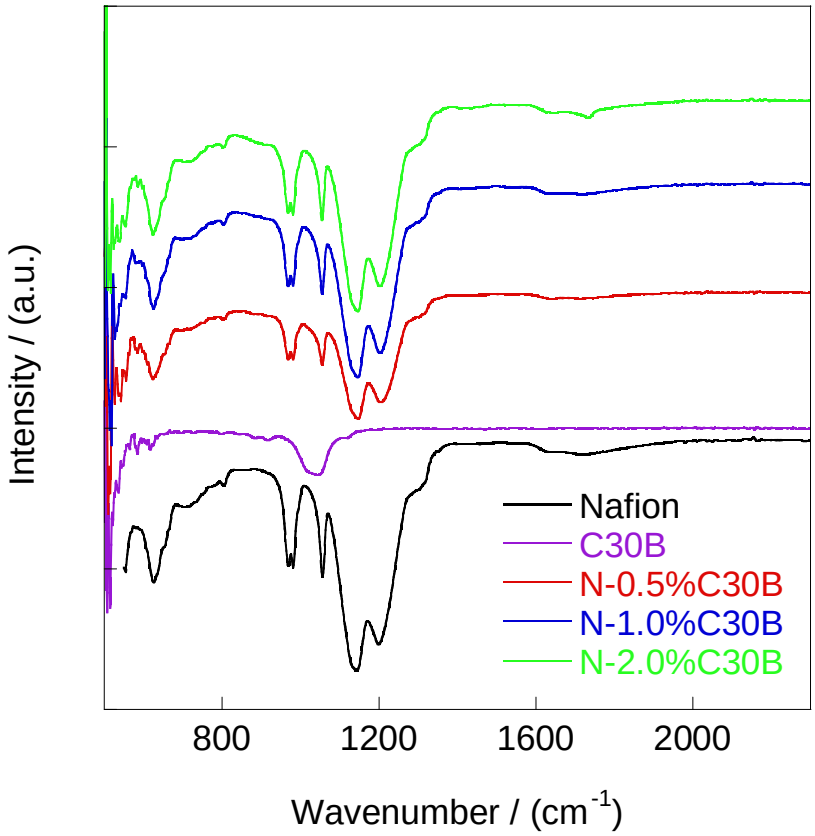

Figure 7.2 Fourier transform Infrared spectra of Nafion, C30B and Nafion nanocomposite films with different loading of C30B.

7.3.3 XRD Patterns

Figure 7.3 shows the XRD patterns of the Nafion resin and corresponding nanocomposites containing various contents of C30B in the 2θ range 5–70°. The membranes show the main peak at 18°, and this is related to the hexagonal structure of Nafion. The broad peak around 40° is associated with the fluorocarbon chains of Nafion, and it highlights the poor crystallinity of Nafion matrix.[20–22] The *d*-spacing values of Nafion and its nanocomposite membranes are calculated and summarized on **Table 7.2**. The average interlayer spacing for Nafion, 0.5 wt% and 1 wt% nanocomposites obtained from XRD measurements is 0.5 nm (2θ = 16°). The peaks shifted towards higher angles after incorporation of C30B. This suggests a decrease in d-spacing

with an increase in C30B content. The change in the crystallinity or crystal structure may improve the properties of Nafion.

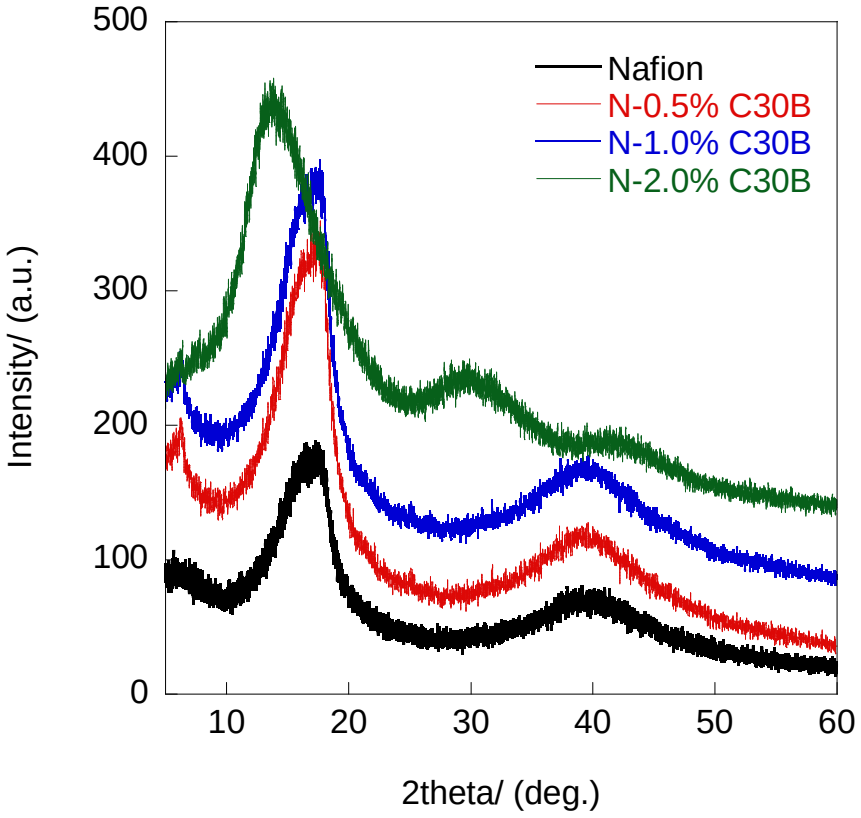

Figure 7.3 X-ray diffraction patterns of Nafion and its C30B composites with different C30B loadings: 0.5wt%, 1 wt%, and 2 wt%.

Table 7.2 Interlayer distances of Nafion and various Nafion-C30B nanocomposite membranes.

Samples	**Interlayer distance *d* /nm**
Nafion	0.50
N-0.5 wt% C30B	0.48
N-1.0 wt% C30B	0.48
N-2.0 wt% C30B	0.55

7.3.4 Thermal Stability

The thermal stability of Nafion resin and its C30B-containing nanocomposite films was investigated by TGA. Nafion showed weight loss of about 5% between 25–150°C whereas the Nafion-C30B nanocomposite showed about 2.5% weight loss. This weight loss is due to the loss of physically adsorbed water. Between 150–350°C, Nafion showed a weight loss of 5% whereas N-C30B nanocomposite showed weight loss of about 7.5% (see **Fig. 7.4**). This is attributed to the loss of SO_2 and CO_2 gases as a result of Nafion decomposition.[23] The last degradation stage between 350–500°C is attributed to the further loss of SO_2, CO_2, and the release of SF_4, CO, CF, and CF_2 from the backbone of Nafion.[24] It is observed that the weight loss associated with backbone of Nafion is moderate for nanocomposite compared to Nafion resin.

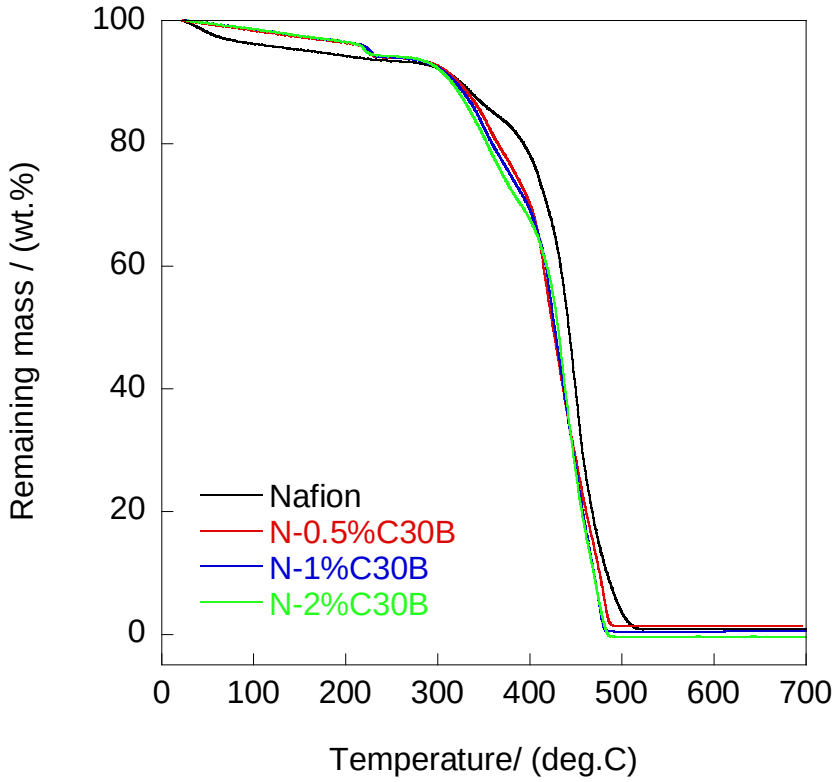

Figure 7.4 Thermogravimetric analysis scans of Nafion and its C30B-based composites with different C30B loadings: 0.5 wt%, 1 wt%, and 2 wt%, measured in air at 5°C/min.

7.3.5 Mechanical Properties

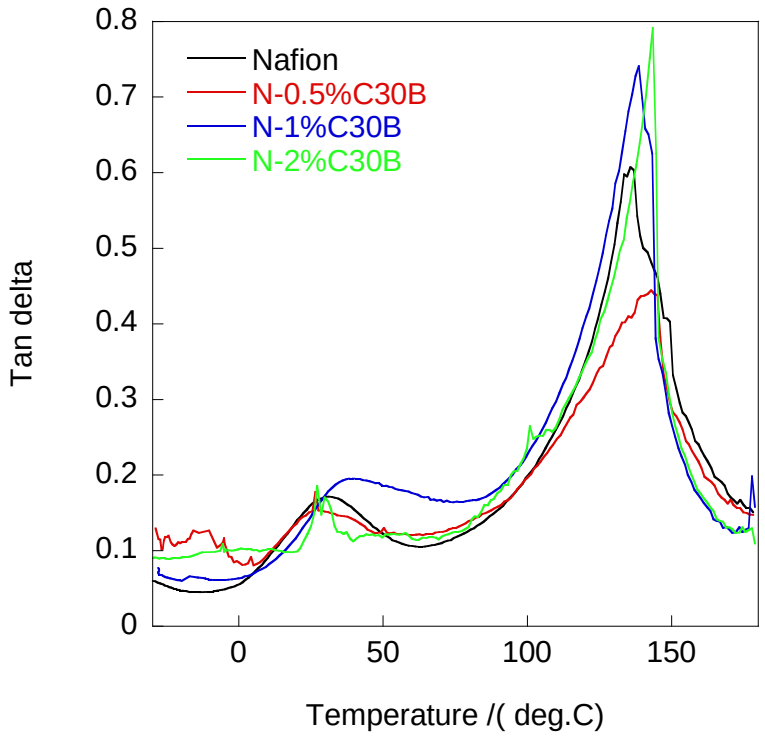

Figure 7.5 The temperature dependence of tan delta (tan δ) of neat Nafion and its C30B-containing nanocomposite membranes with different C30B loading.

DMA results in **Figure 7.5** show the temperature dependence of tan δ curve of the neat Nafion resin and C30B-containing composite membranes, with different C30B loadings. There are two peaks observed in the temperature range examined from –30 to 180°C. The first peak (30°C) is attributed to the transitions between SO_2 and CF groups of Nafion. The second peak at about 140°C is assigned to the α-relaxation, which is close to the glass transition temperature (T_g) of the ionic clusters of Nafion resin. [24] The higher the T_g of the material, the better their thermo-mechanical stability. For neat Nafion membrane the maximum tan δ or T_g peak appears at about 140°C. However, when C30B was incorporated into the Nafion matrix, the T_g of Nafion matrix shifts to the higher temperature range. The highest T_g of about 150°C is observed in the case of N-2 wt% C30B composite membrane. This confirms that N-2 wt% C30B composite membrane

has an excellent thermo-mechanical stability compared to other membranes. This dramatic improvement in mechanical stability is due to the good dispersion of 2 wt% C30B into Nafion matrix observed by optical microscopy. The results showed that as the amount of C30B is increased within Nafion, T_g also increases. This indicates an improvement in mechanical stability. This suggests a possible strong interaction between the ammonium salt used to modify MMT and sulphonic groups of Nafion matrix.

7.3.6 Electrical Conductivity and Water Uptake of the Membranes

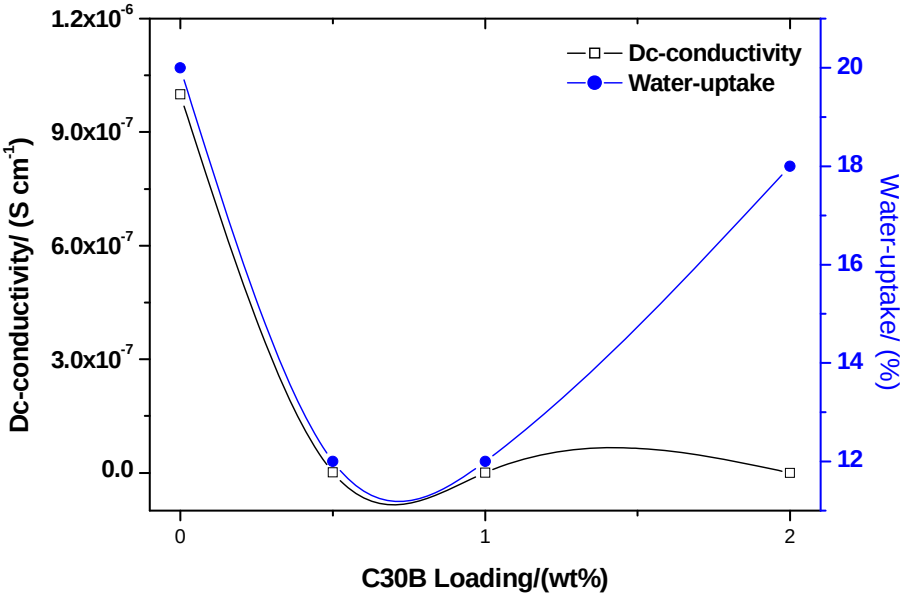

Figure 7.6 Electrical conductivity and water uptake measurements of Nafion and nanocomposite membranes with different C30B loadings**.**

Figure 7.6 shows the relationship between both water uptake and electrical conductivity versus the weight fraction of C30B in the nanocomposite membranes. The water uptake of N-0.5 wt% C30B and N-1 wt% C30B nanocomposite membranes decrease to about 12% compared to 20% of neat Nafion. However, water uptake of N-2 wt% C30B slightly increases to about 18%. This might be due to the surface modification of MMT with a quaternary ammonium salt. [25–26] These results suggest that water uptake is dependent on the amount of C30B dispersed in Nafion. As

shown in **Figure 7.6**, the bulk electrical conductivity decreased to zero after incorporation of C30B in Nafion. The electrical conductivity remains zero independent of the C30B amount. This is a good beneficial effect for the fuel cell application as short-circuiting will not be possible and such results have never been reported before. Nanocomposite preparation methods and dispersions play a huge role in these observations.

7.3.7 Proton Conductivity and Methanol Permeability

Table 7.3 shows the methanol permeability and proton conductivity of neat Nafion and Nafion nanocomposite membranes with different C30B loadings. The methanol permeability of neat Nafion is higher, with a value of 2 x 10^{-8} $cm^2.s^{-1}$, than that of Nafion-C30B nanocomposite membranes (1 x 10^{-8} $cm^2.s^{-1}$). This suggests that methanol permeability can be controlled by the addition of C30B to Nafion. On the other hand, proton conductivity decreased with the incorporation of C30B. This is associated with the lower water uptake of the nanocomposite membranes. This suggests that C30B modified membranes allow selective permeability of water molecules or hydrogen ions. The lowest decrease is observed with N-0.5 wt% C30B. This might be caused by the poor cohesion of 0.5 wt% C30B into Nafion.

Table 7.3 Comparison of proton conductivity (C) and methanol permeability (P) of neat Nafion resin and Nafion-C30B nanocomposite membranes, with different C30B wt% loadings measured at 25°C and 100% humidity.

Samples	**C /S.cm^{-1}**	**P /cm^2.s^{-1}**	**C/P /S.cm^{-3}**
Nafion	70 x10^{-6}	2x10^{-8}	4x10^3
0.5 C30B	4.5 x10^{-6}	1x10^{-8}	5x10^2
1.0 C30B	15 x10^{-6}	1x10^{-8}	2x10^3
2.0 C30B	30 x10^{-6}	1x10^{-8}	3x10^3

It can be seen from **Table 7.3** that a decrease in proton conductivity is minor compared to a decrease in methanol permeability. The methanol permeability of the nanocomposites is independent of the amount of C30B. However, the proton conductivity is affected by the amount of C30B incorporated into Nafion. As the amount of C30B in Nafion increases, the proton conductivity slightly increases. This also depends on the dispersion of C30B in Nafion matrix.

7.4 Conclusion

Dispersion of various C30B amounts into Nafion varied with poorest dispersion observed with 1 wt% of C30B. The variation of C30B loading resulted in an increase in crystallinity as shown in XRD peaks. Thermal stability and mechanical properties of Nafion were improved by dispersing C30B within matrix. The modification of Nafion membrane with C30B resulted in the reduction of MeOH permeability and was found to be independent of the C30B loading. A slight decrease in proton conductivity was observed. N-0.5 wt% C30B shows a higher ratio of proton conductivity: methanol permeability (C:P), which is indicative of higher fuel cell performance. The electrical conductivity remained zero regardless of the C30B amount. This is a good beneficial effect for fuel cell applications.

7.5 References

[1] J.C. Tsai, J.F. Kuo, and C.Y. Chen, *J. Power Sources* **2003**, *174*, 103–113.

[2] A. D'Epifanio, B. Mecheri, E. Fabbri, A. Rainer, E. Traversa, and S. Licoccia, *J. Electrochem. Soc*. **2007**, *154*, B1148–B1151.

[3] J. Sauk, J. Byun, Y. Kang, and H. Kim, Korean *J. Chem. Eng.* **2005**, *22*, 605–610.

[4] H.K. Kim and H. Chang, *J. Membr. Sci.* **2007**, *288*, 188–194.

[5] N.M. Benetatos, C.D. Chan, and K.I. Winey, *Macromolecules* **2007**, *40*, 1081–1088.

[6] N.W. DeLuca and Y.A. Aladb, *J. Membr. Sci*. **2006**, *282*, 217–224.

[7] H.C. Chen, JD. Snyder, and Y.A. Elabd, *Macromolecules* **2008**, *41*, 128–135.

[8] H. Ohya, K. Matsumoto, Y. Negishi, T. Hino, and H.S. Choi, *J. Membr. Sci*. **1992**, *68*, 141–148.

[9] J.G. Liu, T.S. Zhao, Z.X. Liang, and R. Chen, *J. Power Sources* **2006**, *153*, 61–67

[10] M.A. Navarra, S. Materazzi, S. Panero, and B. Scrosati, *J. Electrochem. Soc.* **2003**, *150*, A1521–A1532.

[11] P. Dimitrova, K. A. Friedrich, U. Stimming, and B. Vogt, *Solid State Ionics* **2002**, *150*, 115–22.

[12] D. H. Jung, S. Y. Cho, D. H. Peck, D. R. Shin, and J. S. Kim, *J. Power Sources* **2003**, *118*, 205–211.

[13] R.F. Silva, S. Passerini, and A. Pozio, *Electrochim. Acta.* **2005**, *50*, 2639–2645.

[14] W.S. li, D.S. lu, J.L. luo, and K.T. Chuang, *J. Power Sources* **2005**, *145*, 376–438.

[15] J. James, T.Z. McMaster, J.M. Newton, and M.J. Miles, *Polymer* **2000**, *41*, 4223–4234.

[16] M. Ludvigsson, J. Lindgren, and J. Tegenfeldt, *Electrochim. Acta* **2000**, *43*, 2267–2272.

[17] S. Banerjee, and D.E. Curtin, *J. Fluor.Chem.* **2004**, *125*, 1211–1216.

[18] L. Zhang, J. Xu, G. Hou, H. Tang, and F. Deng, *J. Colloid Interface Sci.* **2007**, *311*, 38–44.

[19] S.K. Young, W.L. Jarret, and K.A. Mauritz, *Polymer* **2002**, *43*, 2311–2325.

[20] K.A. Mauritz and T.J. Payne, *J. Membr. Sci.* **2000**, *168*, 39–45.

[21] M. Fujimura, T. Hashimoto, and H. Kawai, *Macromolecules* **1981**, *14*, 1309–1315

[22] P. Staiti, A.S. Arico, V. Bablio, F. Lufrano, E. Passalacqua, and V. Antonucci, *Solid State Ionics*, **2001**, *145*, 101–107.

[23] Y.S. Park and Y. Yamazaki, *Euro. Polym. J.* **2006,** *42*, 375–387.

[24] T.-H. Yang, Y.-G. Yoo, C.-S. Kim, S.-H. Kwak, and K.-H. Yoo, *J. Power Sources* **2002**, *106*, 328–337.

[25] S. Sinha Ray and M. Okamoto, *Prog. Polym. Sci*. **2003**, *28*, 1539–1550.

[26] C.A. Wilkie, J.R. Thomsen, and M.L. Mittleman, *J. Appl. Polym. Sci*. 1991, *42*, 901–912.

8

Nafion-Titania Nanotubes Nanocomposite Electrolytes for High Temperature Direct Methanol Fuel Cells

Abstract

Nafion-based nanocomposite membranes containing various amounts of titania nanotubes as an inorganic filler have been prepared using melt-mixing method and have been investigated for proton exchange membrane applications. The one-dimensional nanotubes have been prepared with potassium hydroxide using a hydrothermal route and conventional heating. Nafion R1100 in a protonated form was used and nanotubes contents were in a range of 0.5–2.0 wt%. The acid treated composite membranes, at the lowest inorganic additive content, exhibited improved properties in terms of thermal stability and MeOH permeability. The best performing nanocomposite was the membrane containing only 0.5 wt% TNTs showing ionic conductivity value of 7.2×10^{-2} S.cm^{-1} at 26°C and 100% of relative humidity.

8.1 Introduction

Currently, titanium dioxide or titania derived nanotubes (TNTs) are examined with respect to their possible prominent applications such as catalyst supports,[1] photocatalysts,[2] gas sensing elements,[3] and anode materials for batteries.[4] Titanium dioxide supported noble metal catalysts, such as gold,[5] silver[6] or platinum,[7] are effective in many important processes, such as selective oxidation and hydrogenation, automobile engine exhaust systems,[8] etc.

The principal advantages of the nanotubular form seem to be related to their high specific surface area, which allows diffusion of active species. The crystal structure of TNTs seems to be a derivative for many photo-catalytic applications. Another property is that TNTs are often open-ended and accessible for the interaction with gaseous substances. TNTs are also thermally stable up to 600°C.[6–9] These are some of the essential criteria for fuel cell electrolytes membranes. This promotes the study of the Nafion-TNT nanocomposite membranes behavior.

Nafion, whose primary structure consists of acid-tipped side chains dangling from a perfluorinated backbone, is expected to be compatible with TNTs, due to its reactive nature. Because of the strong interaction between positively charged ions and C=C bonds, the metal ions present in TNTs, such as K^+, is expected to increase thermal stability of the Nafion membrane. The resistance of TNTs in the presence of H_2 is likely to improve swelling and mechanical properties of Nafion membranes at higher temperatures greater than 100°C. Therefore, to understand the effect of the interactions between Nafion and TNTs on the proton exchange membrane properties, further investigations were carried out. In this study, the effects of TNTs on Nafion properties, such as water uptake, thermal stability, methanol (MeOH) permeability and ion conductivity, were investigated. The nanocomposite membranes were prepared using the melt-extrusion method by varying the nanofiller loadings. The mechanical, thermal properties and ionic conductivity of membranes were investigated using DMA, TGA, and EIS. Vibrational studies were carried out by FT-IR spectroscopy, providing information on the nanofiller-Nafion, nanofiller-H_2O, Nafion-H_2O interactions and also the conformation of fluorocarbon chains of Nafion hydrophobic domains. Methanol permeability was also investigated using gas chromatography.

8.2 Experimental

8.2.1 Membrane Preparation

Recently Sikhwivhilu et al.[9] reported the synthesis of self-organized TNTs using a hydrothermal conventional heating method. The TNTs were annealed at 300°C for 12 h and used as filler. Nafion nanocomposite membranes were prepared by melt-mixing the Nafion precursor (R1100) with TNT nanotubes at 250°C in a micro-extruder Reomix OS (HAAKE) instrument, at a rotor speed of 60 rpm for 10 m. The TNT amount was varied from 0.5 to 2.0 wt%.

8.3 Results and Discussions

8.3.1 Structure, Morphology and Thermal Stability of TNTs

Figure 8.1 shows the surface morphology of self-organized TNT structures, annealed at 300°C. The SEM images show that TNTs are tangled together forming bundles. The wide-angle X-ray diffraction patterns of TNTs are shown in **Figure 8.2**. Diffraction patterns of TNTs show sharp peaks at about 25, 38, 48 and 55°, representing both anatase and rutile phases of titania in the sample. A detailed study of these TNT structures showed that crystalline TNTs have BET surface area of 263 m^2/g and pore volume of 0.84 cm^3/g. [9] TEM also showed that these TNTs have an average diameter of 10 nm. TGA of TNTs in **Figure 8.3** shows that TNTs had a weight loss of about 18% at temperatures ranging from 25–300°C. This decomposition is attributed to the loss of adsorbed water within TNTs. This suggests that TNTs have the ability to adsorb more water even after annealing at 300°C. TNTs are thermally stable after 300°C.

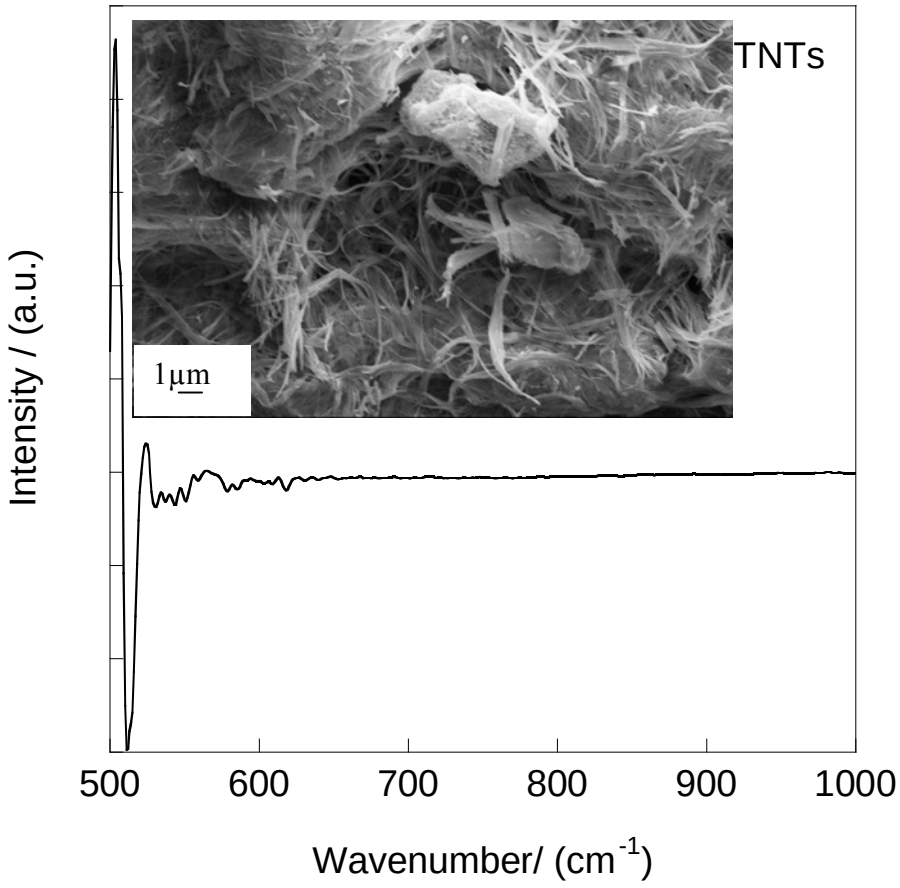

Figure 8.1 The scanning electron microscopy images and FT-IR spectra of titanium dioxide nanotubes synthesized using hydrothermal conventional heating method at 150 °C and annealed at 300 °C.

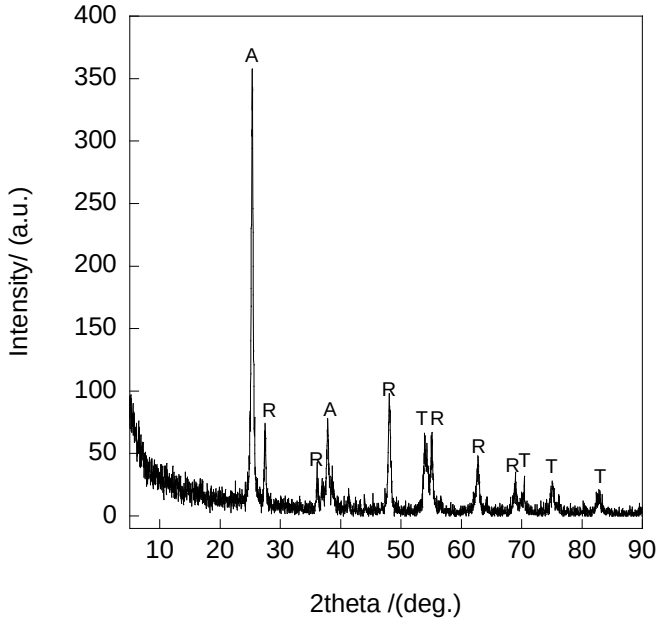

Figure 8.2 X-ray diffraction patterns of titanium dioxide nanotubes synthesized using hydrothermal conventional heating method at 150°C and annealed at 300°C in oxygen ambient. A, R, and T represent the reflections from anatase crystallites, rutile crystallites and the titanate, respectively.

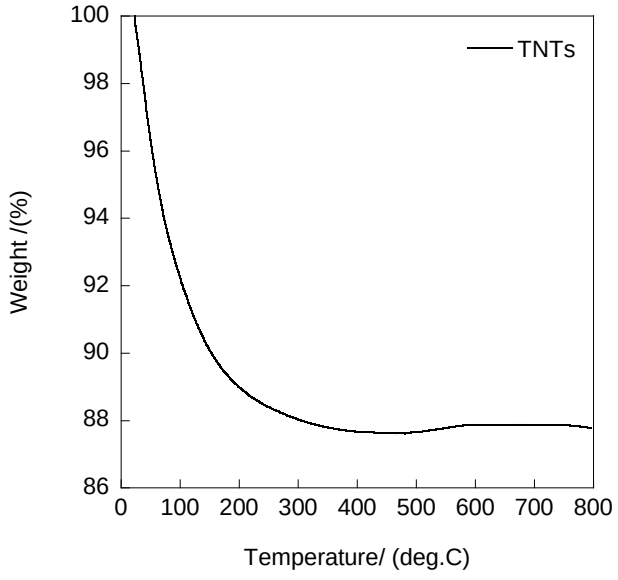

Figure 8.3 The thermogravimetric analysis scans of titanium dioxide nanotubes synthesized using hydrothermal conventional heating procedure at 150°C and annealed at 300°C in oxygen ambient.

8.3.2 Structural Properties of Nanocomposite Membranes

To study the interaction between sulphonic acid groups of Nafion and TNTs, composite films were characterized with FT-IR. The FT-IR spectra showing vibration bands of neat Nafion, CF-CF2 (600–950 cm^{-1}), SO_2–O (1200–1400 cm^{-1}) is shown in **Figure 8.4**.[10] After the incorporation of 0.5 and 1.0 wt% of TNTs into Nafion, additional bands are observed. These additional bands, approximately at 800 cm^{-1} and 1500 cm^{-1}, are attributed to the vibrations between S–O and Ti–O groups. However, the positions of Nafion bands remain unchanged. The 2 wt% of TNTs shows similar bands as Nafion. This suggests that as the amount of TNT nanotubes increases within Nafion, the interaction becomes weaker.

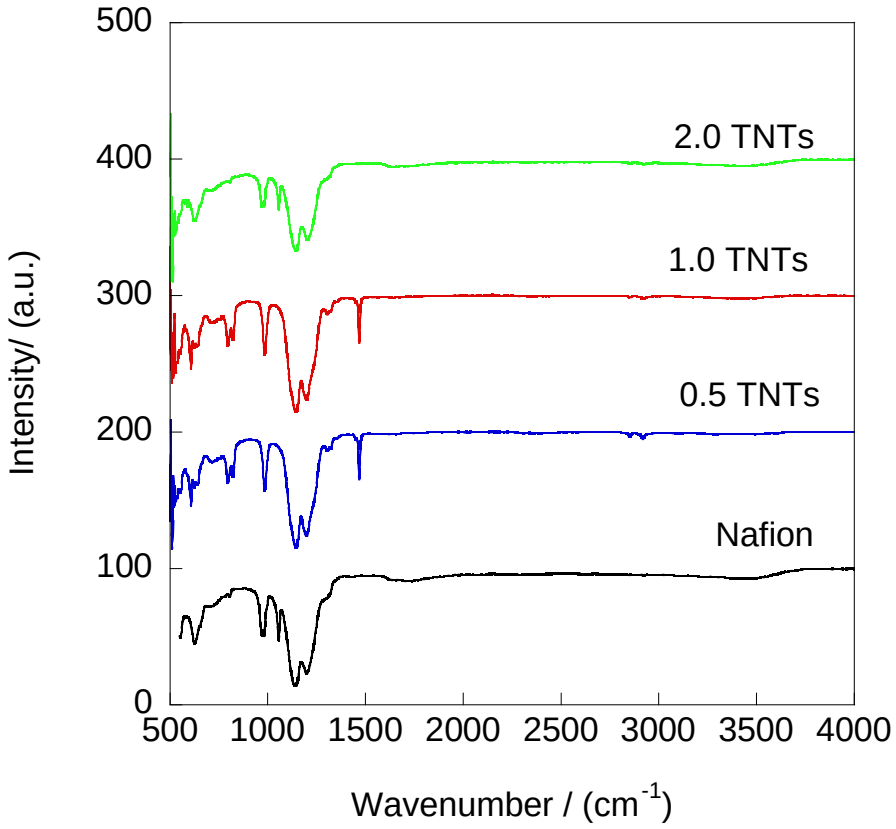

Figure 8.4 Fourier transform Infred spectra of Nafion and its TNT-based nanocomposite membranes with different TNT loadings in wt% taken from 500 to 4000 cm^{-1}.

XRD patterns of Nafion, and TNT-modified Nafion membranes, with different TNT loadings are shown in **Figure 8.5**. Nafion in the protonated form is considerably crystalline. In the wide angle, a diffraction pattern of Nafion R1100 usually shows two reflection peaks. The peaks at about 16° (100) and 40° (101) are attributed to the crystalline perfluorinated backbone (–CF2–CF2–) of Nafion.[11] The peaks from anatase and rutile phase of TNTs are dominant in the nanocomposite membranes. The Nafion peaks (100) and (101) shifted to lower angles after the TNT modification. The intensity of the peaks is also reduced, and this is attributed to the interaction of TNTs with CF_2-CF groups of Nafion and reduced crystallinity.

The XRD patterns of nanocomposite showed the peak ascribed to a basal (200) d-spacing or interlayer distance. This is due to the present of intercalated compound. It is also worth noticing that the XRD peak for nanocomposite membranes is observed at lower 2theta angles compared to that of TNTs and neat Nafion. This suggests that the interlayer distance among TNTs has expanded, as a possible consequence of polymer intercalation.[12] This also indicates electrostatic interaction forces between polymer and inorganic filler. In this case, this indicates the electrostatic interaction among the polar polymeric groups of Nafion (acid moieties and carbonyl functions) and negatively charged titania nanotubes. This is also expected to affect the adhesion of the filler to the polymeric matrix. The greater the chemical affinity, as in the polar polymer chains and charged TNTs, the larger the polymer-filler adhesion and the interfacial interaction [12–13].

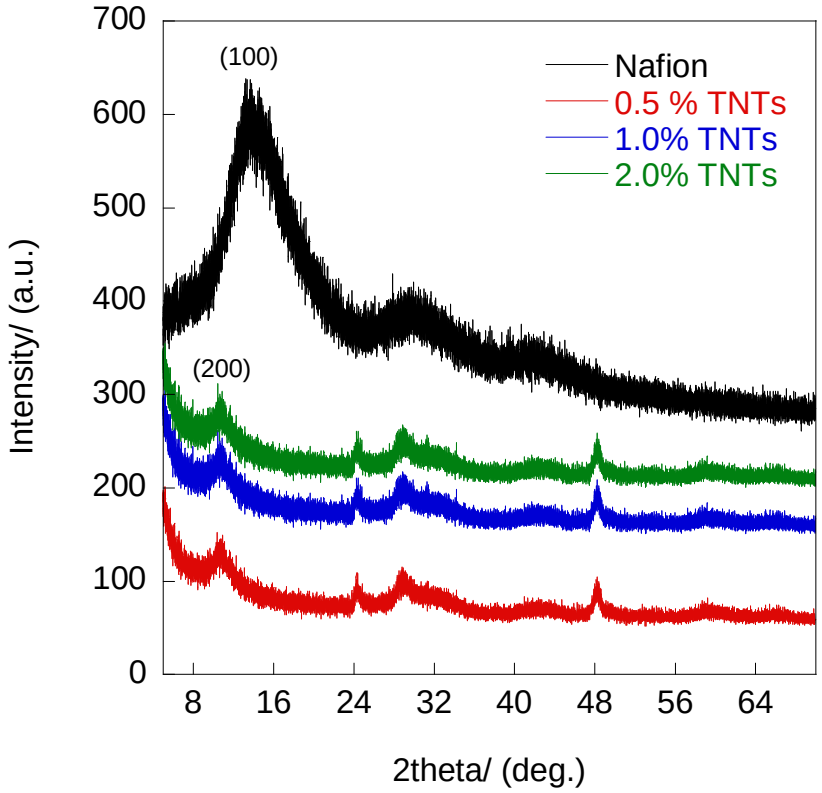

Figure 8.5 X-ray diffraction patterns of Nafion, TNTs, and its TNT-based nanocomposite membranes with different TNT loadings.

8.3.3 Morphology

Since dense morphology is an essential requirement for polymer electrolytes, a SEM investigation was performed on the nanocomposite membranes. **Figure 8.6** show freeze fractured surface of the nanocomposite membranes containing various amounts of TNTs in wt% (a) 0.5, (b) 1 and (c) 2. The micrographs show the presence of inorganic structures, homogeneously dispersed into polymer matrix. This indicates the presence of bundle TNTs into a Nafion matrix. SEM images show similar dispersion for all TNTs loadings. This is in agreement with XRD results, demonstrating that TNTs nanocomposite had the same *d*-spacing independent of TNT loadings. This good dispersion suggests that the number of accessible sites on the surface of TNTs is high contributing to the adhesion and electrostatic interaction.

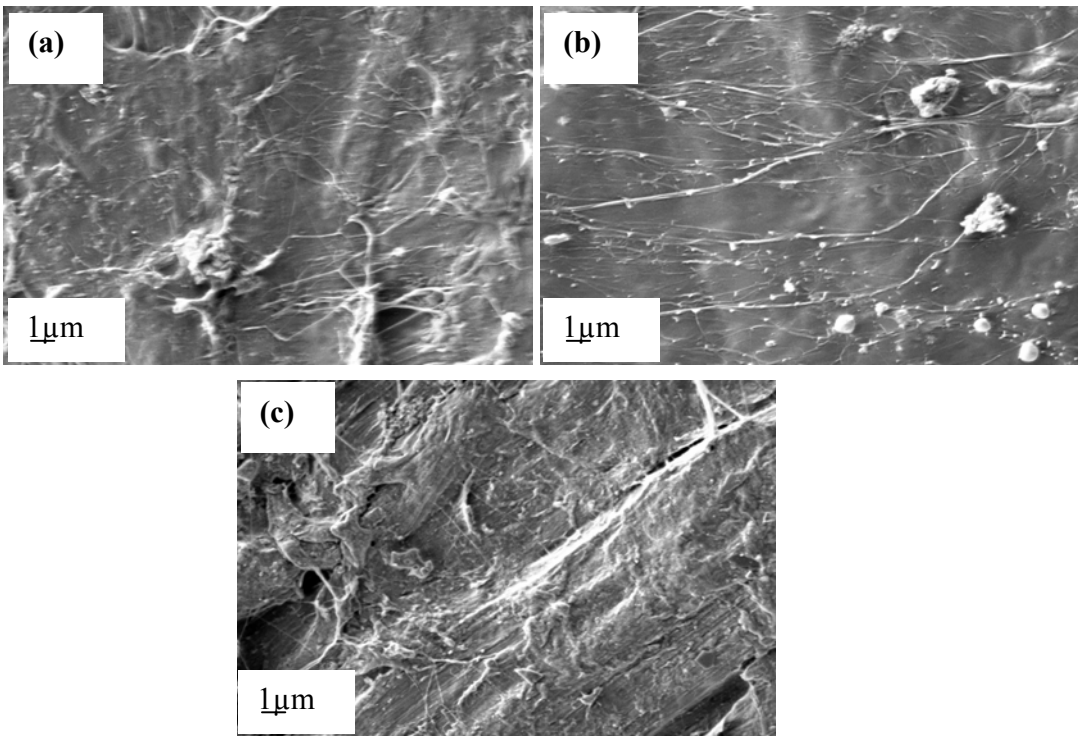

Figure 8.6 The scanning electron microscopy images of the nanocomposite membranes containing various amounts of TNTs in wt%: (a) 0.5, (b) 1, and (c) 2.

8.3.5 Water Uptake and Electrical Conductivity

The water uptake increases from 19% for neat Nafion to a maximum of 22% for 1.0 wt% TNT composite as shown in **Figure 8.7**. The water uptake of N-0.5 wt% TNTs and N-2 wt% TNTs remains at about 20%. The increase in water uptake with the addition of TNTs suggests an increase in the hydrophilic nature of Nafion. Different loadings of TNTs influence the water uptake of the Nafion membrane. This is due to the water loving nature of TNTs observed in TGA results.

The bulk electrical conductivity of Nafion and its TNT-based nanocomposite membranes is shown in **Figure 8.7**. The electrical conductivity of Nafion increases from 0 to 0.06 $S.cm^{-1}$,

when modified with 0.5 wt% of TNTs, it further increases to about 0.08 $S.cm^{-1}$, with 1.0 wt% incorporation. As the amount of TNTs into Nafion matrix increases to 2 wt%, the electrical conductivity decreases to zero that is the same as that of neat Nafion. This decrease is associated with the electrical percolation threshold of Nafion and also the poor interaction between Nafion and TNTs as observed in FTIR spectra for 2 wt%.

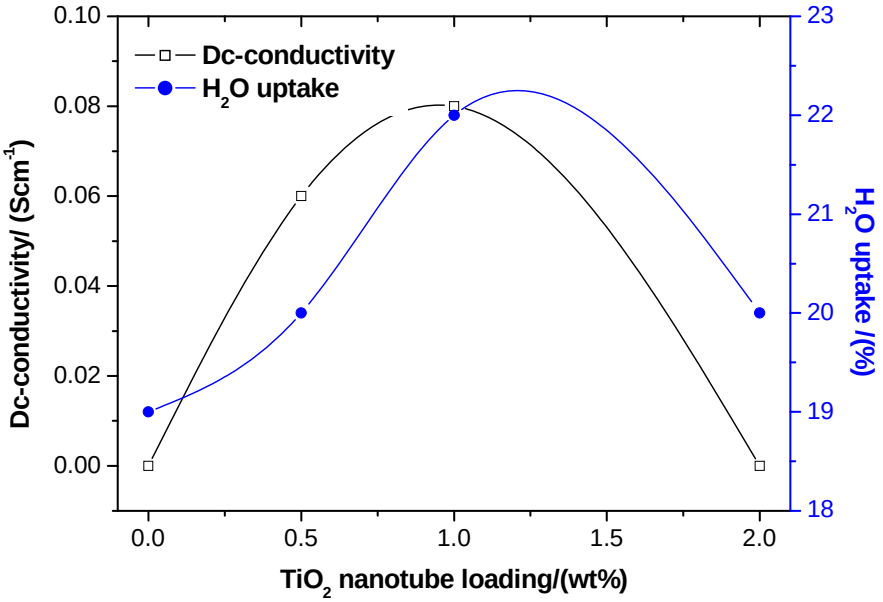

Figure 8.7 The bulk electrical conductivity and water uptake plots of Nafion, and its TNT-based nanocomposite membranes containing various amounts of TNTs.

8.3.6 Thermal Stability

TGA scans of Nafion and its TNT-based nanocomposite membranes are shown in **Figure 8.8**. Thermal degradation profiles of the samples are similar and show that the membranes are thermally stable up to 160°C. The first degradation stage in a range of 30–120°C is assigned to the decomposition of physically adsorbed water present in the membranes. The weight loss in the range of 250–400°C is associated with the degradation of $–SO_3H$ groups and polyether side chains of Nafion.[11–14] A slight increase in thermal stability of Nafion was observed after incorporating TNTs. This increase in thermal stability is due to the presence of TiO_2 nano-structures in Nafion. The weight loss observed in the range of 400–480°C is associated with the

thermal degradation of fluorocarbon chains of PTFE (polytetrafluoroethelyne) backbone of Nafion.[11–16] The results show that 0.5 and 2.0 wt% of TNTs increase thermal stability of $–SO_3H$ groups and polyether side chains, but decreases the thermal stability of the PTFE backbone. Whereas, 1.0 wt% of TNTs has the opposite effect, which is attributed to the poor interaction between Nafion and 2 wt% TNTs observed in FTIR results.

8.3.7 Proton Conductivity and MeOH Permeability

To evaluate the influence of TNTs on the membranes electrochemical behavior, electrochemical impedance spectroscopy measurements were performed. **Figure 8.9** shows a Nyquist plot of Nafion and TN- based nanocomposites at 100% relative humidity. The plot gives electrolytes resistance (R1) of the materials. The nanocomposite containing 0.5 wt% TNTs has the lowest R1 = 210 Ω (see **Table 8.1)**. The R1 decreases from 230 to 210 Ω with the addition of 0.5 wt% TNTs, but increases as TNT loading increases to 1 and 2 wt% (i.e., 690 and 1150 Ω). The electrolyte resistance increases as the TNT loading increases to 1.0 and 2.0 wt%. This is indicative of a decrease in proton conductivity. This suggests that the amount of TNTs strongly influence the proton conductivity of Nafion. This decrease in proton conductivity can be due to the TNT structures hindering the permeability of hydrogen ions. Whereas, the electrolytes resistance decreases when 0.5 wt% TNTs was incorporated, indicating an increase in proton conductivity compared to neat Nafion. This increase in proton conductivity is related to the increased water uptake observed with 1 wt% TNTs nanocomposite.

Table 8.1 also shows the comparison between methanol permeability and proton conductivity of the samples. The MeOH permeability of neat Nafion measured at room temperature was 2×10^{-8} $cm^2.s^{-1}$ and as 0.5 wt% of TNTs were incorporated, it remained unchanged. MeOH permeability was increased to 3×10^{-8} $cm^2.s^{-1}$ with 1.0 wt% TNT nanocomposite, and sharply decreases to 1×10^{-8} $cm^2.s^{-1}$ as the amount of TNTs increases to 2 wt%. This behavior is due to the MeOH permeability percolation threshold, which is affected by TNTs dispersed in Nafion. It can also be associated with water uptake of the nanocomposite membranes.

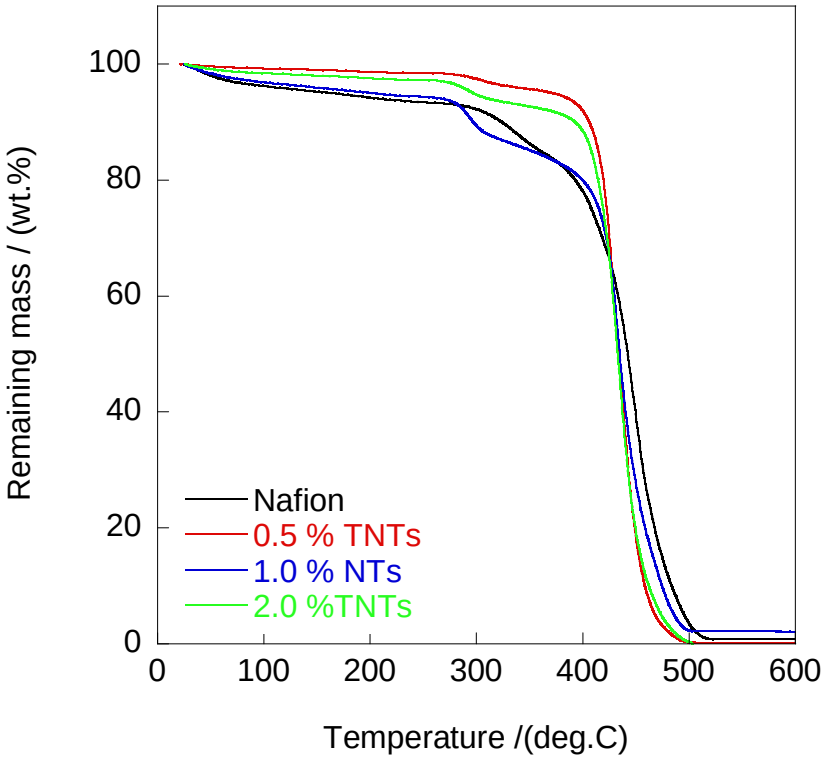

Figure 8.8 Thermogravimetric analysis scans of Nafion and TNT-based nanocomposite membranes, with different loadings measured in air at 5°C per minute.

The ratio of proton conductivity (C) and methanol permeability (P) was calculated in order to estimate the performance of these nanocomposite membranes in fuel cell applications. The calculated values of proton conductivity and MeOH permeability are shown in **Table 8.1**. A decrease in the ratio was observed with an incorporation of TNTs in difference proportions. This indicates that TNT-based nanocomposite will give poor fuel cell performances compared to neat Nafion. However, further studies will be conducted as such studies have never been done before.

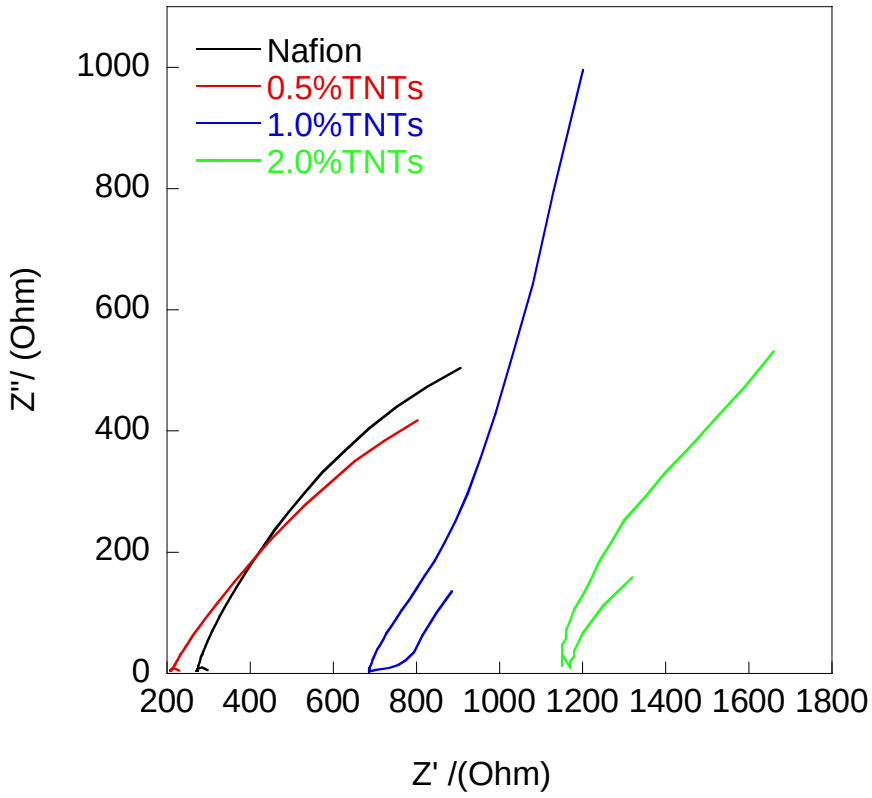

Figure 8.9 Nyquist impedance plots of Nafion and its TNT-based nanocomposite membranes, with different TNT loadings ranging from 0.5 to 2.0 wt%, measurements done at 26°C and 100% relative humidity.

Table 8.1 Proton conductivity (C) and MeOH permeability (P) values of Nafion and its TNT-based composite membranes with different TNT loadings in wt%.

Samples	**Thickness /cm**	**R1 /Ω**	**C /S.cm^{-1}**	**P /cm^2.s^{-1}**	**C/P /s.S.cm^3**
Nafion	0.020	230	0.070	$2x10^{-8}$	$3.5x10^6$
0.5	0.022	210	0.072	$2x10^{-8}$	$3.6x10^6$
1.0	0.022	690	0.022	$3x10^{-8}$	$7.0x10^5$
2.0	0.021	1150	0.014	$1x10^{-8}$	$1.0x10^6$

8.4 Conclusion

In this chapter TNT-based Nafion nanocomposite membranes were prepared in different proportions by the melt-extrusion method. Water uptake of nanocomposite membranes were higher than that of neat Nafion, with N-1.0 wt% TNTs reaching maximum of 21.5%. The highest electrical conductivity was observed with 1.0 wt% TNT nanocomposite, but remains at zero with 2.0 wt% TNT nanocomposite. The thermal stability of SO_3H groups of Nafion increases with N-0.5 and N-2.0 wt% of TNT composite. However, the thermal stability of PTFE backbone decreases with an increase in TNT content. A reduced MeOH permeability was observed with 2.0 wt% TNT nanocomposite membrane. The proton conductivity of Nafion slightly increases when 0.5 wt% TNTs and then decreases with further increase in the amount of TNTs. The best performing nanocomposite was the membrane containing only 0.5 wt% TNTs showing ionic conductivity value of 7.2×10^{-2} Scm^{-1} at 26°C and 100% of relative humidity

8.5 References

[1] J.-Z. Xu, W.-B. Zhao, J.-J. Zhu, G.-X. Li, and H.-Y. Chen, *J. Colloid Interf. Sci*. **2005**, *290*, 450–454.

[2] I. Paramasivam, J.M. Macak, and P. Schmuki, *Electrochem. Commun*. **2008**, *10*, 71–75.

[3] S.K. Hazra and S. Basu, *Sens. Actuators* **2006**, *B 115*, 403–411.

[4] J. Xu, C. Jia, B. Cao, and W.F. Zhang, *Electrochim. Acta* **2007**, *52*, 8044–8047.

[5] L. Armelao, D. Barreca, G. Bottaro, A. Gasparotto, S. Gross, C. Maragno, and E.Tondello, *Coord. Chem. Rev*. **2006**, *250*, 1294–1314.

[5b] G.M. Nun˜ez, R.J. Fenoglio, and D.E. Resasco, React. Kinet. *Catal. Lett*. **1989**, *40*, 89–94.

[6] S.C. Chan and, M.A. Barteau, *Langmuir* **2005**, *21*, 5588–5595.

[7] Y. Ishibai, J. Sato, S. Akita, T. Nishikawa, and S. Miyagishi, *J. Photochem. Photobiol*. **2007**, *A 188*, 106–111.

[8] M.M.V.M. Souza, N.F.P. Ribeiro, and M. Schmal, Int. *J. Hydrogen Energy* **2007**, 32, 425–429.

[9] L.M. Sikhwivhilu, S.Sinha. Ray, and N.J. Coville, *Appl. Phys.* **2009**, A*94*, 963–973.

[10] S. Wang, Z. Liang, T. Liu, B. Wang, and C. Zhaung, *Nanotechnology* **2006**, *17*, 1551–1557.

[11] H.W.J. Starkweather, *Macromolecules* **1982,** *15*, 320–323.

[12] S. Pavlidou and C.D. Papaspyrides, *Prog. Polym. Sci*. **2008**, *33*,1119–1128

[13] R.K.Shah, D.H. Kim, and D.R. Paul, *Polymer* **2007**, *48*, 1047–1052.

[14] T.D. Fornes and D.R. Paul, *Macromolecules* **2004**, *37*, 1793–1798.

[15] J. Wootthikanokkhan and N. Seeponkai, *J. Appl. Polym. Sci.* **2006**, *102*, 5941–5947.

[16] V. Di Noto, R. Gliubizzi, E. Negro, and G. Pace, *J. Phys. Chem.* **2006**, *B110*, 24972–24981

9

General Conclusions

9.1 Conclusions

The general connection in all the chapters is the use and synthesis of different nanoparticles as fillers for the preparation of Nafion nanocomposite membranes. The conclusions on the study of the newly developed composite membranes and their properties are described and summarized as follows:

The twin screw extruder, melt-blending method was used in this study and the processing conditions such as temperature, rotor speed, and time were kept constant for all the sample preparations. This method provides improved results in terms of thermo-mechanical properties, electro-chemical properties; methanol permeability, water uptake, and ionic conductivity compared to previously reported methods such as solvent casting and ball-milling. The improved results are attributed to the advantages, such as sheer forces, involved during processing. The system generates a shear flow and maximum separation forces on the nanoparticles when orientated in a 45 degree position.[1–2] The magnitude of the force trying to separate agglomerated particles is given in the **Appendix A4**.

Multi-walled CNTs were modified using a literature-based [3–4] method with few innovative changes in our laboratories. The modification of multi-walled CNTs has improved its interaction with Nafion membrane. This is attributed to the fact that Nafion is an inorganic semi-crystalline

polymer, with higher equivalent weight of 1100. Therefore, organically modified multi-walled CNTs are more compatible with Nafion, especially the nitric acid treated CNTs.

CNTs were dispersed in Nafion using a melt-blending technique. Nafion-CNT-composite membranes show much improved thermal stability with only 1 wt% loading of CNTs. The thermal stability of PTFE backbone of Nafion increases from approximately 400 to about 450°C after dispersed with CNTs. CNTs also favor good mechanical properties such that glass transition temperature of Nafion was increased from 140°C to about 160°C. This improved thermo-mechanical property is attributed to the good dispersion of CNTs in Nafion matrix observed with SEM. The incorporation of CNTs in Nafion polymer favors the reduction of water uptake and methanol permeability. The methanol permeability results and BET surface area values of Nafion-CNT composite membranes are tabulated in **Appendix A5**. The lowest water uptake was observed when amine functionalized CNTs were incorporated in Nafion. This is associated with the lowest BET surface area of about 39.5 cm^2/s compared to 123.5 cm^2/s for other fillers. However, CNT incorporation leads to the reduction in proton conductivity of Nafion. This is because water uptake is directly proportional to the proton conduction, such that the presence of acid OH groups on the nanocomposite membrane's surface facilitates water, which acts as a vehicle for proton migration.

The thermo-mechanical and barrier properties of Nafion were improved by dispersion C30B in polymer matrix using the twin-screw melt-blending method. However, this resulted in reduction of proton conductivity and reduced MeOH permeability. This is due to the low chain mobility of the C30B layers and the lower molecular weight compared to Nafion. However, C30B nanocomposite membranes show much improved crystallinity. This suggests that the crystalline material does not promote good impact on the ionic conductivity of the membrane.

The water uptake of TNT-based nanocomposite membranes was higher than that of neat Nafion. The thermal stability of Nafion increases with an incorporation of TNTs. A reduced MeOH permeability was observed with TNT nanocomposite membranes. The proton conductivity of Nafion slightly increases from 7.0 $x10^{-2}$ to about 7.2$x10^{-2}$ Scm^{-1} at 26°C and 100% of relative humidity, when TNTs were incorporated. This was expected as the water uptake of these

nanocomposite membranes also increases. This is also attributed to the physical properties of TNTs, such as water sorption, its 1-dimensional structure, and excellent electrochemical properties compared to other previously used nanofillers.[5–6] These results show that TNT-based nanocomposite membranes are suitable for the high operating fuel cell temperature range (100–150°C) by larger water retention properties than Nafion and higher proton conductivity. This shows a good benefit for higher temperature operation of PEM fuel cells.

9.2 References

[1] Z. Tadmor, *Ind. Eng. Fund*. **1976**, *15*, 346–373.

[2] T.A. Osswald, Polymer processing and fundamentals, *Hanser/Gadner*, **1998**, *Ch5*, 111–120

[3] J.A. Kim, D.G. Seong, T.J. Kang, and J.R. Youn, *Carbon* **2006**, *44*, 1898–1905.

[4] T.X. Liu, I.Y. Phang, L. Shen, S.Y. Chow, and W.D. Zhang, *Macromolecules* **2004**, *7*, 7214–7222

[5] M. Paulose, G. K. Mor, O. K. Varghese, K. Shankar, and C.A. Grimes, *J. Photochem. A: Chem.* **2006**, *178*, 8–15.

[6] O.K. Varghese, M. Paulose, K. Shankar, G.K. Mor, K. Gopal, and A. Craig, *J. Nanosci. and Nanotechnol.* **2005**, *5*, 1158–1165.

Appendixes

Appendixes A1 to A5 describe some of the polymer concept, conversions, characterizations and materials properties covered in this study.

A1. Constants and Conversions

Avogadro's number $N_A = 6.02 \times 10^{23}$ atoms/ mole
Electron charge $e = 1.02 \times 10^{-19}$ C
Faraday's constant = $N_A e = 9648.34$ C/mol

Concentration (1 part per million) = 1 mg/kg

A2. Bode Plots Interpretations

Phase angle (φ) is the angle between

For neat capacitor $\varphi = 90°$
For neat resistor $\varphi = 0°$
If diffusion is dominant $\varphi = 45°$
If adsorption is dominant $\varphi = 60°$

If the slope (Z *vs.* ω) = –1, that means the material has ideal capacitor behavior and if < –1 the material has pseudo capacitive behavior.

A3. Small-angle X-ray Patterns

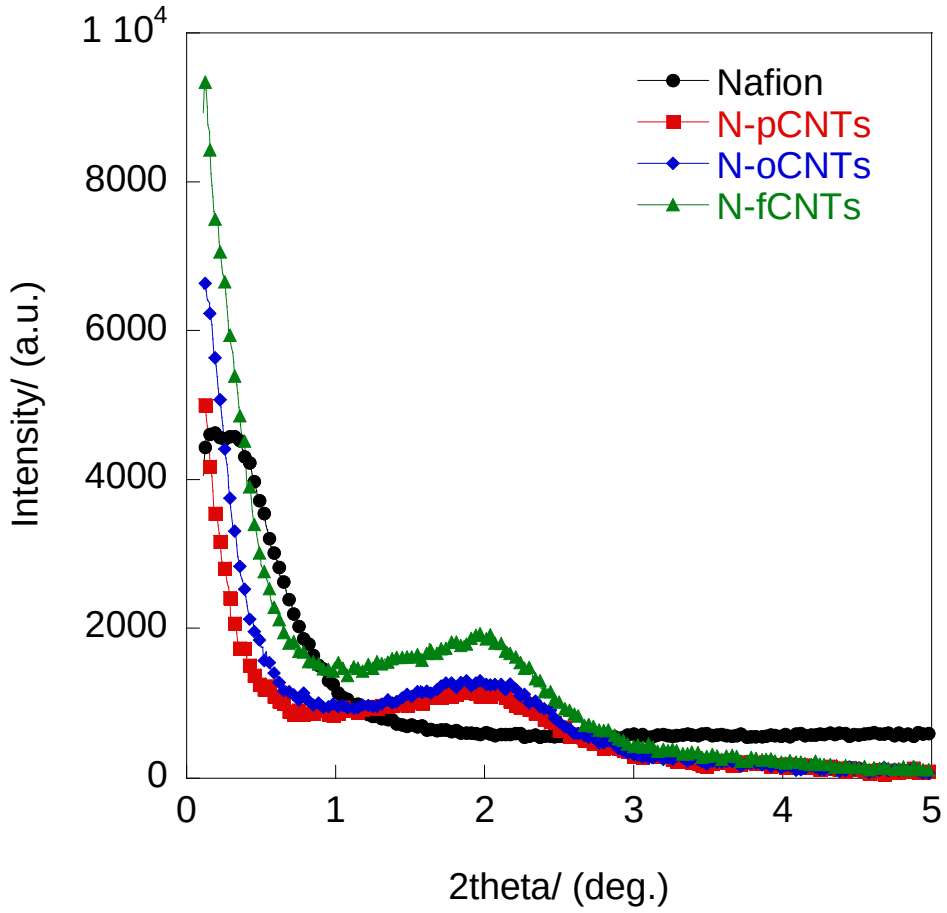

Figure A: Small-angle X-ray patterns of oxidized CNT-Nafion composites with different oCNTs loading.

A4. The Magnitude of the Forces in the Twin Extruder

When the particles are orientated in 45 degrees position, the magnitude of the forces trying to separate the agglomerate is given by:

$$F_{shear} = 3\pi\eta\gamma r^2$$

Where η is the viscosity of the carrier fluid, γ the magnitude of the strain rate tensor and r is the radii of the particles.

However, if the flow field generated by device is neatly elongational, the particles always are orientated at 0 degrees, to the position of maximum force. The magnitude of the force for this system is given by:

$$F_{elong} = 6\pi\eta\gamma r^2$$

A5. Methanol Permeability and BET Surface Area

Table A: Methanol permeability and BET surface area for neat CNTs (pCNTs), nitric acid treated CNTs (oCNTs), and amine functionalized CNTs (fCNTs)

Samples	**MeOH permeability /$cm^2.s^{-1}$**	**BET surface area /$m^2.g^{-1}$**
pCNTs	$7.63x10^{-9}$	122.95
oCNTs	$7.47x10^{-9}$	123.43
fCNTs	$4.90x10^{-8}$	39.56